TIME-OF-FLIGHT MASS MEASUREMENTS OF NEUTRON RICH ISOTOPES AT THE NSCL

By

Alfredo Estradé

A DISSERTATION

Submitted to
Michigan State University
in partial fulfillment of the requirements
for the degree of

DOCTOR OF PHILOSOPHY

Physics and Astronomy

2010

ABSTRACT

TIME-OF-FLIGHT MASS MEASUREMENTS OF NEUTRON RICH ISOTOPES AT THE NSCL

By

Alfredo Estradé

Experimental knowledge of nuclear masses of exotic nuclei is important for understanding nuclear structure far from the valley of β-stability, and as a direct input into astrophysical models. In the case of astrophysical processes involving neutron rich nuclei, such as nucleosynthesis during the r-process and the evolution of matter in the crust of an accreting neutron star, we are mostly limited to using theoretical mass models.

The time of flight (TOF) mass measurement technique allows measuring very short-lived nuclei. It has been effectively applied using the fast fragment beams produced at the A1900 fragment separator at the National Superconducting Cyclotron Lab (NSCL) to reach masses very far from stability. This dissertation presents the development of the experimental setup for time-of-flight mass measurements at the NSCL, and the results of a first experiment in the region of neutron rich isotopes around the N=32 and N=40 subshells. The mass of six isotopes was determined for the first time.

The impact of the new measurements, and of different theoretical mass models, in the calculation of electron capture processes in the crust of accreting neutron stars were studied. It was confirmed that these processes are very sensitive to the odd-even staggering predicted by the models. In addition, the new result for the mass of ^{66}Mn affects the electron capture threshold for one of the more relevant transitions in the case of a crust composition given by the ashes of carbon superbursts, and it could have important implications for the ignition depth of this type of X-ray bursts.

DEDICATION

To Michelle.

ACKNOWLEDGMENT

I would like to thank my advisor, Hendrik Schatz, who was always helpful and always had the right hint to keep my research moving in the right direction. He also provided with the opportunity to get involved in many different activities during my Ph. D. work that made for a rich and enjoyable experience.

I would especially like to thank Milan Matos, who dedicated his post-doc stay at the NSCL to work in the time-of-flight experiment. He shares a large part of the credit for the successful completion of this project.

I would like to thank the NSCL staff and outside collaborators for their help with the TOF experiment. Daniel Bazin was always available to answer my questions about the S800 spectrometer, and together with the A1900 group provided us with a nice beam during the experiment. I would like to thank Andreas Stolz, John Yurkon, and Dan Shapira for their help with designing and testing detectors. I would like to thank Jorge Pereira, Andrew Rogers, Ed Smith, Alexandra Gade, and Daniel Galaviz for their help setting up and running the experiment. In addition, Richard Cyburt and Sebastian George provided valuable discussions during the data analysis.

I would like to thank Sanjib Gupta for his enthusiastic discussions about nuclear processes in neutron stars, and Rita Lau for her help debugging network codes.

I would like to thank all my group members for the good times spent drinking mate at the atrium or beer at Harpers, including, but not limited to, Ana Becerril, Fernando Montes, Thom Elliot, Paul Hosmer, Matt Amthor, Karl Smith, Zach Meissel. I should give a especial mention to Giuseppe Lorusso; our long discussion in the office taught me the value of a timeless classic.

Finally, I would like to thank my family for being always supportive of my adventures in Michigan, and providing me, among many other things, with an adequate supply of woolen sweaters and scarfs. I am also very thankful to my wife, Michelle, whose support and encouragement at all times was so important to me.

TABLE OF CONTENTS

LIST OF TABLES

LIST OF FIGURES

Images in this dissertation are presented in color.

Chapter 1

Introduction

1.1 Astrophysics motivation

A precise knowledge of nuclear masses has been important to address questions in nuclear astrophysics since the beginning of the field. Ashton's discovery of the mass excess of hydrogen with respect to helium in his pioneering mass spectrometry experiments [1] was one of the key ingredients that led Edington and others to postulate nuclear energy as the energy source of the sun [2]. The current interest in the study of nuclear masses for astrophysics applications is centered on the masses of unstable isotopes. Radioactive isotopes play an important role in many processes in the cosmos. A precise knowledge of their properties is a necessary input for the astrophysical models that allow us to understand astrophysical observations. What is more, there are many processes for which the properties of the nuclei involved are a dominant feature. A classical example is the nucleosynthesis of the heavy elements by both the slow- and rapid- neutron capture process (the s- and r-process), where the observed pattern in the abundance of the isotopes produced is a reflection of the structure of the isotopes near and far from stability (the location of the neutron shell closures) [3].

The largest need for new nuclear mass data, at least in terms of the number of

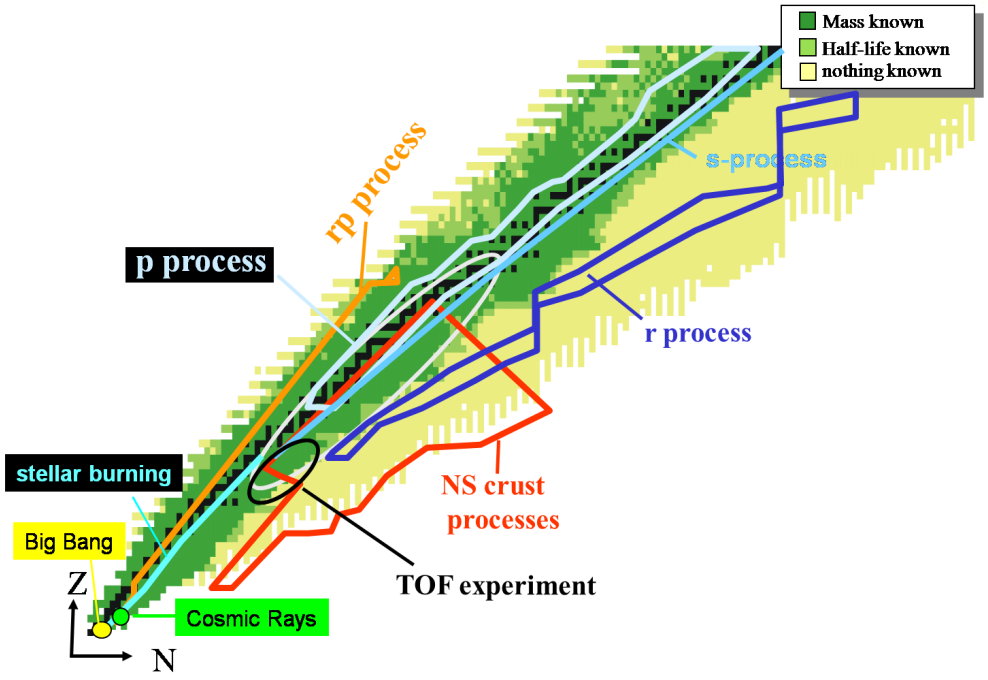

Figure 1.1: Knowledge of nuclear masses across the chart of the isotopes (data in the 2003 Atomic Mass Evaluation [4]). The region of the isotopes relevant for astrophysical calculations, and the region explored in the present time-of-flight experiment is also indicated.

isotopes involved, is on the neutron rich side of β stability [5] (Figure 1.1). The r-process, responsible for the production of approximately half of the isotopes heavier than iron in the universe, runs through a series of neutron captures and β decays that drive the nuclear composition many mass units away from stability [6]. For the path predicted by most models, which spans isotopes with A$\approx$100 up to the Uranium region, only a handful of nuclear masses are experimentally known. Another scenario involving neutron rich isotopes is that of nuclear reactions taking place in the crust of accreting neutron stars. In this case the relevant nuclear masses are those for nuclei with A$\lesssim$100, all the way from the stable isotopes to the neutron drip line [7].

On the proton rich side of β stability the knowledge of nuclear masses reaches much closer to the drip line. There are still cases where new measurements are necessary, such as for the masses near the waiting point isotopes of the rapid proton capture process (rp-process). The rp-process drives thermonuclear explosions in the surface of accreting neutron stars that are observed as X-ray bursts. The aforementioned isotopes act as a bottleneck that controls the flow of matter to heavier isotopes, and their mass must be known with a precision of about 10 keV to put strong constraints on their effective lifetime during the bursts [8].

The nuclear masses of neutron rich isotopes with A$\approx$65 were measured in the present experiment. These masses are a direct input for the calculation of crust processes in accreting neutron stars, which are discussed in more detail in the following section. Section 1.1.2 introduces the FRDM and the HFB mass models that were used in astrophysical network calculations performed to assess the impact of the new mass results.

1.1.1 Nuclear processes in accreting neutron star crusts

Low mass X-ray binaries (LMXB) are binary stellar systems formed by a compact object (often a neutron star) in close orbit with a low mass companion star, and

where matter is being transferred through an accretion process [9]. The X-rays produced when matter falls onto the surface of the neutron star makes them some of the brightest X-ray sources in the sky. X-ray observatories launched in recent years (BeppoSAX, RXTE, XXM-Newton, and Chandra) have lead to the discovery of many new systems, which now number in the hundreds, as well as exciting new phenomena. In particular, the observation of their light curves as they go into periods of quiescence, and the very energetic X-ray bursts (aptly named superbursts) discovered in a few systems, are sensitive to the nuclear physics studied in this dissertation.

Transiently accreting neutron stars are a particular subsystem of LMXB that have been observed to go from periods of actively accreting material (outbursts), to periods where the accretion process is shut off or greatly suppressed (quiescence). These periods can be of the order of years, so it has been possible to construct decay curves for the luminosity of the neutron star as it cools down during quiescence [10]. It has been proposed that the cooling curves map the thermal profile of the interior of the star [11] providing a probe into the physics processes happening in its dense interior. The thermal properties of the star are sensitive, for example, to the thermal conductivity of the solid lattice that forms the crust [12] or the presence of superfluid neutrons in the inner crust [13]. They are also sensitive to the state of matter in the core of the neutron star, and in particular its different neutrino cooling mechanisms [14]. In addition, nuclear reactions occurring in the crust of the star during accretion have been proposed to provide a significant heat source affecting the decay of the stellar luminosity when the accretions turns off [15]. All these phenomena must be well understood for a correct interpretation of the observed cooling curves.

Many X-ray binaries show fairly regular X-ray bursts produced by thermonuclear explosions that burn the accreted material by the rp-process. The rp-rpocess operates on the surface of the star and it burns the accreted H and He into heavy isotopes with masses up to A$\approx$104 [16]. In a few systems some very energetic X-ray bursts

have been observed. These so called superbusts are about 1000 times more energetic than regular X-ray bursts, they last for about one hour instead of tens of seconds, and have recurrence times of years. The most widely accepted explanation for the superbursts is unstable burning of the carbon remaining in the ashes of regular bursts, which ignites in a deeper layer of the star [17]. The depth at which the burst occurs has been inferred from the observed light curves. However, it is about an order of magnitude smaller than the ignition depth for carbon calculated from current models of the crust. A possible solution for this discrepancy is that nuclear reactions in the crust of the star can provide more heating than currently assumed in the models. This would allow for carbon ignition at smaller densities and bring the calculations in better agreement with the observations [18].

However, the nuclear physics of crustal heating is not well understood. One critical quantity are nuclear masses - they set the thresholds for electron captures and therefore the depth distribution of heat sources. The threshold differences of consecutive captures, and in particular the odd even staggering of electron capture thresholds in even A electron capture chains, together with the excitation energies of the final states, directly determines the amount of heat released. The details of the process are discussed together with the astrophysical simulations presented in Chapter 6. The relevant nuclei are neutron rich isotopes ranging from near stability to the neutron drip line. Of particular interest is the mass range of the nuclear composition resulting from superbursts. These so called superburst ashes set the initial composition for the process in systems that show superburst behavior, and have been shown to lie in the range of A=48-68 [19]. The results from this work cover part of the relevant mass region, and extend our knowledge of masses along the reaction paths of neutron star crust processes. In chapter 6 the impact of nuclear masses in calculations of the crust of accreting neutron stars is discussed in detail.

1.1.2 Mass models

Mass models are an essential tool for astrophysics calculations, as many relevant isotopes do not have experimentally known masses. The measurements of the mass of unstable nuclides historically advanced at a pace of about one mass unit away from stability per decade, which is a consequence of the rapid drop in the yields of the more unstable isotopes in the production of radioactive ion beams [20]. The situation has been improved by recently completed and planned radioactive ion beam facilities, such as RIBF at RIKEN, FRIB at MSU, and FAIR at GSI, as well as with the development of new experimental techniques, but several of the masses required for astrophysical calculations are not expected to be measured in the foreseeable future [5].

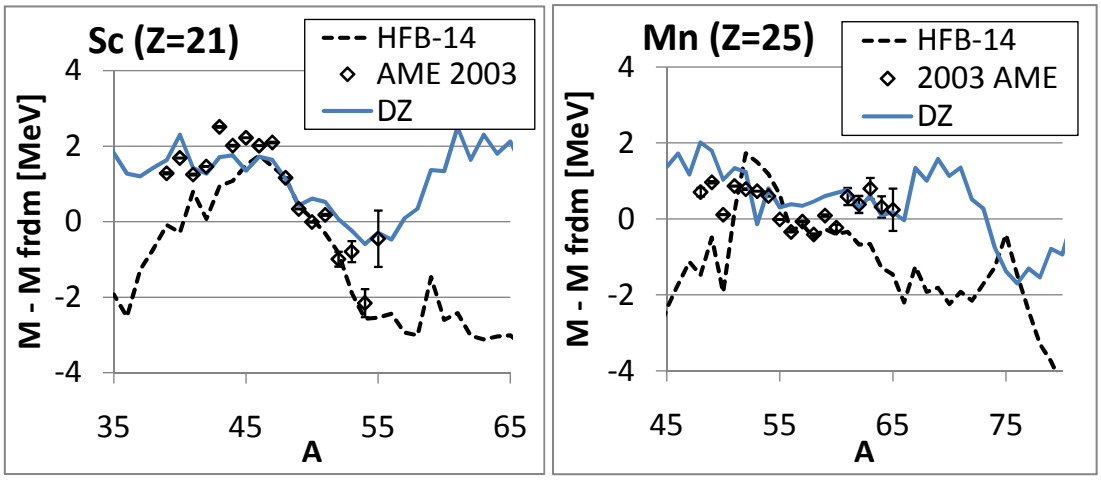

Figure 1.2: Mass results for the FRDM [21], HFB-14 [22], and Duflo-Zucker [27] mass models are compared to the data in the 2003 Atomic Mass Evaluation [4]. The nuclear masses are shown with respect to the FRDM model (zero). There is an increasing divergence of the mass predictions as one leaves the region of known data.

Global mass models constructed from a semi-empirical formula fit to the known masses are most commonly used in astrophysics applications. All the models available provide a similar fit to the known data, but their results rapidly diverge when the formulas are used to predict unknown masses (Figure 1.2). In this work two models will be compared to the experimental results and used for the calculations of nuclear

processes in accreting neutron stars: the Finite Range Droplet Model (FRDM [21]) and the Hartree-Fock-Bogoliubov (HFB-14 [22]) mass models. These represent the two main theoretical approaches for the construction of a mass model. FRDM belongs to the class of the so called microscopic-macroscopic models that use Weizsacker's liquid drop model [23] as a basis for the model, and then add microscopic correction terms to account for the details of the nuclear structure. The HFB-14 model belongs to the class of microscopic models that rely on a simplified solution of the nuclear many-body problem, and they usually use some model form for the functions and an effective interaction for the nuclear forces.

The nuclear binding energy calculated with the liquid drop model, using the formula adjusted by Bethe and Bacher [25], is as follows:

$$E_B(N,Z) = \alpha_1 A - \alpha_2 A^{2/3} - \frac{3e^2}{5r_0} Z^2 A^{-1/3} - \alpha_3 (N-Z)^2/A \qquad (1.1)$$

The term linear in A scales with the nuclear volume and provides the main binding energy. The second term, proportional to $A^{2/3}$, represents the decrease in the binding energy for the protons and neutrons on the surface for the nucleus, and the third term is the decrease on binding energy due to Coulomb repulsion. The final term, which scales with $(N-Z)^2$, is represents the symmetry energy due to the isospin dependence of the nuclear force. When this formula is fitted to the known masses it provides a remarkably good description of the data considering its simplicity. The RMS deviations from the known masses are $\sigma \approx 3$ MeV. However, there are clear trends in the residuals that reflect the elements of the nuclear structure that are left out (for example, the shell effects).

The macroscopic part of the FRDM model [21] uses the basic idea of the liquid drop formula (1.1) but it is modified to include a "droplet model". This droplet model includes two additional degrees of freedom: the nucleus is allowed to compress and change its density, and surface effects are introduced by allowing the surface density

to be different than in the bulk of the nucleus (a neutron skin can emerge). The microscopic components of the model are introduced as a Strutinsky correction for the shell effects, and a Wigner term to account for the additional binding observed in the N=Z isotopes. The final microscopic element of the model introduces the pairing correlations. Pairing describes the fact that nucleons in time-reversed single particle states tend to couple to a total angular momentum of zero, and is in large part responsible for the observed odd-even staggering of the nuclear binding energy. Pairing is introduced using a *seniority* scheme for the pairing force, which is treated with the BCS approximation. The emphasis on fitting the pairing interaction is put on reproducing the pairing gap across all nuclei, rather than on the pairing force itself [5].

In the Hartree-Fock-Bogoliubov models an approximate solution for the quantum many-body problem $H\Psi = E\Psi$ is obtained by the variational method. The model uses single-particle wave functions as the trial functions for the minimization of the energy:

$$E = \langle \Phi \mid H \mid \Phi \rangle \tag{1.2}$$

The wave functions are antisymmetrized by a Slater determinant $\Phi = \det(\phi_i(x_i))$. To make the problem tractable an effective Hamiltonian is adopted:

$$H^{eff} = -\frac{\hbar^2}{2M} \sum \nabla_i^2 + \sum v_{ij}^{eff} \tag{1.3}$$

A 10-parameter Skyrme force is used for the mean field part of the interaction (v_{ij}). The pairing correlations are treated with the Bogoliubov method introducing a pairing force $V_{\pi q}\delta(r_{ij})$ in the Hamiltonian. Therefore, pairing effects are also included in the variational step of the mass fit and are treated on the same footing as the Skyrme forces. In addition, a Wigner correction is added to the resulting binding energy, and because the total angular momentum is not conserved in the non-spherical field

a spurious rotational energy has to be subtracted. There have been several HFB formulas published by the same collaboration since 2002 [26]. In the HFB-14 version [22] used in this work a phenomenological term was added to adjust a vibrational correction at large deformations, and it resulted in a better fit to the experimental data on fission barriers.

Both the FRDM and the HFB-14 have similar RMS deviations from the measured masses used to fit the mass formulas. It is $\sigma = 669$ MeV for the FRDM model, and $\sigma = 792$ MeV for the HFB-14. Since the FRDM model was published in 1995, it was fit to a smaller subset of the data used in the HFB-14 case (published in 2007). Nonetheless, the masses predicted by the FRDM model agree very well with the results of experiments performed after 1995 (the mass residuals are not increased for the extrapolations). However, the major part of these new masses have been measured in the proton rich side of β-stability where both models perform better. The FRDM mass model is also the one most commonly used in astrophysical calculations.

There are several more models in the market, as well as other approaches to the problem (a good review is presented in Lunney et al. [5]). As an example, the results of the Duflo-Zuker [27] model are also included in Figure 1.2. This is the global mass formula that provides the smallest root-mean-square deviation to the experimental data ($\sigma = 360$ keV), but it has some important disadvantages; namely that it only provides information on the ground state energy. There are other nuclear physics properties important for astrophysics calculations where it is an advantage if the necessary data can be calculated in a consistent way with one theoretical mass model. For example, fission barriers for the heavy isotopes are important to calculate fission rates for the r-process [24]. Besides, the physical origin of the terms in the Duflo-Zuker, and other models, is not as transparent as is the case for the FRDM and the HFB mass models. In general, there is no consensus on what is the best model to use for extrapolations of nuclear masses beyond the known data, and more mass

measurements are necessary to test the different models.

1.2 Nuclear physics motivation

Since the mass is a fundamental property of the nucleus - its ground state energy - it reflects many interesting properties of its structure. Nuclear masses play an important role as a diagnostic tool for nuclear structure far from stability.

In particular, studies of the systematic trends in the masses across the chart of the isotopes are an important complement to other techniques, such as measurements of excited states in even-even nuclei and interaction cross sections. One of the most surprising results these studies have led to is the appearance and disappearance of the magic numbers of the nuclear shell model. There is now considerable evidence for a new magic number at N=32 for nuclides with four or fewer protons in the $\pi f_{7/2}$ orbital. The first hints came from the study of excited states in the Ca to Ti region (see [29] and references therein). Recent precise mass measurements of Cr isotopes in ISOLTRAP [30] confirmed changes in the nuclear structure in this region. They detected change in the slope of the two neutron separation energies (S_{2n}), which are about 400 keV larger for isotopes beyond N=32 (compare to the trend followed by lighter isotopes). It was also predicted that the continued monopole shift of the $\nu f_{5/2}$ orbital may also lead to the development of a shell closure at N=34. However no evidence for such a shell closure in Ti isotopes was reported, and β-decay studies of $^{53-56}$Ca were inconclusive in respect to its existence [29].

The nucleon number 40 has also been postulated as a subshell closure. The effect has been determined for ^{90}Zr (Z=40, N=50), but there is conflicting evidence for the nature of the N=40 subshell. From spectroscopic and β-decay and Coulomb excitation studies it was found that ^{68}Ni (Z=28 and N=40) shows some properties of doubly magic nuclei [28, 31], but the effect of a N=40 closure seems to diminish rapidly in nearby isotopes [32]. This question motivated recent precision mass measurements,

of Ni, Cu and Ga isotopes at ISOLTRAP [33], Ni and Cu isotopes at JYFLTRAP [34], and Fe and Co isotopes at LEBIT [43]. A weak localized subshell closure was observed for ^{68}Ni, confirming spectroscopic results.

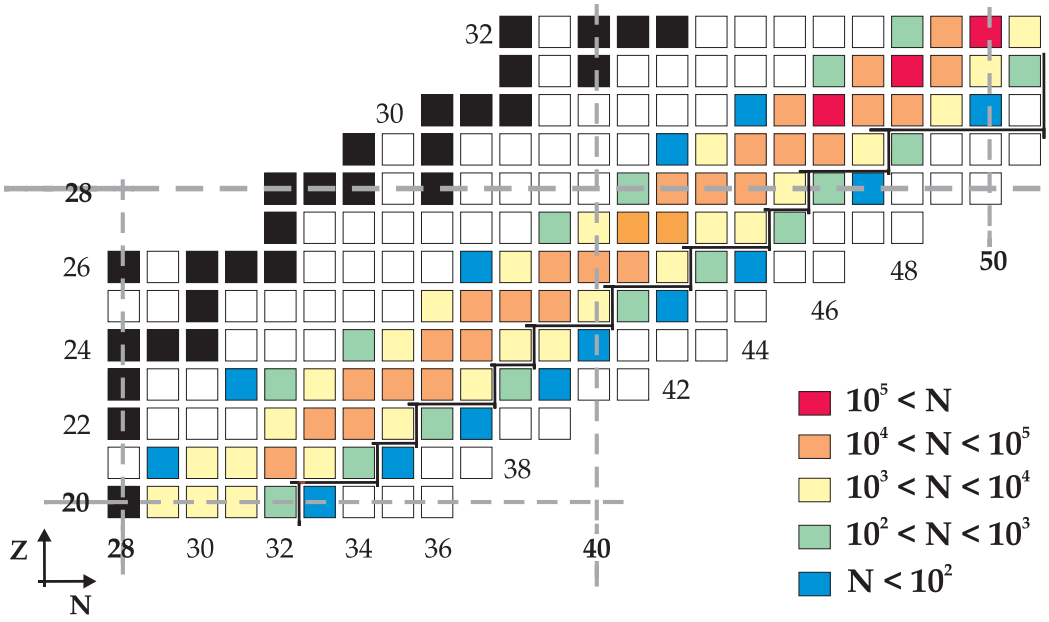

Figure 1.3: Region in the chart of the nuclides covered in the present time-of-flight experiment. The colored chart shows the number of events observed for each isotope in the secondary beam during the present time-of-flight experiment. Stable isotopes are indicated in black, and the solid black line indicates the limit of previously measured masses (Section 1.3).

The present work extends the reach of experimental masses in the region (Figure 1.3), since six new masses are presented and the uncertainty in the mass of ten other isotopes is reduced. In particular the mass of a few isotopes across the possible closure at N=34 was measured: the uncertainty in the masses of ^{55}Sc (Z=21 and N=34) and ^{57}Ti(Z=22 and N=35) is significantly reduced, and the mass of ^{58}Ti (Z=22 and N=36) is measured for the first time. In addition, a new mass was measured for ^{65}Mn, which is the first measurement beyond N=40 for the Mn isotopic chain.

1.3 Previous measurements

The most complete source of information on nuclear masses is the Atomic Mass Evaluation (AME), which was most recently published in 2003 [4]. Besides a compilation of all previous measurements this work checks the consistency between all the published experimental masses. This is important when data from different experiments have to be combined, for example for an astrophysical calculation, or to be used as reference masses in the calibration of an experimental setup (Section 4.5.1).

The masses of most of the neutron rich isotopes identified in the secondary beam of our experiment (Figure 1.3) have been previously measured. This is of critical importance for this work, where new masses are measured relative to a set of reference masses. The different techniques used and the precision of these earlier measurements illustrate the variety of methods available to determine nuclear masses.

The masses of most isotopes observed in the present work have been measured with the SPEG spectrometer in GANIL (for isotopes up to Ca) [35, 36] and the TOFI spectrometer at Los Alamos (reaching masses up to Cu) [37, 38]. The time-of-flight technique has also been applied in this work. The basic principle is to determine the mass of a nucleus by the simultaneous measurement of its momentum and velocity, the momentum being determined by the rigidity of the ions in a magnetic system and the velocity by the time it takes the nucleus to pass between two detectors located at some distance from each other.

A number of masses for Zn, Ga, and Ge, and a few isotopes of V, Ti and K have been measured with the β-endpoint technique at the Studsvik facility [39]. This technique determines the beta decay Q-value from the maximum energy of the continuous energy spectrum of the emitted electrons. If the mass of the daughter nucleus and the decay scheme is known, the mass of the parent can be determined from the Q-value. The time-of-flight and β-endpoint techniques produce masses with a similar uncertainty, ranging from about 100 keV to close to 1 MeV for the most neutron rich

isotopes measured with time-of-flight experiments.

Closer to stability, more precise mass measurements are possible with Penning traps and reaction spectroscopy experiments. Several neutron rich isotopes in the Ca region have been measured with different reactions using ^{48}Ca as a target [40, 41, 42]. The most precise measurements available are from Penning traps. As mentioned in the previous section, several masses in the region of Fe to Ga have recently been measured with ISOLTRAP [33], JYFLTRAP [34], and LEBIT [43].

1.4 The time-of-flight mass measurement technique

Precise time-of-flight mass measurement experiments were developed at GANIL using the high resolution SPEG spectrometer [44]. In their experimental campaigns a large number of neutron-rich isotopes in the regions of N=20 and N=28 have been measured for the first time. An experimental program for time-of-flight mass measurements was also established at the TOFI spectrometer at Los Alamos, which was designed with the purpose of performing this type of measurements [45]. Time-of-flight experiments have also been performed at the Experimental Storage Ring (ESR) at GSI, where the increased flight path of the ions turning around the ring provides measurements with a very good resolution [46]. The largest resolving power ($\sim 2 \times 10^6$) has been obtained with the Schottky mass spectrometer method, but it requires a few seconds to cool the ions in the beam placing some limitations on the half life of the isotopes accessible in such experiments. This limitation can be overcome when the ESR is operated in isochronous mode and a mass resolving power of 1×10^5 is achieved.

The time-of-flight technique is very sensitive in the sense that it requires the lowest beam intensities to determine a mass. The mass of an isotope can be determined with statistics as low as several hundred events, so the technique is suitable to measure isotopes with production rates bellow 0.01 particles per second. In addition, and there is practically no limitation on their half lives because the time of flight is typically

$< 1\mu$s. It also has the advantage that several new masses can be determined in a single experiment, so the technique is suitable to efficiently map the mass surface in regions far from stability.

The mass of a nucleus is derived from the equation of motion of the ion through a magnetic system, by a simultaneous measurement of their velocity and momentum:

$$B\rho = \frac{\gamma p}{q} = \frac{\gamma m_0}{q}\left(\frac{L}{TOF}\right) \tag{1.4}$$

In this equation Bρ is the magnetic rigidity of the beam particles, which is equivalent to their momentum p per unit charge q; γ is the Lorentz factor, and m_0 the rest mass of the ions. The velocity is determined from the measurement of the time of flight TOF along the flight path L.

The central Bρ is selected by the strength of the field of the beamline dipole magnets. Beamline systems usually have a finite Bρ acceptance, and particles with different Bρ will have different momenta and follow trajectories with slightly different path lengths. Therefore, in many cases, such as the present work, the Bρ of each particle is measured (relative to that of a reference trajectory) to correct the measured TOF for the spread of velocities in the beam particles.

Reference isotopes with previously known masses provide a calibration for the correlation between the time of flight and the mass. In addition, they are used to correct systematic errors that affect the measured time of flight, for example due to energy losses in the beamline detectors and beam optics effects.

The resolution achieved with this technique is dominated by the resolution of the timing detector system and is typically 1×10^4. This results in a mass uncertainty of (~ 200 keV) in the mass region of A ~ 70 and statistics of a few thousand events.

This dissertation presents the development of the experimental setup for time-of-flight mass measurements at the NSCL. The setup is similar to the one used in GANIL, but it was adjusted for the constraints of the S800 spectrometer at the NSCL. The

details of the setup are discussed in Chapter 3. The results of a first experiment in the region of neutron rich isotopes around the N=32 and N=40 subshells are discussed in Chapter 4 and 5.

Chapter 2

Time-of-flight detectors

The dominant contribution to the mass resolution in the present experiment experiment comes from the resolution of the timing detectors. The desired mass resolution is $\sim 1 \times 10^{-4}$, as it would allow for the determination of nuclear masses with an uncertainty of a few hundred keV if the statistics are a few thousand events. The time of flight (TOF) of the beam particles in the NSCL setup, which is described in detail in Chapter 3, was between $440\,\text{ns} \lesssim \text{TOF} \lesssim 480\,\text{ns}$, so a detector system with a resolution better than 50 ps is necessary to achieve the desired mass resolution. Throughout this chapter, the values given for the detectors resolution represent the root mean square deviation (σ) in their measurements.

Another desirable characteristic for the beamline detectors is that they would have a small thickness. Energy and angular straggling on materials in the beam path generally increase the emittance of the beam and affect the achievable TOF resolution. Because the interaction of the beam particles with matter strongly depends on their nuclear charge (Z^2), the energy loss in the detectors can also introduce systematic shifts in the TOF for different elements.

2.1 Detector design

Timing detectors made with fast scintillating materials and photomultiplier tubes (PMT) provide very good timing characteristics with large detection efficiency, as well as the ability to sustain high count rates. The molecules in an organic scintillator get excited by interacting with the beam particles, and a light signal is produced in the material by the photons emitted in their deexcitation. The surface of the PMT in contact with the scintillator contains a photocathode. When the photons reach this surface they trigger electron emissions by the photoelectric effect. This electron signal is then accelerated and amplified by the PMT in a series of dynode stages that are held at a differential high voltage [47].

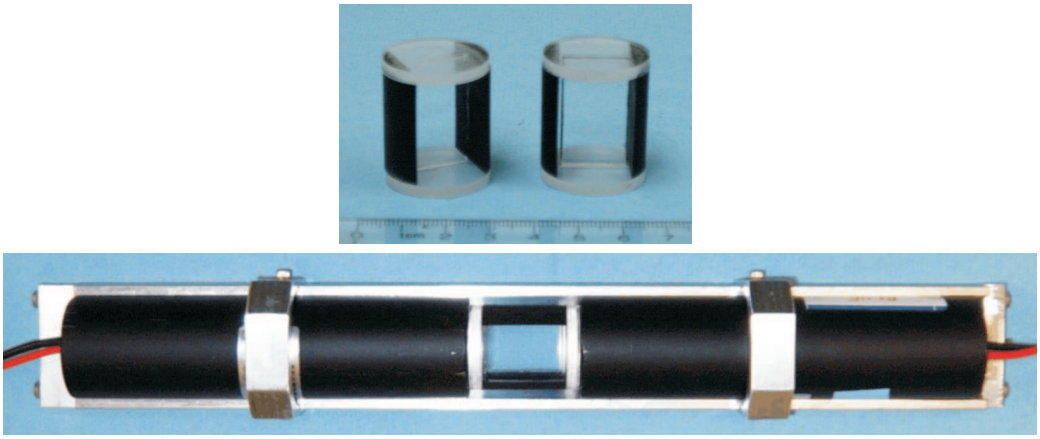

Figure 2.1: Fast timing scintillator detectors assembled for precise time-of-flight measurements. The top panel shows an image of the plastic mount that holds the thin scintillating material (0.254 mm thick BC418 plastic). The lower panel shows the detector assembled in its final configuration. Silicon pads are used for optical coupling of the scintillator to the two R4998 PMTs, which are held together by the pressure applied with plastic screws at each end of the mount.

Timing scintillators were constructed following a design similar to the work done in reference [48], which describes a systematic study of such timing detectors and presents resolutions as good as 10 ps. Figure 2.1 shows a picture of the time-of-flight scintillators. Each detector consists of a small rectangular piece of scintillating material read with fast photo-multiplier tubes in both ends. The scintillating material

used was a BC418 plastic from Saint-Gobain crystals, which is characterized by fast photon emission (signal rise time of 0.5 ns). The small area of the detector (1.5×2.54 cm) minimizes the spread of the light signals as they travel to the PMTs. In addition, the edges not attached to a PMT were roughened and covered with black aerosol paint to avoid light reflections inside the scintillator. Both a 1 mm and a 0.254 mm thick detector were considered, but the thinner scintillator produced sufficient light output during the test run to obtain a good timing resolution, therefore it was the one used.

The light signals were collected by two Hamamatsu R4998 PMTs, which were attached to each side of the scintillator using silicon pads for optical coupling. The short rise time of these PMTs (0.7 ns) resulted in a signal with fast rise time (less than 1 ns). The PMTs assembly was Hamamatsu's H6533, which provides magnetic shielding of the PMT. The model commercially available has a foam filling of the magnetic shielding case, and the PMTs were found to spark when biased under vacuum (the air trapped in the foam does not allow for a low enough vacuum near the detector). PMTs assembled without this foam were specially ordered for this experiment. The detector was placed in an aluminum mount that provided ample contact with the case of the PMT and helped cooling the detectors when operated at high voltage. The mount also supported a 2 cm copper block that collimates the beam to the area of the scintillator.

2.2 Primary beam test run

The performance of the detectors was tested using a heavy ion primary beam at the NSCL. The setup for this test run is shown in Figure 2.2. A ^{124}Xe beam with energy of 140 MeV/u was produced by the NSCL coupled cyclotrons and directed at the timing detectors installed in the N3 vault for their test. The experimental setup is shown in Figure 2.2, and a diagram of the electronics is shown in Figure 2.3. The signal from each PMT was divided using passive two-way splitter modules to obtain a

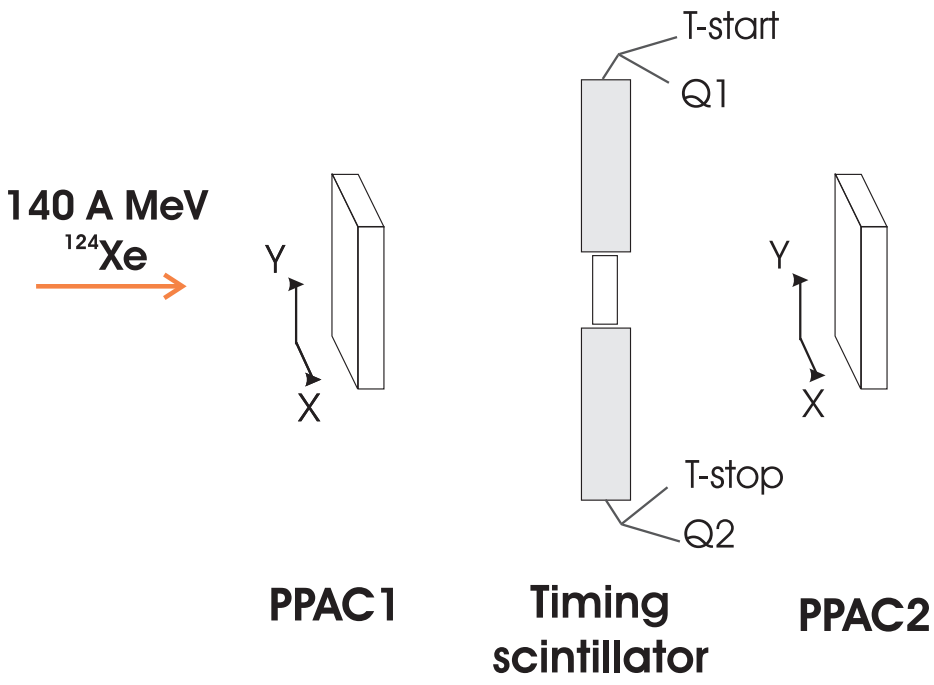

Figure 2.2: Detectors setup for the test run of timing scintillators with primary beam. A ^{124}Xe beam was produced by the NSCL coupled cyclotrons. The signal from each photomultiplier tube was split for a time and charge integral measurement. Position sensitive PPAC detectors upstream and downstream from the timing scintillator provided beam tracking.

simultaneous time and amplitude measurement. The signal used for timing was sent to a constant fraction discriminator (CFD), which produces a NIM logic pulse whose timing ideally is independent of the input pulse height. The time difference of the logic pulse corresponding to one PMT versus the delayed pulse from the second PMT was then digitized using a time-to-amplitude converter (TAC) and a amplitude-to-digital converter (ADC) module. The amplitude of the other fraction of the analog PMT signal was measured by integrating its charge (Q) with a charge-to-digital converter (QDC) module. The position of the point of interaction of each beam particle with the plastic scintillator was calculated from the position measurement in two position sensitive parallel-plate avalanche counter (PPAC) detectors [49] placed at both sides

of the scintillator.

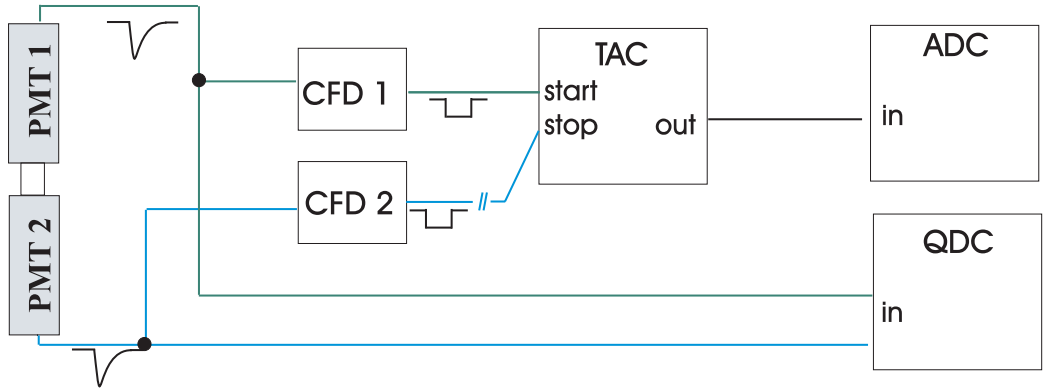

Figure 2.3: Diagram for the electronics used during the timing scintillator test run. The analog signal from each PMT was converted into a NIM logic pulse by a Tennelec 455 CFD, and an Ortec 566 TAC and an Ortec AD413 were used to digitize their time difference. The pulse of the PMT2 was delayed by $\sim$ 13 ps. The amplitude of each PMT signal was also recorded by a Phillips 7166 QDC.

A few spectra summarizing the behavior of the timing detector are shown in Figure 2.4. The time between the signals from each PMT is correlated with the vertical position (y), which measures the distance from the point of interaction of the beam particles with the plastic to the surface of each PMT. The difference between the measured times is explained by the time it takes the light signal to arrive to each PMT, and this effect has to be taken into account to obtain a timing resolution of tens of picoseconds. Furthermore, it is important to understand the relationship between the time difference and the y position. If the relationship is linear, the delay introduced by the light travel time can be corrected simply by averaging the time from each PMT, and there is no need for extra corrections. However, during the time-of-flight experiment the detector's signals had a wide range of amplitudes because of the many different isotopes in the secondary beam (the energy deposited in the scintillator goes as Z^2), and for some of them a dependence of the timing on the signal amplitude was present (Section 4.3.1).

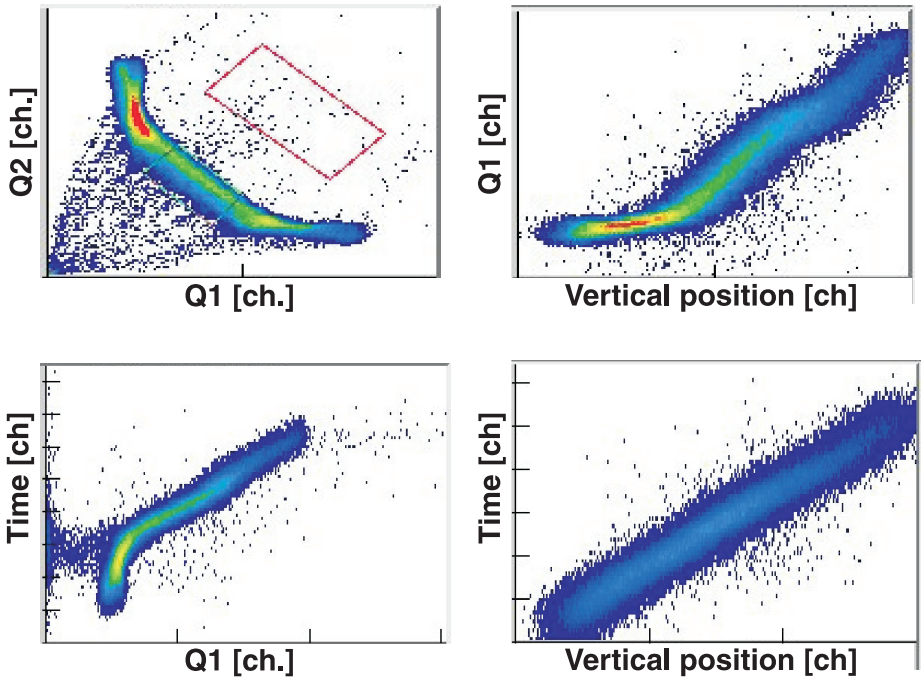

Figure 2.4: The upper panels show the correlations between the signal amplitude (Q) recorded in each PMT, and between the vertical position in the plastic scintillator and the signal amplitude in the PMT1. The spectra in the lower panels show the time difference between the signals from the photomultiplier tube PMT1 (start) and PMT2 (stop) as a function of the signal amplitude in one PMT and the vertical position in the plastic scintillator. They correspond to a run with a bias voltage of -1.6 kV of the PMTs. In this run the width of the time spectra obtained using a linear correction for the vertical position is 26.5 ps (Figure 2.6).

2.2.1 Photomultiplier tubes voltage

The voltage in the PMTs was varied from -1.2 kV to -2.0 kV in the test run (the maximum rating for the R4998 is -2.5 kV). A large operational voltage will increase the electron gain in each dynode stage and result in signals with larger amplitude. Since the rise time does not change significantly, this could improve the time resolution because a steeper signal is less sensitive to electronic noise (jitter). On the other hand, in experiments with a high count rate and heavy ions that produce a large light signal it is desirable to operate at a low voltage to avoid a large current in the PMT. The resolution was measured as the standard deviation (σ) of the time spectra for events

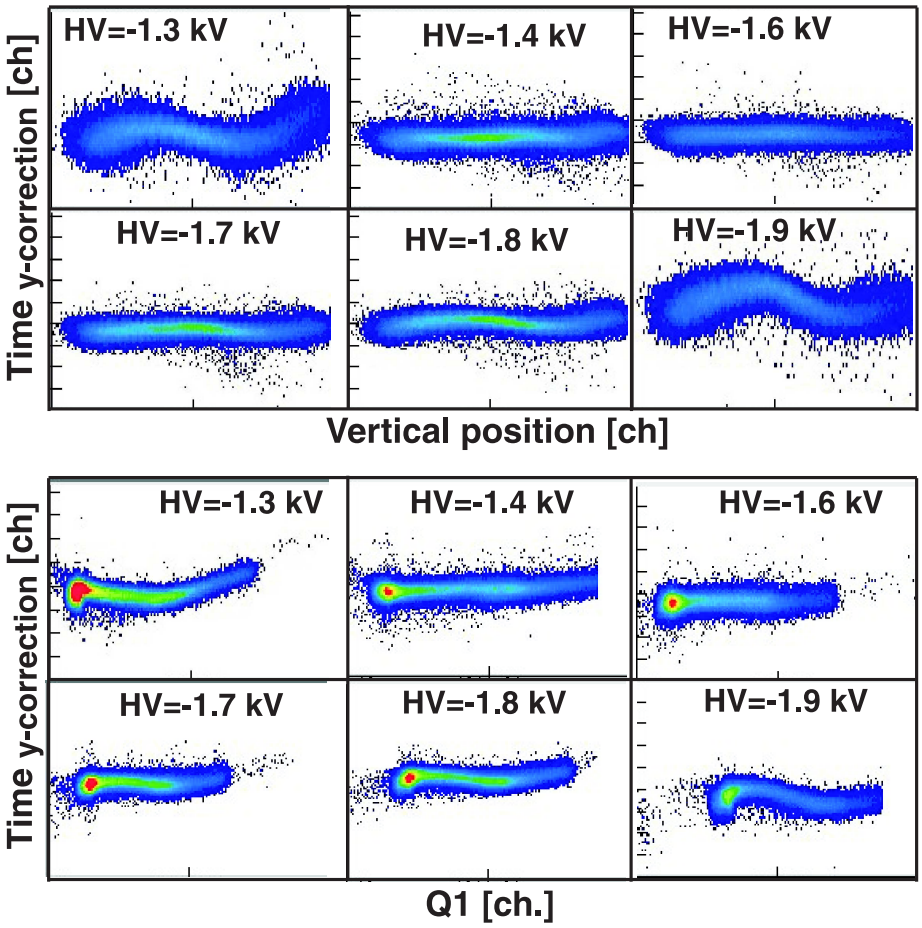

Figure 2.5: The top panel show the spectra for the time difference between the signals in each PMT as a function of the distance from the stop PMT. The lower panel shows the time difference as a function of the integrated charge in the start PMT ($Q1$). In both cases the time was corrected by subtracting a linear function of the position (Equation 2.1). Uncorrected time spectra are shown in Figure 2.4. The measured timing resolution for each voltage is shown in Figure 2.6.

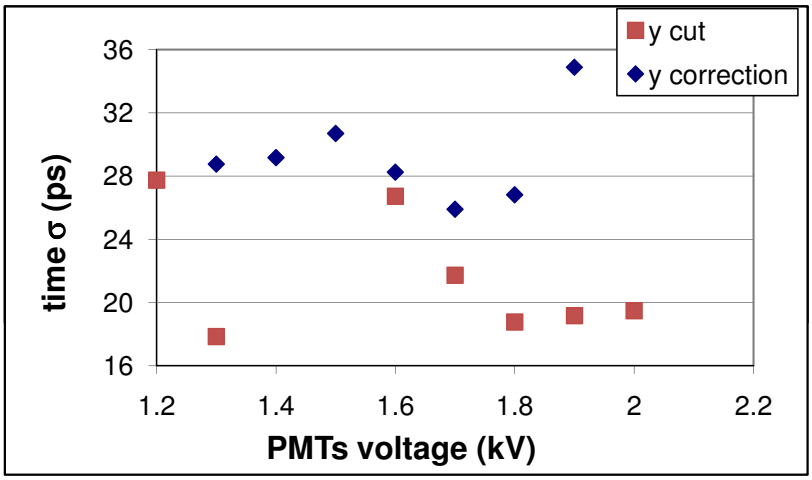

Figure 2.6: Time resolution measured as the standard deviation (σ) of spectra for the time difference between the signals of both PMTs of the detector. The width was measured for events in a narrow band in the middle of the plastic scintillator (red squares), and for the time corrected with a linear function of the vertical position in the scintillator (blue diamonds). For -1.3 kV PMT bias the position dependence of the time cancels out with its pulse height dependence for events in the middle of the detector, and this explains the narrow width measured (see Figure 2.5).

on a narrow region at the middle of the scintillator. It was observed to improve by increasing the voltage up to -1.8 kV but it was roughly constant for higher voltages (Figure 2.6). In all cases σ for the position gated time spectra was smaller than 30 ps.

Changing the PMT bias voltage affects the nature of the correlation of the measured time with the y position and with the integrated charge Q. For voltages from -1.4 kV to -1.7 kV the measured time difference is a linear function of the vertical position at the plastic scintillator. For higher and lower voltages there is an additional dependence of the timing on the signal amplitude, which results in a nonlinear time vs y spectra (Figure 2.5). This could result from the CFD module, whose settings were kept constant, not functioning properly for a wide range of signal amplitudes (see next section). The time resolution was also obtained from time spectra that were corrected by a linear function of the y position:

$$time_{\text{y position}} = time + a_{\text{HV}} \cdot y_{\text{position}} \tag{2.1}$$

The slope a_{HV} was fit to the time vs position spectra for each high voltage value. As expected, the width of the corrected time spectra that showed additional correlations with the signal amplitude increases with respect to the width of the spectra gated on a region in the center of the scintillator. For the voltage settings where the correlation of time and y position is linear both widths are comparable. These results are shown in Figure 2.6.

2.2.2 Constant fraction discriminator settings

In precise timing applications there are two main techniques that can be used to avoid a time dependence on the amplitude of the detector analog pulse (an effect referred to as walk). One option is to use a leading edge discriminator, which produces a standard NIM logic pulse once the signal rises above a certain threshold, and correct

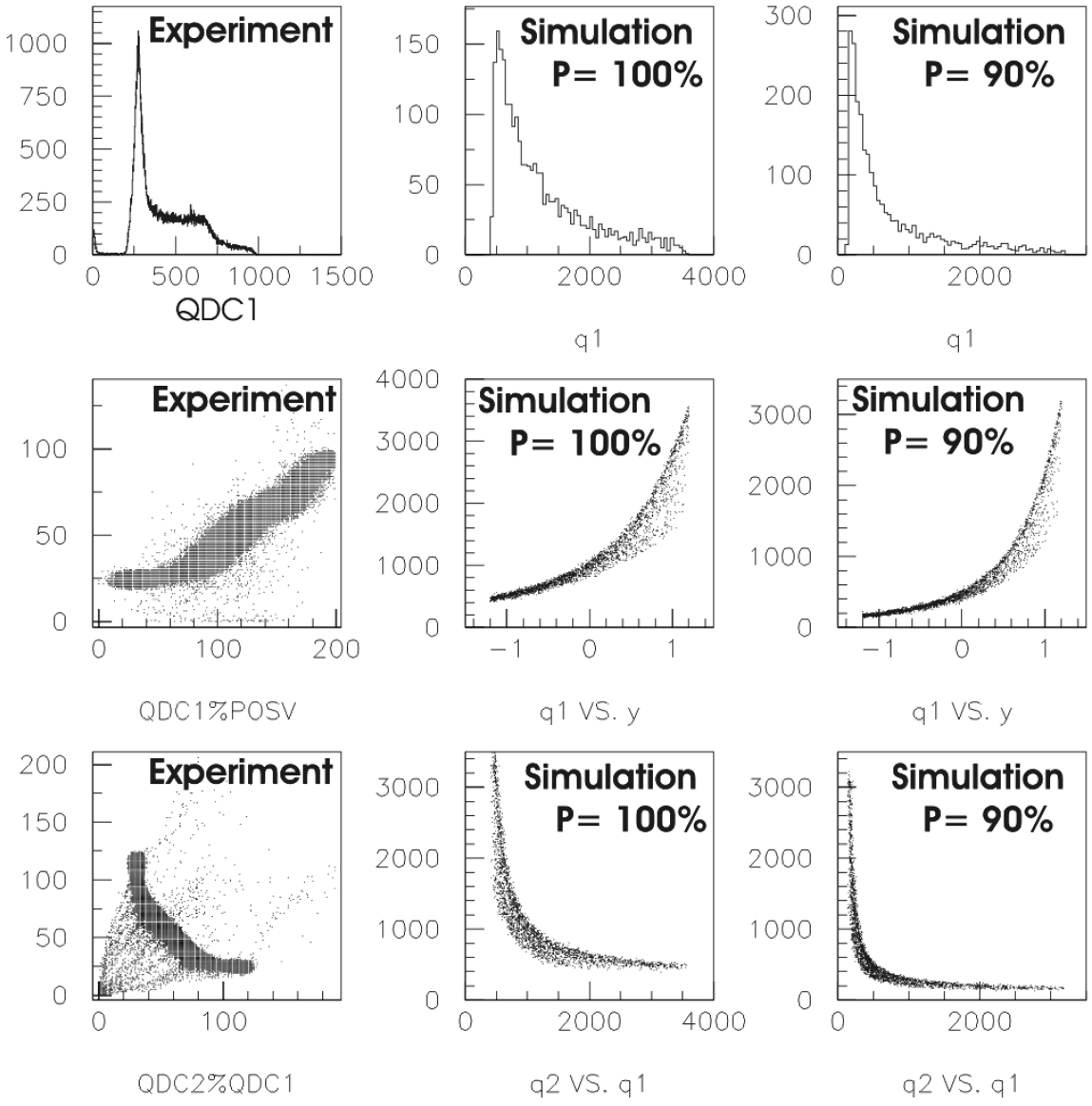

Figure 2.7: The spectra on the left show experimental data for the signal amplitude of PMT1 ($QDC1$) as a function of y position in the plastic scintillator ($POSV$) and the signal amplitude of the second PMT ($QDC2$). The figures in the center and right columns were constructed with a Monte Carlo simulation of the photon transport to the PMTs surface. In this simulations, 4000 beam interactions were randomly distributed in the plastic scintillator volume, and for each of them the emission of 70000 photons in random directions was tracked. The amplitude of the signal from each PMT (qi) was considered as being proportional to the number of photons arriving at their surface. The difference between the simulation shown in the center column ($P = 100\%$) and the left one ($P = 90\%$) is the probability P of reflection when a photon hits the surface of the plastic scintillator at an angle bellow the critical one.

the time by a simultaneous measurement of the signal amplitude. On the other hand, a constant fraction discriminator (CFD) works by splitting the analog signal in two and subtracting a delayed and attenuated component from the other fraction of the signal. If the rise time of the detector signal is independent of its amplitude, the internal bipolar signal of the CFD crosses the baseline at a point that is independent of the original amplitude (the zero-crossing point). This question is relevant to a time-of-flight experiment where the secondary beam usually contains a wide range of elements that will produce a large range of signal amplitudes (from $Z = 16$ to $Z = 33$ in the present case).

The amplitude of each PMT pulse had a distinct behavior if the beam interacted with the scintillator in the region near or far from the PMT. The main features of the observed spectra were understood with the aid of a simple simulation of the transport of the photons to the surface of the PMTs (Figure 2.7). The shape of the amplitude signal spectra is then explained as a geometrical effect assuming the signal amplitude is proportional to the number of photons that arrive at the surface of the PMT. A Monte Carlo simulation was used to calculate the fraction of emitted photons that would arrive at the PMT surface. Because the solid angle subtended by the area of contact of the plastic and the PMT decreases slowly when the beam passes through plastic in the farthest from the PMT a similar trend is observed for the amplitude of the photon signal. This nonlinearity in the correlation between Q and y could be translated into nonlinear correlations for the timing if the CFD settings do not compensate for the signal walk properly.

A Tennelec 455 CFD was tested in the primary beam run and also used for the time-of-flight experiment. The delay of the internal CFD signal can be adjusted with an external cable. The module also presents a potentiometer ($Z_{monitor}$) that controls the attenuation factor for the delayed signal and can be externally adjusted for walk compensation. During the study of the detector sensitivity to the bias voltage

the CFD was used with an internal delay of 1.25 ns and a potentiometer setting of $Z_{monitor}$=−1 mV (chosen with the technique described in the CFD manual). The settings of the CFD were then adjusted for runs with −1.3 kV, −1.7 kV and −1.8 kV PMT bias (see Figure 2.5). The results are summarized in Tables 2.1 and 2.2. Changing the internal signal delay was found to have the larger effect on the time resolution than adjusting the $Z_{monitor}$. However, neither of the two variables were effective in modifying the linearity between the timing and the y position along the scintillator.

Table 2.1: Behavior of the timing system for different cable delays for the internal signal of the CFD module. The high voltage (HV) setting of the PMTs is indicated, and in all runs the CFD's $Z_{monitor}$ level for walk compensation was set to −1 mV. The table lists the width of the time spectra for a narrow gate in the vertical y distance from the PMTs (σ_{time}).

CFD delay [ns]	PMT HV [kV]	σ_{time} [ps]
0.25	−1.3	139.7
0.5	−1.3	42.1
1.0	−1.3	17.7
1.25	−1.3	17.9
1.5	−1.3	18.0
2.0	−1.3	18.5
0.75	−1.7	18.6
1.0	−1.7	18.9
1.75	−1.7	22.2
0.25	−1.8	32.4
0.5	−1.8	18.4
1.0	−1.8	18.1
1.25	−1.8	18.8
1.5	−1.8	18.6
2.0	−1.8	18.3

In summary, it was found that a given setting of the constant fraction discriminator can not compensate for the time walk for a wide range of signal amplitudes. However, in the case when such effect is present it can also be observed in the time vs integrated charge spectra, so a position measurement is not required in the time-of-flight experiment (Figure 2.5). A cable delay of 1.0 ns provided the best resolution

Table 2.2: Behavior of the timing system for different $Z_{monitor}$ levels for walk compensation of the CFD module. The high voltage (HV) setting of the PMTs as well as the cable delay of the internal CFD signal is indicated. The table lists the width of the time spectra for a narrow gate in the vertical y distance from the PMTs (σ_{time}).

$Z_{monitor}$ [mV]	CFD delay [ns]	PMT HV [kV]	σ_{time} [ps]
-0.3	1.0	−1.3	18.0
-1.0	1.0	−1.3	17.7
-1.6	1.0	−1.3	18.3
-0.3	1.25	−1.8	19.0
-1.0	1.25	−1.8	18.8
-1.6	1.25	−1.8	18.7

for different settings of the PMT's high voltage (different signal amplitudes). The settings of the CFD $Z_{monitor}$ were not found to affect the behavior of the detectors, so it was decided to follow the procedure described in the manual to set its voltage during the time-of-flight experiment.

Chapter 3

Experiment

A time-of-flight mass measurement experiment for neutron-rich isotopes in the region of Ca to Zn was performed at the National Superconducting Cyclotron Laboratory (NSCL). The experimental setup is shown in Figure 3.1. The NSCL coupled cyclotrons [50] are used to accelerate a ^{86}Kr stable beam and produce an intense radioactive ion beam by fragmentation in a Be target located at the entrance of the A1900 fragment separator. The A1900 fragment separator [51] is used to collect and separate the nuclides of interest, and to transport them to the S800 spectrometer [52] beamline where the mass measurement takes place.

The nuclear mass is derived from a simultaneous measurement of the time of flight (TOF) and magnetic rigidity (Bρ) of the beam fragments. The TOF was measured from the exit of the A1900 fragment separator to the focal plane of the S800 spectrometer using the fast plastic scintillators described in Chapter 2. This arrangement provided a flight path of 58.7 m. The magnetic rigidity was obtained from a position measurement at the dispersive plane of the spectrometer, where the beam x position is proportional to its momentum (Section 3.2), using position-sensitive microchannel plate (MCP) detectors. The standard detectors in the focal plane of the S800 provided beam tracking and energy loss information for the identification of the beam fragments.

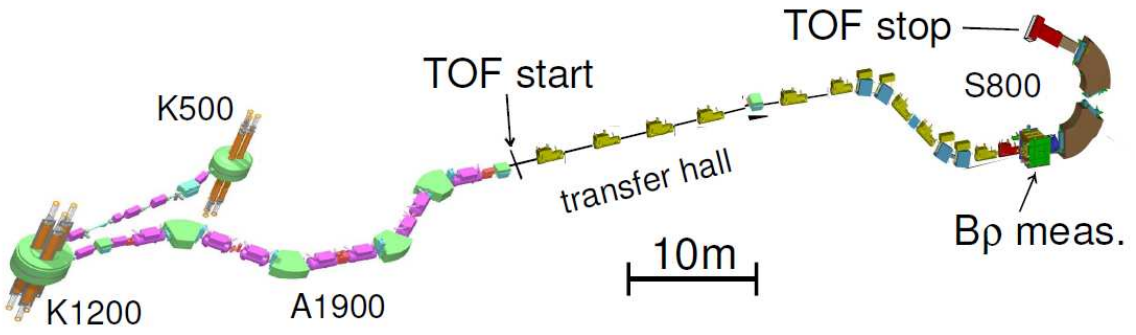

Figure 3.1: Experimental setup for TOF-Bρ mass measurements at the NSCL. The time of flight is measured with timing scintillators located at the extended focal plane of the A1900 (TOF start) and at the S800 spectrometer focal plane (TOF stop). The magnetic rigidity is measured with position-sensitive microchannel plate detectors located at the S800 dispersive plane (Bρ measurement).

This was the first mass measurement with the time-of-flight technique performed at the NSCL. The present chapter describes the elements of the experimental setup in detail.

3.1 Production of a fast beam of unstable nuclei

The NSCL coupled cyclotron facility was developed with the aim of producing fast beams of very exotic isotopes [53]. The coupled cyclotrons can accelerate intense beams of stable isotopes to typical energies around 100 MeV per nucleon, depending on the isotope. A ^{86}Kr with 100 MeV/u was used for this experiment. The beam impinges on a stable target, and a secondary beam with many different nuclear species is produced by fragmentation reactions [20]. The high acceptance A1900 fragment separator is located after the production target to collect the particles of the secondary beam, and acts as a filter to transport only the isotopes of interest to the experimental beamlines.

The A1900 offers two complementary ways to separate the beam fragments. The strength of the magnetic field of the A1900 dipole magnets determines a range of

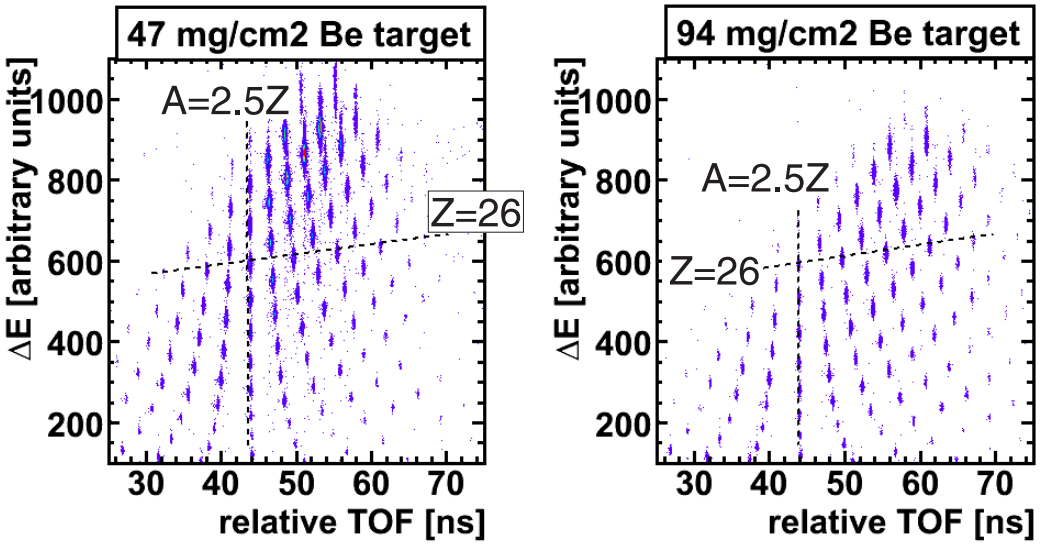

Figure 3.2: TOF–ΔE particle identification plot for runs with the calibration masses (left) and exotic isotope (right) production target settings. The vertical dashed line indicates the isotopes with a mass to charge ratio of 2.5, and the horizontal dashed line the location of the Fe isotopes. The solid line indicates the limit of experimentally known masses in the 2003 Atomic Mass Evaluation [4].

Bρ , or momentum per unit charge, of the transmitted beam particles. Because the products of the fragmentation reactions have roughly the same velocity as the incoming primary beam, the A1900 provides a filtering according to their mass to charge ratio. In addition, a degrader material (usually a thin plastic or aluminum foil) can be placed at the intermediate image plane of the A1900. Since the energy loss in the degrader is a strong function of the nuclear charge, only a certain range of elements will have the right momentum to be transmitted through the second stage of the A1900. Thus this provides separation according to the isotopes Z.

The secondary beam particles were identified by the $TOF - \Delta E$ technique [53], by a simultaneous measurement of their time of flight, which is proportional to the fragments' mass to charge ratio, and their energy loss in a beamline detector, which is proportional to their nuclear charge ($\propto$ Z^2). At the beginning of the experiment the particle identification was done using the standard detector setup at the focal plane of the A1900 fragment separator, where plastic scintillators (for timing) and

Si detectors (for energy loss) were installed. The magnetic rigidity of the A1900 was chosen so that particles close to stability were transmitted to the focal plane, and since no degrader was present at the intermediate image of the fragment separator, very light isotopes were present in the secondary beam. With these settings isotopes in the N=Z line (same TOF) were identified, and the absence of an isotope with Z=4 (the unbound ^{8}Be) was used to obtain an absolute calibration of the particle identification plot. Such calibration was used to identify the fragments as the Bρ of the A1900 was scaled to the neutron rich setting. Once the particle identification at the A1900 was established for the desired setting, it was used to calibrate the particle identification spectra of the experimental runs obtained with the time of flight at energy loss measured with the detectors at the S800 focal plane (Section 3.3.4). Figure 3.2 shows the particle identification spectra for the experiment and indicates the limit of previously known masses. We identified about 100 neutron-rich isotopes in the region of $16 \leq Z \leq 33$.

A time of flight experiment requires a secondary beam with a significant number of isotopes of known mass to be used as calibration masses. For some isotopic chains the masses that are precisely known are several mass units away from the more exotic masses (see the discussion of the selection of reference masses in 4.5.1), so it is necessary to have isotopes with a wide range of mass to charge ratio in the beam. For this reason, two beryllium production targets of different thickness (47 mg/cm^2 and 94 mg/cm^2) were alternated during the experiment without modifying any other settings of the beamline. The thinner target produced a secondary beam with isotopes closer to stability. Because of the larger energy loss in the thicker target, the momentum distribution of the secondary beam particles is shifted to lower values, and the transmission of more neutron-rich ions is favored. Figure 3.2 shows the particle identification plot corresponding to run with each target thickness. The experiment time was divided roughly in 60 % with the thick target for the most neutron rich iso-

topes and 40 % with the thin target setting. To increase the beam transmission the A1900 was operated in the full momentum acceptance mode ($\delta p/p = 5\%$). However the acceptance of the whole setup was restricted to $\delta p/p = 0.5\%$ by the size of the MCP detectors located at the S800 dispersive plane (section 3.2). No degrader was used at the A1900 intermediate image, even though a thin aluminum degrader was ready to be inserted in case the particle rate from light isotopes in the beam turned out to be too large.

The parameters of the beamline were optimized for the production of the fragments of interest [54] using the program LISE [55]. The Bρ of the A1900 beamline magnets was set at 3.722 Tm. The Bρ of the transfer hall and the S800 analysis beamline was 3.6745 Tm, the S800 spectrometer magnets were set at 3.6617 Tm. The Bρ of these last two sections of the beamline is reduced to take into account the energy loss of the beam fragments in the *TOF start* scintillator, and the MCP detectors.

3.2 Beam optics

The beamlines of the Transfer Hall and the S800 spectrometer [52] provided a long baseline for the time-of-flight measurement ($\sim$ 58.7 m). The S800 was operated in dispersion matched optics mode. In this mode the spectrometer provides the highest momentum resolution (up to one part in 5000). The momentum is obtained by a beam position measurement at the target position of the spectrometer (referred to as dispersive plane in this work), where the dispersion of the beam is about 10 cm/%. The momentum acceptance of this mode is limited to 1 %, although in the present experiment this was further reduced to 0.5 % because the MCP detectors used for the position measurement were only 5 cm wide in dispersive direction (see section 3.3.3).

In this optics mode the beamline from the A1900 extended focal plane (XFP) up to the S800 focal plane (S800 FP) is achromatic, which means that the beam position at the S800 FP is independent of its momentum spread. Therefore, the beam spot size is

kept small and timing detectors with a small plastic scintillator (and good resolution) could be used. However, because of misalignments of the beamline magnets, the beam did not hit the plastic scintillator when it was positioned at the center of the S800 FP detector chamber. The S800 analysis beamline magnets offered limited steering options, so the timing detector was moved 1.7 cm towards the south direction.

The standard beam optics notation for the coordinates of the beam is used throughout this work. The coordinates of the beam are defined with respect to the central trajectory, which is the one followed by a particle with a momentum corresponding the Bρ of the beamline magnets and that follows the beamline axis. The x position and a angle are defined as those in the bending plane of the beamline dipole magnets, and y and b respectively for the transverse plane. δp is the relative momentum difference to the reference trajectory, and l the difference in path length. The distance travelled along the beamline (z) is used as the independent variable. It should be noted that the dipole magnets of the S800 are rotated 90° with respect to the dipoles in the A1900 and Transfer Hall (Figure 3.1), and the coordinate system is also rotated at the S800 object.

Equation 3.1 shows the first-order transfer matrix from the A1900 XFP to the S800 FP (the location of the *stop* and *start* timing detectors), calculated with TRANSPORT [56] for the optics setting of the experiment (*V13M27x05* [57]). It describes how the coordinates of the beam particles at the S800 FP depend on their initial conditions at the A1900 XFP.

$$\begin{pmatrix} x_i \\ a_i \\ y_i \\ b_i \\ l_i \\ \delta_i \end{pmatrix} = \begin{pmatrix} 0.0000 & 0.0000 & 0.3096 & -0.0213 & 0.0000 & -0.0007 \\ 0.0000 & 0.0000 & -68.4031 & 7.9308 & 0.0000 & 0.0062 \\ 1.1181 & -0.0087 & 0.0000 & 0.0000 & 0.0000 & -0.0263 \\ 64.6534 & 0.3890 & 0.0000 & 0.0000 & 0.0000 & 1.1662 \\ -0.3001 & 0.0000 & 0.0042 & -0.0005 & 1.0000 & -10.5174 \\ 0.0000 & 0.0000 & 0.0000 & 0.0000 & 0.0000 & 1.0000 \end{pmatrix} \begin{pmatrix} x_0 \\ a_0 \\ y_0 \\ b_0 \\ l_0 \\ \delta_0 \end{pmatrix} \tag{3.1}$$

In 3.1 the distances are expressed in units of cm, the angles in mrad, and momentum deviation as a percentage. The main contribution to the variation in length of the path the particles have to travel comes from their momentum deviation: $(l|\delta) = -10.5\,\mathrm{cm}/\%$. Higher order terms can also have significant contributions to the length of the trajectories, and if the emittance of the beam is large they can restrict the resolution of the measurement [58]. Beam tracking detectors at the S800 FP allow for studying these effects.

3.3 Detectors setup

3.3.1 Monitors

Several parameters of the experimental set up were continuously monitored during the experiment. The count rate in each particle detector was monitored with scalar modules in the electronics setup (Figure 3.5). In addition, the primary beam intensity was periodically measured with a Faraday cup at the K1200 cyclotron. The temperature at the S800 experimental vault was measured with several thermometers placed in the racks for the electronics setup near the S800 focal plane, and near the S800 target position. The magnetic field of each dipole magnet in the S800 analysis beamline and spectrometer were also monitored.

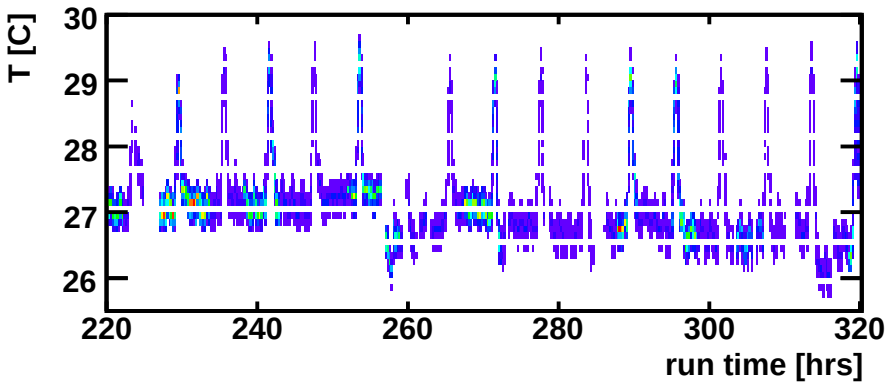

Figure 3.3: Temperature measured in the S800 experimental vault as a function of run time. The periodic behavior of the air conditioning unit in the vault is observed from the temperature increase every six hours.

It was discovered that the temperature in the S800 vault had clear periodic fluctuations. The air conditioning unit would temporarily turn off every 6 hours resulting in a steady increase of the vault temperature by about $2\,^{\circ}C$ for half an hour, at which point the unit would start working again (see Figure 3.3). The temperature fluctuations were also correlated with variations of the strength in the magnetic field of the S800 dipoles. This correlation is explained because the cooling system for the air conditioning unit and the power supply for the dipole magnets share the same water. The probes that monitored the B_{dipole} fields did not have a good resolution, and only for the magnetic field of the first spectrometer dipole (I265DS) a correlation with the temperature could be established. An additional problem with the magnetic field measurement was that the data for a fraction of the experiment could not be retrieved from the recorded data files. The temperature and magnetic field measurements were transmitted through the Experimental Physics and Industrial Control System (EPICS), and several of its channels were included in the data acquisition system (DAQ) and recorded in an event by event basis together with the particle detectors data.

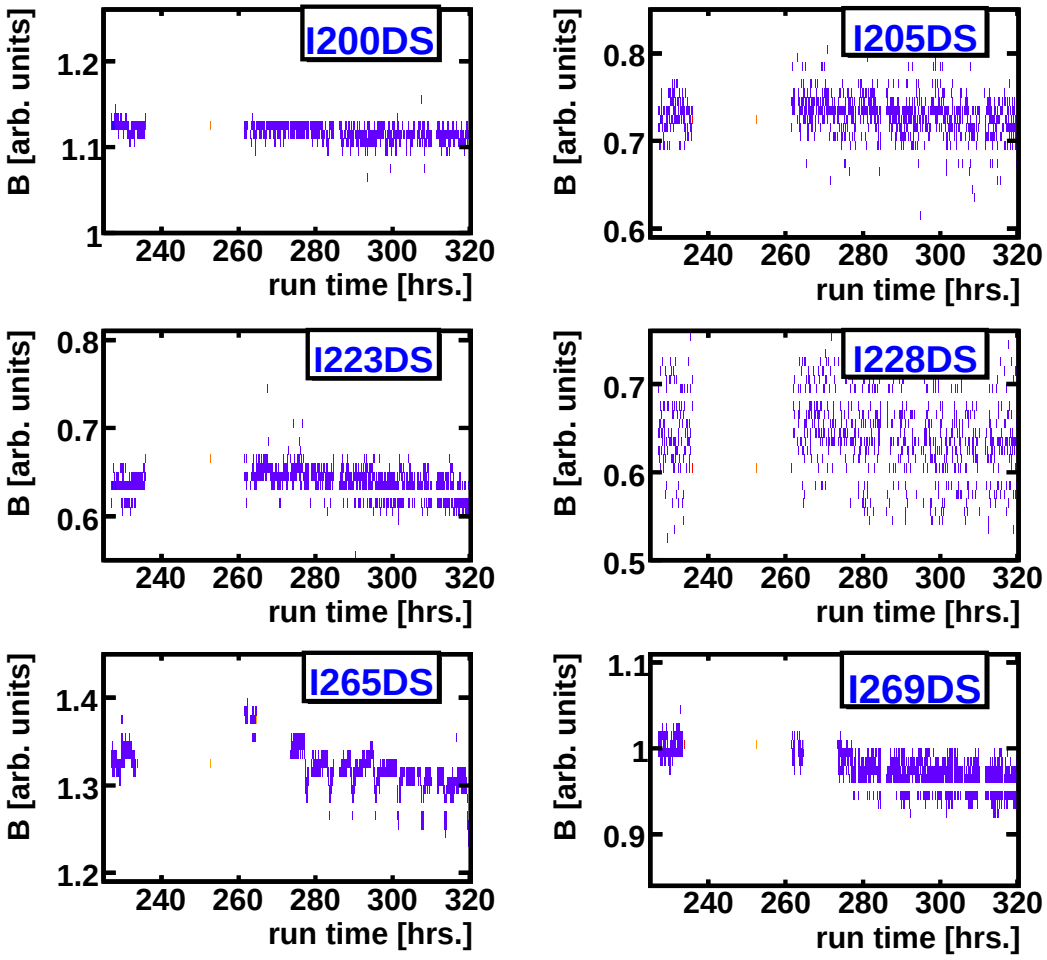

Figure 3.4: Measurements of the magnetic fields of the S800 beamline dipoles as a function of run time. The most clear time variation is observed for the I265DS magnet (bottom left), which is the first dipole in the S800 spectrometer. The information for a fraction of the runs could not be retrieved from the recorded data files.

3.3.2 Time of flight measurement setup

Timing scintillators

The time of flight (TOF) of each particle was measured using the fast timing scintillators described in Chapter 2. As shown in Figure 3.1, the TOF-start detector is placed at the extended focal plane position of the A1900 (A1900 XFP), and the TOF-stop at the focal plane of the S800 (S800 FP). The S800 detector was placed in the middle of the focal plane detector box (described in section3.3.4), 15 cm after

the first CRDC detectors. This arrangement provided the length of 58.7 m for the path of the ions. Both timing detectors were mounted in a vertical position, so their PMTs were labeled as *up* and *down*.

Table 3.1: Setting for the PMTs of the timing detectors and the corresponding CFD modules (the operation of the CFD modules is described in section 2.2.2). The threshold of the S800down CFD was lowered to −50 mV after ten hours of experiment as it was observed its count rate was about 5 times lower than the rate in S800up. The observed range in the count rates is due to variations in the primary beam intensity and the use of two different production targets.

PMT	voltage [kV]	CFD $Z_{mon.}$ [mV]	CFD threshold [mV]	rate [pps]
XFPup	-1.84	-5.7	-100	6000 - 23000
XFPdown	-1.65	-5.6	-50	6000 - 21000
S800up	-1.65	-1.0	-100	30 - 130
S800down	-1.96	-1.1	-100	15 - 45

The analog signal of the each PMT was divided with a passive two-way splitter after $\sim$ 15 ns of cable delay. One signal was converted to a NIM logic pulse with a constant fraction discriminator (CFD) module and used for timing. The other fraction was sent to a charge-to-digital converter (QDC) to record the amplitude of the detector pulse. The operational voltage of each PMT was chosen so that the largest amplitudes of their signals (monitored through an oscilloscope in the S800 vault) was 5 V, which is at the limit of the dynamic range of the CFD. Table 3.1 lists the voltage settings of each PMT, as well as the settings of the corresponding CFD. The observed detector rate at the XFP scintillator was about 200 times higher than for the S800 detector because of a higher rate of light particles in this position. In addition, the count rate in the S800down PMT was smaller than the S800up PMT. During the data analysis it was observed that the beam was more intense in a region of the scintillator closer to the S800down PMT, which explains the difference in count rate.

Cables for timing signal transmission and delay

Because of the physical separation of both timing detectors, a long cable is necessary to transmit the signals from one of the detectors to the location of the electronics setup. What is more, the detector located at the end of the beam path (the S800 FP) was used as the start timing signal because the beam rate is significantly lower at this location, and because the computer readout of the data was triggered by signals from other S800 focal plane detectors (a negative time of flight is actually measured in this way). The expected TOF of the isotopes in the beam is between 400 to 500 ns. Therefore, cables with $\sim$ 600 ns of signal delay are necessary to transport the signals from the timing detector at the XFP position and produce the correct timing with respect to the S800 signals.

The transport of a logic NIM pulse through long coaxial cables was tested, and a RG-8 cable was found to have the lowest signal attenuation and best timing properties. Four RG-8 cables of the model 7810a from Belden, of 590 ns of delay, equivalent to $\sim$ 150 m of length, were installed from the A1900 XFP position to the S800 FP (two carry the CFDs timing signals and two the PMTs analog signals). An NSCL 4×4 logic fan module was used at the S800 FP location to reconstruct and to produce multiple NIM logic pulses from each XFP PMT signal. The time resolution obtained from reconstructing a logic signal with different electronic modules was tested. The Lecroy 428 logic fan, the Phillips 710 leading edge discriminator, and the NSCL 4×4 logic fan were found to have a time resolution smaller than the bin width of the electronics ($\sigma < 6$ ps).

Timing electronics

The time between the signals from each timing scintillator was measured and digitized using a combination of a time-to-amplitude converter (Ortec 566 TAC), and an analog-to-digital converter (Ortec AD413). The TAC produces a square pulse whose

amplitude is proportional to the time difference between its input start and stop logic pulses. The ADC module transforms the output signal from the TAC into a digital number that is proportional to its voltage. Because of the large binning of the Ortec AD413 ADC (8192 channels) these modules allow for time spectra with only 6 ps/bin when the TAC is operated at its shortest dynamic range (50 ns). The setup was similar to the one in the timing scintillator test run (section 2.2), except that the multiple timing signal where produced from each PMT analog signal, and the time differences between various signals could be measured. In addition, one signal from each PMT was measured with respect to a clock. Using a clock minimizes the systematic uncertainties in the time measurement introduced by the nonlinearities of the electronic modules (Section 3.3.2). The signal from the internal clock of the Ortec 462 time calibrator module was used for this purpose. The electronics diagram in Figure 3.5 shows in detail all the time measurements recorded.

The time difference between PMTs at each end of the beam path provide a rough measurement of the fragments TOF. Two of these measurements were obtained; one between the S800 Up PMT and the XFP Down PMT (t_{SUXD}), and second between the S800 Down PMT and the XFP Down PMT (t_{SDXD}). These time measurements include the time it takes the photons generated by the beam interaction with the scintillators to reach the surface of the PMT, which can be up to 100 ps. Therefore, the average between the timing from the Up and Down PMT of each timing detector is used to correct for these effects (section 2.2). This is obtained by measuring the time between the the Up and Down PMT of each detector: t_{SUSD} and t_{XUXD}. Any of these time measurements can also be obtained by combining two of the measurements done with respect to the clock: t_{SUclk}, t_{SDclk}, t_{XUclk}, and t_{XDclk}. Table 3.2 lists the PMT signals that are combined for each time measurement, as well as some characteristics of the electronics modules used to digitize them. It should be noted that the TAC setting for all signals provides a binning of ~ 6 ps/ch except for the

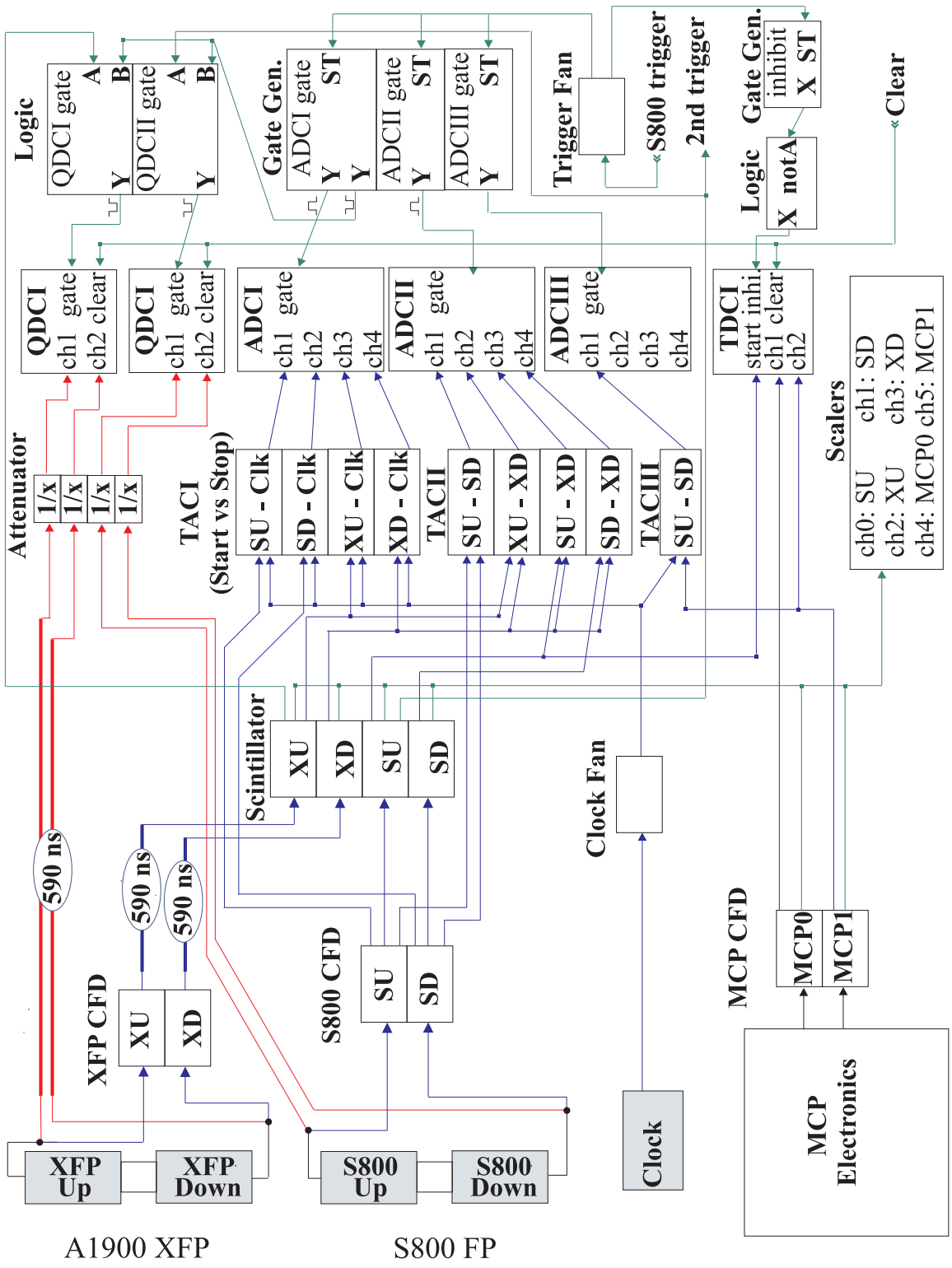

Figure 3.5: Electronics diagram for the measurement of the time of flight and the PMT signal amplitude.

measurements t_{SUXD} and t_{SDXD}. For these two measurements the TAC range was set at 100 ns to accommodate for the spread in TOF of the different beam fragments, and the resulting spectra had a binning of ~ 12 ps/ch. On the other hand, the period of the clock used was 40 ns, so a fraction of the dynamic range of the TACs connected to the ADC2 (50 ns) was not used.

Table 3.2: Timing signals measured with each ADC channel. The Ortec 566 TAC and Ortec AD413 ADC modules are identified by their id number in the NSCL electronics database. The dynamic range for the operation of each module is indicated in the fifth column. The differential nonlinearity (DNL) of each module was calculated as the root mean square deviation of Equation 3.4, and is expressed as a percentage of the bin size (6 ps/bin for 50 ns range, and 12 ps/bin for 100 ns range).

time	start	stop	TAC id	range [ns]	ADC id	TAC DNL [%]
t_{SUclk}	S800up	clock	2692	50	2722 ch1	1.4
t_{SDclk}	S800down	clock	2730	50	2722 ch2	1.3
t_{XUclk}	XFPup	clock	2731	50	2722 ch3	1.3
t_{XDclk}	XFPdown	clock	2965	50	2722 ch4	1.4
t_{SUSD}	S800up	S800down	2696	50	2019 ch1	1.4
t_{XUXD}	XFPup	XFPdown	1763	50	2019 ch2	1.4
t_{SUXD}	S800up	XFPdown	2690	100	2019 ch3	1.5
t_{SDXD}	S800down	XFPdown	2729	100	2019 ch4	2.0

The TOF of the beam fragments was constructed using timing detector signals for both the start and the stop inputs of the TAC (direct timing) in two ways:

$$\begin{aligned} TOF_1 &= t_{\mathrm{offset}} - t_{\mathrm{SDXD}} - (t_{\mathrm{SUSD}} - t_{\mathrm{XUXD}})/2 \\ TOF_2 &= t_{\mathrm{offset}} - t_{\mathrm{SUXD}} + (t_{\mathrm{SUSD}} + t_{\mathrm{XUXD}})/2 \end{aligned} \tag{3.2}$$

To construct the equivalent TOF measured with respect to the clock the number of pulses N_i has to be counted. This is done in the spectra that compare the clock measurements with the direct timing measurements. N_1 is obtained from the t_{SDXD} spectrum, N_2 from t_{SUSD}, and N_3 from t_{XUXD} (Figure 3.6). The clock period is $T =$ 40 ns. The TOF of the beam particles is then derived from the clock measurements as follows:

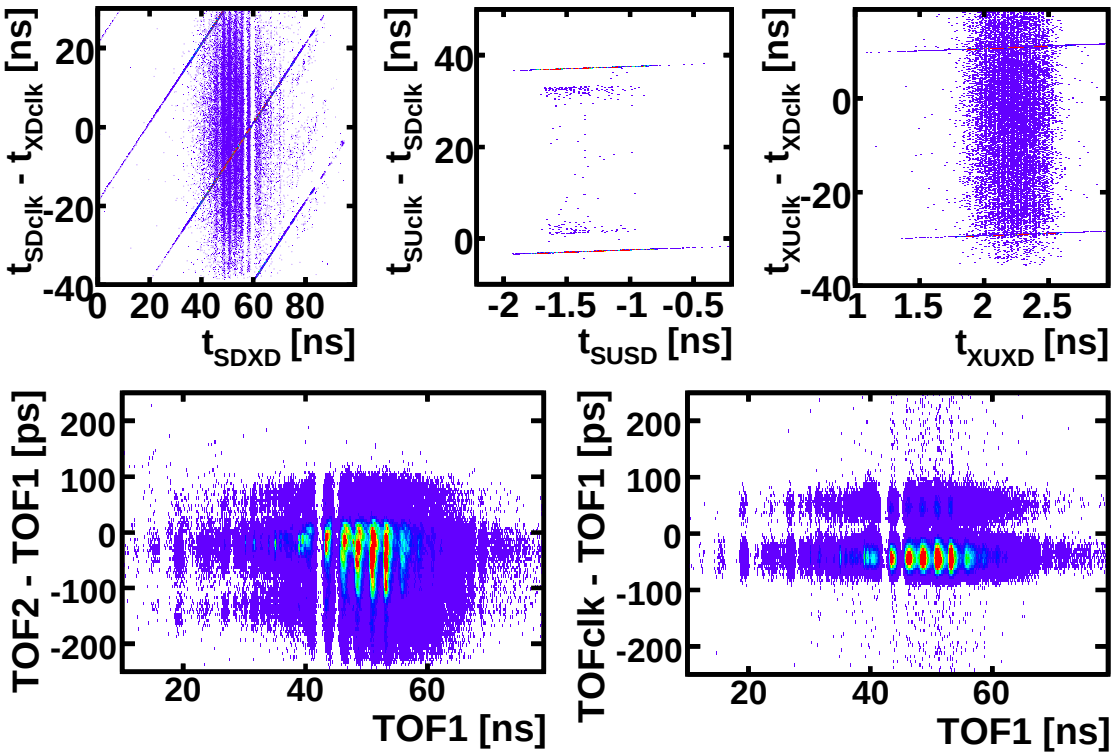

Figure 3.6: The spectra compare the different TOF values (equation 3.2 and 3.3) constructed from the time measurements between the PMTs and clock signals (table 3.2). The upper row contains the spectra used to count the clock pulses between the signals from each PMT. There is a notoriously larger number of random coincidence between the signals from the A1900 XFP PMTs and the clock than for the S800 signals (compare t_{SUSD} with t_{XUXD}). The lower plots show the difference between the three semi-independent TOF measurements used. There is a systematic shift of ~ 90 ps in the measured TOF in about 10 % of the events that was produced by the response of the logic fan modules; its origin and impact in the determined TOF is discussed in Section 4.3.4.

$$TOF_{\mathrm{clk}} = t_{\mathrm{offset}} + T \cdot (N_1 + \frac{N_2 - N_3}{2}) + \frac{t_{\mathrm{XUclk}} + t_{\mathrm{XDclk}} - t_{\mathrm{SUclk}} - t_{\mathrm{SDclk}}}{2} \tag{3.3}$$

Therefore, together with TOF_1 and TOF_2, three redundant measurements of the TOF were available, and they were used for consistency checks during the analysis.

Time and nonlinearities calibration

The time calibration of each ADC channel was done using an Ortec 462 time calibrator. This time calibrator produces regularly spaced pulses (10 ns) that can be used as start and stop signals for the TACs. Figure 3.7 shows the residuals of a linear time calibration function obtained in this way.

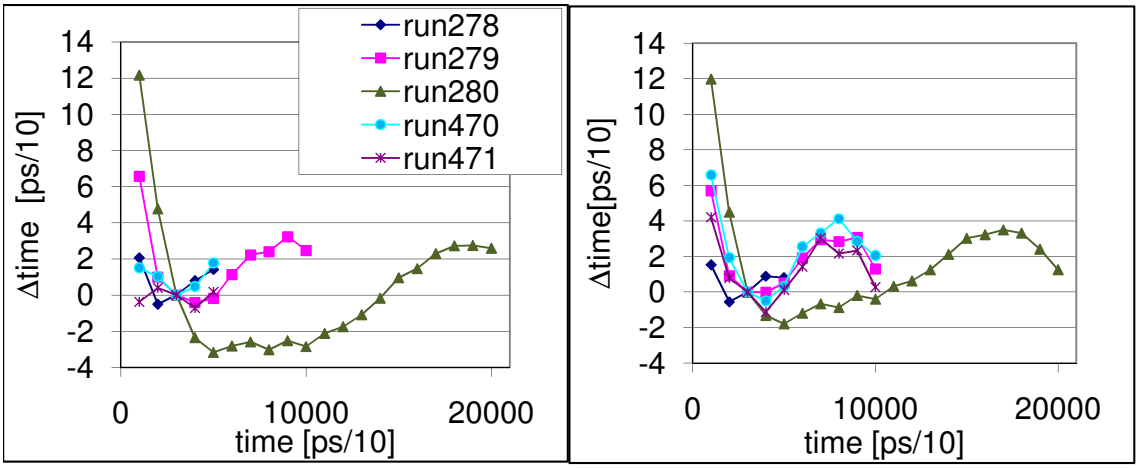

Figure 3.7: Results of the time calibrations for channel 1 of ADC2 (left) and channel 3 of ADC2 (right). The figures show the residuals from a linear calibration function for runs with different settings for the TAC range: 50 ns in run 278, 100 ns in run 279, 200 ns in run 280, and range used in the experiment for runs 470 and 471 (50 ns for channel 1 and 100 ns for channel 3).

An important feature of the TAC and ADC modules that must be considered for a precise time measurement is the nonlinearity in their response. The voltage of the output signal from a TAC can have deviations from a linear relationship with the input time signals. Besides this, there are nonuniformities in the mapping between the step of ADC input voltages and the corresponding bins in its digitized output. Figure 3.8) shows again the residuals from the time calibration of the TAC-ADC, but plotted as a function of the uncalibrated ADC channels. In that case, the pattern of the residuals for runs with different TAC ranges match each other, so the nonlinearities can be attributed to the TAC-ADC and not to the output of the time calibrator model. A fourth order polynomial was fit to these residuals, and the results provided the global

correction function for the nonlinearities that was used in most of the analysis.

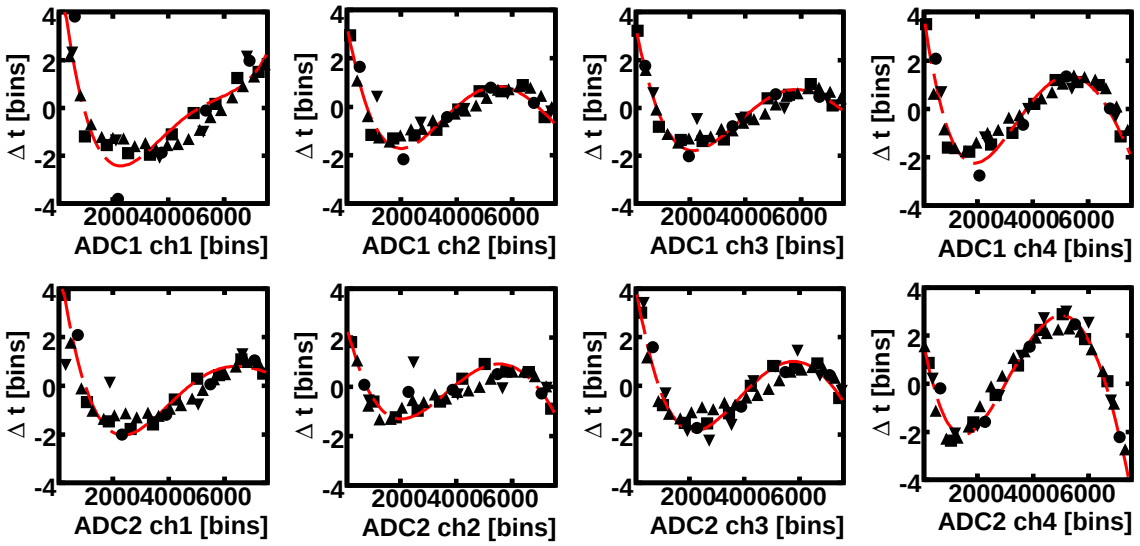

Figure 3.8: Residuals of a linear calibration function of the TAC-ADC modules expressed in units of the ADC bin width. Data are shown for the calibration runs described in Figure 3.7 (circles for run 278, squares for run 279, triangles for run 280, and inverted triangles for run 470). The solid line shows a fourth order polynomial fit to the residuals of run 280.

A more precise method to correct for the nonlinearities is achieved by measuring the nonlinearity in each ADC bin (the differential nonlinearity). This is done using uncorrelated start and stop signals for the TAC-ADC modules and uniformly filling their spectra. The differential nonlinearity is then calculated from:

$$DNL_i = (\frac{n_i}{\langle n \rangle} - 1) \cdot \Delta t \tag{3.4}$$

n_i is the number of counts in each ADC bin, $\langle n \rangle$ the average counts for all bins, and Δt the time width of each bin. The nonlinearities of the TAC and ADC modules were tested before the experiment and it was found that it was possible to correct them at the level of $\sim 0.5\%$ of the bin width (see Figure 3.9). Furthermore, it was found that the features of the nonlinearities that vary smoothly over a few hundred ADC channels (the integral nonlinearities) are the easier ones to correct. Such nonlinearities were

attributed to the TAC modules, since the same trends were observed by connecting a given TAC to different ADCs. The nonlinearities in each TAC module used in the experimental setup was measured and is presented in Table 3.2.

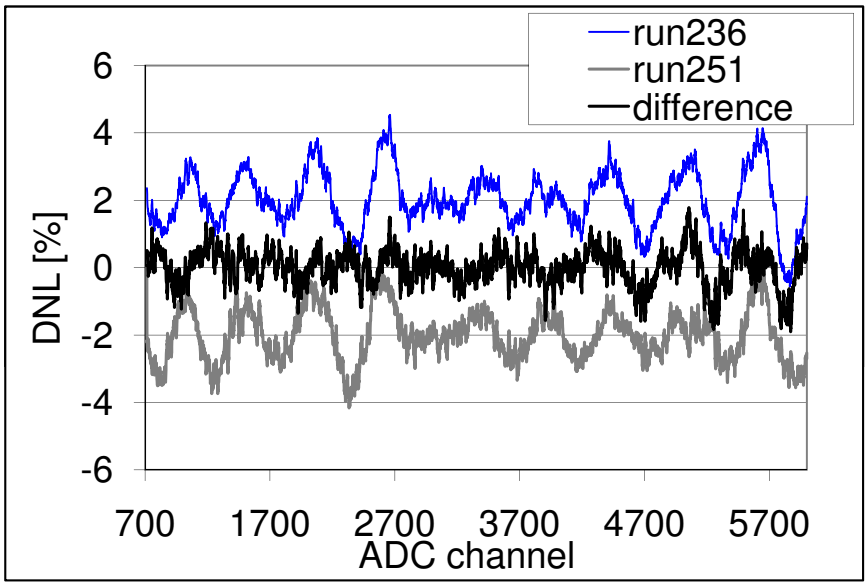

Figure 3.9: The differential nonlinearity (DNL) for one TAC-ADC channel, expressed as a percentage of the bins width, is shown for two calibration runs done one week apart. For a better visualization the data for run 236 is offset by 2 %, and that of run 251 by −2 %. The first and last few bins of the spectra usually show much larger nonlinearities, so the integration of the DNL is done starting from bin 700.

The differential nonlinearities in the final electronics configuration were calibrated immediately before and after the experiment. For this setup, which included the electronics for the S800 and MCP detectors, the computer readout was much slower than for the stand alone mode of the timing electronics. Because the time to access the experimental vault after the experiment was limited, the statistics accumulated did not allow for a good calibration of the differential nonlinearities. However, as it is discussed in the next chapter, this was not a significant obstacle for the experiment and the global correction obtained from residuals in the time calibration spectra was used.

One of the advantages of measuring the time with respect to the clock is that the measurements are distributed across the whole dynamic range of the ADC. Conse-

quently, nonlinearities in the electronics should not introduce any systematic shift to the measured TOF (they will only add a small statistical uncertainty to the measurement). Nonetheless, there is still some structure in the spectra of the events used to calculate TOF_{clk}. The Ortec 566 TAC requires a minimum time between the start and the stop signal for a successful conversion (≤ 5 ns). Because there is some correlation between the timing of the PMT signals, this *blind* range in the TAC translates to a nonuniform distribution of the events with a valid signal in all four ADC channels that use the clock. This is shown in Figure 3.10. The TOF_{clk} measurement is still fairly insensitive to the nonlinearities, but has the additional problem of significantly reducing the number of valid events (about 35 %) because of the blind range of the TAC.

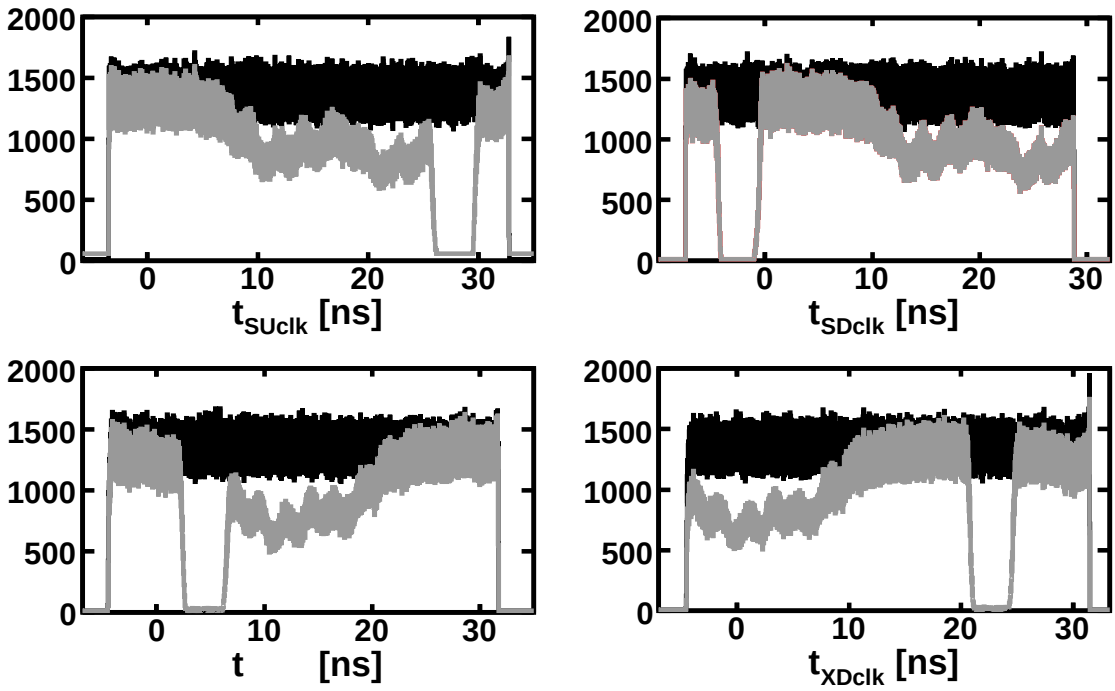

Figure 3.10: ADC spectra for the four channels that time each PMT signal with respect to the clock. All events for isotopes with Z $\gtrsim$ 15 are shown. The grey spectra correspond to events where a valid signal is required in all four ADC channels. Because the signals of the two PMTs in each timing scintillator are correlated in time, the blind region of the TAC range (short time from start to stop) is observed in the spectra from the signal of the companion PMT. The spectra also present a large channel to channel variation that is an artifact of the bin width used.

Stability with temperature

The quoted temperature stability of the electronic modules is $\leq$ 100 ppm/°C or $\pm$10 ps/°C (whichever is greater) for the Ortec 566 TAC, and $\leq$ 50 ppm/°C for the gain and zero offset of the Ortec AD413 ADC. As discussed in section 4.3.3, the changes in the response of the modules due to the variations in the temperature at the S800 vault can be observed in the measured TOF of the beam particles, and is has the same order of magnitude as the model specifications. In addition, it was observed that the frequency of the clock in the Ortec time calibrator (25 MHz) changed at the level of 1 part per million per °C. Such effect is very small and only changes the period of the clock in $\sim$ 0.04 ps/°C. Since the number of clock pulses counted to construct the TOF_{clk} measurement (equation 3.3) is at most seven, the frequency change will affect the measurement by less than 0.5 ps.

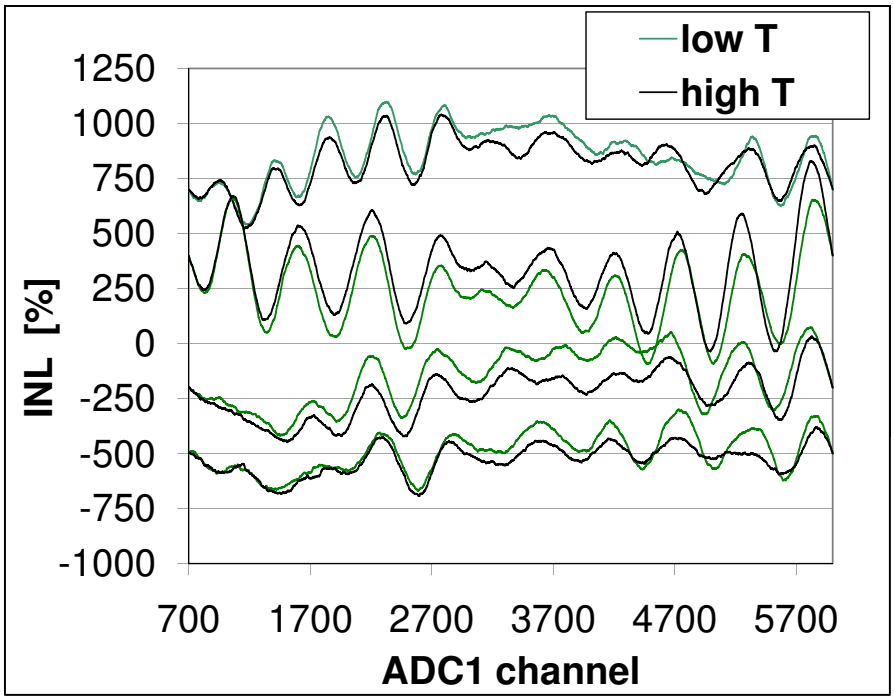

Figure 3.11: Calibration of the nonlinearities in the four channels of ADC1. During one of the runs (high temp.) the cooling fans for the NIM crate were turned off to increase the operational voltage of the modules. The integral nonlinearities (INL) are shown, and the data of each channel is offset by a multiple of 250 for a better visualization.

The effect of the operational temperature of the electronic modules on their nonlinearities was also tested during the preparation for the experiment. It was found that the integral nonlinearities are not very sensitive to the temperature, and the observed changes can be attributed to a change in the gain or the offset of the modules (Figure 3.11).

3.3.3 Position sensitive micro channel plate detectors

The magnetic rigidity (Bρ) of the beam particles was determined from a position measurement at the S800 dispersive plane, where the dispersion is $\sim -11\,\mathrm{cm}/\%$. Given the velocities of the beam fragments and the total path length this dispersion results in a correlation between the TOF and dispersive plane position of $\sim 300\,\mathrm{ps/cm}$. Therefore a detector with a position resolution better than 1 mm is necessary so that its contribution to the final TOF uncertainty is below the level of the resolution of the timing scintillators (better than 30 ps, as discussed in Chapter 2). Two position-sensitive microchannel plate detectors were used in the time-of-flight experiment. The one located at the S800 dispersive plane (MCP1) provided a measurement of the momentum of the beam. The other one (MCP0) was placed upstream from the dispersive plane and was used to calculate the beam angle.

Microchannel plate detectors (MCP) offer the possibility to track the beam position with a small amount of material in the beamline, and can sustain high count rates [59, 60]. A system for use with heavy fragment beams had been developed at the NSCL [61], and was also used for this experiment. A diagram of the MCP detectors is shown in Figure 3.12. A thin foil is placed in the path of the beam for the emission of secondary electrons from the point where the beam fragments strike its surface. Both an electric field and a magnetic field are applied in the direction from the foil to the microchannel plate. Therefore, the electrons are accelerated towards the microchannel plate, and their position information is preserved as they spiral

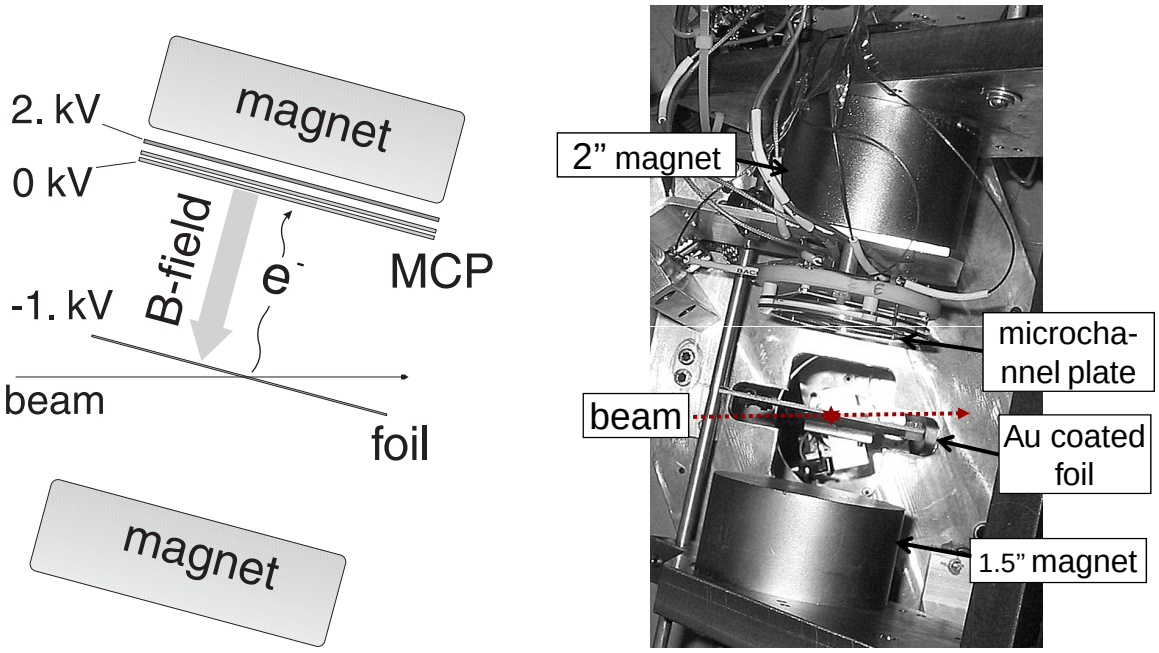

Figure 3.12: Diagram of microchannel plate (MCP) detectors used for position measurement at the S800 dispersive plane [61]. The picture shows the MCP1 detector arranged in a close configuration to increase the magnetic field at the channel plate; the x_{mcp} position measured with this detector was used to determine the momentum of the beam particles.

around the magnetic field lines. The microchannel plate consists of densely packed glass tubes that act as a continuous channel photomultiplier when a voltage is applied across it. In the present design, two plates with an active area of 40 mm were used in a chevron configuration. A resistive plate behind the microchannel plates acts as an anode collecting the amplified charge. The position is determined from the amplitude of the signal measured in each of the four corners of the anode.

The first experience using these detectors with heavy ion beams at the NSCL showed that there was a possibility to improve their resolution. For the present work the set up was modified by increasing the strength of the magnetic field in the area between the foil and the channel plate. This decreases the radius of the curvature of the electrons as they drift to the channel plate and improve the position resolution [61]). A stronger permanent magnet was used, and the elements of the detector

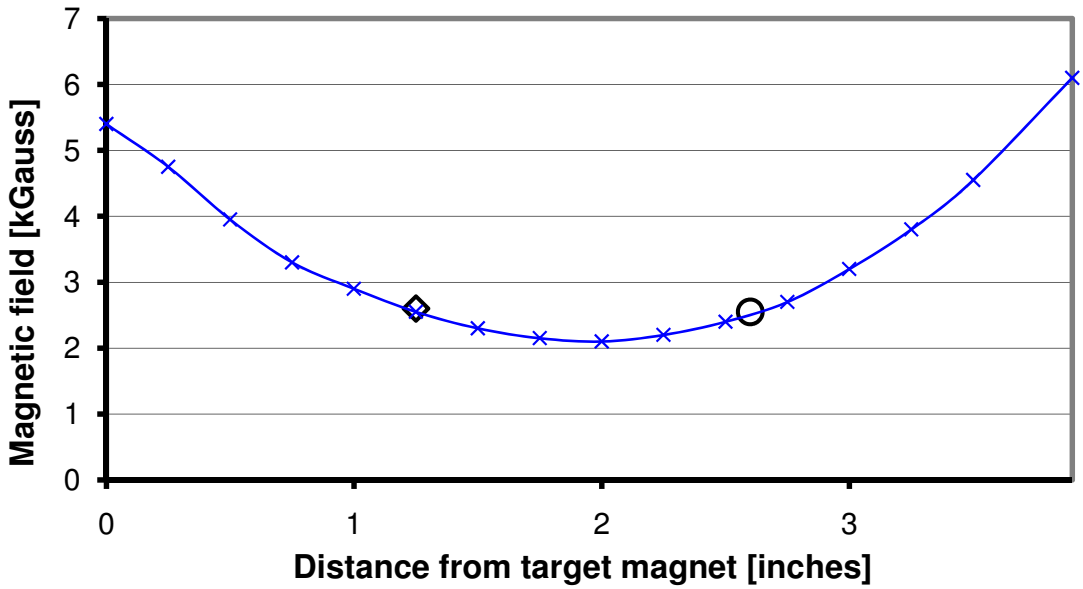

Figure 3.13: Magnetic field strength along axis of the MCP1 detector. The diamond indicates the position of the gold-coated foil located in the path of the beam, and the circle the location of the channel plate.

were arranged in a closer configuration (this required the MCP to be placed at 20 degrees with respect to the beam trajectory). Figure 3.13 shows the strength of the magnetic field in this configuration, which is the one used for MCP1 (at the dispersive plane). The MCP0 detector is placed 59 cm before the dispersive plane position at 30 degrees from the beam direction, and its configuration was not modified with respect to [61]. Thin mylar foils ($70\,\mu g/cm^2$) with $1.5\,\mu m$ of evaporated gold were used for both MCPs.

The position calibration of both MCP detectors was done with an alpha source before and after the experiment. In addition, a mask calibration run with a degraded Kr primary beam was used to check the resolution of the detector with heavy ions, and to confirm the calibration with alpha particles. These spectra are shown in Figure 3.14 where the calibration function suggested in [61] was used. The position resolution of the MCP detector was extracted from the observed spectra of the mask holes for the primary beam. The measured standard deviation of the projection of the mask spectra in the x_{mcp} position was compared to Monte Carlo simulations

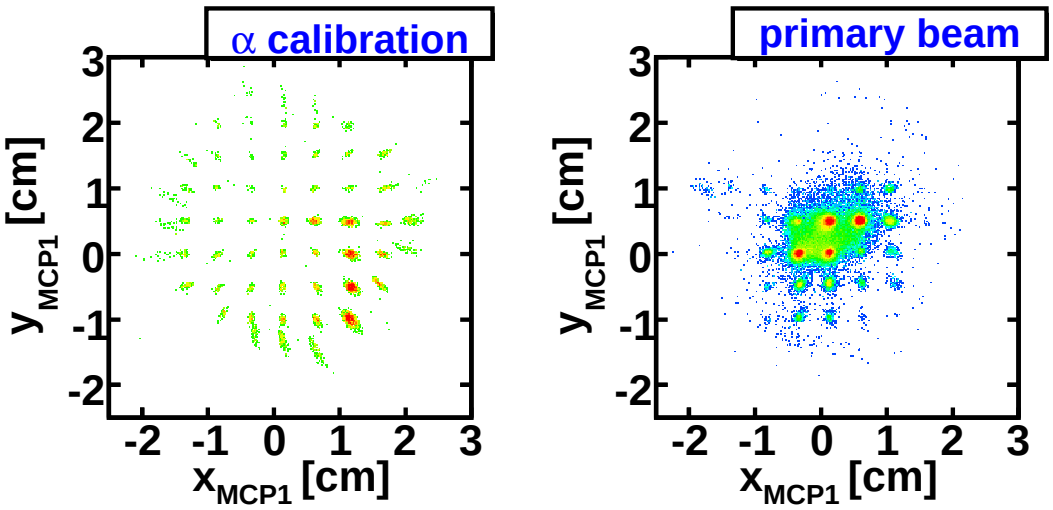

Figure 3.14: Mask position calibration of the MCP detector. A calibration function [61] for the raw detector spectra was obtained with a calibration done with an alpha source (left). A mask run was performed with a degraded primary beam (^{86}Kr) to check the calibration for the position measured with heavy ions (right).

calculated for different detector resolutions. Figure 3.15 compares the experimental data and the simulation. A MCP resolution of about 0.3 mm was estimated for the MCP1 detector.

During the experiment it was observed that the efficiency of the MCP1 detector decreased away from the center of the detector, in particular for the heavier fragments. The voltage applied across the microchannel plate was reduced in two steps from 2.0 kV to 1.9 kV to improve the efficiency (Figure 3.16).

3.3.4 S800 focal plane detectors

The standard S800 focal plane detectors provided energy loss (ion chamber) and position measurements (CRDC) of the beam particles [52]. The thick scintillators usually used for total kinetic energy measurement were only used as trigger signal for the data acquisition.

The position and angles of beam particles in the S800 focal plane were measured with two cathode readout drift chambers (DRDCs) 1.07 m apart. These measure-

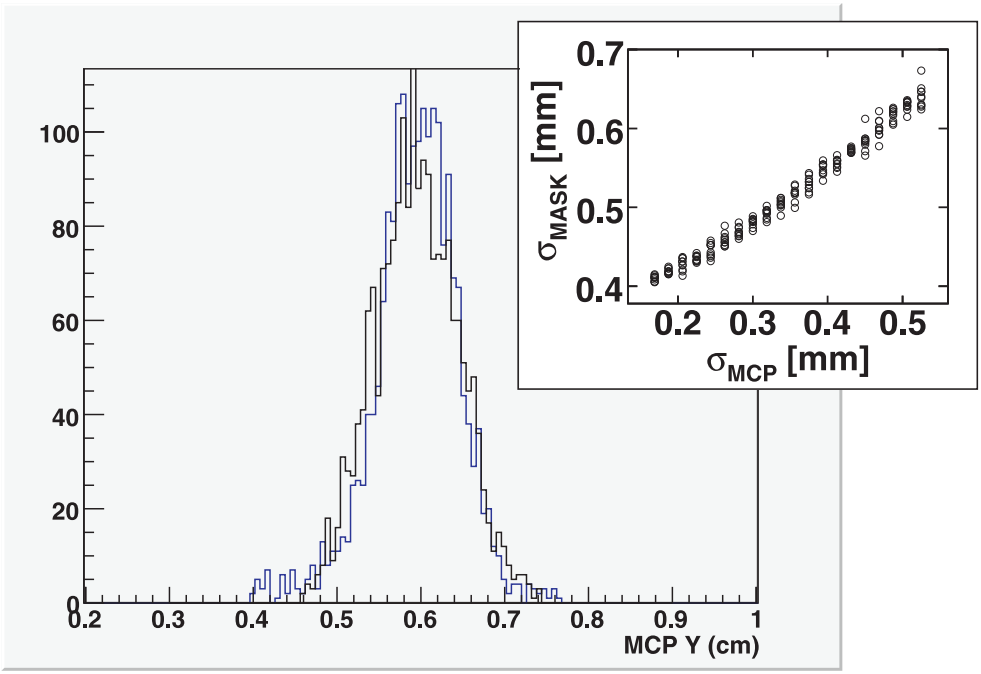

Figure 3.15: MCP position spectra for one of the mask holes ($radius$ = 0.75 mm) obtain during the calibration run. The experimental data (grey) is compared to a Monte Carlo simulation using a detector resolution of σ_{mcp} = 0.4 mm (black). The insert shows how the standard deviation of the simulated mask spectra (σ_{mask}) depends on the assumed detector resolution. The measured value of σ_{mask} during the calibration run is 0.45 mm.

ments were used to calculate the position of the beam at the S800 FP timing scintillator. Because of variations in the gas pressure of the detectors during the experiment, their calibration for the y (nondispersive) coordinate changed over time (Figure 3.17). This would require modifying the parameters of the calibration for each run, but it was found during the analysis that this position measurement was not essential to obtain the mass results.

The energy loss (ΔE) was measured with the ionization chamber detector (IC). Besides using it for particle identification of the isotopes in the beam, the ΔE information was also used to separate charge state contaminants in the beam (Section 4.1). In an attempt to get a better separation of charge states, the measured energy loss was corrected by the momentum (x_{mcp1} position) of the beam particles and for variations of the temperature in the S800 experimental vault. In addition, the spectra

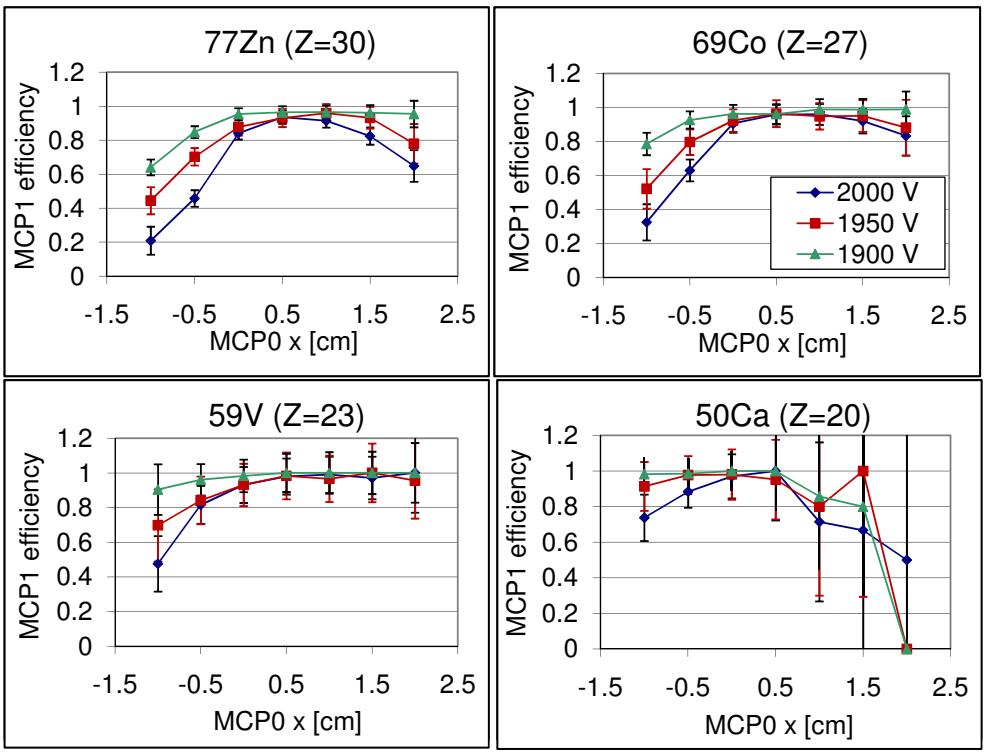

Figure 3.16: During the experiment the high voltage (HV) bias for the channel plate of the MCP1 detector was reduced to 1950 V, and subsequently to 1900 V to improve the detection efficiency (in particular for heavy fragments). The plots show the MCP1 efficiency as a function of the beam dispersive position for four different isotopes in the secondary beam. The efficiency was measured as the ratio of events with a valid MCP1 position to the number of events in selection cuts in the x_{mcp0} spectra of MCP0 (the x position in both detectors was correlated).

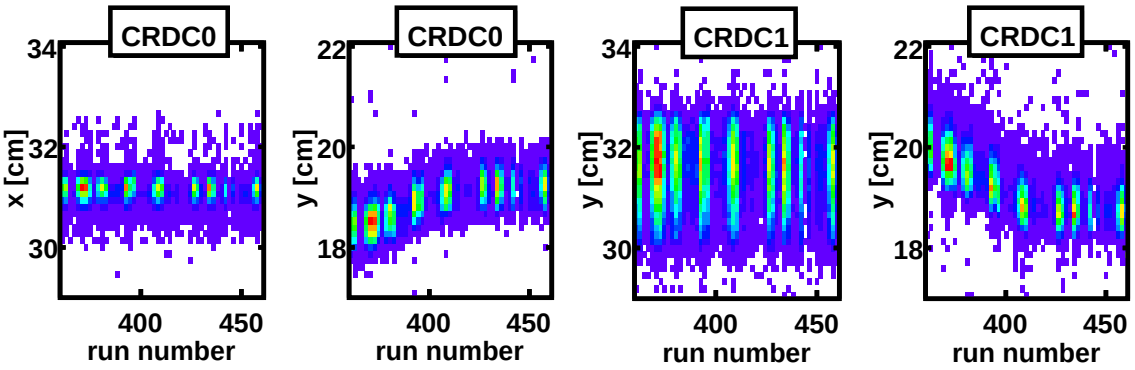

Figure 3.17: Position measurements at the S800 focal plane with the two cathode readout drift chambers (CRDCs). The calibration in the vertical position is sensitive to the pressure of the detector gas, and it was observed to drift during the experiment.

of the 16 pads of the detector, which are averaged to obtain a ΔE measurement, were gain matched (pad zero was not used since it was zero for most events). However, these corrections had a negligible effect on the ion chamber resolution.

Chapter 4

Data Analysis

4.1 Charge state contaminants

The particles in the secondary beam were identified by a simultaneous measurement of their TOF and energy loss in the S800 ion chamber detectors (the details are described in Section 3.1). This method provides a good separation of most isotopes, except for the heavier nuclei with $Z \gtrsim 29$. Because of their large nuclear charge, these fragments are more likely to pick up an electron during the fragmentation reaction in the production target, while all other nuclei in the beam are fully stripped of their electrons. Because of their similar mass-to-charge ratio, fully stripped fragments of $^{A}Z^{Z+}$ will have a very similar TOF as hydrogen-like fragments of $^{A}Z{+}1^{Z+}$, and their energy loss spectra in the S800 ion chamber will partially overlap. If the charge states are not resolved, the measured TOF will be an average of the TOF of both isotopes, and could introduce a systematic shift in the measurement. The region of the particle ID spectrum where charge state contaminants are present is shown in figure 4.1.

Since the thick plastic scintillators at the S800 focal plane did not provide a good resolution for total kinetic energy measurement (it was used only as a trigger) such measurement could not be used to separate the charge states. The only measurement available to discriminate these events was their different energy loss in the S800 ion

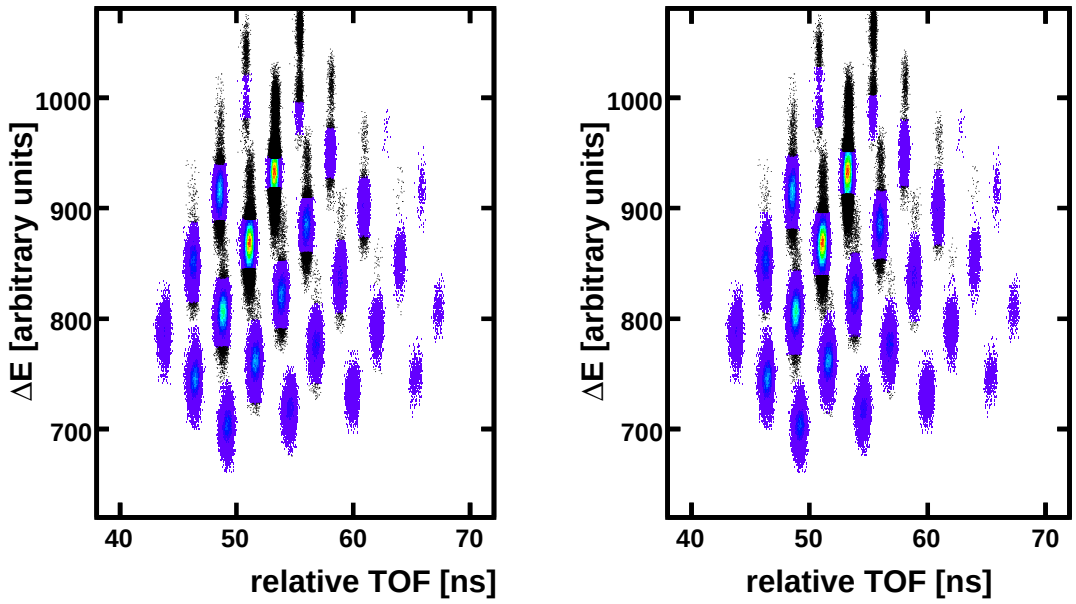

Figure 4.1: Time-of-flight vs energy loss particle identification spectra for the region of high Z isotopes where charge state contaminants are present. The events outside the selection cuts in ΔE used to reject the charge states are shown in black. The left figure shows cuts for which the estimated number of fragments in a charge state that fail to be rejected is $n_{\text{ch. st.}} = 0.25$, and in the right figure the rejection criteria is $n_{\text{ch. st.}} = 1$ (Equation 4.1). The momentum corrected TOF is used to construct the particle ID spectra (Section 4.2).

chamber, which results from their different nuclear charge (Chapter 2 of [47]). Figure 4.2 shows the energy loss spectra corresponding to the overlapping distributions of fully stripped isotopes ($^{A}Z^{Z+}$) and the corresponding charge states ($^{A}Z{+}1^{Z+}$) for a few selected cases. Figure 4.3 shows the TOF of these isotope obtained by rejecting events based on their ΔE; the measured TOF changes by up to 4 ps if some charge state contaminants are not rejected (for example for ^{83}Ge).

The location of the rejection cuts used was based on the fits of a double Gaussian function to the energy loss spectra, like the ones shown in Figure 4.2. The centroid of the energy loss distribution of the fully stripped fragments, ΔE_0, is in all cases ≈ 55 channels smaller than centroid of the distribution for the corresponding charge state,

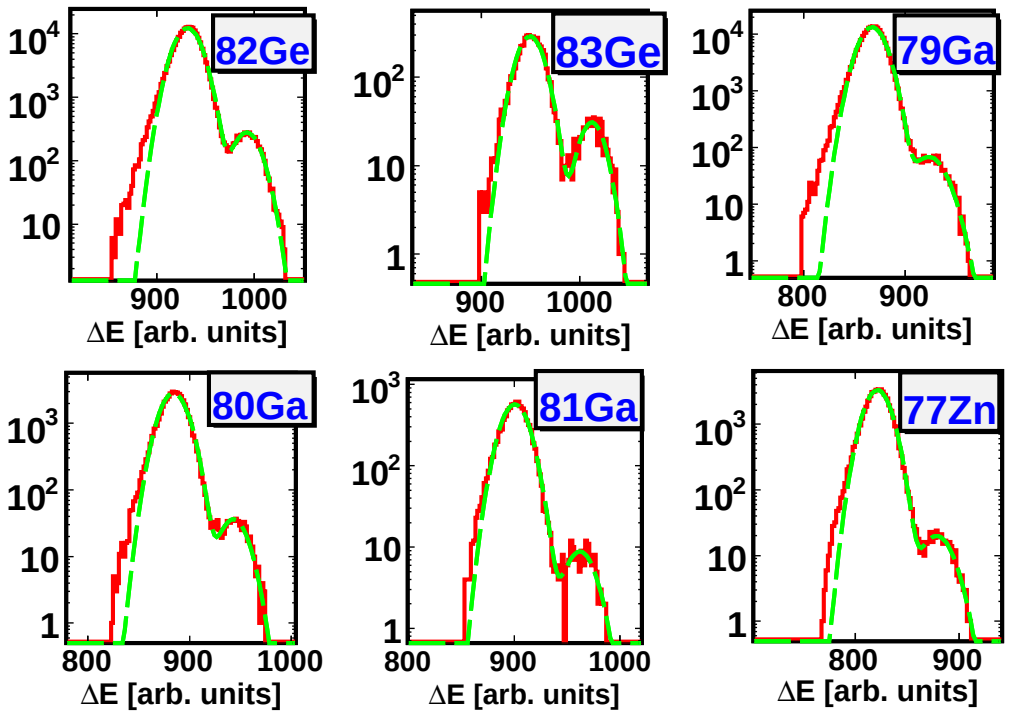

Figure 4.2: Energy loss spectra for a few ions and the overlapping charge states (higher ΔE), and a double gaussian fit to it.

$\Delta E_{\text{ch. st.}}$ (an absolute calibration of the energy loss of the ion chamber detector was not performed). Both distributions also have similar widths ($\sigma_{\Delta E} \sim 12$ channels). Trends in the ratio of the population of charge states to fully stripped fragments were used to estimate the normalization coefficient (a_0) for the ΔE distribution of charge states in the cases of fragments with low statistics, where the population of charge states could not be well determined. The number of beam particles in hydrogen-like charge states that is not rejected ($n_{\text{ch. st.}}$) given the location of a cut in the energy loss spectra (ΔE_{cut}) can be estimated as:

$$\int_{-\infty}^{\Delta E_{\text{cut}}} a_0 \cdot exp\left[-\frac{(\Delta E - \Delta E_{\text{ch.st,}})^2}{2\sigma_{\Delta E}^2}\right] \mathrm{d}\Delta_E = n_{\text{ch. st.}} \tag{4.1}$$

Since there is a slight correlation between the TOF of the particles of a given fragment and their energy loss in the ion chamber detector (slower particles have a larger energy loss) a cut in ΔE could introduce a systematic shift in the TOF. Therefore, a

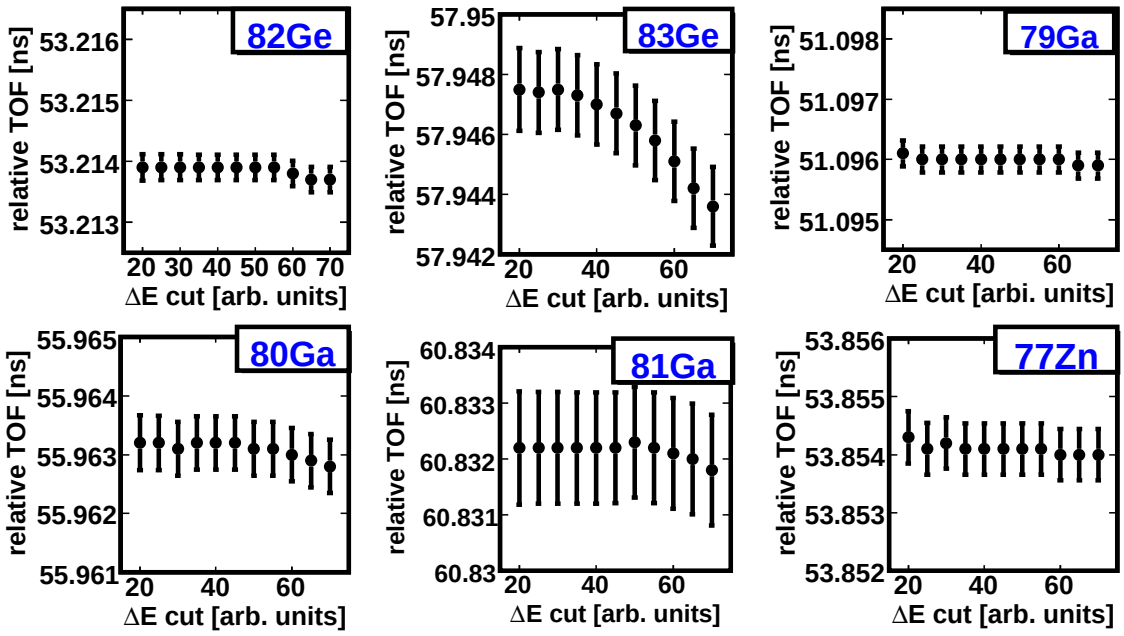

Figure 4.3: Measured TOF for a few isotopes using different cuts to reject events according to the energy loss (ΔE) in the S800 ion chamber detector. Events with $\Delta E > \Delta E_0 + \Delta E_{\rm cut}$, where ΔE_0 is the centroid of the energy loss distribution of the fully stripped ions (Figure 4.2), were rejected. The $\Delta E_{\rm cut}$ selected for each ion depends on the relative population of charge state contaminants (equation 4.1).

symmetric cut above and below the centroid of the fully stripped fragments ΔE_0 was used. Given $\Delta = \Delta E_{\text{cut}} - \Delta E_0$, only events within $\Delta E_0 \pm \Delta$ were accepted. Figure 4.1 shows the cuts necessary to reject charge state contaminants for two different criteria ($n_{\text{ch. st.}} = 0.25$, and $n_{\text{ch. st.}} = 1$).

For the remainder of this analysis the cuts calculated for an estimated number of contaminants of $n_{\text{ch. st.}} = 0.25$ were used. This requires rejecting a large number of good events for isotopes with $Z \geq 31$. The large cuts could also introduce additional systematic errors in the TOF measurement if it has some residual correlation with the ΔE. For some of the heavier isotopes there might also be contamination from charge states of isotopes with lower Z (for example ^{77}Zn in ^{82}Ge). Besides this, as discussed in section 4.5.1, most isotopes for which a new mass is measured in the present work have $Z \leq 27$, and using the heavy isotopes as reference points does not have much effect in constraining the fit in the lower Z region. Therefore, the isotopes with $Z \geq 31$ are not considered in the analysis.

4.2 Correction of TOF for the Bρ of the fragments

An important step of the data analysis is finding the best procedure to determine the TOF that corresponds to the central trajectory of each isotope, which is the quantity that will be related to the nuclear mass. Because of the finite acceptance of the beamline there are many different trajectories a fragment can follow through the magnetic system, and this results in a broadening of the measured TOF spectra that would reduce the resolution of the measurement. The main contribution to this broadening comes from the Bρ acceptance in the experimental setup (0.5 %), which impacts the TOF in two different ways:

$$TOF = \frac{L(\vec{x})}{c}\sqrt{1 + \left(\frac{mc}{qB\rho}\right)^2} \tag{4.2}$$

In 4.2 c is the speed of light, m and q the mass and charge of a given fragment, and $L(\vec{x})$ is the path length of the trajectory they follow through the beamline (which depends on the initial coordinates $\vec{x}$ of the fragment). Since Bρ is equal to momentum per unit charge (p/q) it determines the velocity of each fragment. In fact, in beam optics jargon the percentage momentum deviation from the central trajectory ($\delta p = (p - p_0)/p_0$) is usually used interchangeably with Bρ . In addition, Bρ determines the radius of the orbit the fragments follow in the dipole magnets of the beamline, and this is the major contribution to variations in the path length of the trajectories $L(\vec{x})$ for the beam optics setting of this experiment (Section 3.2).

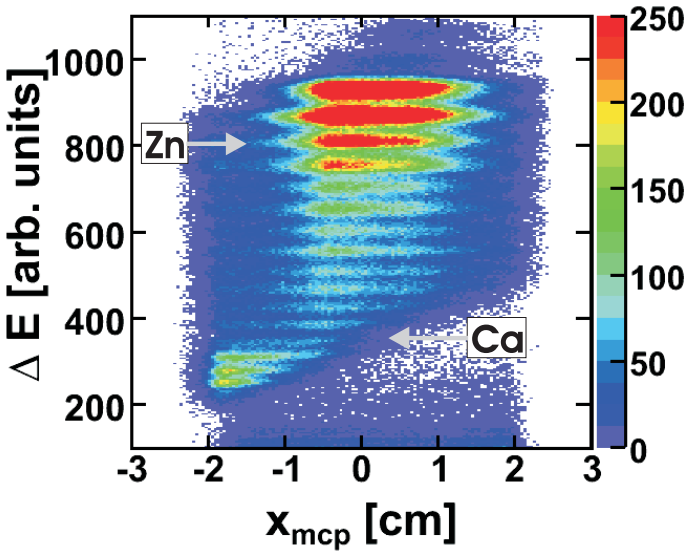

Figure 4.4: Momentum distribution of the different fragments transmitted to the S800 focal plane. The energy loss in the ion chamber detector is roughly proportional to the nuclear charge of the fragments, and the location of the events for Zn (Z=30, $\Delta E \sim 800$) and Ca (Z=20, $\Delta E \sim 350$) is indicated. The position at the S800 dispersive plane (x_{mcp}) is proportional to the momentum of the particles.

The variation of TOF with Bρ is large compared to the precision required for the TOF determination (order of 1 ps). The need for a good correction can be illustrated with a simple order of magnitude estimate. As explained in 3.3.3 the Bρ is inferred from the position of the beam particles at the dispersive plane of the S800

spectrometer, as measured with the MCP detector (x_{mcp}). The dispersion at this position is about $-12.5\,\mathrm{cm}/\%$ for the optics setting used. Therefore, the variation of the path length of the trajectories with momentum, $L(\delta p)$, is about $2\,\mathrm{cm}/\%$ (using the $(l|\delta)$ coefficient in the transfer matrix of the system, equation 3.1). Considering a path length of 58.7 m and a Bρ of 3.67 Tm for the central trajectory, the dependence of TOF on Bρ for ^{66}Fe is to first order about $4000\,\mathrm{ps}/\%$, or $315\,\mathrm{ps/cm}$ using x_{mcp} to determine the Bρ. The linear term of a correction function has to be know at a better than percent level if the TOF of a fragment whose trajectory is 1 cm away from the center is to be corrected with an accuracy at the sub-picosecond level. The slope for the dependence of TOF on Bρ observed in the experiment matches this estimate (it is $\approx 300\,\mathrm{ps/cm}$ for ^{66}Fe).

The other important reason to correct the measured TOF is that, because of its strong correlation with Bρ , the shape of the uncorrected TOF distribution is entangled with the momentum distribution of the transmitted particles. The situation is complicated by the fact that the shape of the observed Bρ distribution differs significantly for different isotope. This results from a combination of different momentum distributions after the production target, energy losses in the beamline detectors, and efficiencies of the MCP detector as a function of position and of the ions' charge. Figure 4.4 shows the Bρ distribution for all isotopes in the secondary beam, and the Bρ distribution for a few isotopes are shown in Figure 4.5. The main trend is that the lower Z fragments have a distribution shifted towards the large Bρ particles (negative x_{mcp}). These isotopes will be more sensitive to errors in the determination of a momentum correction of the TOF, which is also more difficult to fit at the narrow x_{mcp} range covered by the data. As described in Section 4.5, this is the main reason why isotopes with $Z \leq 20$ (Ca) were not included in the final mass calibration of the experiment.

4.2.1 Correction functions

A function $F(x_{\mathrm{mcp}})$ that describes the TOF dependence on the position at the S800 dispersive plane was used for the Bρ correction. Both a linear and a quadratic polynomial on x_{mcp} were considered. The correlation between TOF and x_{mcp} has a clearly quadratic form, in particular for the heavier elements, and in the end it was found to provide the best mass fit. However, the linear correction was also used during the analysis as it provided a simpler parameterization of the correction, and was a useful tool to understand the level of precision required.

There is a smooth variatio in the correlation between TOF and x_{mcp} for the different species in the ion beam, which is a consequence of their different velocities and energy losses in the beamline detector, so a parameterization of the correction function was obtained for each isotope i. Then, the corrected TOF (TOF_{corr}) is obtained by subtracting $F_i(x_{\mathrm{mcp}})$ from the measured TOF:

$$TOF_{\mathrm{corr}} = TOF - F_i(x_{\mathrm{mcp}}) \tag{4.3}$$

The polynomial functions were fit to the spectra of each isotope. The linear fit was performed to a subset of the data that fills a uniform x_{mcp} distribution around $x_{\mathrm{mcp}} = 0$. The results of these fits for a few selected isotopes are shown in Figure 4.5. It should be noted that for some events with low statistics (including the isotopes with unknown nuclear mass) a satisfactory fit cannot be obtained. The same is true for isotopes where the x_{mcp} distribution is very asymmetric, in particular for isotopes with $Z \lesssim 20$. The results of the fits to each isotope $TOF\,vs\,x_{\mathrm{mcp}}$ distribution are shown in appendix A.

The functions fitted to the individual spectra were not applied directly for the TOF correction, but a global correction function obtained from trends in the fit results versus A and Z was used. Such a function has a smooth variation across the region of isotopes studied, and avoids the scatter of the fit parameters affecting

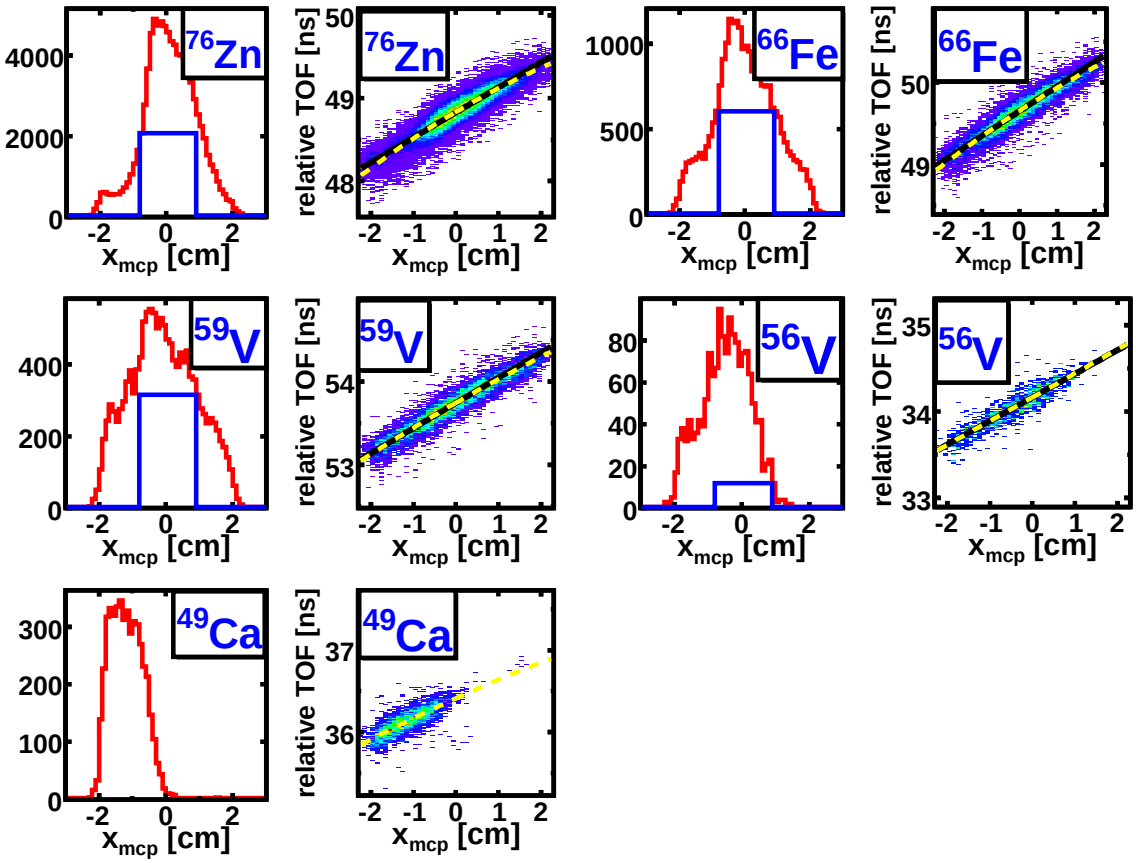

Figure 4.5: For five isotopes in the secondary beam their momentum distribution (x_{mcp} at dispersive plane) and its correlation with TOF are shown. A linear (solid black line) and a quadratic (dashed yellow line) fit to the $TOF\,vs\,x_{\mathrm{mcp}}$ spectra are also shown (the residuals can be better appreciated in Figure 4.9). For the linear fit only events that fill a uniform distributions for $-0.8\,\mathrm{cm} < x_{\mathrm{mcp}} < 0.9\,\mathrm{cm}$ were used (blue). For the case of ^{49}Ca, and other isotopes with similar mass, the x_{mcp} distribution was too shifted to the left to obtain a linear fit with such constraints. The spectra for all isotopes in the secondary beam are shown in appendix A.

Table 4.1: Parameters used to calculate the coefficients of the linear (equation 4.4) and the quadratic (equation 4.5) momentum correction functions for the TOF.

Parameter	$p1_{\text{lin}}$	$p1_{\text{quad}}$	$p2_{\text{quad}}$
a_0	-0.274845721	-0.495819765	0.0457694275
a_1	-0.222951004	0.226370782	0.00790747553
a_2	0.135510969	0.0142303718	-0.00471765307
a_3	0.0465997738	-8.89489657e-05	6.48102481e-05
a_4	-0.000305486697		
a_5	-0.0111523041		

the fits to the spectra of individual isotopes. In addition, it provides more reliably parameters of the correction function for the isotopes with low statistics. The linear and quadratic Bρ correction functions obtained are as follows:

$$TOF_{\text{corr}}[ns] = TOF - p1_{\text{lin.}} \times x_{\text{mcp}} \tag{4.4}$$

$$TOF_{\text{corr}}[ns] = TOF - p1_{\text{quad.}} \times x_{\text{mcp}} - p2_{\text{quad.}} \times x_{\text{mcp}}^2 \tag{4.5}$$

The parameterization of their coefficients is given by:

$$p1_{\text{lin.}}[ns/cm] = a_0 + a_1 A/Z + a_2 (A/Z)^2 + a_3 Z + a_4 Z^2 + a_5 A \tag{4.6}$$

$$p1_{\text{quad.}}[ns/cm] = a_0 + a_1 (A/Z) + a_2 Z + a_3 A \cdot Z \tag{4.7}$$

$$p2_{\text{quad.}}[ns/cm^2] = a_0 + a_1 (A/Z) + a_2 Z + a_3 Z^2 \tag{4.8}$$

The data used to obtain this parameterization is shown in figures 4.6, 4.7, and 4.8, and the results are summarized in table 4.1. Different options were explored to obtain this parameterization, and the results shown provide the best global fit as evidenced by its χ^2 value, the trends in its residuals and a qualitative comparison to

the data. For the fit of the linear correction function a small number of data points with $Z \leq 20$ were available because they do not fill the Bρ distribution. However, for both the linear and the quadratic correction functions a good global parameterization that would extend the range of isotopes with $16 \leq Z \leq 32$ could not be obtained, and the fits were restricted to $Z \geq 20$. The weight of each isotope in the fit was calculated from its number of events (N):

$$w = (1/N + 1/5000)^{-1/2} \tag{4.9}$$

The constant uncertainty of $1/\sqrt{5000}$ was added to all points to avoid that some isotopes with high statistics ($\approx 10^5$) dominated the fit. In addition, some outliers data points from isotopes with low statistics were not included in the fit.

Figure 4.9 shows the agreement of the global correction functions obtained in this way with the TOF vs Bρ (x_{mcp}) data for a few isotopes (see Appendix A.1 for the spectra of all isotopes). There is a clear quadratic component on the dependence of TOF on Bρ , which is larger for higher Z isotopes and is much reduced for isotopes with $Z \sim 20$ and lower. It is interesting to note that this term is of the opposite sign of what would be expected from the expansion of 4.2. This equation does not consider the energy loss in the MCP detectors at the S800 dispersive plane, which has a small variation with the momentum of the fragments and is larger for higher Z isotopes. It is also possible that higher order terms in the beam optics of the system (for example, in the path length of the particles $L(\vec{x})$) or in the position calibration of the MCP detector create this effect. The TOF shows deviations from a quadratic Bρ dependance for $x_{\mathrm{mcp}} < -1.5$ cm (and to a smaller extent for $x_{\mathrm{mcp}} > 2.0$ cm), as can be seen in the spectra for ^{76}Zn in Figure 4.9. This coincides with the x_{mcp} position range where the resolution of the MCP detector begins to degrade (Figure 3.14). Only events with $-1.5\,\mathrm{cm} \leq x_{\mathrm{mcp}} \leq 2.0\,\mathrm{cm}$ were used to obtain the final mass results (Section 4.6.2).

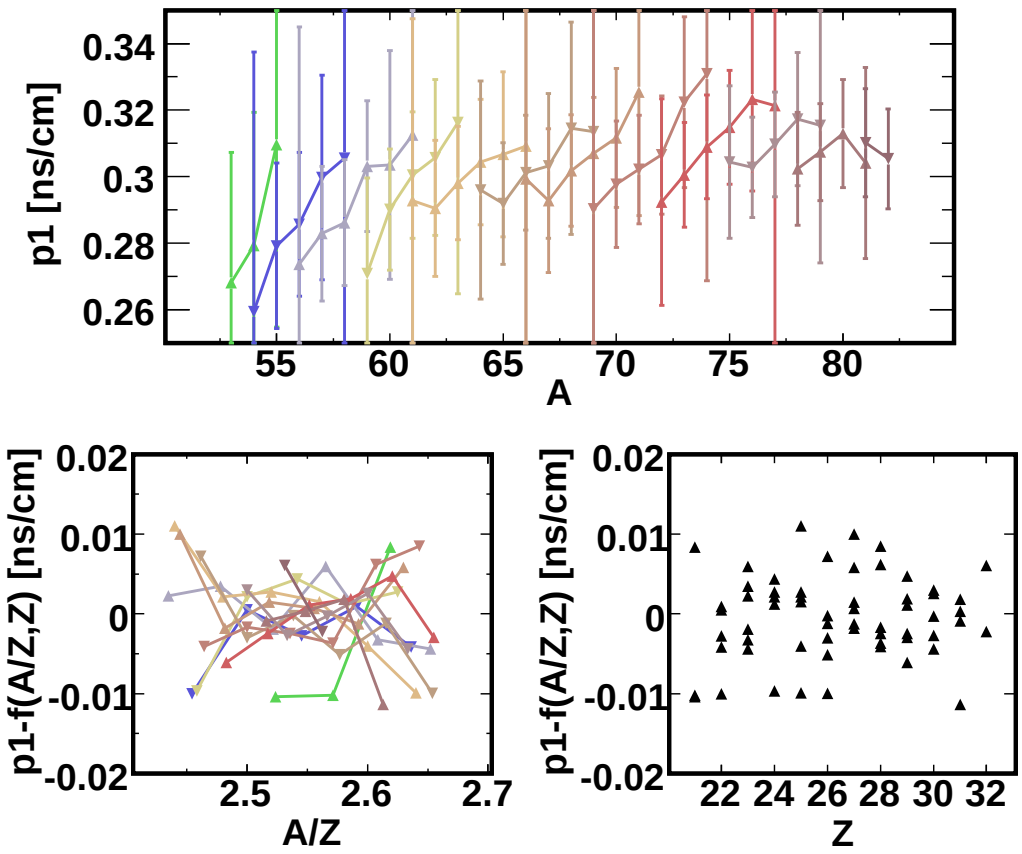

Figure 4.6: Fit for the slope (p_1) of a TOF momentum correction function linear in x_{mcp}. The top plot shows the slope of fits to the spectra of individual isotopes as a function of their mass (A). The lower plots show the residuals of the parameterization of these slopes by the equation 4.6. The error of each data point, only shown in the first frame, was calculated from the statistics of each isotope (Equation 4.9).

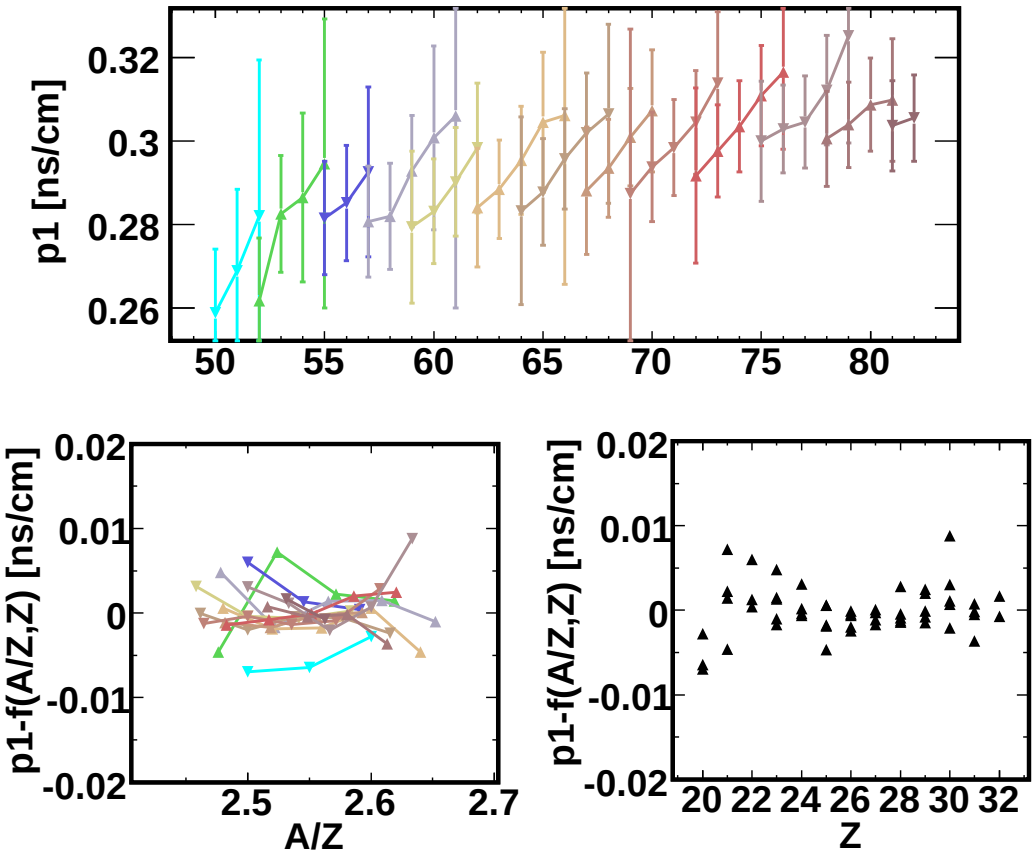

Figure 4.7: Fit for the slope (p_1) of a TOF momentum correction function quadratic in x_{mcp}. The top plot shows the linear term of fits of fits to the spectra of individual isotopes as a function of their mass (A). The lower plots show the residuals of the parameterization of these slopes by the equation 4.7. The error of each data point, only shown in the first frame, was calculated from the statistics of each isotope (Equation 4.9).

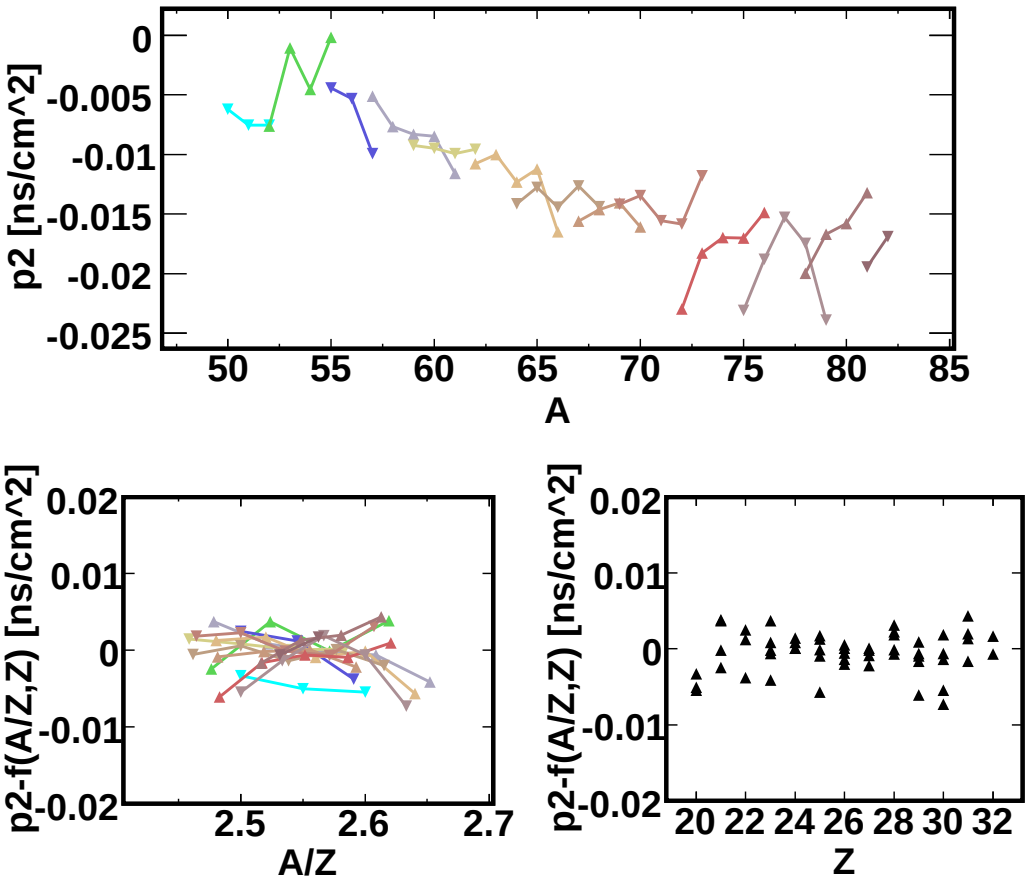

Figure 4.8: Fit for the quadratic term (p_2) of a TOF momentum correction function quadratic in x_{mcp}. The top plot shows the quadratic term of fits of fits to the spectra of individual isotopes as a function of their mass (A). The lower plots show the residuals of the parameterization of these slopes by the equation 4.8. The weight given to each data point in the fit is the same as the one shown in Figure 4.7.

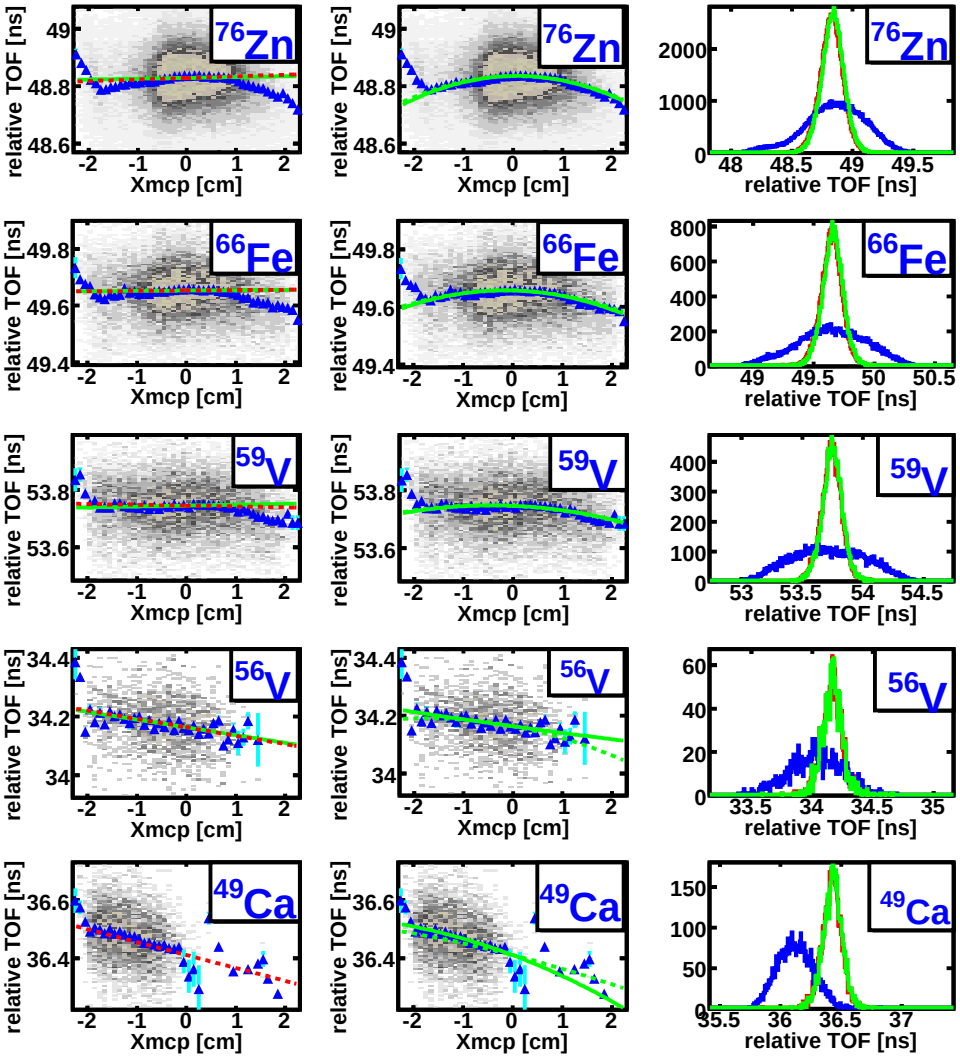

Figure 4.9: TOF vs x_{mcp} spectra for selected isotopes. The fits to each spectra using a linear (left graphs) and a quadratic (center graphs) are shown as black lines. In addition, the global parameterizations of the momentum corrections are shown as a dashed red line for the linear case, and as a dashed green line for the quadratic correction. For a better visualization of the results, a constant slope of 0.30 s/cm was subtracted from all functions and from the data. The data is also shown as a *Profile histogram* (blue triangles), which plots the average content of each bin. The figures in the right column show the uncorrected TOF spectra (blue), as well as TOF_{corr} for the linear (red) and the quadratic (green) momentum corrections. Results for all isotopes in the secondary beam are shown in Appendix A.1.

Figure 4.9 also shows a comparison of the uncorrected TOF and the momentum corrected TOF_{corr} for both correction functions. It is clear that both the linear and the quadratic momentum correction functions produce a large improvement in the TOF resolution of the measurement. The centroid of the TOF_{corr} spectra is also significantly shifted (by hundreds of picoseconds) compared to the uncorrected one, in particular for the isotopes that do not fill their momentum distribution. The difference between both corrections is at the picosecond level.

4.3 Additional corrections to the time of flight

The finite momentum acceptance of the beamline is the dominant effect in the spread of the time of flight of the isotopes. However, there are other additional factors in the experimental set up that can produce a broadening, or a systematic shift, in the measured TOF of the beam particles. These were investigated to decide if additional corrections to the TOF were necessary, and to characterize the experimental setup for future measurements.

As a first step, a correction of the dependence of the measured TOF on the amplitude of the timing detector's signals is discussed. The correlations of the TOF with the beam coordinates were also studies. If the path length followed by the beam fragments depends on their initial coordinates this will change the measured TOF, and could limit the resolving power of the setup when the emittance of the beam is large [58]. Finally, the effect of the temperature variations in the S800 experimental vault and the behavior of the timing electronics are discussed.

4.3.1 Correction for timing between PMTs

The momentum corrected TOF was found to have a residual correlation with the timing between the Up and Down photomultiplier tubes (PMTs) of the two timing

detector, one located at the A1900 extended focal plane (t_{XUXD}) and the other at the S800 focal plane (t_{SUSD}). There are several possible causes for these correlations, but because of their dependence on the isotopes charge (Z) they are attributed to a pulse height dependence in the response of the timing electronics. This effect is refered to as timing walk, and it was discussed in Section 2.2.2. A linear correction using t_{XUXD} and t_{SUSD} as variables was implemented and it reduced the TOF resolution by up to 10 ps for some isotopes. However, as described in Section 4.6, such correction did not improve the mass fit and it was not used to obtained the final results.

The measure value of the TOF is obtained by combining the signals of the Up and Down PMT of each timing detector (Section 3.3.2). As a reminder, the TOF_1 value is constructed in the following way:

$$TOF_1 = t_{\mathrm{offset}} - t_{\mathrm{SDXD}} - (t_{\mathrm{SUSD}} - t_{\mathrm{XUXD}})/2 \tag{4.10}$$

The difference between one signal from the S800 focal plane detector and one from the A1900 extended focal plane detector (t_{SDXD}) provides a rough measurement of the TOF of each beam particle. Because the piece of scintillating material used in the timing detector is 2.54 cm long it can take up to 134 ps for the photon signal generated by the beam particles to travel to one of the PMTs (the refractive index of the scintillator material is 1.58). Therefore, to achieve a resolution of tens of picoseconds the time between the two PMTs of each detector (t_{SUSD} and t_{XUXD}) is averaged and included in the measured TOF. The resulting TOF value should not be sensitive to the distance between the beam interaction with scintillator and the surface of the PMTs where the photons are collected. An equivalent TOF value is constructed for the measurements of each PMT signal with respect to a clock (TOF_{clk} in Equation 3.3).

The residual correlation observed between the measured TOF (either TOF_1 or TOF_{clk}) with t_{SUSD} and t_{XUXD} is of up to $\approx 200\,\mathrm{ps/ns}$. A possible origin for

it would be that the time delay due to the photon signal in the scintillator is not completely accounted for in Equation 4.10 (for example, this could happen if the time calibration of the electronic modules is not accurate enough). In addition, the time difference between both PMTs of each detector is strongly correlated to the beam position at the detectors location, and to the amplitude of the pulse from the PMTs. Such correlations were observed during the test run of the timing scintillators discussed in Chapter 2, and the same behavior was observed during the mass measurement experiment (the spectra for a few isotopes are shown in Figure 4.10 to 4.11). For this reason, the effect these variables have on the measure TOF is entangled and the source of the residual TOF correlation is not obvious. For instance, the difference in the path length of the beam particles that arrive at different positions at the S800 focal plane could produce the observed TOF correlation [1].

As constant fraction discriminator module (CFD) was used in the timing electronics to eliminate any dependence of the timing signals on the amplitude of the PMTs analog output (Section 2.2.2). However, it can be inferred from the data that such effect was not completely cancelled and it explains the observed TOF dependence on t_{SUSD} and t_{XUXD}. The PMT's signal amplitude is proportional to the energy deposited by the beam particles in the scintillator material, so it has a strong dependence on the nuclear charge of the fragments (Z), and to a lesser extend on their velocity [48]. Because more than one hundred different isotopes were present in the secondary beam during the experiment a large range of signal amplitudes were generated from the PMTs. Figures 4.12 through 4.15 show the correlation between the measured TOF and the signal amplitude from the PMTs (the integrated charge Q of the signal is the value actually recorded in the experiment), as well as the correlation with the timing between the Up and Down PMT of each detector. In the case of the signal from the XFP Up PMT, the measured TOF shows clear variations with the

[1] Given the path length of ≈ 58 m for the central trajectory and a the TOF through the beamline around 460 ns, the TOF of one fragment would change by about 8 ps if the path length it follows changed by 1 mm.

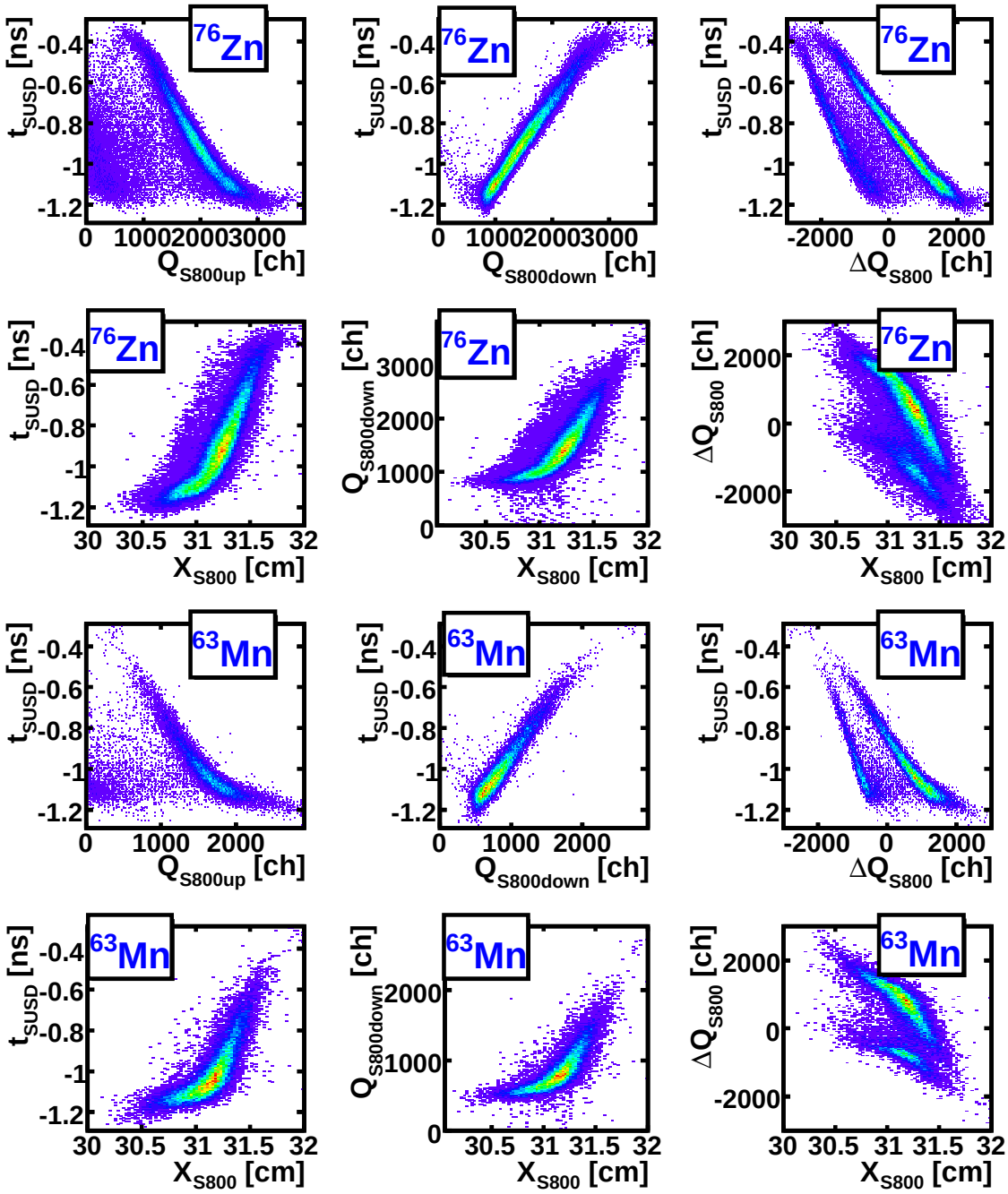

Figure 4.10: Correlations between signal amplitude from the S800 PMTs with the timing between both PMTs and the x_{S800} position for ^{76}Zn (Z=30) and ^{63}Mn (Z=25) events. The difference between both signal amplitudes is also shown ($\Delta Q_{\mathrm{S800}} = Q_{\mathrm{S800up}} - Q_{\mathrm{S800down}}$).

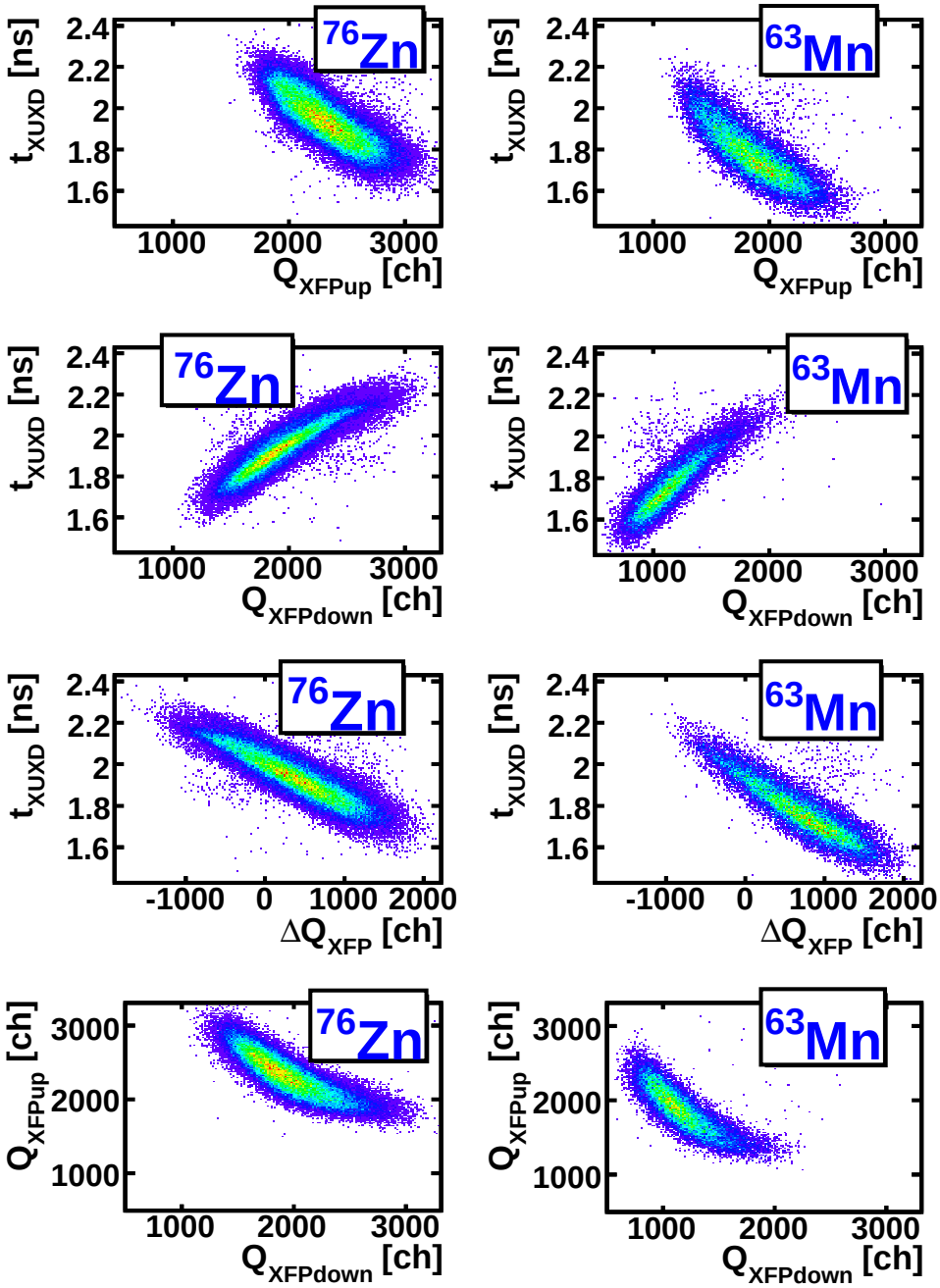

Figure 4.11: Correlations between signal amplitude from the S800 PMTs and the timing between its signals for ^{76}Zn (Z=30) and ^{63}Mn (Z=25) events. The difference between both signal amplitudes is also shown ($\Delta Q_{\mathrm{XFP}} = Q_{\mathrm{XFPup}} - Q_{\mathrm{XFPdown}}$).

signal amplitude for the isotopes with $Z \lesssim 25$, but the trend is not so clear for the heavier fragments. The trend is reversed for the TOF dependence on the output of the S800 Up PMT; in this case the CFD did not compensate the timing in the case of large signal amplitudes for the heavier fragments, and their measured TOF was observed to vary by up to ≈ 100 ps across the range of the integrated charge spectra.

In addition, the operational voltage of the PMTs was adjusted after the first run of the experiment, affecting their signal amplitudes. During the analysis a noticeable shift in the timing of some isotopes after this first run was found, and this provides further evidence of the presence of timing *walk* in the electronics.

The integrated charge, Q, of each PMT signal is the most direct method available for a correction to a pulse height dependence of the measured TOF. The difference between the integrated charge of each Up and Down PMT ($\Delta Q_i = Q_{i\text{up}} - Q_{i\text{down}}$) can also be used, providing a correction function that relies on less parameters. However, as shown in Figure 4.10, about 20 % of the events have a bad measurement of the integrated charge in the S800 Up PMT, and would have to be excluded if using Q for in a correction function. For that reason, the time difference between the signals from the PMTs of each detector (t_{SUSD} and t_{XUXD}) were selected as the variable for the TOF correction, which as shown in Figure 4.10 and 4.11 are closely correlated with their signal's integrated charge.

The following linear correction functions was fit to the data:

$$TOF_{\text{corrQ}} = TOF_{\text{corr}} + p_{\text{XFP}} \cdot t_{\text{XUXD}} + p_{\text{S800}} \cdot t_{\text{SUSD}} \tag{4.11}$$

Figure 4.16 shows the parameters in 4.11 obtained for each isotope in the beam. A global parameterization as a function of the mass number A was used to avoid the scatter of the parameters fit to isotopes with low statistics.

The sensitivity of the measured TOF to the signal amplitude is greatly reduced with the linear correction 4.11, but there are still residual dependences that affect the

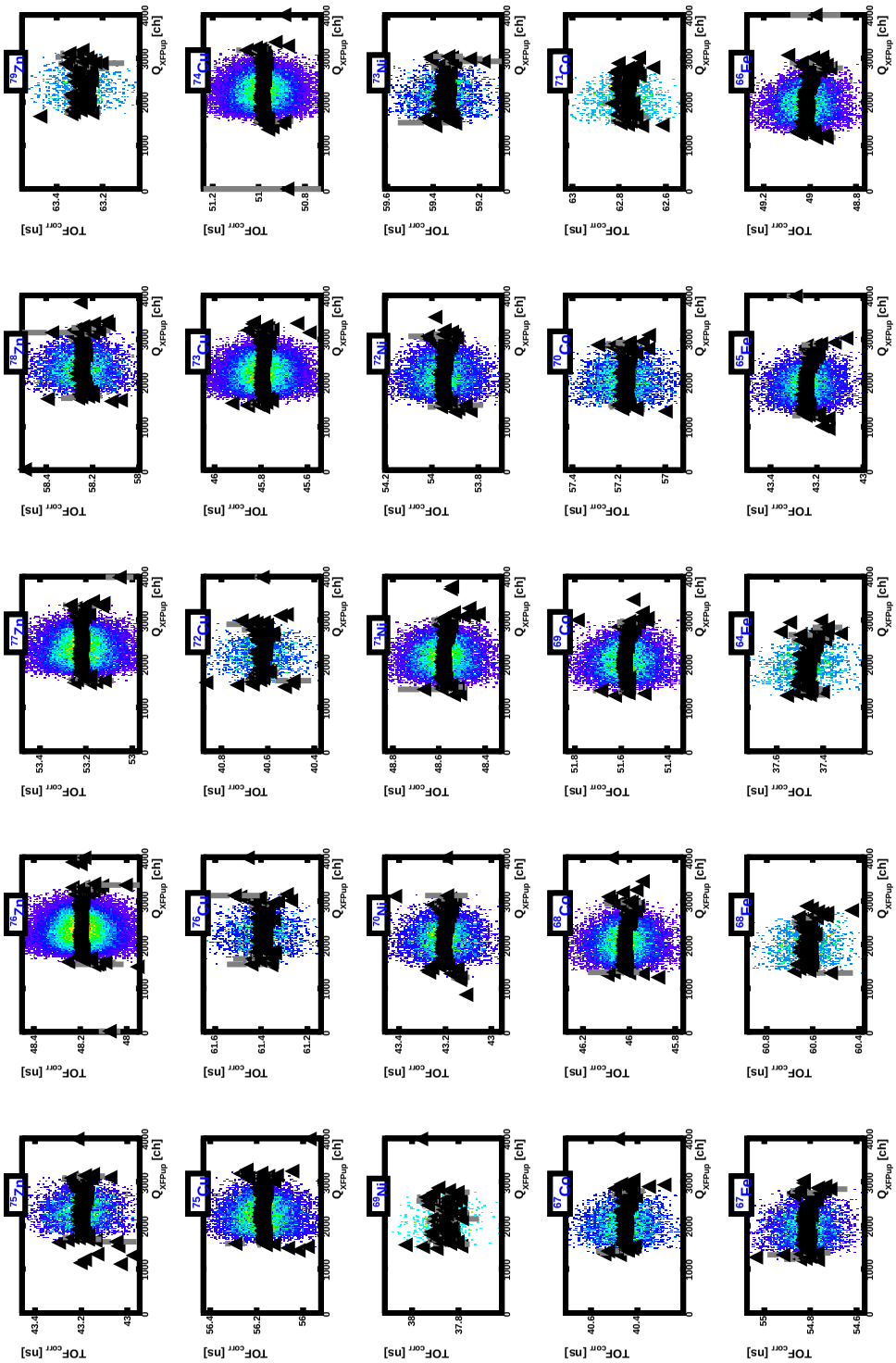

Figure 4.12: Momentum corrected TOF for fragments with a large nuclear charge as a function of the signal amplitude in the *XFP up* PMT. A *profile histogram*, which plots the average TOF value for each bin, is superimposed to the data.

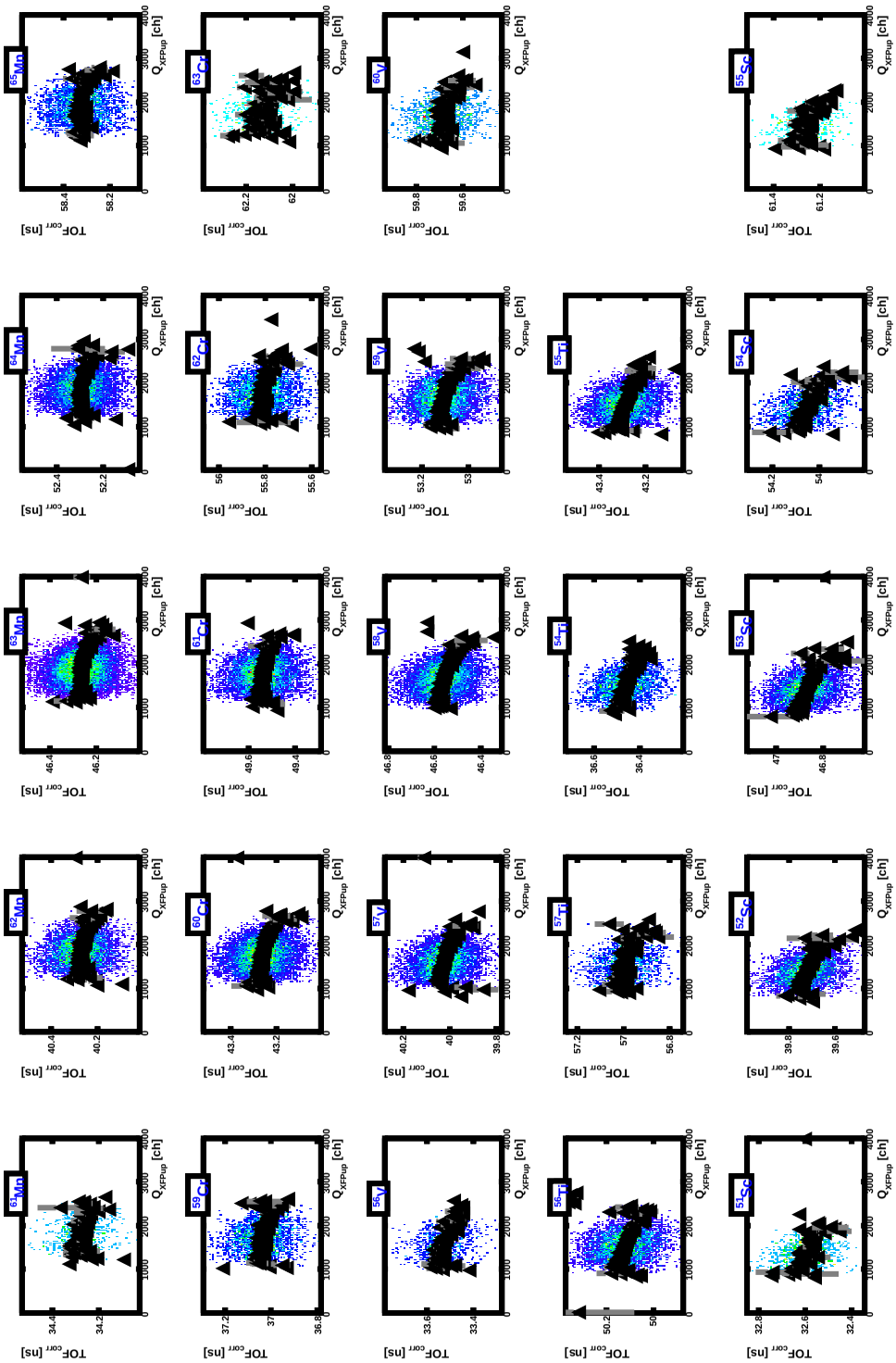

Figure 4.13: Momentum corrected TOF for fragments with a large nuclear charge as a function of the signal amplitude in the *XFP up* PMT. A *profile histogram*, which plots the average TOF value for each bin, is superimposed to the data.

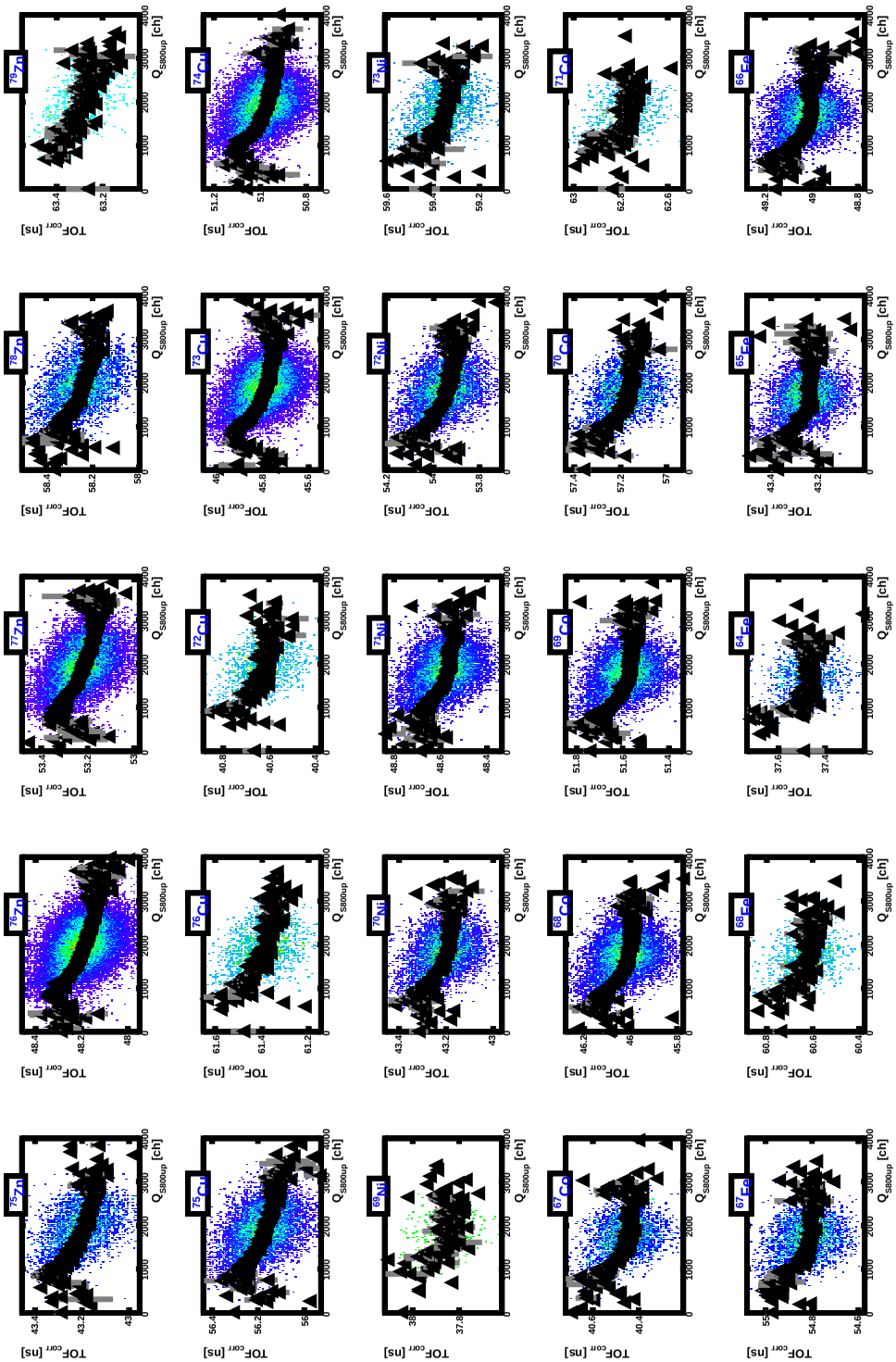

Figure 4.14: Momentum corrected TOF for fragments with a large nuclear charge as a function of the signal amplitude in the *S800 up* PMT. A *profile histogram*, which plots the average TOF value for each bin, is superimposed to the data.

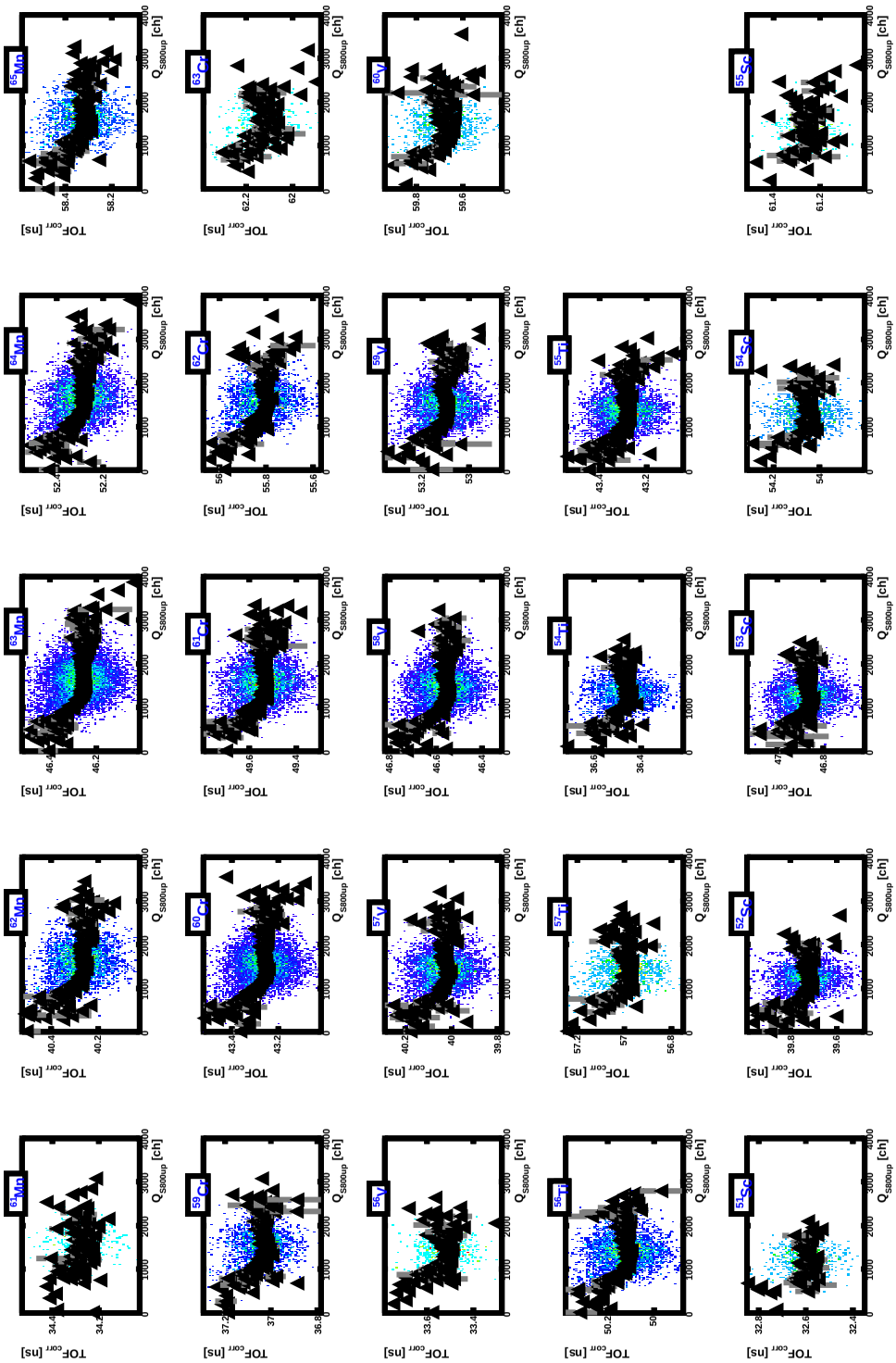

Figure 4.15: Momentum corrected TOF for fragments with a small nuclear charge as a function of the signal amplitude in the *S800 up* PMT. A *profile histogram*, which plots the average TOF value for each bin, is superimposed to the data.

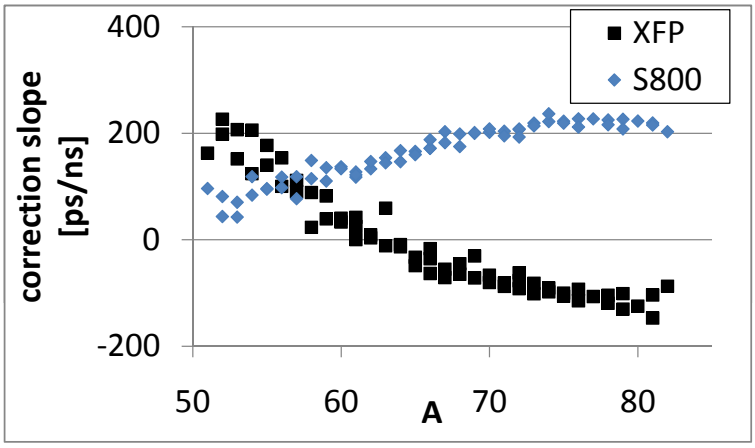

Figure 4.16: Results of the fits to the momentum corrected time of flight as a linear function of the time difference between the two PMT signals from each detector. The slope obtained for a linear fit of the TOF distribution of individual isotopes is shown as a function of their mass number A. A second order polynomial as a function of A was used to parameterize the slope of the correction function (p_{XFP} and p_{S800} in Equation 4.11).

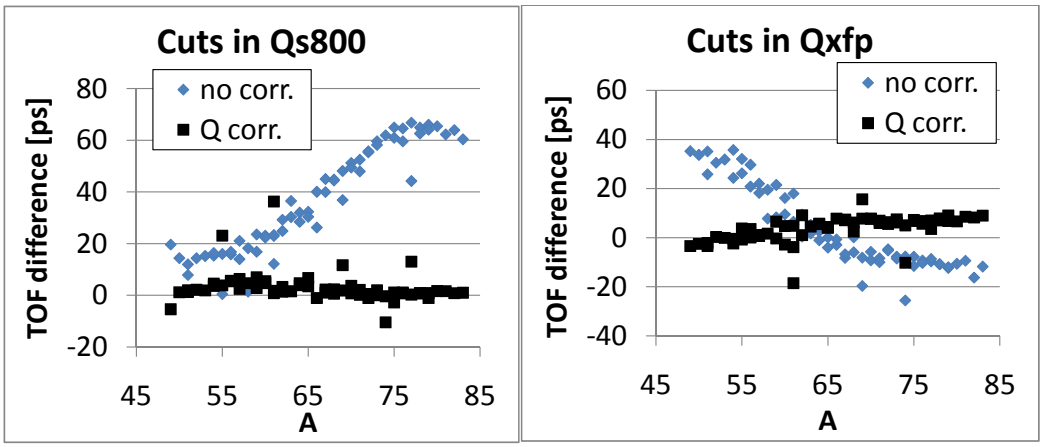

Figure 4.17: TOF determined for events with different amplitude in the PMT signals. The left (right) figure shows the difference in the determined TOF for events with a large signal in Q_{S800down} (Q_{XFPdown}) versus the TOF determined from the events with a low amplitude signal in that detector. The difference is shown for a TOF that was only corrected by the particles momentum (TOF_{corr}, shown as light diamonds), and also for data that was also corrected by their t_{SUSD} and t_{XUXD} following equation 4.11 (TOF_{corrA}, shown as black squares).

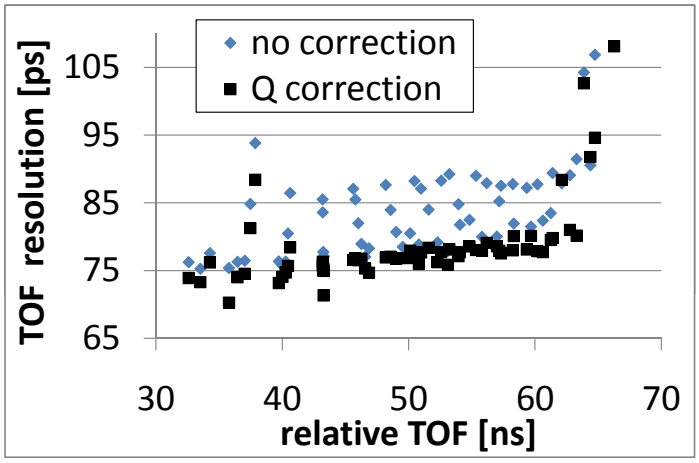

Figure 4.18: Width (σ) of the TOF distribution for events corrected only by their momentum (TOF_{corr}, shown as light diamonds), and those with an additional correction for the signal amplitude in the PMTs following Equation 4.11 (TOF_{corrQ}, shown as black squares).

TOF at the picosecond level. This is illustrated in Figure 4.17, which shows the TOF determined by dividing the data in two sets: one composed of events with a large value of Q in one PMT, and the second with events having a low signal amplitude in the same PMT. The TOF determined for each set of events can differ by up to 60 ps if no correction is used, and the differences are reduced to less than 10 ps with the additional correction. The figure also shows that the correction works better to cancel the timing walk for the S800 detector than for the A1900 XFP one, for which the TOF is overcorrected in the case of the heavier isotopes. The width of the measured TOF distribution is also reduced by $\delta\sigma_{\mathrm{TOF}} = -5.5$ ps on average (Figure 4.18).

Other correction functions were tried, and they gave similar results in terms of the trends of their fit parameters, and their ability to reduce the observed TOF correlations. In particular, these were a linear correction using the difference in the integrated charge (ΔQ) of the PMT, as well as more elaborate functions of t_{XUXD} to improve the the correlations with the signals from the A1900 XFP detector.

It is clear that the correction functions explored do not fully describe the problem. Besides, the form of an appropriate correction function might not be well described

by a global parameterization, which is important to obtain a precise correction for the events with low statistics (including the more neutron-rich isotopes). The distribution of the time between the PMTs signals, and their integrated charge, varied smoothly for the different isotopes in the beam. It can be expected that their effect in the measured TOF will have the similar variations, and that it can be accounted for by the parameters of the mass calibration function. As it was mentioned before, none of these TOF corrections were included in the final mass fit as they did not provide better results than using the uncorrected TOF (Section 4.6.3). However, the correction functions discussed in this section were found to improve the TOF resolution by up to 10 ps, so this is an area for potential improvements of the setup in future experiments.

4.3.2 Time-of-flight dependence on beam coordinates

The correlation of the fragments TOF with the measured beam coordinates (position and angle at the S800 dispersive plane and focal plane) was explored. The most clear effect was found for the dispersive angle at the S800 focal plane, a_{S800}, and it is shown in Figure 4.19 for a few isotopes. As it was the case for the signal amplitude correction, the effect of the beam angle on the TOF is entangled with other beam coordinates. In particular, the S800 timing scintillator was not located exactly at a focus point of the beam, so the fragments' angle and position at this location were correlated (Figure 4.20). Therefore, the correction for the beam angle was done using the TOF corrected by the PMT signal amplitude (TOF_{corrQ} in equation 4.11) to minimize the effect of the walk in the timing electronics in the results.

A cubic polynomial was fit to the TOF_{corrQ} vs a_{S800} spectra of each isotope to obtain the following correction function:

$$TOF_{\mathrm{corrA}} = TOF_{\mathrm{corrQ}} + p_1 \cdot a_{\mathrm{S800}} + p_2 \cdot a_{\mathrm{S800}}^2 + p_3 \cdot a_{\mathrm{S800}}^3 \qquad (4.12)$$

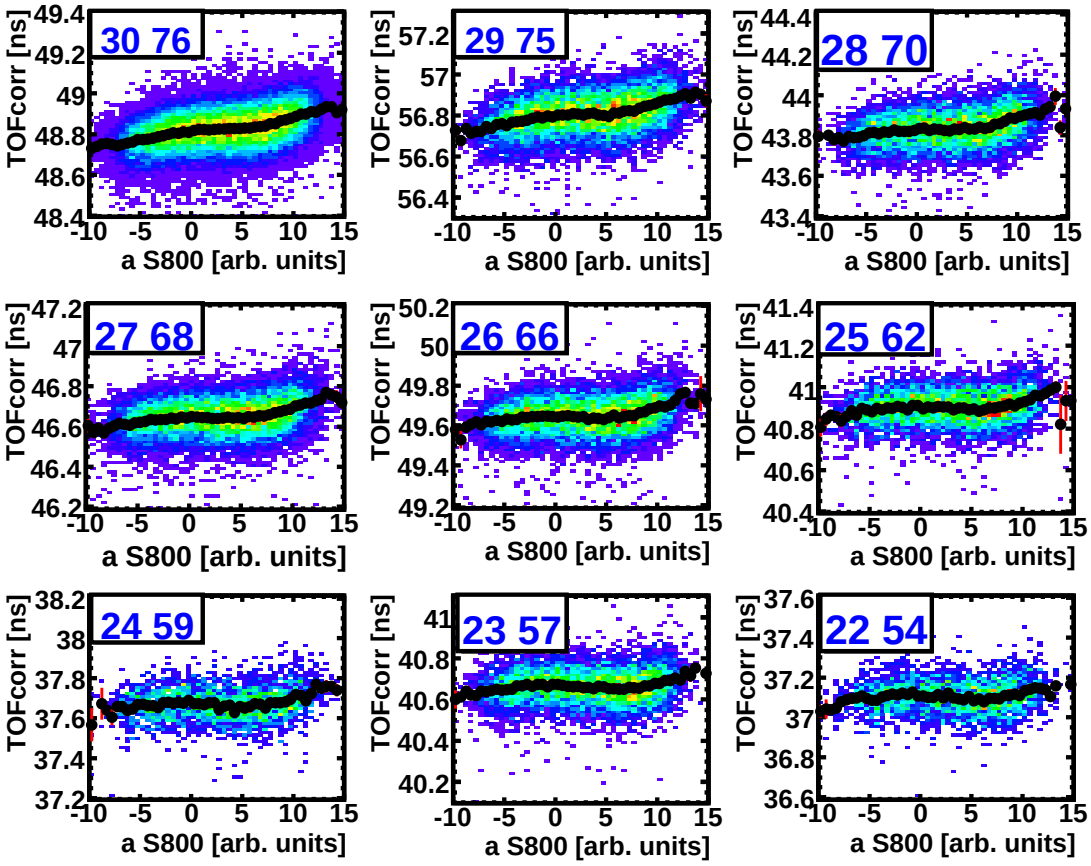

Figure 4.19: Correlation between the momentum corrected TOF and the dispersive angle in the S800 FP (a_{S800}) for selected isotopes in the secondary beam (indicated by their Z and A).

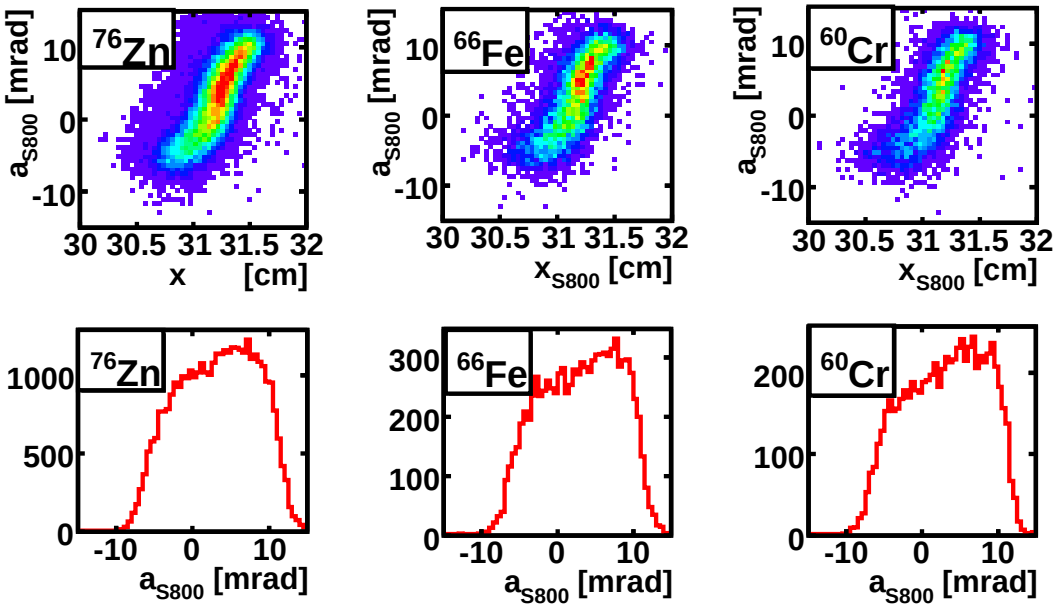

Figure 4.20: The upper figures show the correlation between the angle and position at the location of the S800 timing detector (S800 focal plane) for a few isotopes in the beam. The correlation between both variables shows that the beam was focused a few centimeters after the detector. The angular distribution is very similar for all species in the beam.

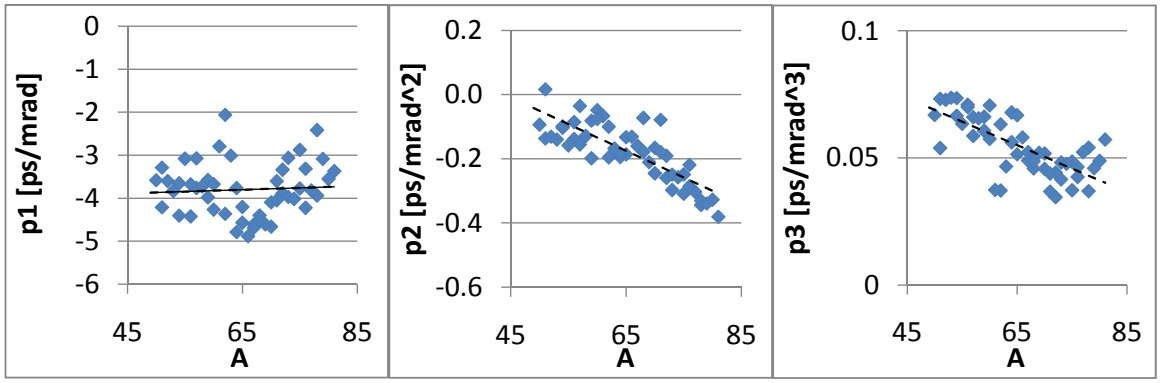

Figure 4.21: Results for the fit of the time of flight correction by the a_{S800} angle. The parameters of a cubic polynomial (Equation 4.12) fit to the TOF distribution of individual isotopes are shown as a function of their mass number A. A linear parameterization of these fit results as a function of A was used for the calculation of TOF_{corrA}.

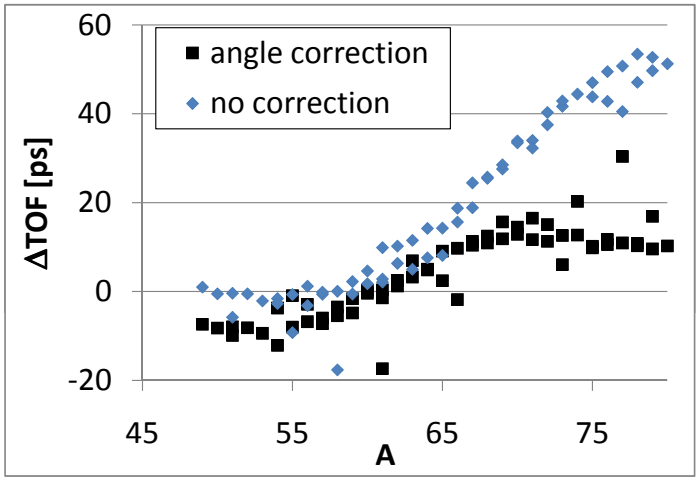

Figure 4.22: Difference in the TOF determined for events with a positive angle in the S800 focal plane versus those with negative angle. The difference is shown for the momentum corrected TOF_{corr} (light diamonds), and for the TOF_{corrA} of Equation 4.12, which is also corrected by the its dependence on the PMT signal's amplitude and the S800 angle (black squares).

The fit results are summarized in Figure 4.21. A linear parameterization of the coefficients of 4.12 as a function of the mass number A was used to correct the TOF to avoid the larger scatter in the fit results for the isotopes with lower statistics. The effect of this correction function in the measured TOF is shown in Figure 4.22. The angular dependence is reduced for the heavier isotopes, but the TOF seems to be overcorrected for the lighter species. In addition, the improvement of the TOF resolution with respect to the TOF already corrected by the PMTs signal amplitude (Figure 4.18) is only ~ 0.4 ps.

4.3.3 Temperature at S800 vault

During the experiment the fields of the S800 dipole magnets had periodic fluctuations that were correlated with the temperature in the experimental vault, as illustrated in Figure 4.23 (see Section 3.3.1 for the details). The measured TOF was found to have a linear correlation with both the temperature and the dipole magnetic fields, but with a large scatter in the slope for different isotopes. The solution adopted was to use a

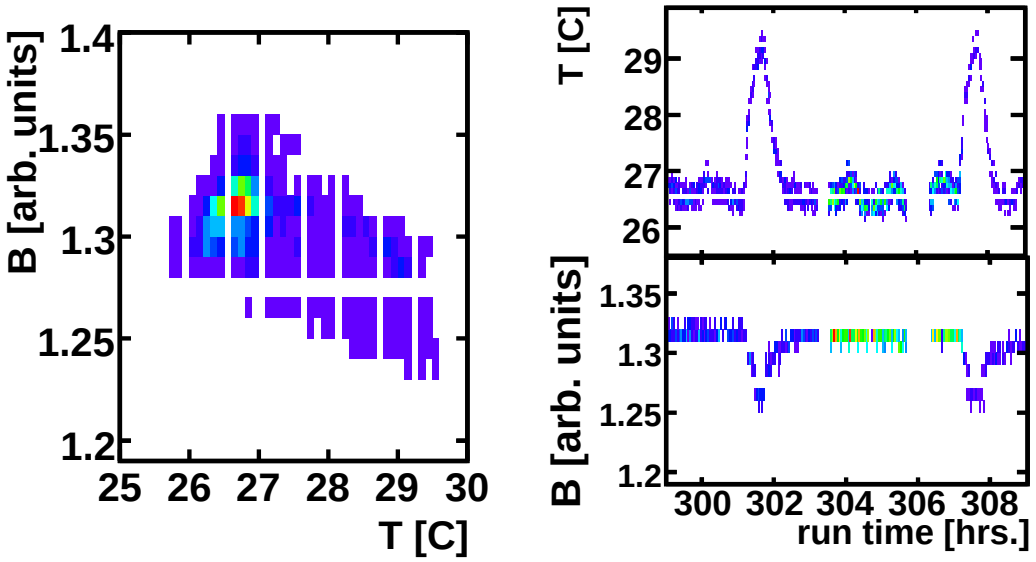

Figure 4.23: Correlation between temperature in S800 experimental vault and the magnetic field of the I265DS spectrometer dipole magnet. As explained in Section 3.3.1, the correlation results from the power supply for the dipole sharing the cooling water with the air conditioning unit in the vault. The figures on the right show data for only a fraction of the experiment.

cut in the temperature spectra to reject mostly the events when the air conditioning unit in the S800 vault switched off and the temperature rapidly increased.

The strength of the magnetic field determines the radius of the orbit the particles will follow and it directly affects their TOF. In addition, the temperature fluctuations can affect the response of the electronics modules used to measure and digitize the time between the signals of the timing detectors. A correlation of the momentum corrected time of flight with both the magnetic field B_{I265DS} and the temperature in the vault is indeed observed in the data (Figure 4.24). Because the variations in the temperature and the magnetic field are simultaneous, it is not possible to assert which one has the largest effect on the measured TOF. However, the correlation of the measured TOF with the vault temperature ($\sim 5\,\mathrm{ps}/^{\circ}\mathrm{C}$) is of the same magnitude as the temperature sensitivity of the ADC modules used (their maximum change in gain or zero offset is 50 ppm, that translates to 5 ps for a 100 ns range). Also, a

different correlation was found for the TOF_1 (direct timing) and the TOF_{clk} timing (measurement with respect to the clock). These two values were constructed from the same timing detectors signals and only differ in the TAC-ADC modules used for their digitization [2]. For these reasons, the major part of the observed variations in the TOF were attributed to changes in the operational temperature of the electronic modules, and corrected using such variable.

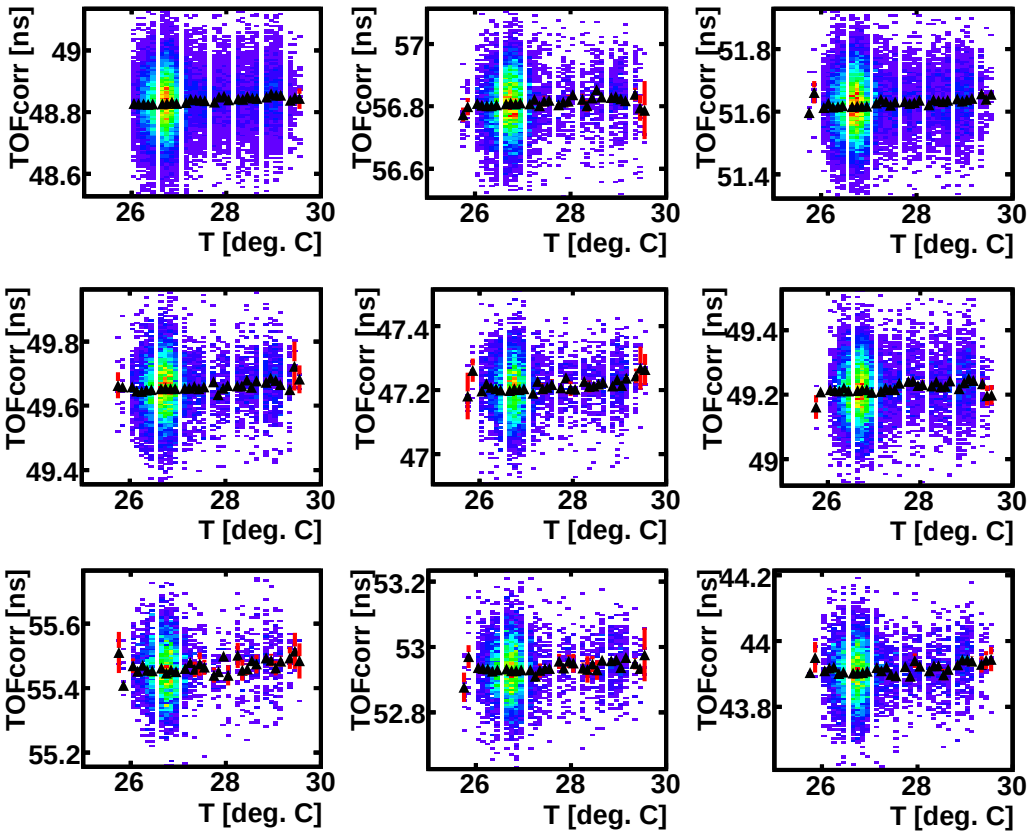

Figure 4.24: For a few isotopes the momentum corrected TOF_{corr} is shown as a function of the temperature in the S800 experimental vault. The observed correlation is of the order of 10 ps/°C for the direct TOF measurement, and about 5 ps/°C for the TOF measured with respect to a clock.

Figure 4.25 shows that the measured TOF changes by up to a few picoseconds when using selection cuts in the temperature spectra. The observed changes in the measured TOF do not follow clear trends for the different isotopes. This is also ob-

[2] As explained in Section 3.3.1, there is also a variation of the clock period with the temperature of ~ 0.05ps/°C, but this contributes to a change in the measured TOF of less than 1ps/°C.

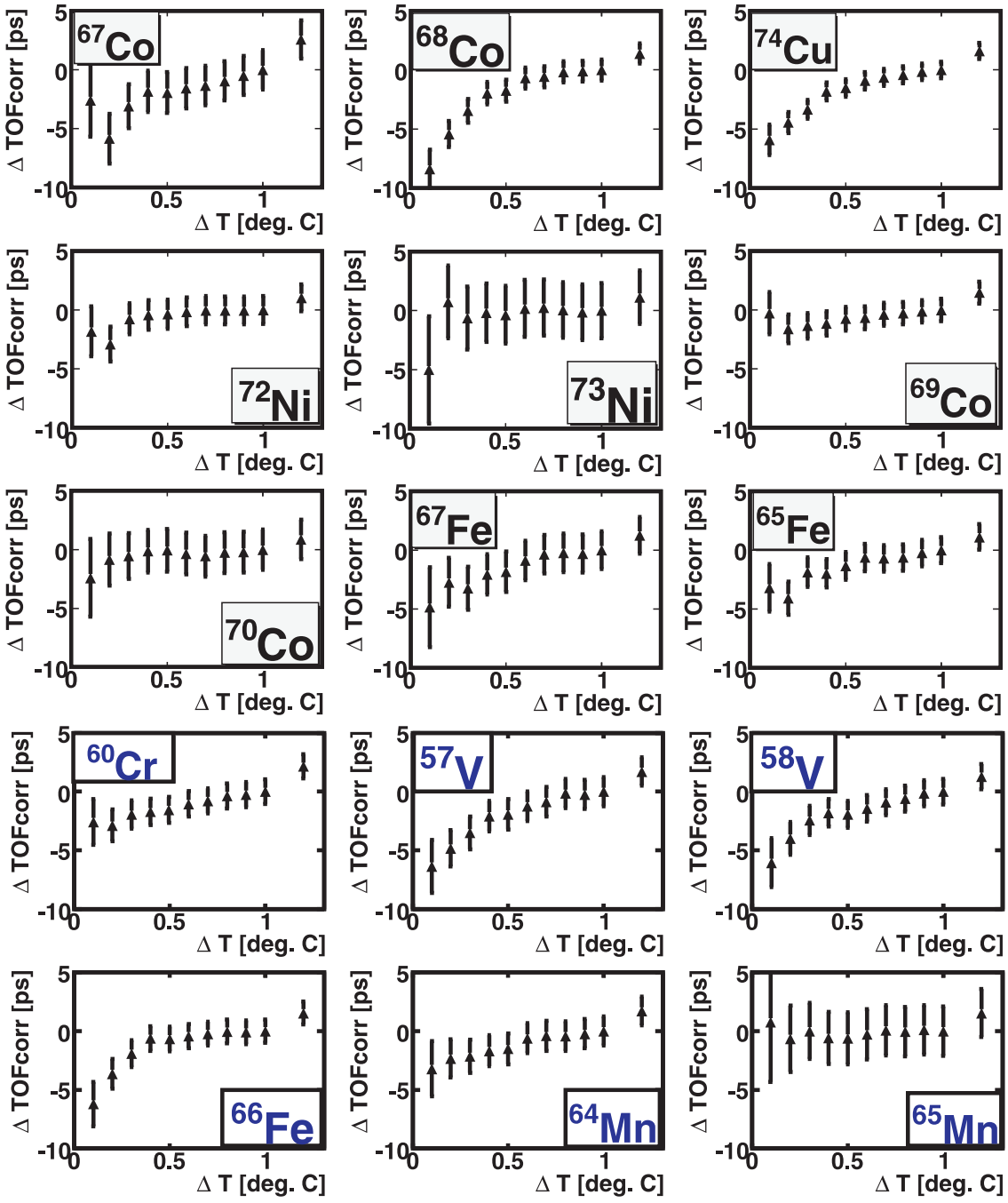

Figure 4.25: Sensitivity of the measured TOF for cuts in the S800 vault temperature spectra. The momentum corrected TOF was determined for events when the measured temperature was in the range of 27°C$\pm\Delta T$, and compared to the TOF determined for 26°C$\leq T \leq$ 28°C.

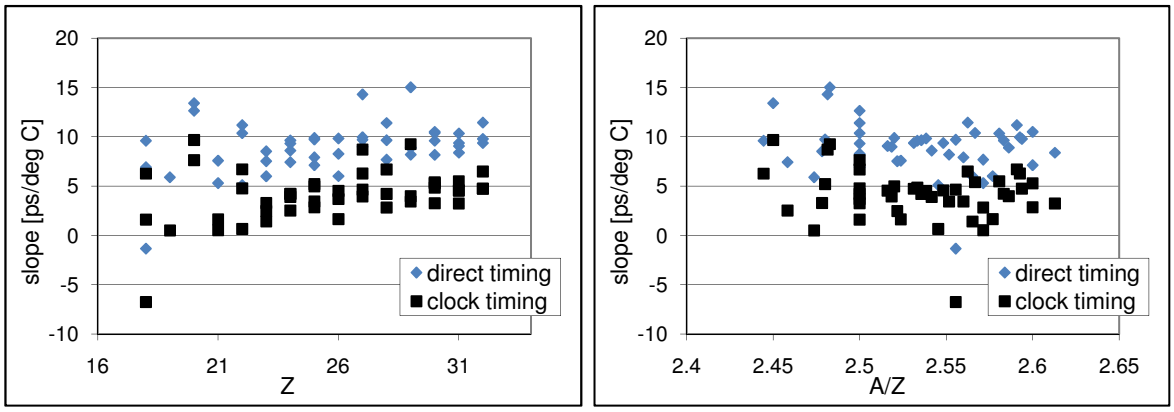

Figure 4.26: Slope resulting from a linear fit to the dependence of TOF_{corr} on the temperature in the S800 vault for the different isotopes in the secondary beam. Note that the correlation between TOF and temperature is always larger for the TOF determined from the direct measurement between the timing signals (TOF_1) than for the measurement with respect to a clock (TOF_{clk}).

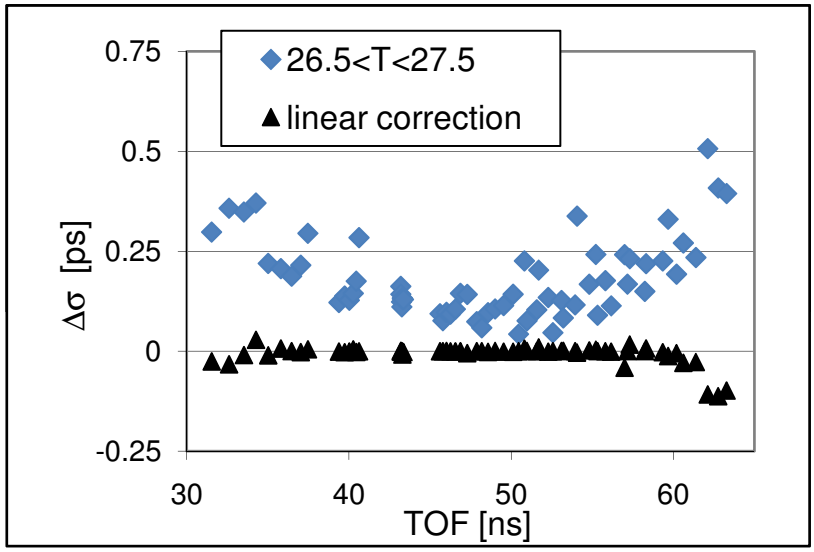

Figure 4.27: Change in the statistical error of the TOF centroid determined for two different corrections for the temperature of the S800 vault: a linear correction using an average slopes from Figure 4.26 (direct timing), and a cut of 1°C in the temperature spectra. The improvement of the TOF resolution when using a cut is canceled by the loss of statistics.

served in the scatter of the parameters obtained for a linear fit of TOF vs temperature (Figure 4.26). This can be understood as a combination of different factors producing the observed distributions. For example, the signals from different isotopes sampled different regions of the dynamic range of the TAC-ADC electronic modules, which might have a different sensitivity to the temperature. In addition, a change in the magnetic field of the dipoles effectively acts as a shift in the Bρ of the central trajectory of the beamline. Since the Bρ is equal to the momentum per unit charge of the fragments, a given change in the magnetic field will produce a larger momentum deviation for isotopes with a larger Z and have a larger effect on the path length for the trajectories they follow.

As evidenced by the smaller slope obtained in the fit (Figure 4.26), the TOF measured with respect to the clock shows a smaller sensitivity to the temperature (about 5 ps/°C) than the one measured directly comparing the signals from each detector (about $10\,ps/°C$). The ADCs used to digitize the TOF_{clock} signal were operated at a full range of 50 ns, while those for TOF_1 (direct timing) were operated at 100 ns full range, so the same change in their gain or zero offset will have an effect on the timing that is twice as large.

The TOF resolution is slightly improved by using only events within a narrow range of temperature in the S800 vault, but this does not compensate for the loss of statistics and the error on the determination of the TOF centroid increases by a fraction of a picosecond for most isotopes. Besides, the use of the linear correction of the TOF has a negligible effect. Both cases are shown in figure 4.27.

As described in Section 4.6.5, all isotopes in the secondary beam were found to have a distribution of events that samples similar temperatures and dipole fields (the individual spectra are shown in Appendix A.3). Therefore the change of the TOF due to these variables would increase the width of the TOF spectra, and could introduce deviation in its shape from a Gaussian distribution, but any systematic shift of the

TOF centroid that affects only a few isotopes should be small. For this reason, it was decided not to introduce additional corrections on the TOF based on the temperature. Instead a cut in the temperature spectra was used to remove the events during the period the air conditioning unit was turned off. A range of 26.°C$\leq T \leq$ 27.65°C was used for the final calculations (Section 4.6.5). With such cut about 14 % of the events were rejected.

4.3.4 Behavior of timing electronics

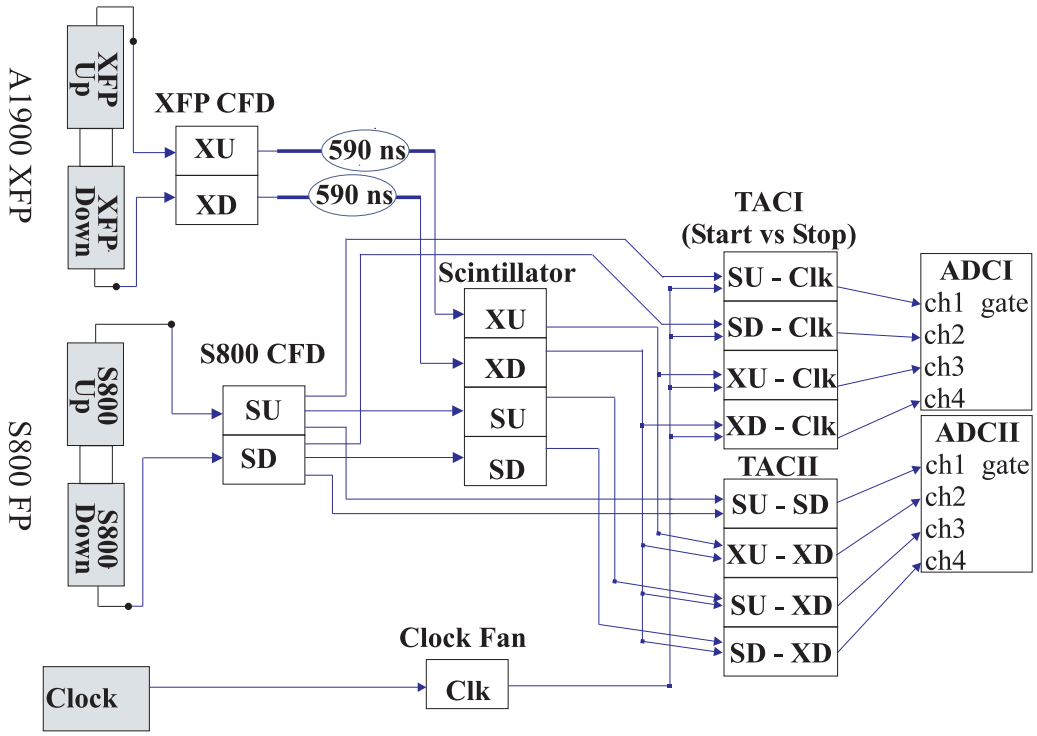

Figure 4.28: Electronics diagram for the timing subsytem.

Since the setup provided different time of flight measurements it was possible to check for the consistency of the TOF values. All the TOF measurements rely on the same timing detector signals, but they differ in some of the electronic modules used to process them. The details of the setup are described in Section 3.3.2, and the electronic modules used for timing are shown again here in Figure 4.28. Equation

4.13 shows three possible TOF measurements: TOF_1 and TOF_2 are constructed of direct measurements between photomultiplier tube (PMT) signals, and TOF_{clk} using PMT signals measured with respect to a clock signal. For example t_{SUXD} represents the time between a signal from the Up PMT at the S800 spectrometer (SU) and the Down PMT at the extended focal plane of the A1900 fragment separator (XD).

$$\begin{aligned} TOF_1 &= t_{\mathrm{offset}} - t_{\mathrm{SDXD}} - (t_{\mathrm{SUSD}} - t_{\mathrm{XUXD}})/2 \\ TOF_2 &= t_{\mathrm{offset}} - t_{\mathrm{SUXD}} + (t_{\mathrm{SUSD}} + t_{\mathrm{XUXD}})/2 \\ TOF_{\mathrm{clk}} &= t_{\mathrm{offset}} - (t_{\mathrm{SUclk}} + t_{\mathrm{SDclk}} - t_{\mathrm{XUclk}} - t_{\mathrm{XDclk}})/2 + N \cdot T \end{aligned} \tag{4.13}$$

In this equation t_{offset} represents an offset to the measurements for all events, and N the number of clock pulses between the signals from the S800 and the A1900 XFP detectors. The details on how each measurement is constructed are explained in Section 3.3.2.

The redundant TOF values were used to detect systematic errors in the measured TOF due to the electronic modules. Figure 4.29 shows spectra comparing the three semi-independent measurements in 4.13, as well as some of the individual measurements that are used to construct them. The spectra show two overlapping distributions (three in the case of $TOF_1 - TOF_2$), which are centered about 90 ps from each other. The situation is better resolved for the measurements relying on t_{SDXD} (TOF_1, and TOF_{clk}), but it is also observed for the TOF measurements that use t_{SUXD} (TOF_2).

A plausible explanation for this difference is a glitch in the logic module used to multiply to signal from the S800 timing scintillators (the Scintillator Fan module in Figure 4.28). The effect of the glitch, which occurred for about 10 % of the events, would be that the output of one of the Scintillator Fan's channels is produced $\delta = 90$ ps earlier compared to the usual electronic delay of the module (i.e. the timing for

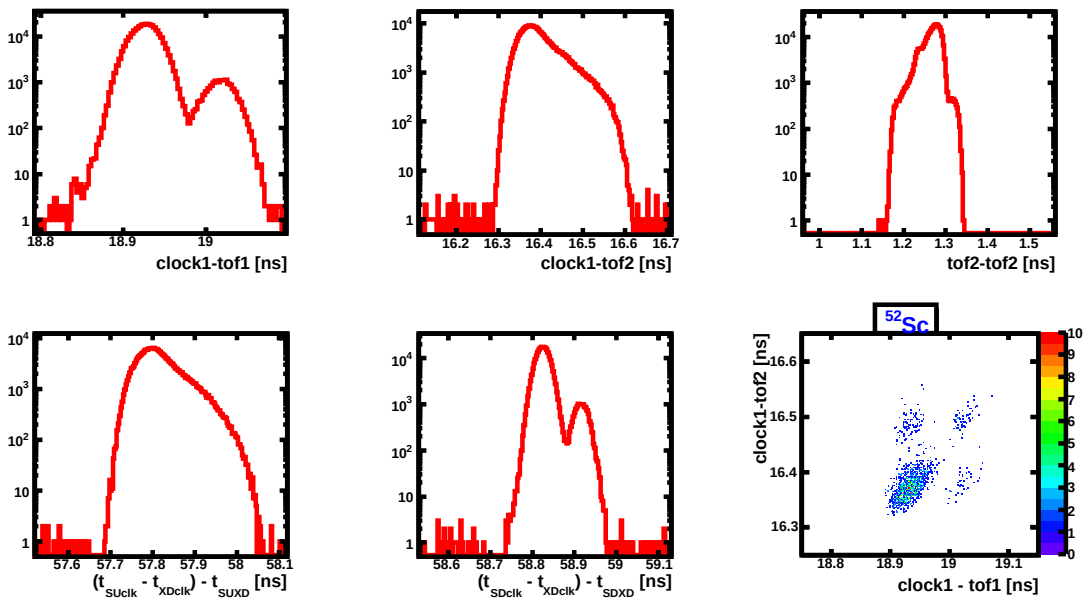

Figure 4.29: Comparison of semi-independent time-of-flight measurements (equation 4.13). About 10 % of the events are shifted by 90 ps by a glitch that was traced to the electronic logic modules that multiply the signals from the S800 timing detectors. The two dimensional spectra only shows events of one isotope (^{52}Sc).

the remaining 90 % of the events). For instance, if the glitch affects the channel corresponding to the signal of the S800 Up PMT (δ_{SU}), the measured time between the S800 Up PMT and the A1900 Down PMT, t_{SUXD}, would be 90 ps longer. The other time measurements that make use of the S800 Up PMT signal (t_{SUSD} and t_{SUclk}) would not be not affected because they are constructed with pulses generated by another electronic module (the SU and SD constant fraction discriminators). As a result, the TOF_2 value would be shifted by $\delta_{\mathrm{SU}} = 90$ ps, but TOF_1 and TOF_{clk} would not be affected. This is illustrated by the following equations:

$$
\begin{aligned}
TOF_{1\,\delta\mathrm{SU}} &= t_{\mathrm{offset}} - t_{\mathrm{SDXD}} - (t_{\mathrm{SUSD}} - t_{\mathrm{XUXD}})/2 = TOF_1 \\
TOF_{2\,\delta\mathrm{SU}} &= t_{\mathrm{offset}} - (t_{\mathrm{SUXD}} + \delta_{\mathrm{SU}}) + (t_{\mathrm{SUSD}} + t_{\mathrm{XUXD}})/2 = TOF_2 - \delta_{\mathrm{SU}} \\
TOF_{\mathrm{clk}\,\delta\mathrm{SU}} &= t_{\mathrm{offset}} - (t_{\mathrm{SUclk}} + t_{\mathrm{SDclk}} - t_{\mathrm{XUclk}} - t_{\mathrm{XDclk}})/2 + N \cdot T = TOF_{\mathrm{clk}}
\end{aligned}
\tag{4.14}
$$

The analogous situation produced by a glitch in the Fan module for the S800 Down PMT (δ_{SD}) would produce a TOF_1 measurement 90 ps shorter, and would not affect TOF_2 and TOF_{clk}. In addition, all TOF measurements use the logic pulses of the A1900 XFP detectors that are produced by the same electronic modules (the XU and XD Scintillator Fan). Therefore a glitch in one of them would have the same effect in all the measured TOFs, and it can not impact their difference. The case for δ_{XD} is presented as an example (all measurements are increased by $\delta_{\mathrm{XD}}/2$):

$$
\begin{aligned}
TOF_{1\,\delta\mathrm{XD}} &= t_{\mathrm{offset}} - (t_{\mathrm{SDXD}} - \delta_{\mathrm{XD}}) - (t_{\mathrm{SUSD}} - (t_{\mathrm{XUXD}} - \delta_{\mathrm{XD}}))/2 = tof1 + \delta_{\mathrm{XD}}/2 \\
TOF_{2\,\delta\mathrm{XD}} &= t_{\mathrm{offset}} - (t_{\mathrm{SUXD}} - \delta_{\mathrm{XD}}) + (t_{\mathrm{SUSD}} + (t_{\mathrm{XUXD}} - \delta_{\mathrm{XD}}))/2 = tof2 + \delta_{\mathrm{XD}}/2 \\
TOF_{\mathrm{clk}\,\delta\mathrm{XD}} &= t_{\mathrm{offset}} - (t_{\mathrm{SUclk}} + t_{\mathrm{SDclk}} - t_{\mathrm{XUclk}} - (t_{\mathrm{XDclk}} + \delta_{\mathrm{XD}}))/2 + N \cdot T \\
&= TOF_{\mathrm{clk}} + \delta_{\mathrm{XD}}/2
\end{aligned}
\tag{4.15}
$$

To test the effect of this glitch in the measured TOF of the beam fragments a selection cut was implemented in the spectrum comparing the time between the S800 Down PMT signal and the A1900 XFP Down PMT signal (the $(t_{\mathrm{SDxlk}} - t_{\mathrm{XDclk}}) - t_{\mathrm{SDXD}}$ spectra in Figure 4.29). The events for which the direct time measurement (t_{SDXD}) was 45 ps longer or shorter than the clock measurement ($t_{\mathrm{SDclk}} - t_{\mathrm{XDclk}}$) were rejected (the difference is measured from the centroid of the events without a glitch). Such criteria rejects almost all events affected by a glitch in the SD Fan, which

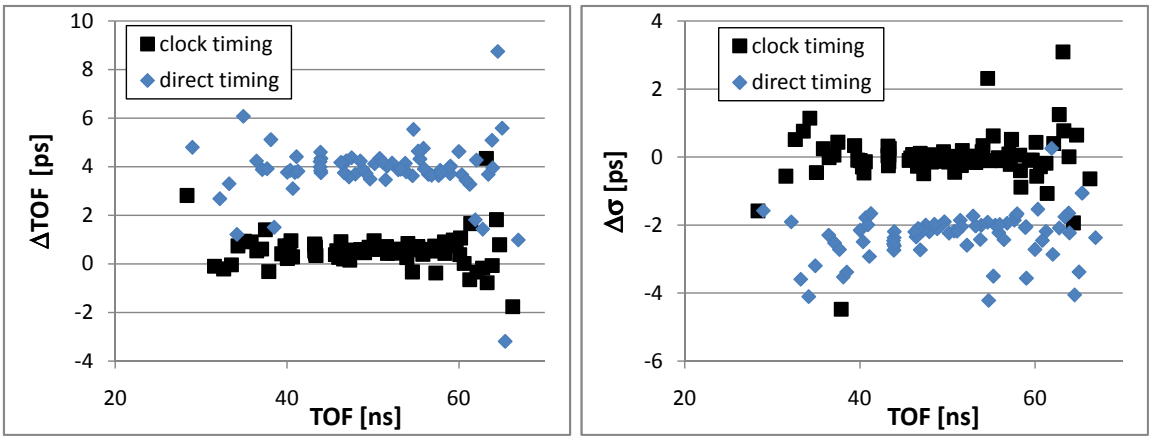

Figure 4.30: The figure shows the change in the measured TOF, and its width, when using the cut to reject events with a glitch in the electronic modules. The cut produces a small improvement in the resolution for the direct time measurement, and shifts the measured TOF of all ions. The clock is also shown to be less sensitive to this effect, since it does not use the Scintillator Fan S3 module (Figure 4.28).

are about 10 % of the total. Figure 4.30 shows the change in the TOF determined with the TOF_1 and $TOF_{\rm clk}$ values when using this rejection criteria. The centroid of the TOF_1 spectra is systematically shifted by about 4 ps for all isotopes, and there is a reduction of its width (σ) of about 2 ps. The clock measurement is much less sensitive to this cut, as it is expected because $TOF_{\rm clk}$ does not use any signal from the SD Fan module.

As discussed in Section 4.6 the final mass results are not sensitive to the use of this rejection cut. Besides, the TOF measured with respect to the clock is used for the final mass fit, and a systematic shift in $TOF_{\rm clk}$ of the type discussed can not be detected with this analysis (neither eliminated with an event selection cut). For that reason, a wide selection cut of $\pm$100 ps in the spectra comparing TOF_1 and $TOF_{\rm clk}$ was adopted. Such cut only rejects a small fraction of events with a large discrepancy between both measurements, mostly produced by random clock coincidences with the A1900 XFP detector signals (Figure 3.6), and accepts those with a glitch affecting TOF_1 (about 10 % of the total).

4.4 Determination of TOF centroid

The time of flight of each isotope was determined as the centroid of the fit of a Gaussian function to the TOF spectra. The fit was restricted to the range of $\pm 3\sigma$ around the centroid to avoid the events in the tail of the distribution, where σ is the standard deviation of the Gaussian fit function. It was iterated using the standard deviation and centroid of each step to calculate the fit range of the next iteration. Four such steps were enough for the results to converge in the case of isotopes $N \gtrsim 200$ events. The binning adopted for the TOF histograms was 6.5 ps per bin. For the isotopes with lower statistics several bins in the fit range had less than 10 events. Therefore, a Poisson distribution for the error of each bin was used in the minimization procedure.

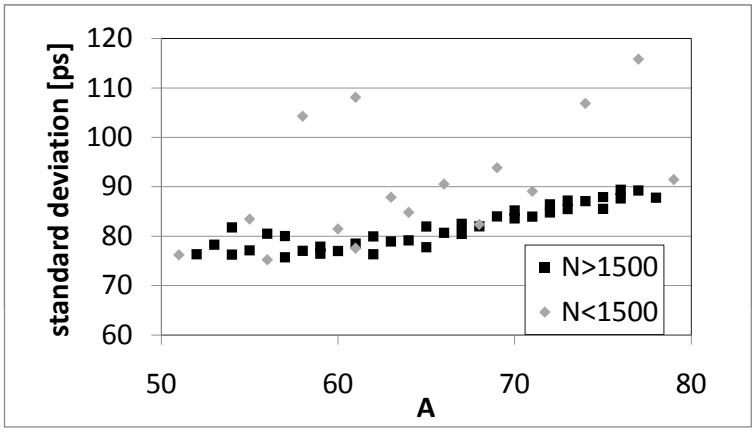

Figure 4.31: Fit results for the standard deviation of a Gaussian fit to the TOF distribution. For the isotopes with a small number of events (N) the width of the Gaussian function was set as a fixed fit parameter, estimating the value from the fit results of isotopes with large statistics.

For the isotopes with lower statistics ($N \lesssim 1000$ events) the results tended to overestimate the value of the standard deviation of the fit function (Figure 4.33). For these cases, the standard deviation of the TOF distribution was treated as a fixed parameter in the fit, using values from the trend observed in isotopes with large statistics. The fit results for individual isotopes are shown in the Appendix A.2.

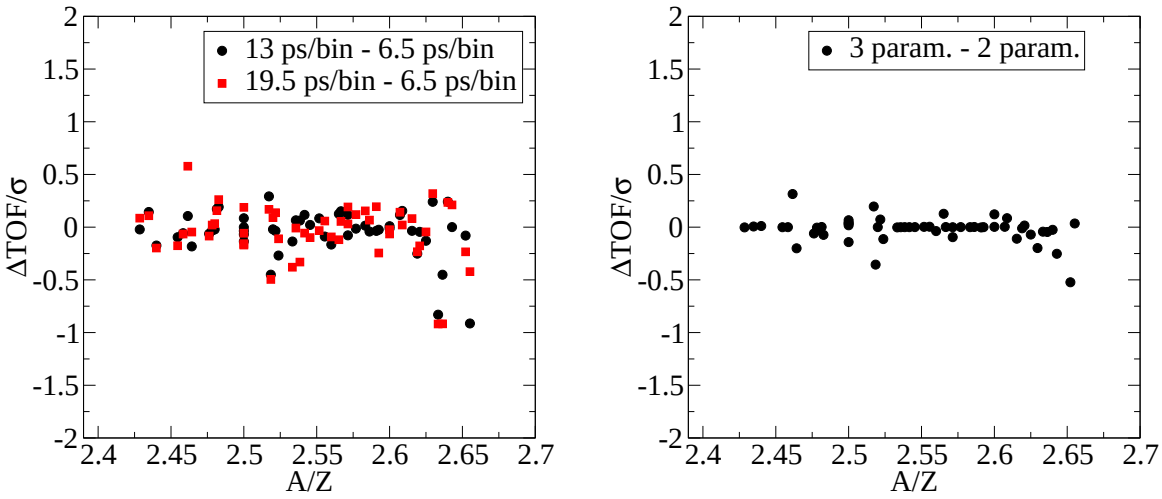

Figure 4.32: Sensitivity of the measured TOF centroid to the binning of the TOF (left) and the use of the standard deviation of the fit function as a free parameter (right). The change in the TOF shown in units of the statistical error in its determination (σ).

Other options for the fit procedure were also explored. For example, the fit was performed for histograms with different binning, and for different fit ranges. The sensitivity of the fit to these parameters is shown in Figure 4.32 and 4.33. The results obtained with the different procedures are in agreement, and no systematic trend in their differences was observed. The error in the determination of the TOF centroid is never smaller than the TOF uncertainty in the adopted fit that was described at the beginning of this section (it can increase, for example in the case of a narrow range for the fit function).

The TOF resolution obtained, shown in Figure 4.33, represents a relative resolution of $1.7 - 1.9 \times 10^{-4}$ (the absolute TOF through the beamline is between 440 to 480 ns for different isotopes). The resolution is worse for the heavier masses because their TOF has a stronger correlation with the a_{S800} angle at the S800 focal plane and the PMTs signal amplitude (in particular for the S800 timing detector), and the used TOF was only corrected by the fragments' momentum (Sections 4.2 and 4.3).

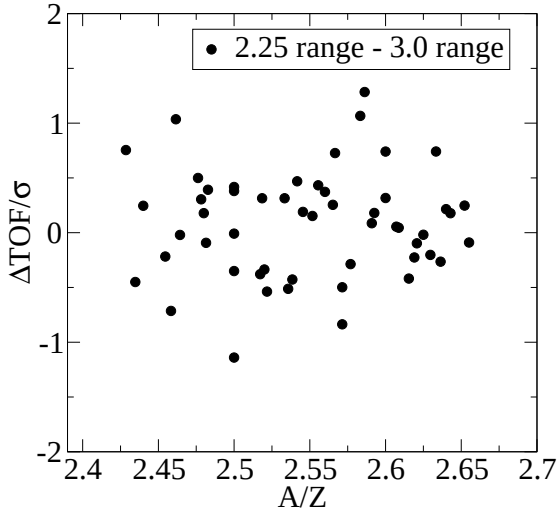

Figure 4.33: Sensitivity of the measured TOF centroid to the range function used to fit the TOF spectra. A Gaussian function was iteratively fit to the TOF spectra using only events within a given number of standard deviations from the centroid. The change in the TOF when using 3 or 2.25 standard deviations as the range shown in units of the statistical error in TOF centroid determination (σ).

4.5 Mass calibration function and fit procedure

The isotopes in the secondary beam with previously measured masses are used to calibrate the relationship between the time of flight and mass-to-charge ratio of the fragments. The calibration function is expected to depend on additional variables besides the time of flight. For the present experimental setup it was found that a function that also includes a dependence on the isotopes nuclear charge Z provided a suitable description.

As explained in the preceding sections, the measured TOF is sensitive to several variables that showed a strong variation with the nuclear charge of the fragments. A clear example is the energy loss in the detectors, which produces a larger reduction on the velocity of the heavier elements and also results in a different momentum distribution of the isotopes transmitted through the beamline. In particular, the momentum distribution becomes very asymmetric for isotopes with $Z \lesssim 20$. An additional source of Z dependence are the large cuts in the energy loss spectra required

to remove charge state contaminants for Ga and heavier isotopes. For that reason it can be expected that the region where a particular calibration function is valid will be restricted to a given range of nuclear elements. For the present case this range was found to be $21 \leq Z \leq 30$, which includes the isotopes for which new masses are measured.

4.5.1 Reference masses

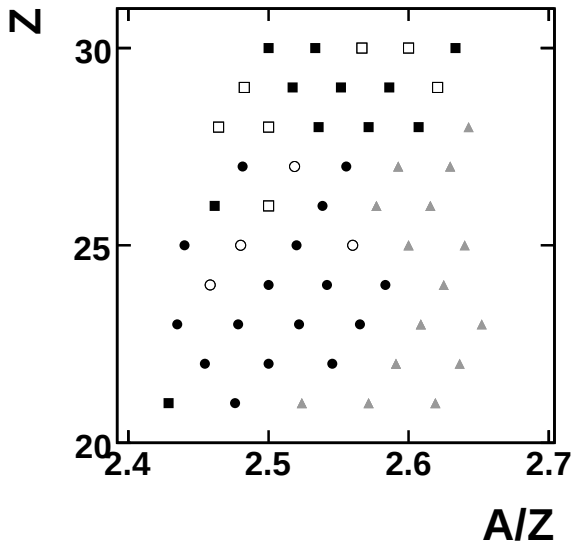

Figure 4.34: Isotopes with known mass available as reference points for the experiment. The isotopes are indicated by their nuclear charge (Z), and their mass-to-charge ratio (A/Z), which is proportional to their time of flight through the beamline. The squares represents isotopes with a mass uncertainty of $\delta m \leq 100$ keV, and the circles those with 100 keV $< \delta m \leq 400$ keV. The isotopes shown with open symbols have known long lived microsecond isomers. In addition, those indicated as grey triangles are the isotopes for which a new mass value was measured in the present experiment.

In order to constrain the parameters of the calibration function it is important to have reference isotopes that span a wide range of its coordinate space (TOF and Z in the present case). In addition, the extrapolation error increases rapidly away from the region that includes the calibration points. In an ideal situation the isotopes with unknown mass would lie within the range of calibrations, and their masses would be

obtained by an interpolation of the function. However, masses to be measured for the first time usually have the more extreme mass to charge ratio and some extrapolation along the TOF coordinate is required.

Table 4.2: Isotopes used as reference points for the mass calibration function. The table shows the mass uncertainty (δm) in the literature values, and the energy (E_i) of long lived isomers in case they are known [62]. For those indicated with a '#' have an uncertain assignment between the isomeric and ground states, and the energy is usually inferred from systematics of neighboring isotopes.

Isotope	δm [keV]	Ei [keV]	Isotope	δm [keV]	Ei [keV]
75Zn	2.0		76Zn	1.9	
77Zn	2.5	772	78Zn	3.0	2673
79Zn	4.2		72Cu	1.5	270
73Cu	4.2		74Cu	6.7	
75Cu	32.2		76Cu	7.2	0# (200#)
69Ni	4	321, 2701	70Ni	29	2860
71Ni	30.1		72Ni	30.1	
73Ni	33.3		67Co	300	
68Co	300	0#(150#)	69Co	400	
64Fe	5.2		65Fe	3.5	364
66Fe	300		61Mn	240	
62Mn	240	113	63Mn	300	
64Mn	300	135, 175	59Cr	300	503
60Cr	230		61Cr	300	
62Cr	400		56V	220	
57V	250		58V	300	
59V	300		54Ti	130	
55Ti	160		56Ti	210	
51Sc	22		52Sc	210	

Table 4.2 lists the isotopes with previously measured masses present in the secondary beam, and their distribution in the coordinates space of the calibration function is shown in Figure 4.34. Only masses with an uncertainty of $\delta m \leq 400$ keV were used as calibration points for the mass fit. As described in Chapter 1, the previous mass measurements in this region have been done with several techniques that produce mass results with various uncertainties. There are no Penning trap measurements, which provide the most precise data, available for calibration isotopes lighter than Fe, and ^{51}Sc is the only one in this region that has a mass uncertainty below

100 keV.

The mass resolution of the time-of-flight technique is not sufficient to separate events where the nucleus is in an excited state. For this reason isotopes with known long-lived isomers ($t_{1/2} \geq 100$ ns) were excluded from the set of calibrants. In principle their observed TOF and its statistical uncertainty can be corrected if the population of the isomeric state is known (the formulas are described in [4]). An attempt at such correction assuming equal populations of the ground and excited nuclear state did not fit the data properly. Nevertheless, it was found that the four isotopes whose isomers have excitation energies below 200 keV (^{76}Cu,^{68}Co,^{62}Mn, and ^{64}Mn) can be included and slightly improve the fit results (Section 4.6.6). ^{76}Cu provides the calibration point with the second largest mass-to-charge ration (and TOF), and the other three add calibration points to the Co and Mn isotopic chains where only two reference masses were available.

4.5.2 χ^2 minimization and error analysis

The calibration function used was a polynomial in TOF and Z that describes the mass-to-charge ratio (m/q) of the isotopes in the beam. It was fit to the known masses through a χ^2 minimization procedure. The use of a function that is linear in the fit parameters (a_{ij} in Equation 4.16) simplifies the problem because it does not require initial conditions for the parameters [63]. The coordinates of the calibration function were transformed by a constant offset to avoid multicolinearity in the fit results (i. e. large correlations in the errors of the fit parameters). The average of the Z and TOF of the calibration isotopes were used as offsets: $t = TOF - \langle TOF \rangle$ and $z = Z - \langle Z \rangle$. The general form of the calibration function is:

$$\frac{m}{q} = f(t,z) = \sum_i a_i \cdot h(t,z) = \sum_j \sum_k a_{jk} \cdot t^j z^k \tag{4.16}$$

Since the events corresponding to charge states of the isotopes in the beam were

excluded from the fit, the charge of the particles q is the same as their nuclear charge Z.

Each data point was weighted by combining its mass uncertainty from the literature and the statistical uncertainty in the determination of its TOF. The TOF uncertainty (σ_{TOF}) is converted to mass units by multiplying it with the calibration function coefficient linear in TOF (a_{10}), which is the dominant term.

$$\sigma^2_{\mathrm{stat}} = \left(a_{10} \cdot \sigma_{\mathrm{TOF}}\right)^2 \tag{4.17}$$

The χ^2 value is constructed from the difference between the previously known masses and the mass values obtained by evaluating the calibration function $f(t, z)$:

$$\chi^2 = \sum_{calibrants} \frac{\left((m/q)_{\mathrm{literature}} - f(t,z)\right)^2}{\sigma^2_{\mathrm{literature}} + \sigma^2_{\mathrm{stat}}} \tag{4.18}$$

Because of the finite number of calibration points available, it is expected that the χ^2 value per degree of freedom will be larger than one. Nonetheless, a large χ^2 can indicate that the statistical uncertainty is underestimated, or point to the presence of systematic errors in the TOF measurement. In this sense, the calibration masses provide an important estimate of the systematic errors of the experiment. The χ^2 value was normalized by including an additional term to the weight of each data point. Such term was added in quadrature to σ_{stat} and attributed to contributions from systematic uncertainties (σ_{sys}) in the experiment:

$$\chi^2 = \sum_{calibrants} \frac{\left((m/q)_{\mathrm{literature}} - f(t,z)\right)^2}{\sigma^2_{\mathrm{literature}} + \sigma^2_{\mathrm{stat}} + \sigma^2_{\mathrm{sys}}} \tag{4.19}$$

The fit was iterated using gradually increasing values of σ_{sys} until the χ^2 per degree of freedom was one. The resulting σ_{sys} is also a measure of the χ^2 value before normalization, so it provides an indication of the goodness of fit when comparing fits to data with similar statistical uncertainty (for example, to compare results when the

Bρ correction of the TOF is done with the linear or the quadratic functions described in Section 4.2).

A third contribution to the mass uncertainty comes from the propagation of the errors in the parameters of the fit function. The fit error ($\sigma_{\rm fit}$) is calculated from the covariance matrix [63]:

$$\sigma^2_{\rm fit} = \sum_j \sigma^2_{a_j} + \sum_{j\neq k} \sigma^2_{a_j a_k} = \sum_j \sum_i \left[{\sigma_i}^2 \left(\frac{\partial a_j}{\partial y_i} \right)^2 \right] + \sum_{j\neq k} \sum_i \left[{\sigma_i}^2 \frac{\partial a_j}{\partial y_i} \frac{\partial a_k}{\partial y_i} \right] \quad (4.20)$$

The first term in this equation is the variance in each parameter a_j of the calibration function. The cross terms in the second sum, the covariance $\sigma^2_{a_j a_k}$, describe the correlation in the errors of the fit parameters. In many cases it has a negative value and reduces the extrapolation error. The sums are carried over each data point i and parameter j.

The final uncertainty in the mass results was calculated by adding in quadrature the different error terms:

$$\sigma^2_{m/q} = \sigma^2_{\rm stat} + \sigma^2_{\rm fit} + \sigma^2_{\rm sys} \quad (4.21)$$

4.5.3 Selection of the calibration function

The fit was performed for all possible polynomials up to third order in t and z, including cross terms (Equation 4.16). The goal of this test was to find a parameterization of the calibration function that included as few parameters as possible. With a small number of parameters these are better constrained by the calibration points, thus the extrapolations of the calibration functions are more robust ($\sigma_{\rm fit}$ is minimized).

The parameterization that offered the best results is:

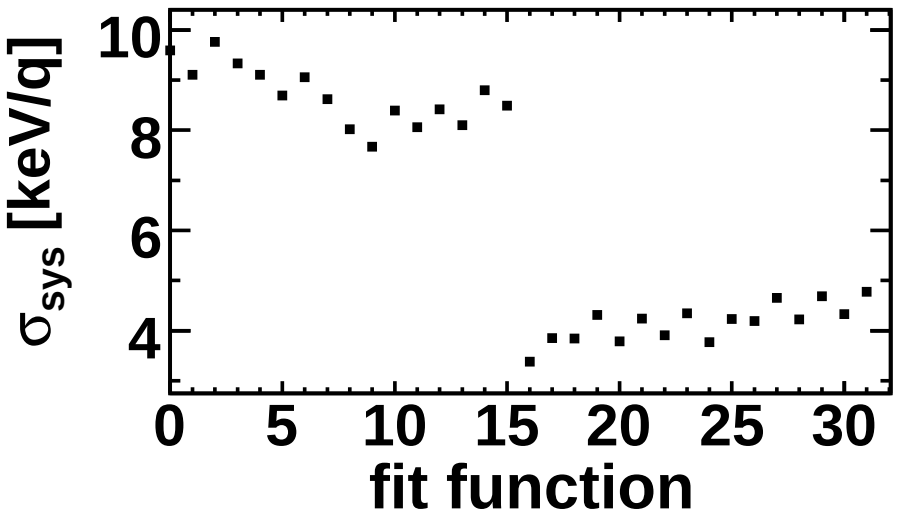

Figure 4.35: Systematic error that normalizes the χ^2 of the fit using different polynomials as the calibration function. All functions include terms in t, t^2, z, and z^2, and all possible combinations of terms up to third order were tried. The additional terms can be read from the binary representation of the function ID, where each bit represents a term in the following order $(z^3)\,(tz^2)\,(zt^2)\,(t^3)\,(tz)$. For example, in the function $0 = 00000_2$ no additional terms were included, and in $31 = 11111_2$ all terms were included. The calibration function used in this experiment (4.22) corresponds to ID $16 = 10000_2$, and all other parameterizations from 17 to 31 also include the z^3 term, which clearly has the largest effect in improving the fit.

$$\frac{m}{q} = a_{00} + a_{10} \cdot t + a_{20} \cdot t^2 + a_{01} \cdot z + a_{02} \cdot z^2 + a_{03} \cdot z^3 \qquad (4.22)$$

This function results in the smallest estimate for the σ_{sys} (i.e. χ^2 per degree of freedom closest to 1), as shown in Figure 4.35. The inclusion of the z^3 term in the calibration function (those with identifier 16 and higher) produces the most improvement in the quality of the fit with respect to the functions with only second order terms (function ID 0 and 1). Including additional terms (functions 17 to 31) does not improve the quality of the fit, while reducing its number of degrees of freedom. In addition, the fit residuals obtained with the function (4.22) do not show any remaining trend with respect to Z and TOF.

4.6 Sensitivity analysis for the mass results

To study the effect of the different cuts and corrections on the results, the mass calibration function was fitted to sets of TOF values obtained with different analysis approaches. Since the calibration function has a strong dependence on the time of flight of the beam particles, the variables that have a large effect on the measured TOF will have the largest effect on the mass results. However, the calibration function will adjust its parameters during the fit procedure, and it might still produce a satisfactory fit for different sets of TOF values. For example, it was described in Section 4.3.4 that the cut used to reject events with a glitch in the electronic modules produced a systematic shift of $\approx$ 4 ps in the measured TOF (using the TOF_1 value for the measurement). Since the shift is the same for all isotopes such offset is taken into account by a calibration function with a different value of its a_{00} coefficient. In other cases the effect in the measured TOF is more complicated and it is not clear a priori if the mass calibration function would be able to compensate for such variation. This can be an issue if the parameters for the TOF correction could not be precisely

determined. An example is the use of selection cuts or a TOF correction for the beam angle at the S800 focal plane (Section 4.3.2), where a stringer effect was observed for the heavier isotopes.

The sensitivity of the mass fit was studied to decide which analysis options discussed in the previous sections, for instance TOF corrections and data selection cuts, would be applied to obtain the mass results. The points described in the present section are: calibration of the nonlinearities in the timing electronic modules (Section 3.3.2), TOF correction for the momentum of the beam particles (Section 4.2), TOF correction for the timing between PMT signals and their amplitude (Section 4.3.1), TOF correction for the beam angle at the S800 focal plane (Section 4.3.2), selection S800 vault temperature (Section 4.3.3), and the choice of the fit calibration masses (Section 4.5.1). The residuals of the fit with respect to the known masses, and the magnitude of the systematic error that normalizes the χ^2 provided a test of the goodness of fit. In some cases, the parameters obtained for a given fit of the mass calibration function were applied to other sets of data without refitting the function. Such test provided a further measure of the sensitivity of the mass fit to the aforementioned variables. Unless otherwise indicated, the TOF_{clk} measurement and the quadratic momentum correction function were used.

4.6.1 Nonlinearities in electronics

The nonlinearities were studied with a preliminary fit routine, which did not include the minimization of the χ^2 by the addition of a systematic error and used the linear Bρ correction for the TOF. Table 4.3 shows the root mean square deviation of the fit residuals for no correction of the nonlinearities in the electronic modules, and for the two corrections described in Section 3.3.2. Using a global correction of the nonlinearities, obtained from the time calibration of the TAC-ADC modules, is better than using a channel-by-channel correction of the differential nonlinearities. The later

Table 4.3: Root mean square deviation of the fit residuals for the nonlinearity corrections of the timing electronics described in section 3.3.2. Results are shown for the TOF measured with respect to a clock signal (TOF_{clk}) and directly between the PMTs signals (TOF_1).

	RMS_{fit} [keV]	
	TOF_{clk}	TOF_1
no correction	310	263
global correction	289	279
channel-by-channel correction	352	775

could not be determined with enough precision because of the low statistics of the nonlinearities calibration runs. As expected, measuring the timing detectors' signals with respect to a clock provides a TOF value (TOF_{clk}) that is more robust against the problems introduced by the channel-by-channel correction. The global nonlinearity correction was adopted to obtain the final mass results.

4.6.2 Bρ correction

Different tests were done to check the correction used to take into account variations in the TOF due to the finite momentum acceptance of the beamline. As described in Section 4.2, a Bρ correction was performed with both a linear and a quadratic function of the beam position at the S800 dispersive plane (x_{mcp}) (equations 4.4 and 4.5), which provided the measurement of the beam particles' momentum. Because of the results presented in this section the function quadratic in x_{mcp} and a selection cut for data within -1.5 cm $\leq x_{\mathrm{mcp}} \leq$ 2.0 cm were selected.

The parameters of the Bρ correction functions were arbitrarily changed by a factor of 1.5 %. A momentum corrected TOF was obtained for each isotope, and used to fit the mass calibration function. The results, which are summarized in Figure 4.36, are more sensitive to the linear term of the momentum correction functions. In the case of the quadratic momentum correction the largest decrease in the quality of the fit happens when the coefficient of the linear term is changed with respect to the

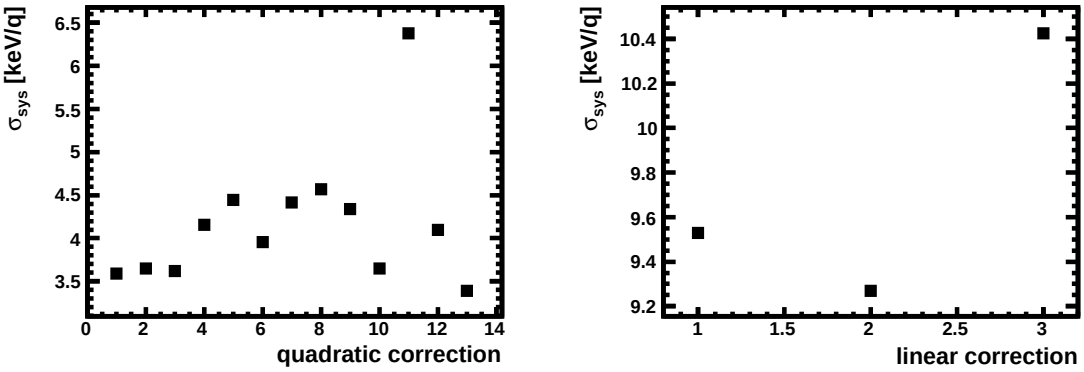

Figure 4.36: Estimate of the fit systematic error ($\sigma_{\rm sys}$) for arbitrary variations in the parameters of the quadratic (left) and linear (right) Bρ correction functions. Fit 1 corresponds to the data evaluated using the original parameters for the correction functions. For the quadratic momentum case (left graph), the fits 2 through 9 are all possible combinations when the coefficients are increased or decreased by 1.5 % (for 2 and 3 only the quadratic coefficient is changed, and for 4 to 9 the linear slope is also changed). The remaining four fits are obtained when increasing or decreasing one of the coefficients by 3 % (10 and 11 for the slope, and 12 and 13 for the quadratic term). For the linear Bρ correction, fit 2 corresponds to TOF data corrected with a slope that was increased by 1.5 %, and decreased by the same amount for fit 3.

values found in Section 4.2. In addition, the linear Bρ correction does not perform as well as the quadratic one, and it results on a systematic error about twice as large ($\sigma_{\rm sys} \geq 9.2\,{\rm keV}/q$). This is expected given the clear quadratic residuals in the TOF vs Bρ spectra.

This conclusion is confirmed when using each momentum correction to events that lie within certain ranges of $x_{\rm mcp}$. Table 4.4 lists the value of the systematic uncertainty ($\sigma_{\rm sys}$) necessary to normalize the fit χ^2 when rejecting events with a large momentum deviation. The quality of the fit for the linear Bρ correction improves if events in the tails of the momentum distribution are rejected, but in all cases it is worse than the corresponding fit using the quadratic Bρ correction.

Given this results, the quadratic momentum correction and cut in the momentum distribution for -1.5 cm $\leq x_{\rm mcp} \leq 2.0$ cm were selected to obtain the final mass results. A more restrictive cut (-1.5 cm $\leq x_{\rm mcp} \leq 1.5$ cm) provides a smaller

Table 4.4: Systematic error in fits for different Bρ corrections and cuts in the x_{mcp} spectra.

	$\sigma_{\mathrm{systematic}}$ [keV/q]	
x_{mcp} range [cm]	linear correction	quadratic correction
no cut	8.2	4.5
-1.5 to 2.0	7.8	3.5
-1.5 to 1.5	4.8	2.3

systematic error, but it also reduces the statistics significantly. On the other hand, if the acceptance is increased the gain in statistics is small because of momentum distribution of the transmitted fragments decreases rapidly outside this range (see figures 4.4 and 4.5), and because there is a steep reduction in the efficiency of the MCP detector and a deterioration of its resolution (Section 3.3.3).

As an additional test, the calibration function obtained with the quadratic momentum correction was evaluated (i. e. without refitting) to obtain the nuclear masses from different sets of TOF values. In the first case the events were divided in two classes: one for beam particles at the center of the momentum distribution ($-0.6\mathrm{cm} \leq x_{\mathrm{mcp}} \leq 0.7$ cm), and another with the events in the tails of the distribution. There is a some scatter in the results as each independent class only includes roughly half of the statistics, but the masses agree within the errors (Figure 4.37). The largest difference is observed for the mass of ^{58}Ti and ^{71}Co (considering masses measured in this experiment), but a closer look at their TOF vs x_{mcp} distributions does not indicate any systematic error in their momentum correction (see the spectra in Appendix A.1).

The same procedure was carried out for the TOF values determined with momentum correction functions whose parameters were systematically changed, and the mass results are shown in Figure 4.38. In this case the calibration function was fitted to the sets of TOFs obtained with the original coefficients for the quadratic Bρ correction function. Then, this parameterization of the calibration function was used to evaluate the masses for the other sets if TOF values. The masses of the

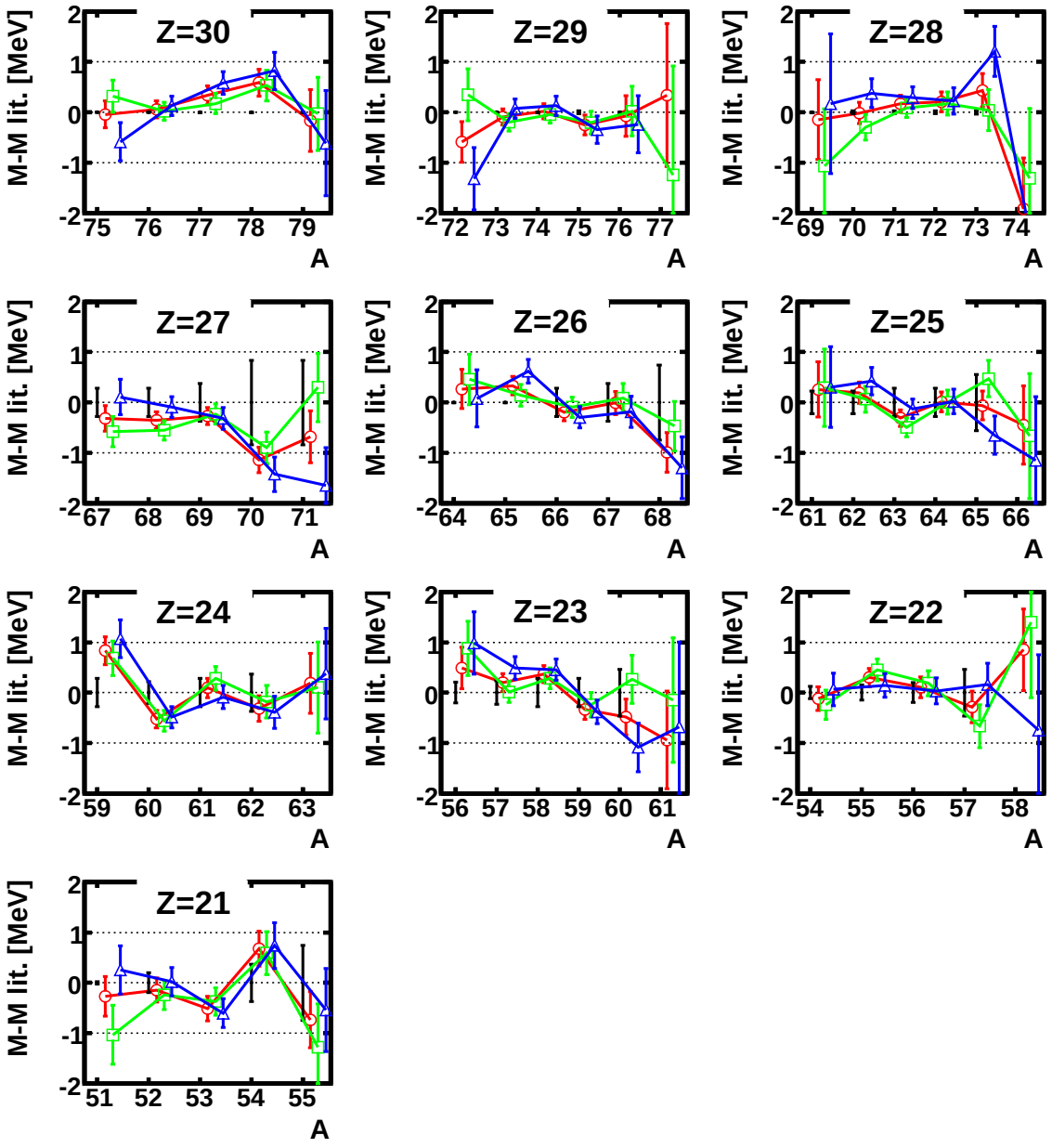

Figure 4.37: Evaluation of the mass calibration function for events with different x_{mcp} distributions. The parameters of the calibration function were obtained for a fit using all events (in red). The masses in blue are obtained for a set of TOFs determined for events in the center of the momentum distribution (-0.6 cm $\leq x_{\mathrm{mcp}} \leq 0.7$ cm), and the masses in green for events in the tails of the distribution. The masses are shown with respect to the literature data, and the extrapolations in [4] are used when the mass is not known. The uncertainty in the literature values is shown as black lines around the zero axis.

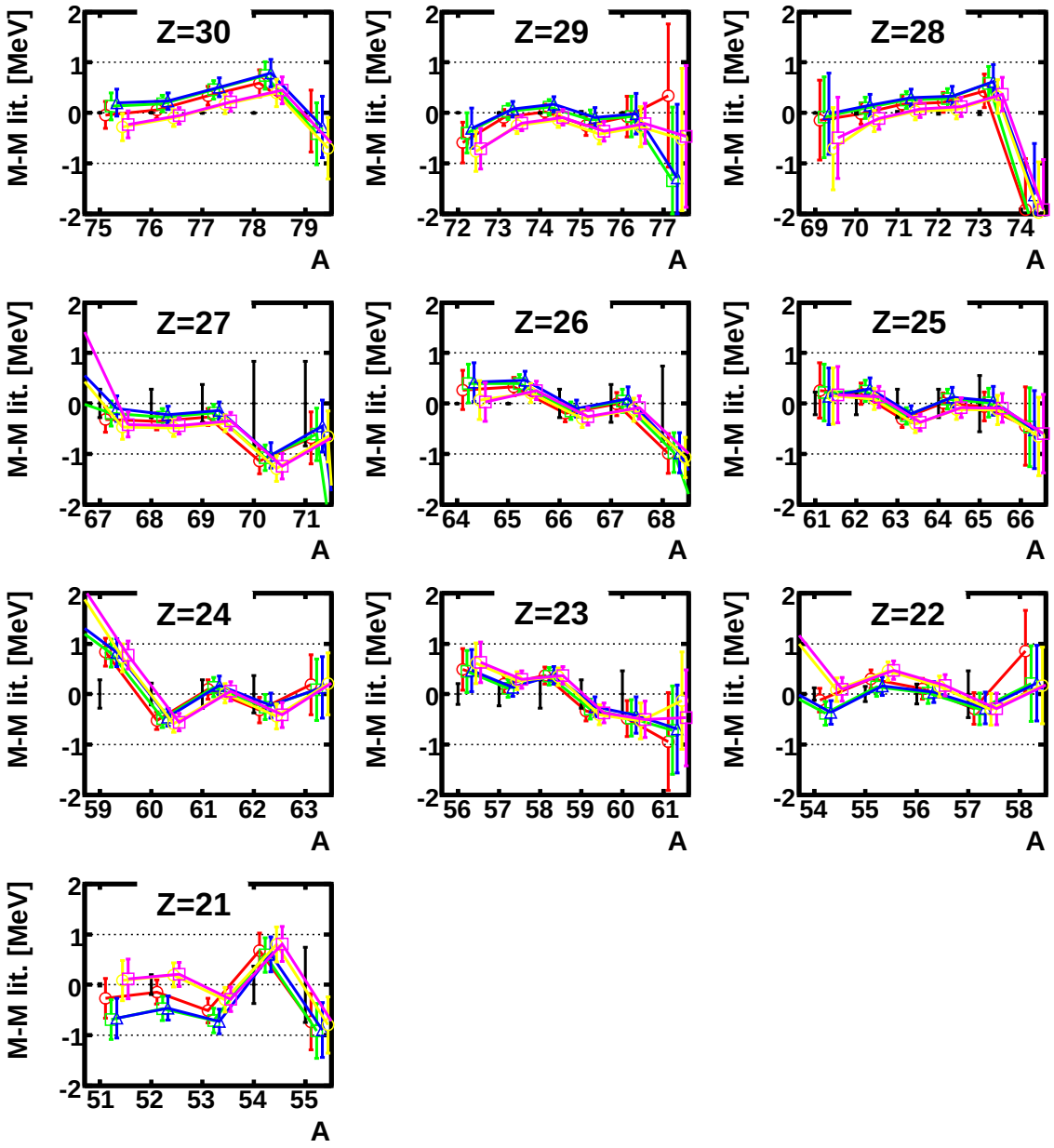

Figure 4.38: Evaluation of the mass calibration function using a sets of TOF values determined with arbitrary parameters of a quadratic Bρ correction. The parameters of the mass calibration function were fitted to TOF data obtained with the Bρ correction of Section 4.2 (red circles). The other series correspond to data when the slope ($p1$) and the curvature ($p2$) of the Bρ correction were changed by: $\delta p1 = -1.5\%$ and $\delta p2 = -1.5\%$ (green squares), $\delta p1 = -1.5\%$ and $\delta p2 = 1.5\%$ (blue triangles), $\delta p1 = 1.5\%$ and $\delta p2 = -1.5\%$ (yellow diamonds), $\delta p1 = 1.5\%$ and $\delta p2 = 1.5\%$ (magenta squares). The masses are shown with respect to the literature data, and the extrapolations in [4] are used when the mass is not known. The uncertainty in the literature values is shown as black lines around the zero axis.

different sets are again in agreement with each other. The results also show a larger sensitivity to the linear term of the Bρ correction function than to the quadratic one. For example, the mass results of Cu and Zn isotopes are systematically more bound when the slope of the TOF correction function is increased by 1.5 % regardless of the change in the other coefficient, and the results are systematically more bound for the Sc isotopes. The lighter Sc isotopes are also the ones that present the largest change in the mass results. This can be understood because the Sc isotopes, and in particular the lighter ones, already present somewhat asymmetric momentum distributions (Figure 4.4 and Appendix A.1).

4.6.3 PMTs timing and signal amplitude

As described in Section 4.3.1 a correlation was found between the measured TOF and the timing between the signals from the two photomultiplier tubes (PMT) of each timing scintillator (t_{SUSD} and t_{XDSD}). The major source of this correlation was attributed to the effect of walk in the electronic modules (correlations of the timing with the detector's pulse height), although additional effects might be present. A linear correction function using t_{SUSD} and t_{XDSD} as variables was fit to the data, and was added to the quadratic Bρ correction of the TOF.

This additional correction reduced the sensitivity of the mass fit to the walk in the electronics, but did not eliminate it completely. This is illustrated by Figure 4.39 and Figure 4.40. The TOF of each isotope was determined for events gated in the integrated charge spectra of two PMTs (Q_{XFPdown} or Q_{S800down}). Then the masses were evaluated with a parameterization of the calibration function fit to all events. The masses obtained for the set of events that have a large (or small) PMT signal amplitude are systematically larger or smaller, depending on what spectra the cut is made on. However, not all isotopes are shifted in the same way. For the isotopes with Z $\geq$ 27 the cut in the Q spectra of the S800 Down PMT has no effect in the mass

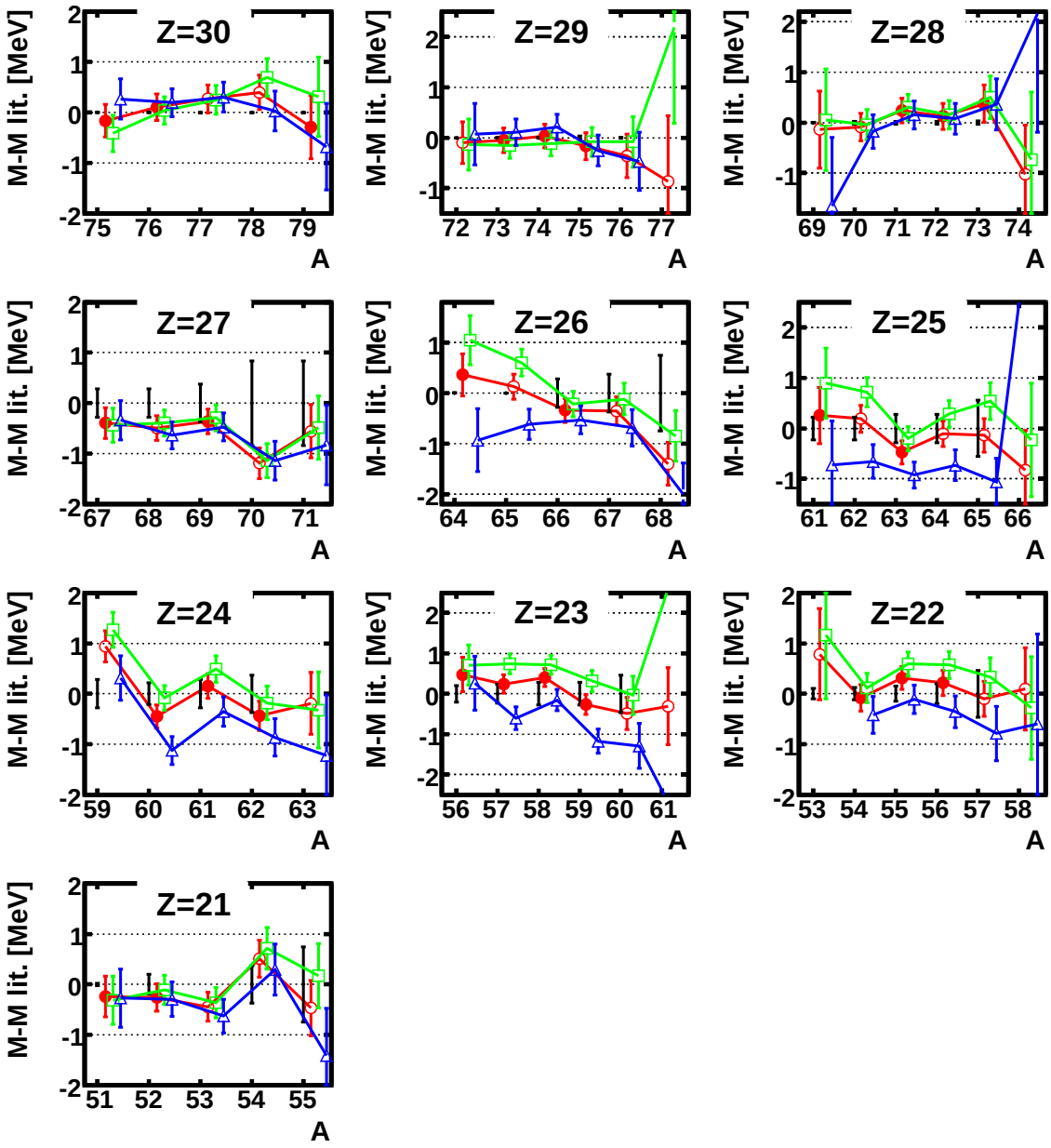

Figure 4.39: Sensitivity of the mass results to timing walk correction. The mass calibration function was fitted to a set of TOF values corrected by t_{SUSD} and t_{XDSD}, and the fit residuals are shown as red circles. The masses were then evaluated for sets of corrected TOF values that were determined with events with a small (green squares) or large (blue triangles) integrated charge values for the S800 Down PMT. The masses for each isotopic chain are plotted with respect to the literature data (black error bars around the zero axis), using extrapolations in [4] when they are unknown.

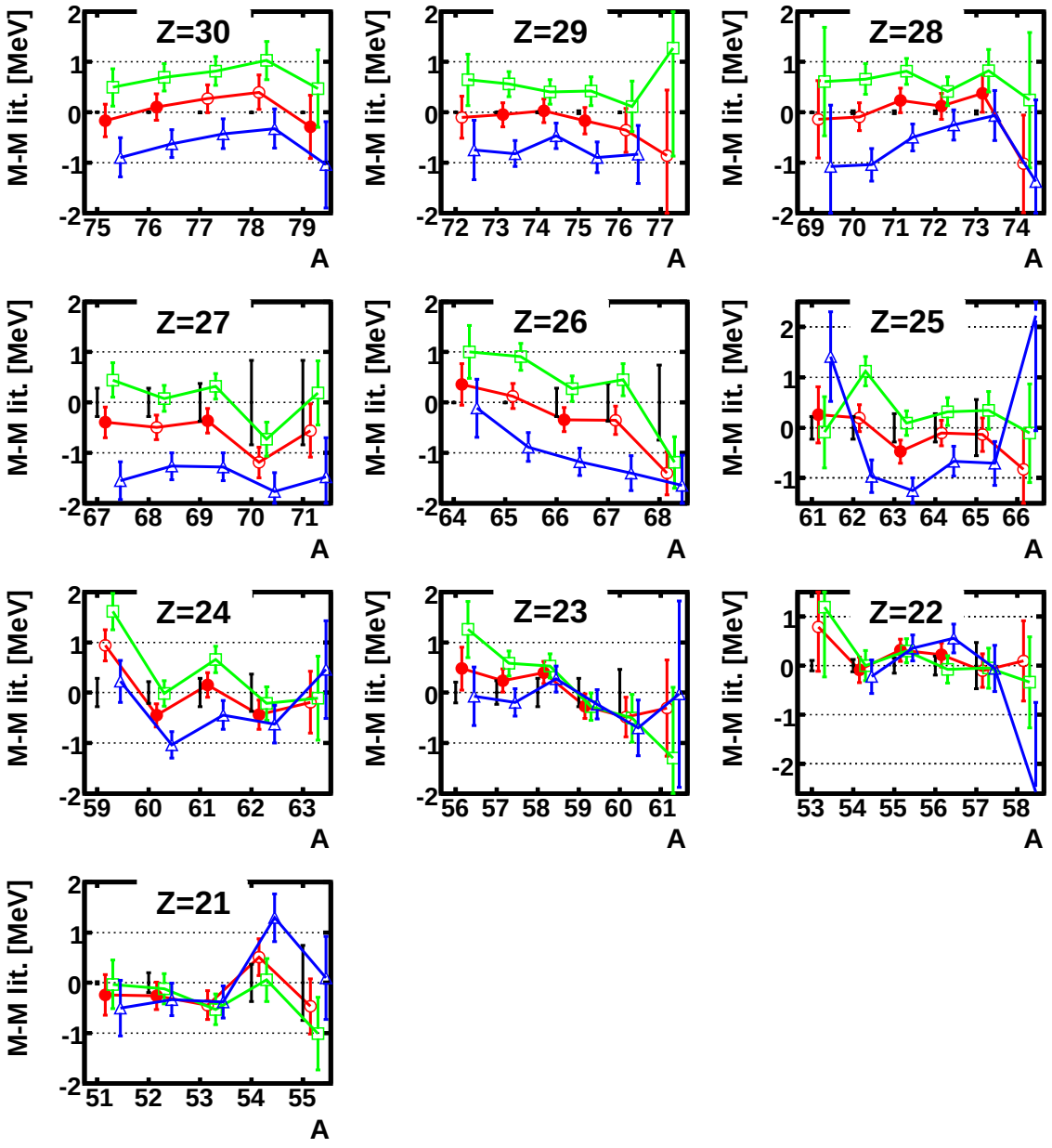

Figure 4.40: Sensitivity of the mass results to timing walk correction. The mass calibration function was fitted to a set of TOF values corrected by t_{SUSD} and t_{XDSD}, and the fit residuals are shown as red circles. The masses were then evaluated for sets of corrected TOF values that were determined with events with a small (green squares) or large (blue triangles) integrated charge values for the XFP Down PMT. The masses for each isotopic chain are plotted with respect to the literature data (black error bars around the zero axis), using extrapolations in [4] when they are unknown.

result; this agrees with the observation that the TOF correction removed the TOF dependence on the signal amplitude from the S800 timing detector for the heavier isotopes, but did not perform as well for the lighter ones (Figure 4.17). The analogous situation is observed for the cut in the A1900 XFP Down PMT signal Q, for which the mass obtained for the lighter isotopes ($Z \leq 23$) is much less sensitive to this variable.

Masses were also determined by refitting the different classes (the TOF values determined for the cuts in the Q spectra) to test whether the calibration function used can account for the *walk* in the timing electronics. Figure 4.41 shows the resulting masses using TOF values corrected for PMT signal amplitude, and Figure 4.42 using TOF values where only the momentum correction was used. When the masses are refitted there is no longer an advantage of using the additional TOF corrections for t_{SUSD} and t_{XDSD}, because the mass results using both TOF corrections have a similar sensitivity to the selection cuts. Besides, the systematic error that normalizes the fit is not reduced: $\sigma_{\mathrm{sys}} = 6.2\,\mathrm{keV}/q$ using only a quadratic Bρ correction, and $\sigma_{\mathrm{sys}} = 6.5\,\mathrm{keV}/q$ when adding the walk correction in the same set of data.

For a few isotopes with unknown masses (^{66}Mn and ^{58}Ti) the difference in the predicted mass is beyond their one σ errors, using either TOF correction. This difference can be explained as a statistical fluctuation. Furthermore, their TOF distribution is not evidently different from that of the isotopes used as reference massesNonetheless, this could be indicative of some systematic error in the mass determined for these isotopes, and should be considered in the final results.

The correction of the TOF by t_{SUSD} and t_{XDSD} did not improve the quality of the fit compared to using only a Bρ correction. In addition, for both TOF corrections the mass calibration function could be refitted to compensate for systematic changes in the TOF values introduced by selection cuts in the integrated charge spectra of the timing detector's signals. The reason for this is that, as described in Section 4.3.1, the linear correction function used is only an approximation to the real TOF

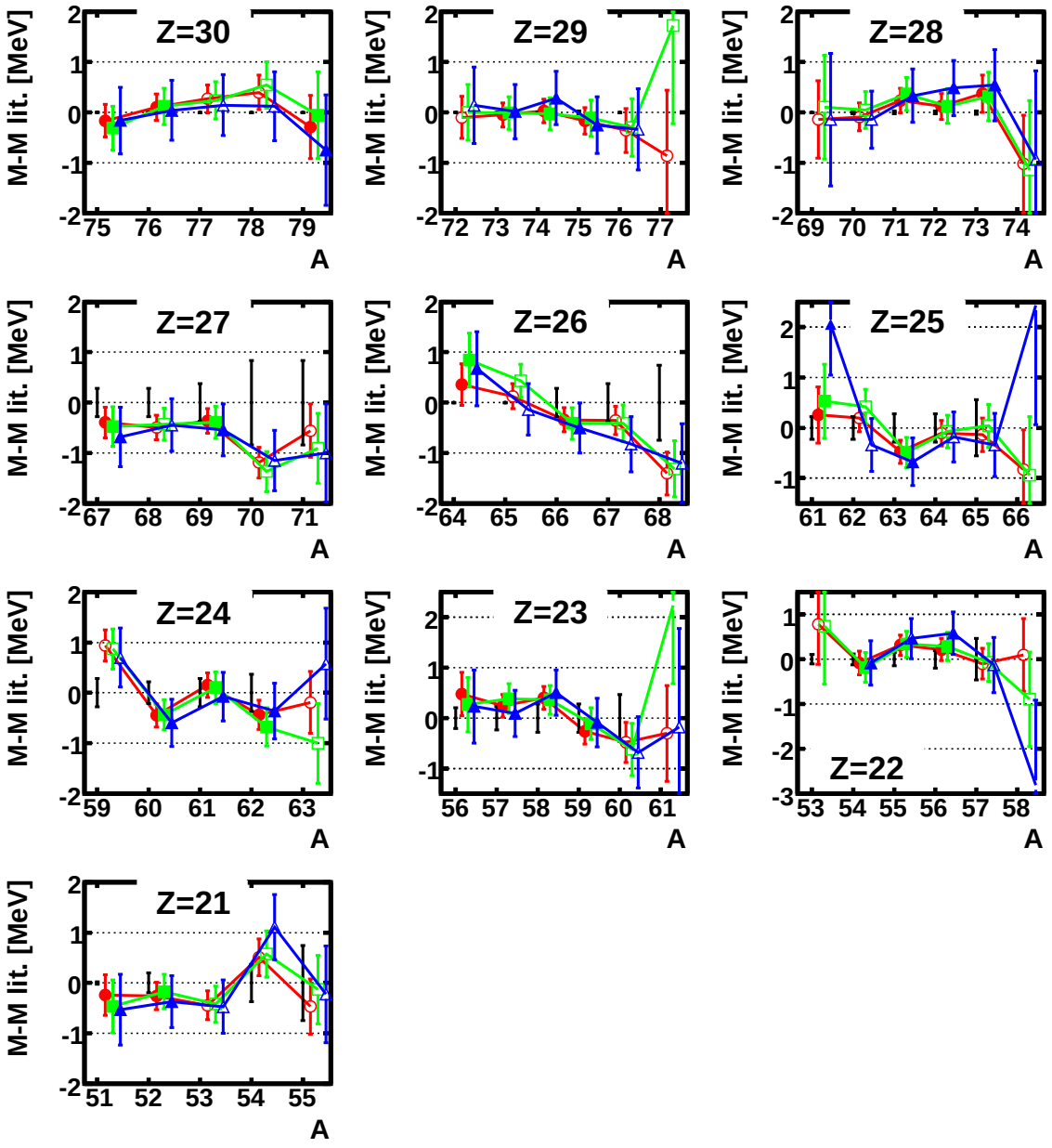

Figure 4.41: Sensitivity of the mass results to walk in the timing electronics. The mass calibration was fit using TOF corrected by t_{SUSD} and t_{XDSD}, and with different cuts in the integrated charge spectra of the PMTs (it was refitted in each case). The red circles are the mass residuals for the fit to the TOF values determined using all events, the green squares to events with a small signal from the S800 Down PMT, and the blue triangles for a large signal in the XFP Down PMT. The masses for each isotopic chain are plotted with respect to the literature data (black error bars around the zero axis), using extrapolations in [4] when they are unknown.

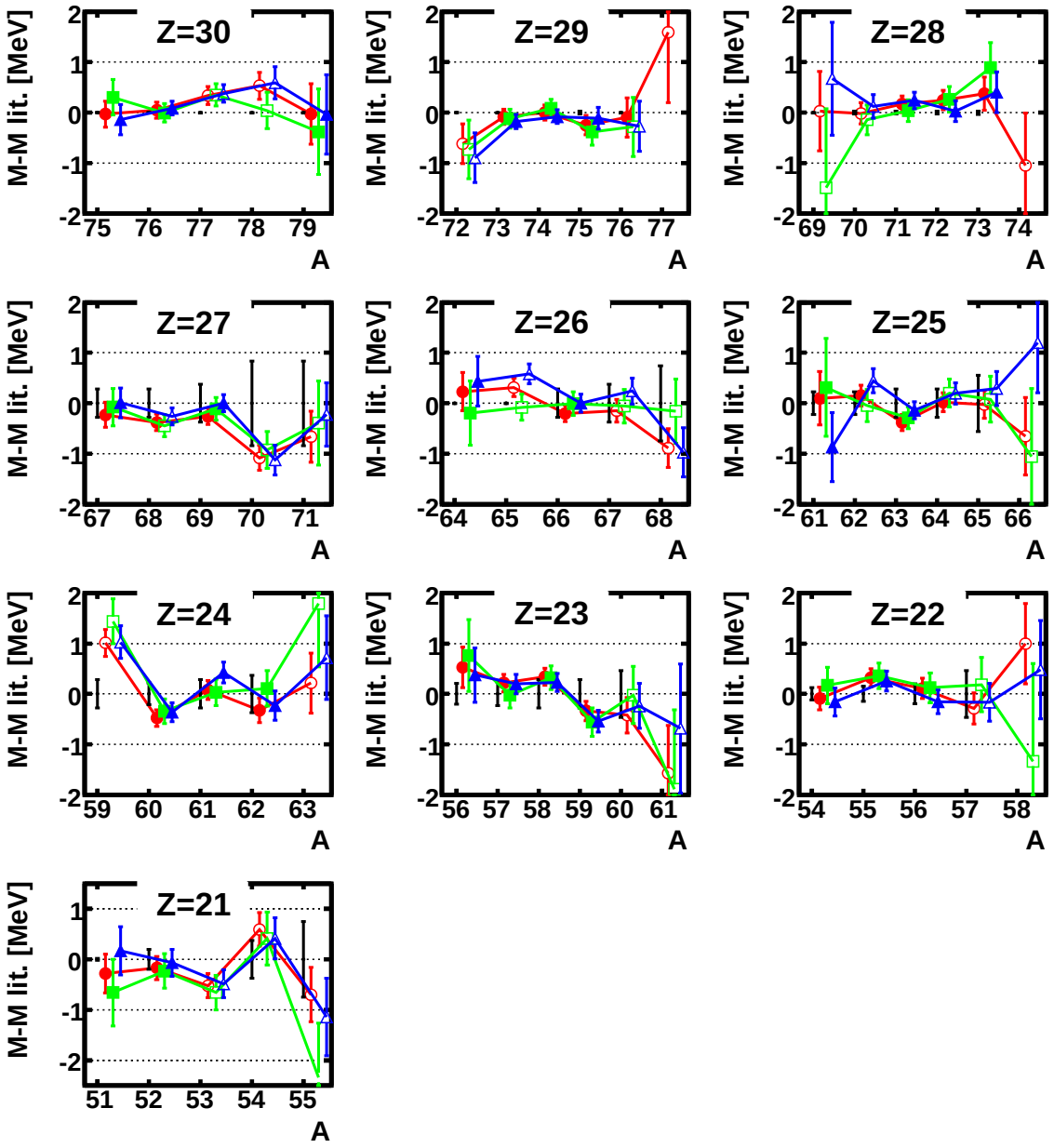

Figure 4.42: Sensitivity of the mass results to *walk* in the timing electronics. The mass calibration was fit using TOF corrected only by the particles momentum, and with different cuts in the integrated charge spectra of the PMTs (it was refitted in each case). The red circles are the mass residuals for the fit to the TOF values determined using all events, the green squares to events with a large signal from the S800 Down PMT, and the blue triangles for a low signal in the XFP Down PMT. The masses for each isotopic chain are plotted with respect to the literature data (black error bars around the zero axis), using extrapolations in [4] when they are unknown.

dependence observed in the data. Therefore, to obtain the final mass results only the TOF corrected by the particles Bρ was used.

4.6.4 Beam angle at S800 focal plane

A a similar procedure was performed to test the sensitivity of the fit to the TOF correction by the dispersive angle at the S800 focal plane (Section 4.3.2), and the conclusions are similar to those for the timing walk correction. As shown before, the correction obtained using cubic polynomial fits to the TOF vs a_{S800} distribution did not eliminate completely the correlation between both variables. The changes in the masses determined (without refitting the calibration function) when different cuts are placed in the angular spectra are reduced. Nevertheless, some correlations are still present, in particular for the heavier fragments whose masses differ by about 2 MeV between the a_{S800} cuts (Figure 4.43).

On the other hand, when the mass calibration function is fitted to the TOF values obtained for these cuts in the a_{S800} spectra it can accommodate for the variations in the TOF, even if the measured TOF is only corrected by the beam particles momentum. As shown in Figure 4.43 the masses agree within their errors. In these case a systematic difference in the results of the Sc isotopes was observed, which can grow to about 1 MeV for ^{55}Sc. In addition, ^{58}Ti also show a large difference in the mass obtained for events with a positive or with a negative angle at the S800.

As was the case for the correction of the timing walk in the electronics, the systematic error of the fit increases when including the angular correction to the TOF. The correction for the S800 angle was not used to obtain the final mass results.

4.6.5 S800 vault temperature

As discussed in section 4.3.3, the temperature in the S800 experimental vault varied by a few °C because of the behavior of the air conditioning unit located there, and

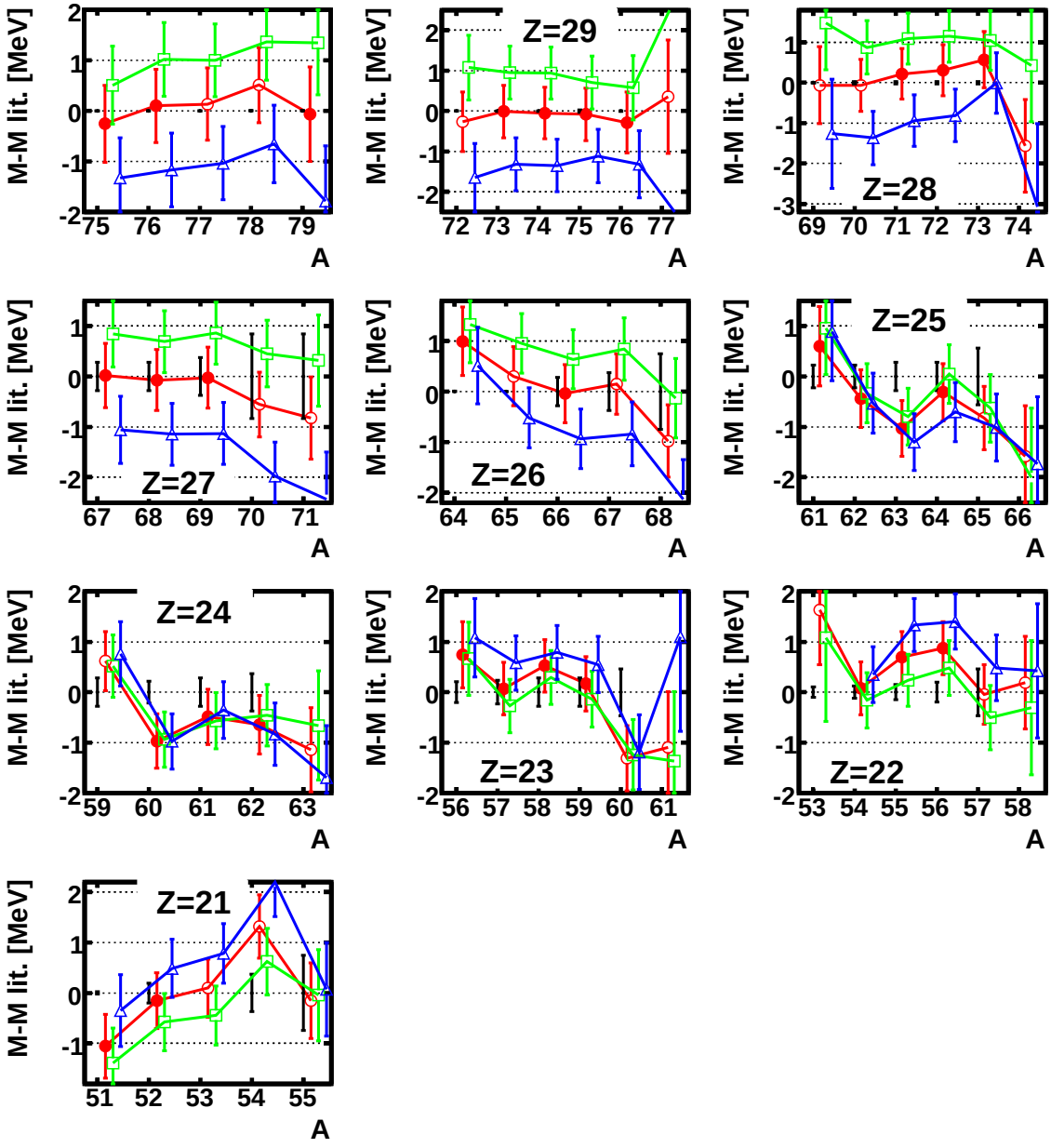

Figure 4.43: Sensitivity of the mass results to TOF correction by the a_{S800} angle. The mass calibration function was fitted to a set of TOF values corrected by a_{S800} angle, and the fit residuals are shown as red circles. The masses were then evaluated for sets of corrected TOF values that were determined with events with a positive (green squares) or negative (blue triangles) angle at the S800 focal plane. The masses for each isotopic chain are plotted with respect to the literature data (black error bars around the zero axis), using extrapolations in [4] when they are unknown.

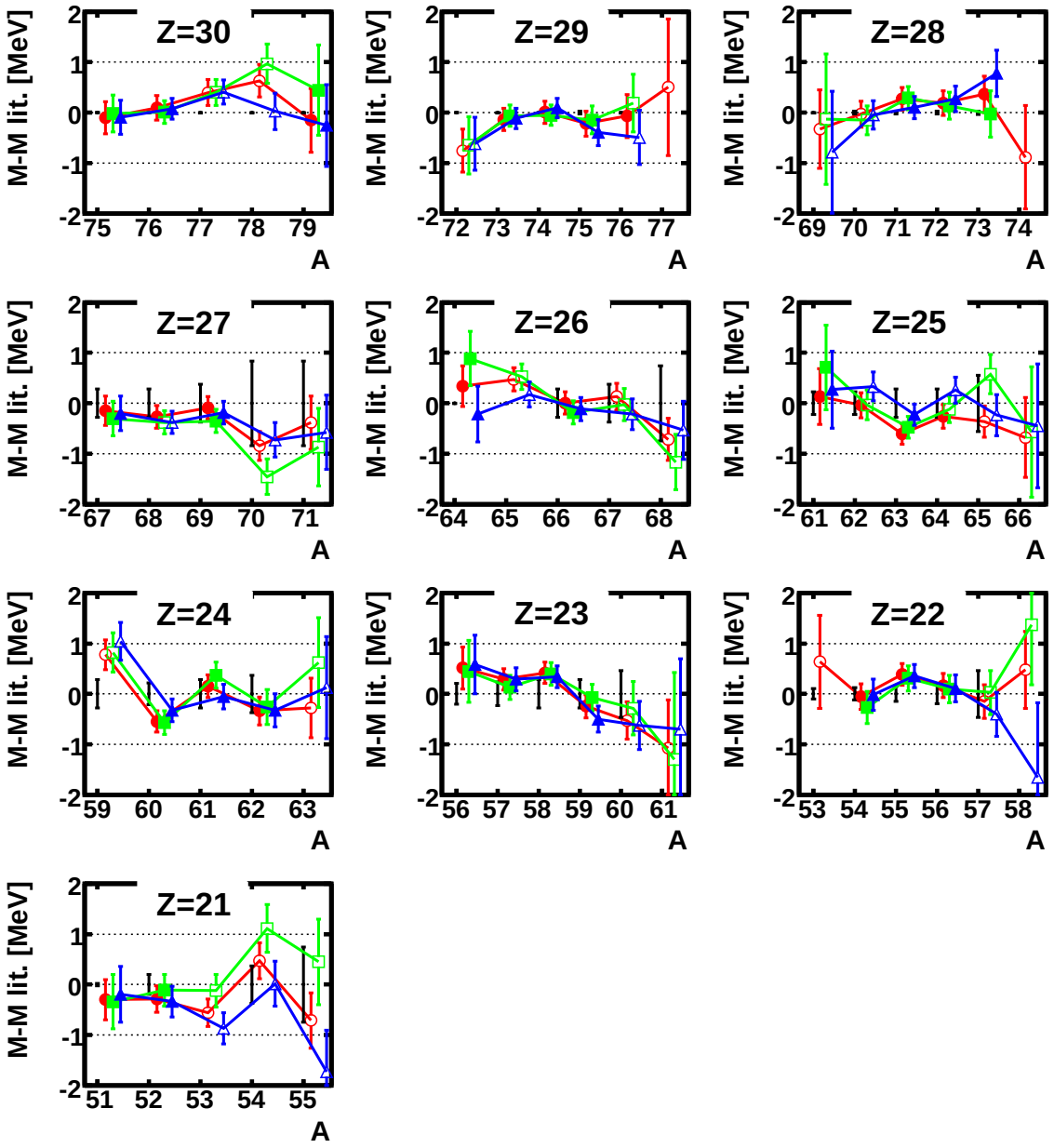

Figure 4.44: Sensitivity of the mass results to a_{S800} distribution. The mass calibration function was fitted to a set of TOF values corrected with a function quadratic in Bρ , and with different cuts in the spectrum for the dispersive angle at the S800 focal plane (it was refitted in each case). The red circles are the mass residuals for the fit to the TOF values determined using all events, the green squares to events with a negative a_{S800} angle, and the blue triangles for with a positive one. The masses for each isotopic chain are plotted with respect to the literature data (black error bars around the zero axis), using extrapolations in [4] when they are unknown.

this has an observable effect in the measured TOF. A TOF correction function linear in the temperature was fit to the data. However, the scatter in the slope of the correction function obtained for different isotopes was too large (Figure 4.26), and a cut to select event with a measured temperature within 26°C$\leq T \leq$ 27.65°C was used instead.

To test the sensitivity of the mass fit to the temperature variations, the TOF was determined for increasingly narrow cuts in the temperature spectra, and the mass calibration function was fit for each of them. As expected, the calculated systematic error decreases by only using events within a narrow range of S800 vault temperature. It is 4.0 keV/q without any rejection cuts (i.e., including data during temperature spikes), 3.4 keV/q for a 2°C range around $T = 27$°C, and 3.0 keV/q for a 1°C range. The calibration function obtained for the 2°C cut was used to evaluate the TOFs determined for the other ranges, and as shown in Figure 4.45 the mass results agree within their uncertainty with the initial fit (the agreement is even better if the calibration function is refitted for each TOF set). In addition, the data was divided in two classes for events with a high and a low temperature, and the masses evaluated with the same calibration function. In this case the agreement between the masses is not as good, but it is still satisfactory (Figure 4.46).

However, in both cases a clear systematic shift in the evaluated masses is observed when the events are separated in two classes, which reflects the dependence of the measured TOF on the temperature. For example, the TOF measured for the set of events with a high temperature (27°C$\leq T \leq$ 28°C) results, for most isotopes, in a mass a few hundred keV smaller, while for the events with a low temperature the shift is in the opposite direction (26°C$\leq T \leq$ 27°C). The effect is similar to that discussed for the correction of the TOF based on the timing between the timing detector signals (and their amplitudes), but the shift to the measured masses due to the temperature fluctuations is smaller. Because the temperature distribution for

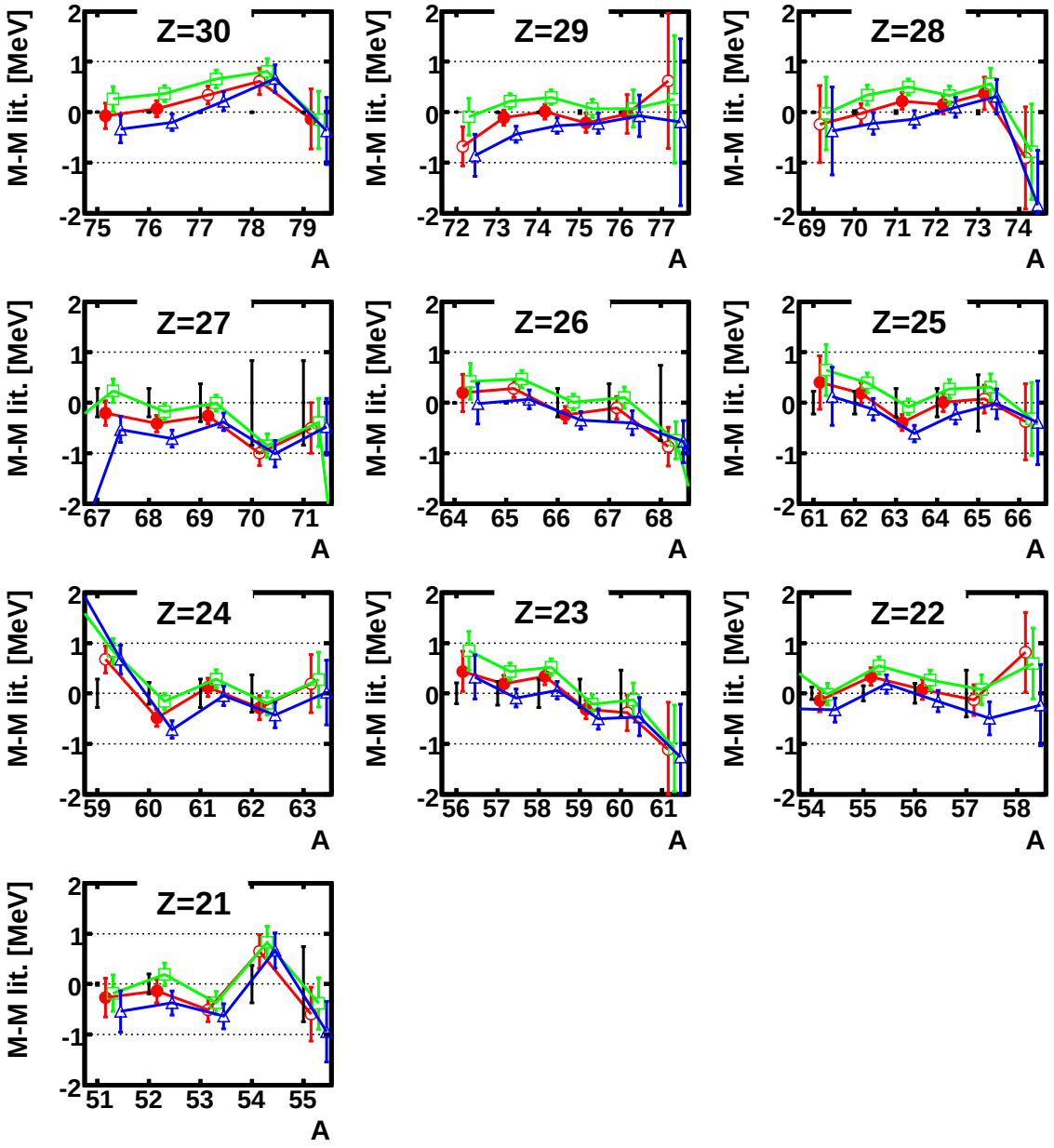

Figure 4.45: The mass calibration function was fitted to a set of TOFs obtained for events in the range of 26°C $\leq T \leq$ 28°C for the S800 vault temperature (shown in red, with the reference masses indicated with filled circles). The TOFs obtained for other cuts in the S800 vault temperature spectra were evaluated using the results of this fit (without refitting the mass calibration function). The mass results when using more restrictive cut (26.5°C $\leq T \leq$ 27.5°C) are shown as blue triangles, and the results for no temperature cut as green squares. The mass along each isotopic chain is plotted with respect to the literature data (black error bars around the zero axis) using extrapolation in [4] when the mass is unknown.

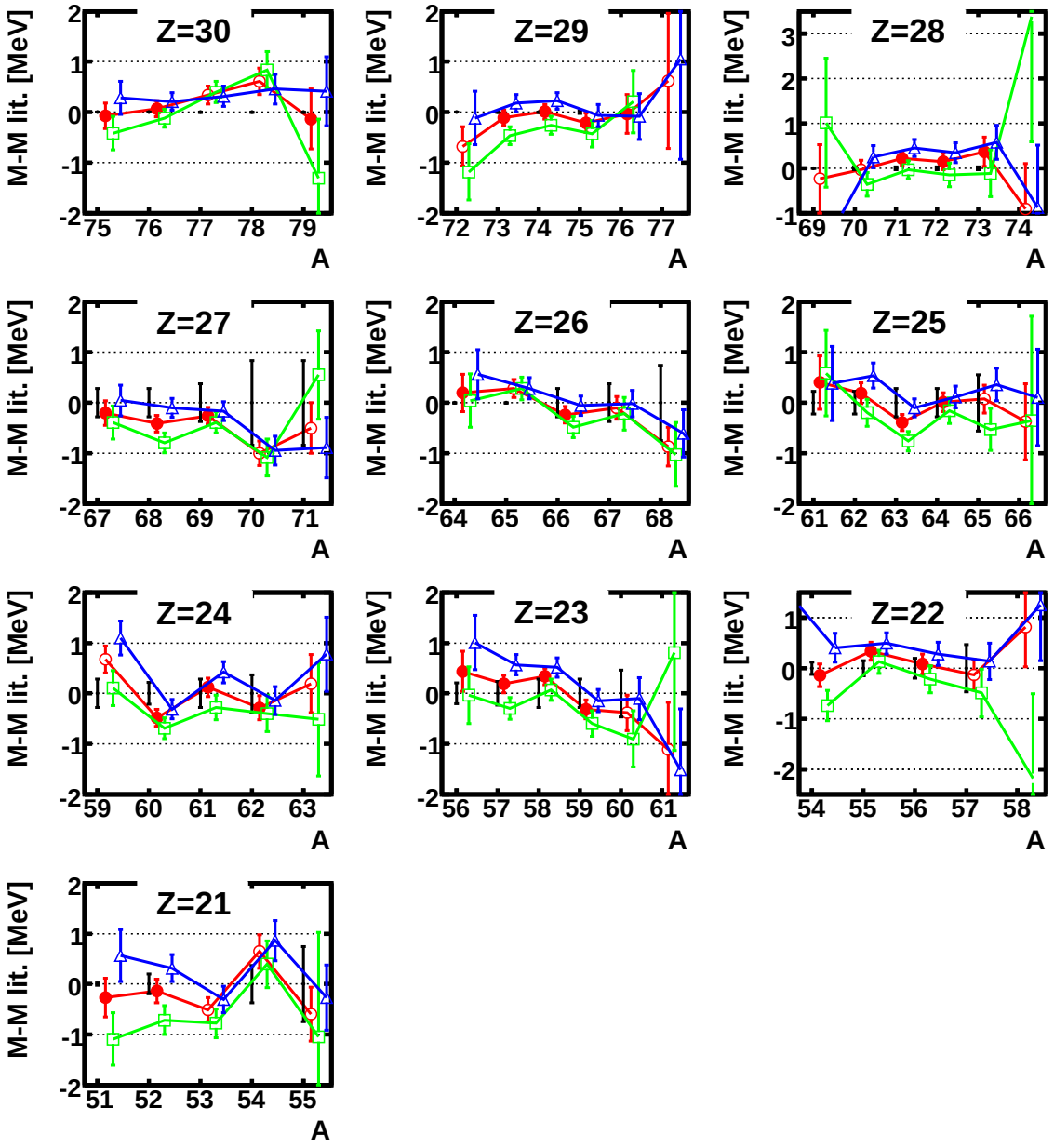

Figure 4.46: The mass calibration function was fitted to a set of TOFs obtained for events in the range of 26°C $\leq T \leq$ 28°C for the S800 vault temperature (shown in red, with the reference masses indicated with filled circles). The TOFs obtained for other cuts in the S800 vault temperature spectra were evaluated using the results of this fit (without refitting the mass calibration function). The TOFs obtained for other cuts in the S800 vault temperature spectra were evaluated using the results of this fit (without refitting the mass calibration function). The mass results for events with a lower temperature in the S800 vault (26°C $\leq T \leq$ 27°C) are shown as blue triangles, and those for a higher temperature (27°C $\leq T \leq$ 28°C) as green squares.

events corresponding to the different isotopes is roughly symmetric the effect on the measured TOF is averaged out for each isotope, and the mass difference observed in Figure 4.46 for the two classes only represents an upper limit to the deviation that could be introduced by this variable.

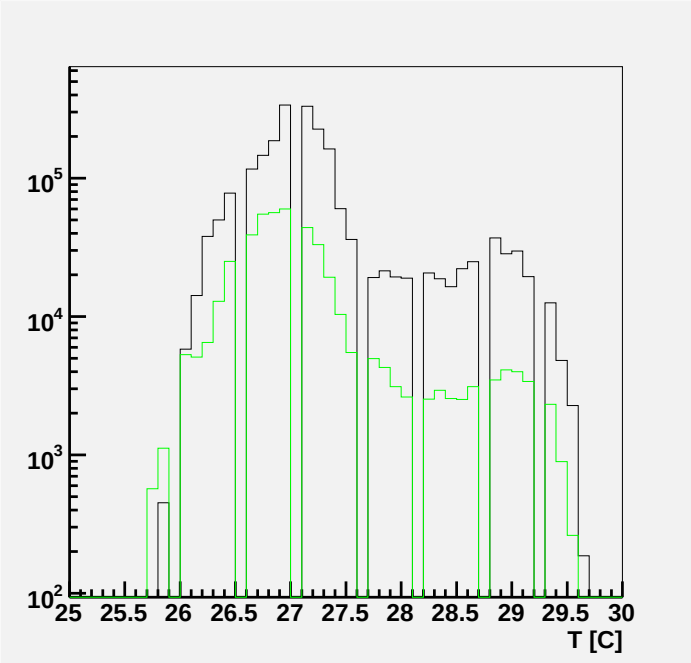

Figure 4.47: Temperature at the S800 experimental vaults for valid events during runs with the 94 mg/cm^2 (green) and the 47 mg/cm^2 (black) Be production targets. As discussed in Section 3.1 different target thicknesses favors the transmission of fragments with different mass to charge ratio, so all isotopes in the beam should have similar temperature distributions in their events.

A particular feature of the variation of the TOF with temperature is that the variable that what creates the temperature changes (the air conditioning unit of the experimental vault turning on and off) was decoupled to the mechanism for the production of the radioactive ion beam. During the experiment two Beryllium production target of different thickness were alternated: a thin target to favor the transmission of the calibration isotopes, and a thick one for more neutron rich isotopes with unknown masses (Section 3.1). In principle it is possible that the time period for the high temperature runs was not distributed equally between both targets. For that reason it

was checked that the temperature distribution for the events of all isotopes is similar, since otherwise the calibration function could not have been reliably extrapolated from the region of the reference isotopes to the more neutron rich ones. Figure 4.47, which shows the temperature distribution for events from each production target run, confirms that this was the case during the experiment. In addition, the temperature spectra for individual isotopes are presented in Appendix A.3.

The range of temperatures adopted to reject events is $26°\text{C} \leq T \leq 27.65°\text{C}$. The systematic error for such selection cut ($\sigma_{\text{sys}} = 3.3\,\text{keV}/q$) is larger than the one for a 1°C cut, but the statistics are increased by about 23 % for the isotopes with unknown masses and the uncertainty in their mass results is decreased by about 8 %. The chosen upper limit for the cut rejects most events corresponding to the periods when the air conditioning unit of the vault would turn off and the temperature had rapid changes (Figure 4.23).

4.6.6 Selection of reference isotopes

Mass fits to different sets of reference isotopes were performed to test the ability of the calibration function to extrapolate its results. All the new masses determined in the present experiment have a larger TOF (are more neutron rich) than the reference masses available of the same element, so some extrapolation along this coordinate is necessary. In principle there is no need to extrapolate the calibration function along Z, but the fit robustness in that dimension was also checked. These tests also help to cross check the calculation of the fit extrapolation error, which should increase to include any variation in the masses as isotopes are removed from the set of calibration masses.

Figures 4.48 through 4.51 show the results of the mass fit using sets of calibrants without the isotopes with the largest and smallest Z and TOF. The fit results were robust to the choice of calibration masses. They were systematically shifted by the

new parameterization of the calibration function, but in general the difference to the masses obtained using all the calibration isotopes was only a few tens of keV. The case where the fit was more sensitive was when the Sc isotopes (Z=21) were not used as calibrants. The resulting masses of the Sc isotopes are about 300 keV smaller for the reduced set of calibration points. Because of the lower number of calibration points with low Z these isotopes are important to constrain the function in this region.

The extrapolation error was found to be a function of the distance from the reference masses, as expected. For example, in the Fe isotopes the extrapolation error for ^{67}Fe and ^{68}Fe, for which are respectively one and two neutrons heavier than the Fe reference masses, was 120 keV and 190 keV. When the fit was repeated removing the eight more neutron-rich reference masses, including ^{66}Fe, the error for extrapolating the calibration one and two mass units became 170 keV for ^{66}Fe and 210 keV for ^{67}Fe. In the second fit the extrapolation error became a bit larger for a comparable distance from the calibration masses because less calibration points were used to constrain the function (23).

The mass fit was also performed by expanding the set of calibration points with isotopes that have known long-lived isomers. When all the isotopes with known isomers listed in Table 4.2 were added to the set of calibrants (11 isotopes), the systematic error in the fit results increased from 4.4 keV/q to 6.6 keV/q. However, if only the isotopes where the known isomers have an energy bellow 150 keV (4 isotopes) were included, then the systematic error of the fit is reduced to 3.4 keV/q. In such case the difference in the mass results with the fit without including isotopes with known isomers is small (it is 15 keV on average of for the masses where new results are provided, and the largest difference is 40 keV for ^{77}Cu).Therefore, these additional 4 calibration points were included in the final fit.

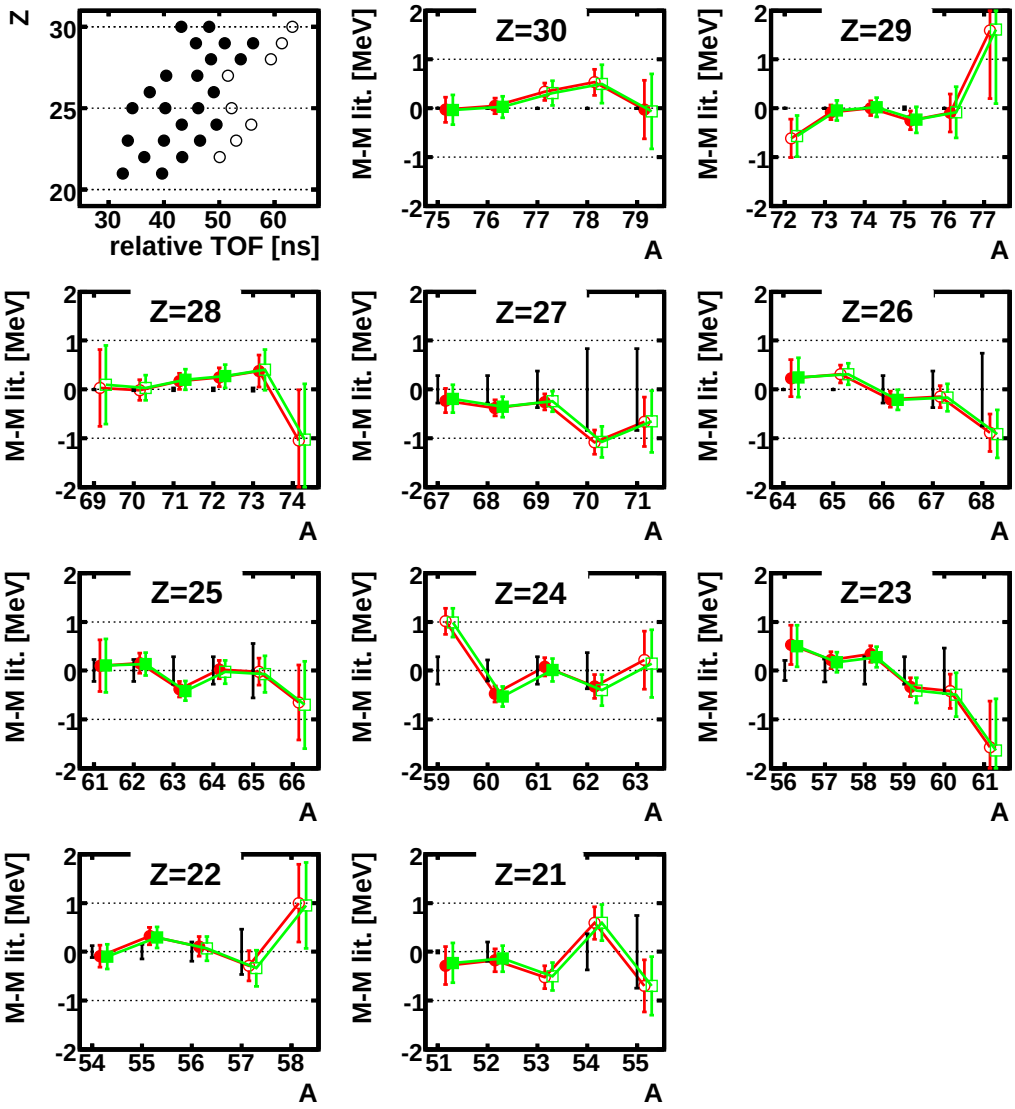

Figure 4.48: Mass fit excluding the most neutron rich calibration isotopes in each isotopic chain. The first figure shows the location of the reference masses in the coordinate space of the calibration function. The open circles are the isotopes excluded in the second fit. The mass residuals shown as red circles correspond to the fit with all refence masses, and the ones shown as green squares are those for the reduced set of calibrants. In these mass residual plots filled symbols correspond to isotopes used as calibration points. The masses for each isotopic chain are plotted with respect to the literature data (black error bars around the zero axis), using extrapolations in [4] when they are unknown.

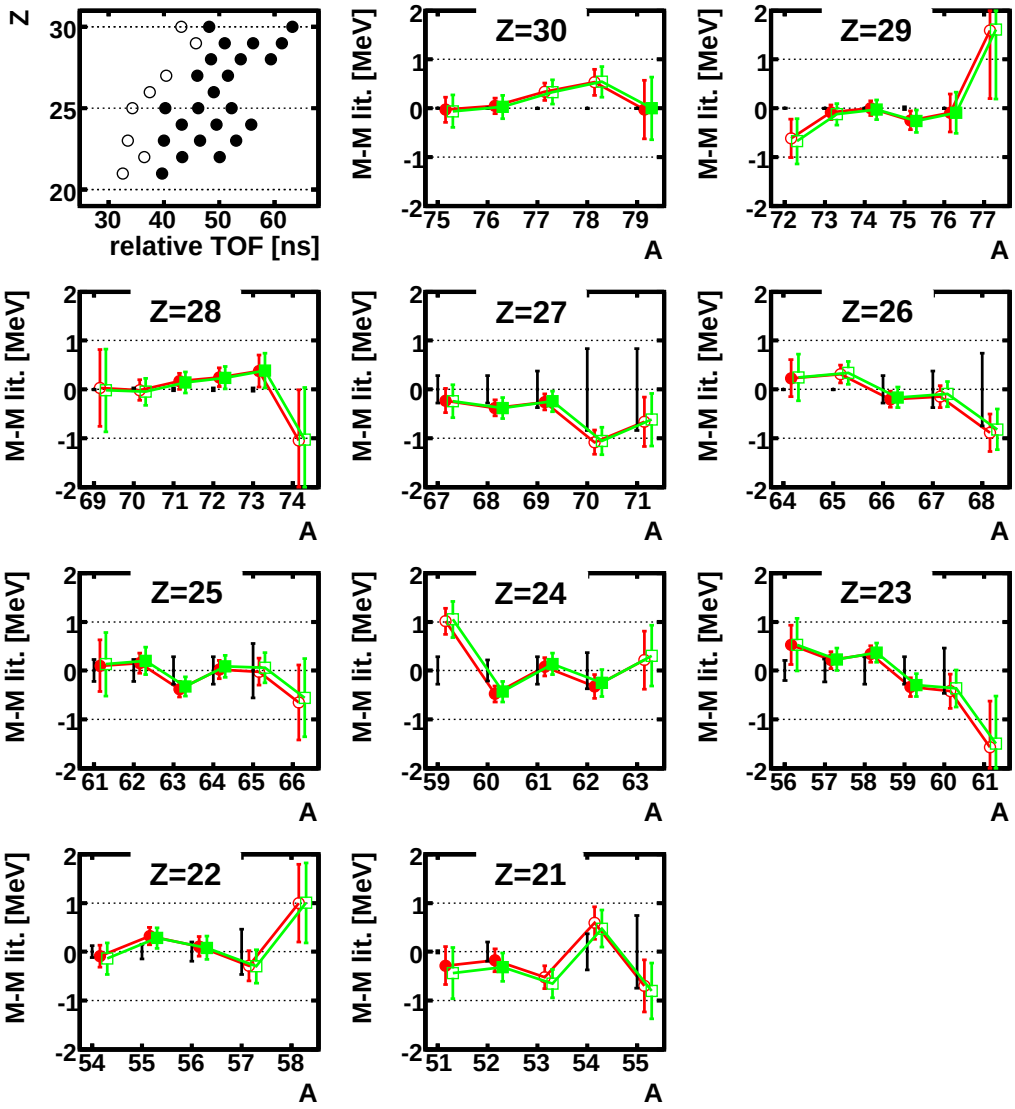

Figure 4.49: Mass fit excluding the least neutron rich calibration isotopes in each isotopic chain. The first figure shows the location of the reference masses in the coordinate space of the calibration function. The open circles are the isotopes excluded in the second fit. The mass residuals shown as red circles correspond to the fit with all refence masses, and the ones shown as green squares are those for the reduced set of calibrants. In these mass residual plots filled symbols correspond to isotopes used as calibration points. The masses for each isotopic chain are plotted with respect to the literature data (black error bars around the zero axis), using extrapolations in [4] when they are unknown.

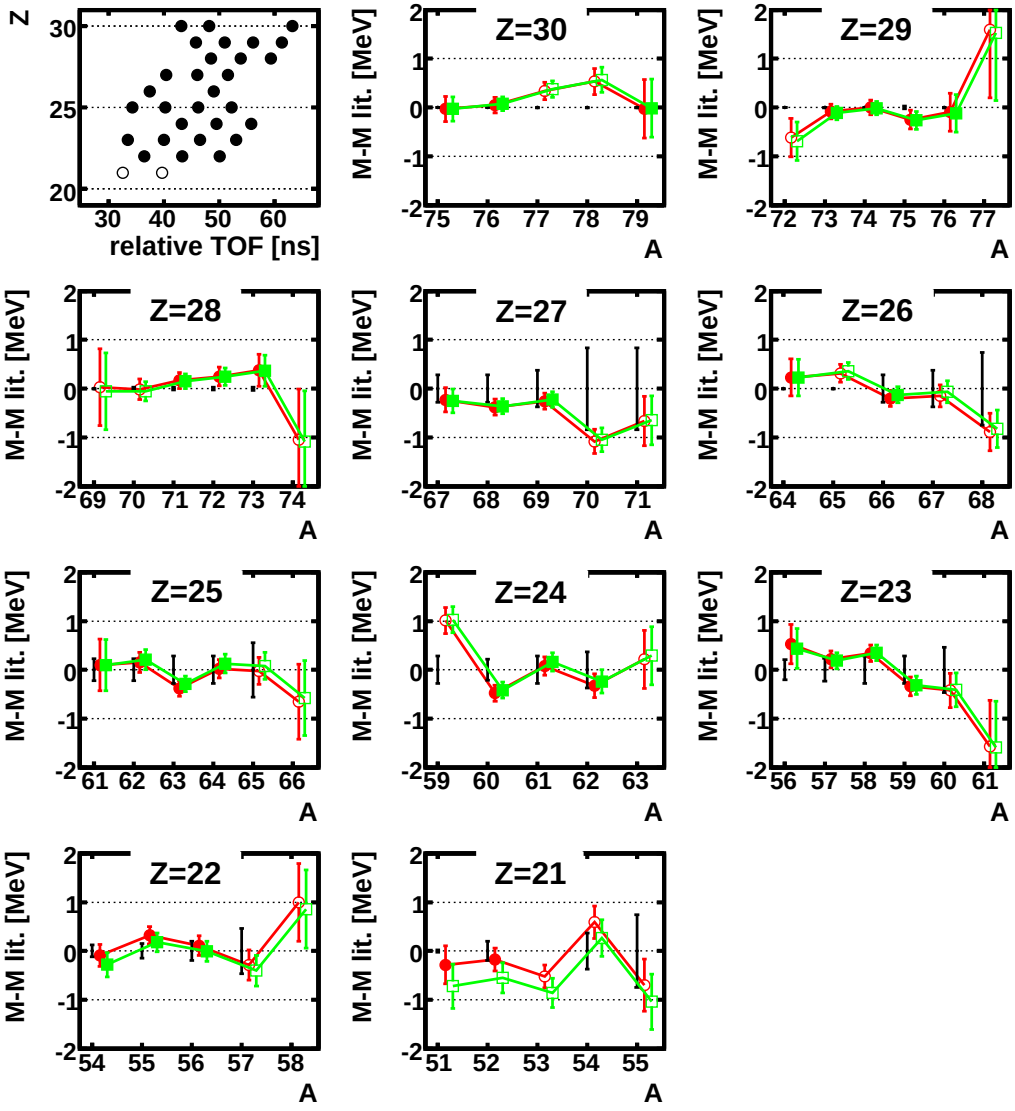

Figure 4.50: Mass fit excluding calibration isotopes with Z=21. The first figure shows the location of the reference masses in the coordinate space of the calibration function. The open circles are the isotopes excluded in the second fit. The mass residuals shown as red circles correspond to the fit with all refence masses, and the ones shown as green squares are those for the reduced set of calibrants. In these mass residual plots filled symbols correspond to isotopes used as calibration points. The masses for each isotopic chain are plotted with respect to the literature data (black error bars around the zero axis), using extrapolations in [4] when they are unknown.

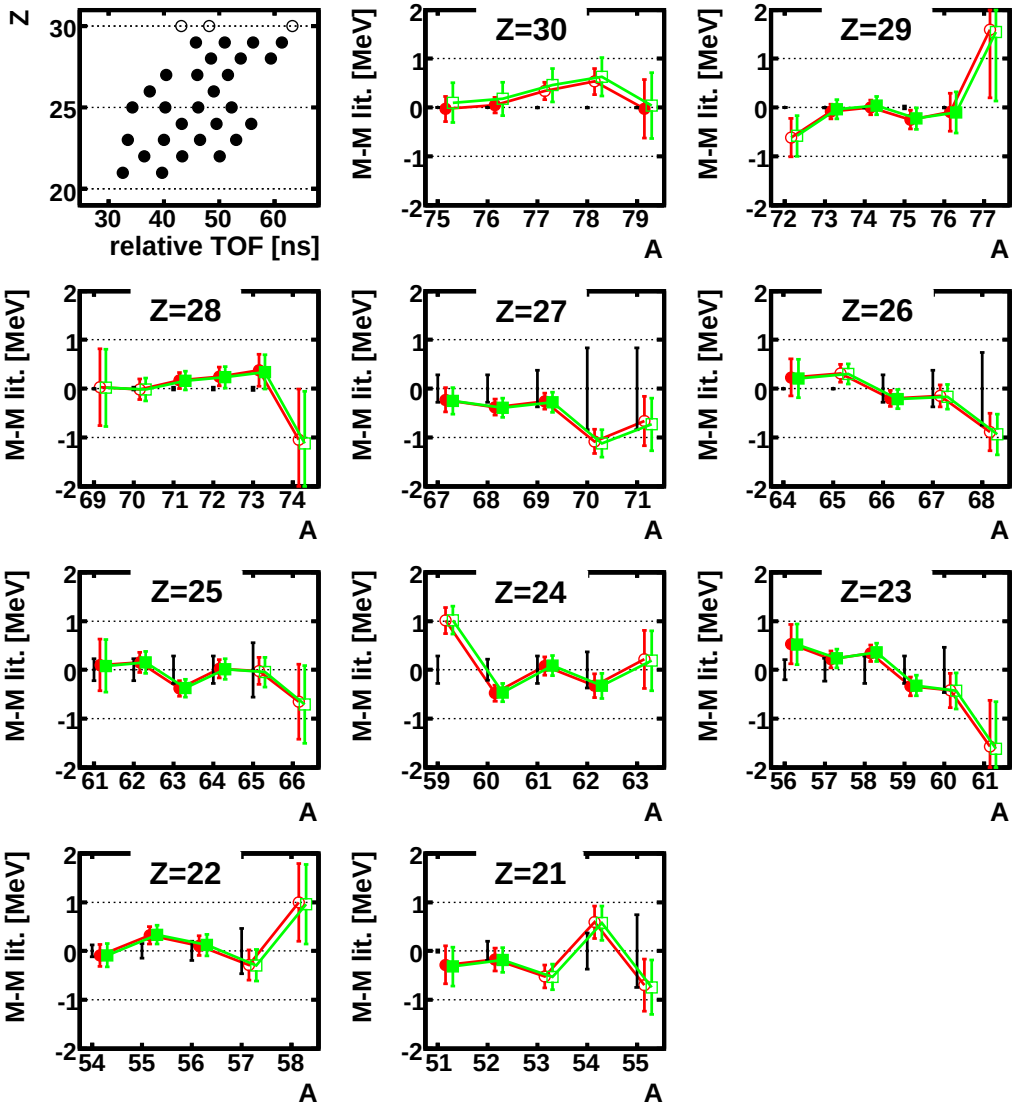

Figure 4.51: Mass fit excluding calibration isotopes with Z=30. The first figure shows the location of the reference masses in the coordinate space of the calibration function. The open circles are the isotopes excluded in the second fit. The mass residuals shown as red circles correspond to the fit with all refence masses, and the ones shown as green squares are those for the reduced set of calibrants. In these mass residual plots filled symbols correspond to isotopes used as calibration points. The masses for each isotopic chain are plotted with respect to the literature data (black error bars around the zero axis), using extrapolations in [4] when they are unknown.

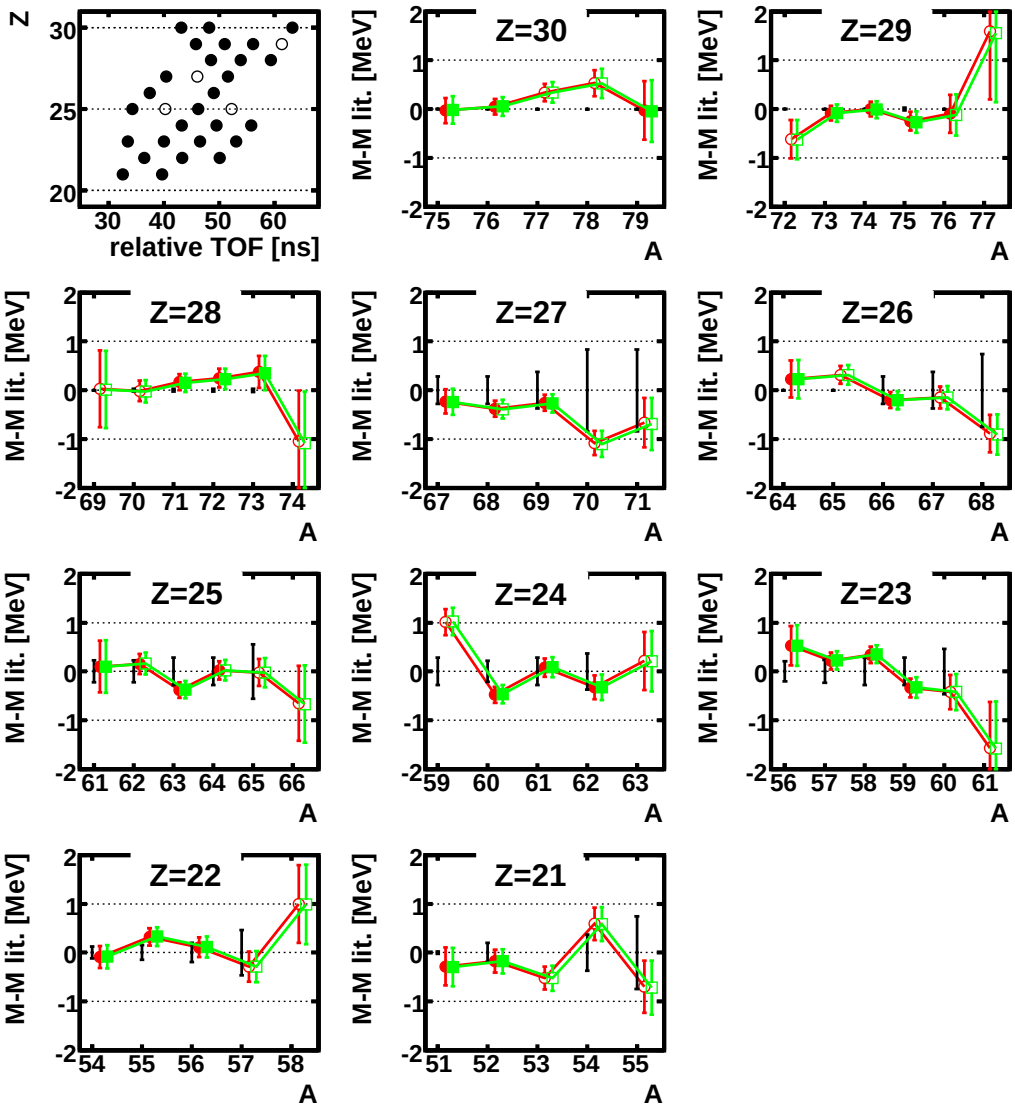

Figure 4.52: Mass fit excluding calibration isotopes with known long-lived isomer with energy bellow 200 keV (Table 4.2). The first figure shows the location of the reference masses in the coordinate space of the calibration function. The open circles are the isotopes excluded in the second fit. The mass residuals shown as red circles correspond to the fit when the four isotopes with known isomers are used as calibration points, and the ones shown as green squares are those for the fit when only isotopes without known long-lived isomers are used. In these mass residual plots filled symbols correspond to isotopes used as calibration points. The masses for each isotopic chain are plotted with respect to the literature data (black error bars around the zero axis), using extrapolations in [4] when they are unknown.

4.6.7 Summary

In this section a sensitivity study of the mass fit results to different variables in the experimental setup was presented. It was confirmed that the things that had the largest effect in the measured time of flight (TOF) are also the ones that influence the mass fit the most.

It was also concluded that correcting the TOF for some residual correlation does not necessarily improve the fit results. If these correlations are not large and have a smooth variation between the different isotopes in the beam, the mass calibration function used can take them into account. Besides, in some cases the attempts to correct the TOF by some of these variables resulted in an overcorrection, and the fit residuals were even larger than in the fit using the uncorrected TOF. For example, this was the case for TOF correlations with the angle at the S800 or the timing between the two signals from each timing detector.

The Bρ correctio proved to be more sensitive to the linear term of the correction function, which is also the dominant term in the TOF dependence on Bρ . The quadratic form of the Bρ correction function was adopted. The masses of the lower Z isotopes, in particular Sc that has the most asymmetric Bρ distribution of the isotopes in the fit range, were the most sensitive to arbitrary avriations in the parameters of this correction.

In addition, the Sc isotopes (Z=21) and ^{58}Ti (Z=22, and the second largest TOF) are in general the isotopes where the largest variation in the mass results was found. This isotopes are in the limit of the Z and TOF range where the calibration function must be extrapolated (Figure 4.34). The calculation of the mass uncertainty, and in particular the extrapolation error for the calibration function, was found to be satisfactory for the other case but it could be increased in the final results to account for the variability of the results for the lower Z fragments.

For the final mass fit it was also decided that the TOF measured with respect to a

clock signal (TOF_{clk}) would be used, as it was less sensitive to the nonlinearities in the electronic modules and temperature changes in the S800 vault. For the temperature variation in the S800 vault a selection cut was used that rejected most events when the air conditioning unit of the vault was turned off. It was also decided that it was not nessesary to reject events based on the glitch detected in the electronic modules.

Chapter 5

Results

5.1 Nuclear masses

The nuclear masses determined in this work are listed in Table 5.1. The mass of six neutron-rich isotopes has been measured for the first time, and in ten cases the uncertainty of the previous measurement has been reduced. In addition, the fit residuals for the calibration function adopted are shown in figure 5.1.

For all the isotopes for which the mass is remeasured, their value in the 2003 Atomic Mass Evaluation (AME03) [4] is derived from time-of-flight experiments with the TOFI spectrometer at Los Alamos [37, 38]. The results agree within the errors with these measurements, but there might be the indication of a trend since most of the new results give more bound masses than TOFI's results (7 out of 9). The results of TOFI experiments in this region have been shown to have systematic errors by recent Penning trap measurements, whose resolution is about two orders of magnitude better. In ISOLTRAP measurements of Ni and Cu isotopes [33] the mass values from TOFI were found to be a few hundred keV too small. In the case of a measurement in JYFLTRAP [34], the measured masses of Cu isotopes were systematically smaller than TOFI values, and the difference was in the opposite direction for Ni isotopes.

One difficulty in interpreting the possible discrepancy with the previous experi-

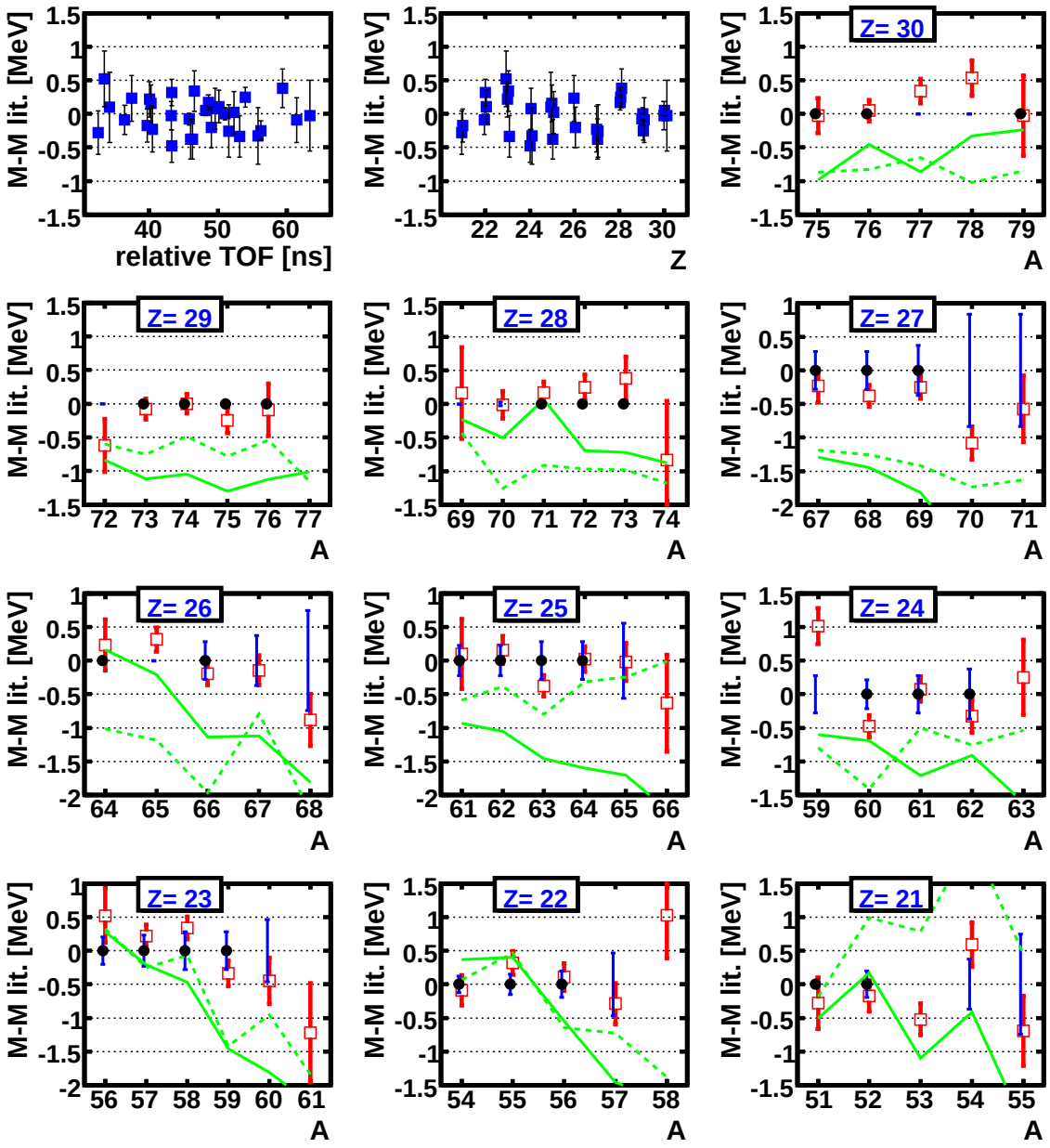

Figure 5.1: Mass results obtained in the present experiment. The first two graphs show the mass residuals for the fit of the calibration isotopes to the know masses as a function of their TOF (A/Z) and Z. These calibration isotopes are also indicated with black circles in the other graphs. The remaining graphs show the measured masses for each isotopic chain (red squares). The uncertainty in the literature data is shown as blue error bars around the zero axis, and extrapolated values from AME 2003 [4] are used to plot the residuals for the unknown masses (no error bars). In addition, the nuclear mass predicted by the FRDM (dashed green line) and the HFB-14 (solid green line) models is shown.

Table 5.1: Mass excess results from the present experiment, and literature values (in keV). All the literature values are obtained from the 2003 AME [4]. The weighted mean is presented in the third column.

	This work	Literature	Mean
^{53}Sc	-38150 (240)	-37630 (280#)	-37930 (180)
^{54}Sc	-33590 (330)	-34190 (370)	-33860 (250)
^{55}Sc	-30320 (540)	-29620 (750)	-30080 (440)
^{57}Ti	-33820 (310)	-33530 (470)	-33730 (260)
^{58}Ti	-29740 (800)		-29740 (800)
^{60}V	-33030 (350)	-32600 (470)	-32870 (280)
^{61}V	-30910 (940)		-30910 (940)
^{63}Cr	-35270 (600)		-35270 (600)
^{65}Mn	-40730 (280)	-40710 (560)	-40720 (250)
^{66}Mn	-36890 (770)		-36880 (770)
^{67}Fe	-45880 (220)	-45740 (370)	-45840 (190)
^{68}Fe	-44010 (390)	-43130 (750)	-43830 (340)
^{70}Co	-46720 (250)	-45640 (840)	-46640 (240)
^{71}Co	-44530 (510)	-43870 (840)	-44360 (430)
^{74}Ni	-49390 (1040)		-49390 (1040)
^{77}Cu	-46940 (1390)		-46940 (1390)

ments is that, as explained in Section 4.5.1, several of the reference masses used for Z$\leq$ 27 are also derived from TOFI measurements. It would be of interest to obtain precise masses of neutron-rich nuclei in this region, in particular for $21 \leq Z \leq 25$. These could be used for a recalibration of the present results, and would provide important calibration data for future time-of-flight experiments. In addition, some isotopes where a new mass has been measured have known long-lived isomers that can not be resolved with the time-of-flight technique (^{60}V, ^{67}Fe, and ^{70}Co [62]). In the 2003 Atomic Mass Evaluation the TOFI results have been adjusted for a possible contamination of isomeric states in their data. This correction has not been performed for the masses of the present experiment shown in Table 5.1. However, any adjustment for the population of isomeric state in the beam fragments would decreased the measured value of the masses, and the discrepancy with the TOFI values would increase even more.

A particular case is the measurement of the mass of ^{53}Sc. This mass was also determined by a TOFI experiment, but was modified to be 1060 keV less bound in AME03 because of disagreements with systematic trends in the nuclear masses in the region. The new result of the present experiment, which has a similar uncertainty than the TOFI measurements (190 keV) and the adopted AME03 value (280 keV), is just in between both mass values.

The systematics of the two neutron separation energies in the region of the experiment are shown in figure 5.2. The new results for Sc and Ti isotopes continue with the trends observed for more stable isotopes, and the mass surface becomes even smoother with the new Sc results. In the case of the S_{2n} values determined with the new Mn, Fe and Co masses the slope as a function of neutron number is small. This trend was already observed in the previously known Mn masses starting at N=37, and now is observed for Fe starting at N=40, and coincides with the onset of deformation for isotopes this region. Deformation due to a lowering in the energy of the $\nu g_{9/2}$ orbital has been determined through spectroscopy studies. A low value for the $E(2_1^+)$ of 573 keV in ^{66}Fe (N=40) found by Hannawald et al [66] was taken as a possible indication of collectivity in the Fe isotopes (some lowering of the $E(2_1^+)$ was already seen for ^{64}Fe at N=38). A lowering of the first excited state on ^{62}Cr and ^{64}Cr has been interpreted as strong deformation of the Cr isotopes starting at N=36 [67]. Recent β-decay spectroscopic studies of Mn isotopes by Crawford et al. [68] have found that the low-energy level structure of ^{61}Mn is similar to that of less neutron-rich Mn isotopes, and ruled out deformation up to N=36. The information about the level structure of more neutron-rich Mn isotopes is insufficient to determine the onset of collectivity for Z=24 [69], but it is expected to occur a few neutrons beyond N=36 given the structure of neighboring Fe and Cr isotopes. Calculations of nuclear masses in the 0f1p shell with a spherical shell model by Richter et al. [70] have found a systematic discrepancy with the experimentally known masses of Cr to Fe isotopes,

and this provides further indication of the correlation of the observed trends in the neutron separation energy with nuclear deformation.

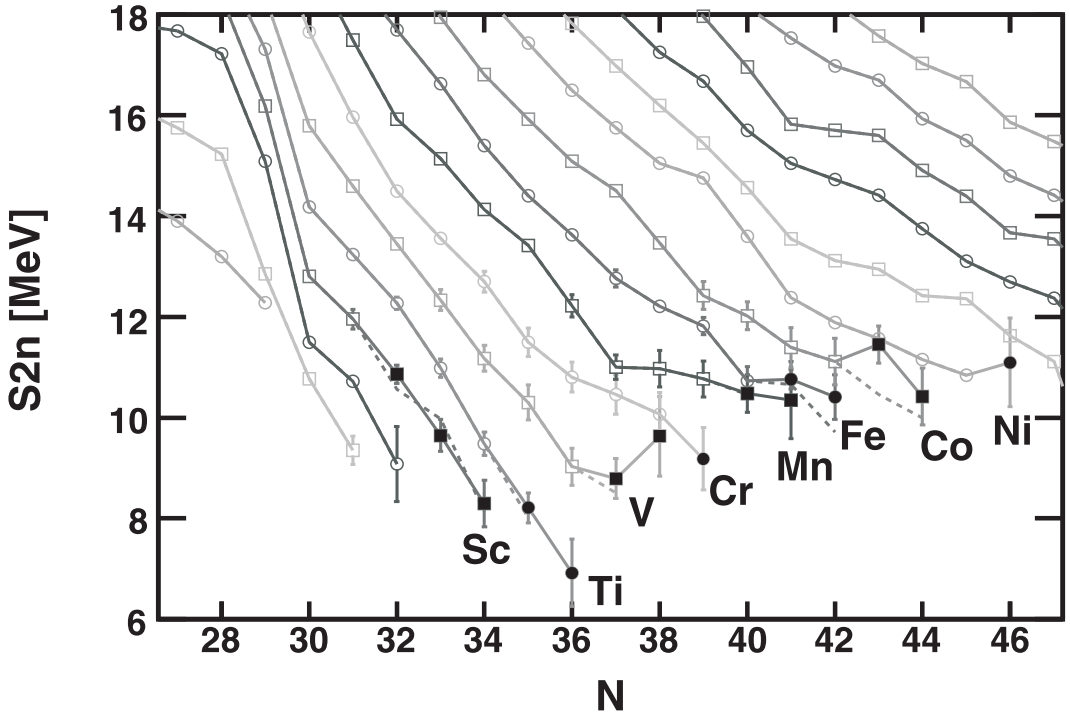

Figure 5.2: Two neutron separation energies in the N=32 and N=40 region. The new masses determined in the present experiment (Table 5.1) are shown as filled symbols. In case the mass was previously known, the weighted mean values are used (column 3). The dashed line corresponds to neutron separation energies calculated using the previously known masses.

Figure 5.3 compares the electron capture Q-values obtained with the mass results of this experiment with the previous experimental data and the HFB-14 [22] and FRDM [21] mass models. These models were described in Section 1.1.2, and are the ones used in the calculations of electron capture processes in accreting neutron stars presented in Chapter 6. The staggering of the Q-values between odd-odd and even-even nuclei plays an important role in determining the energy released in the neutron star crust by these processes. The FRDM model agrees better with the experimental data for the heavier mass chains. For the lighter mass chains ($A \lesssim 65$) the situation is not as clear, and in many cases the odd-even staggering of the

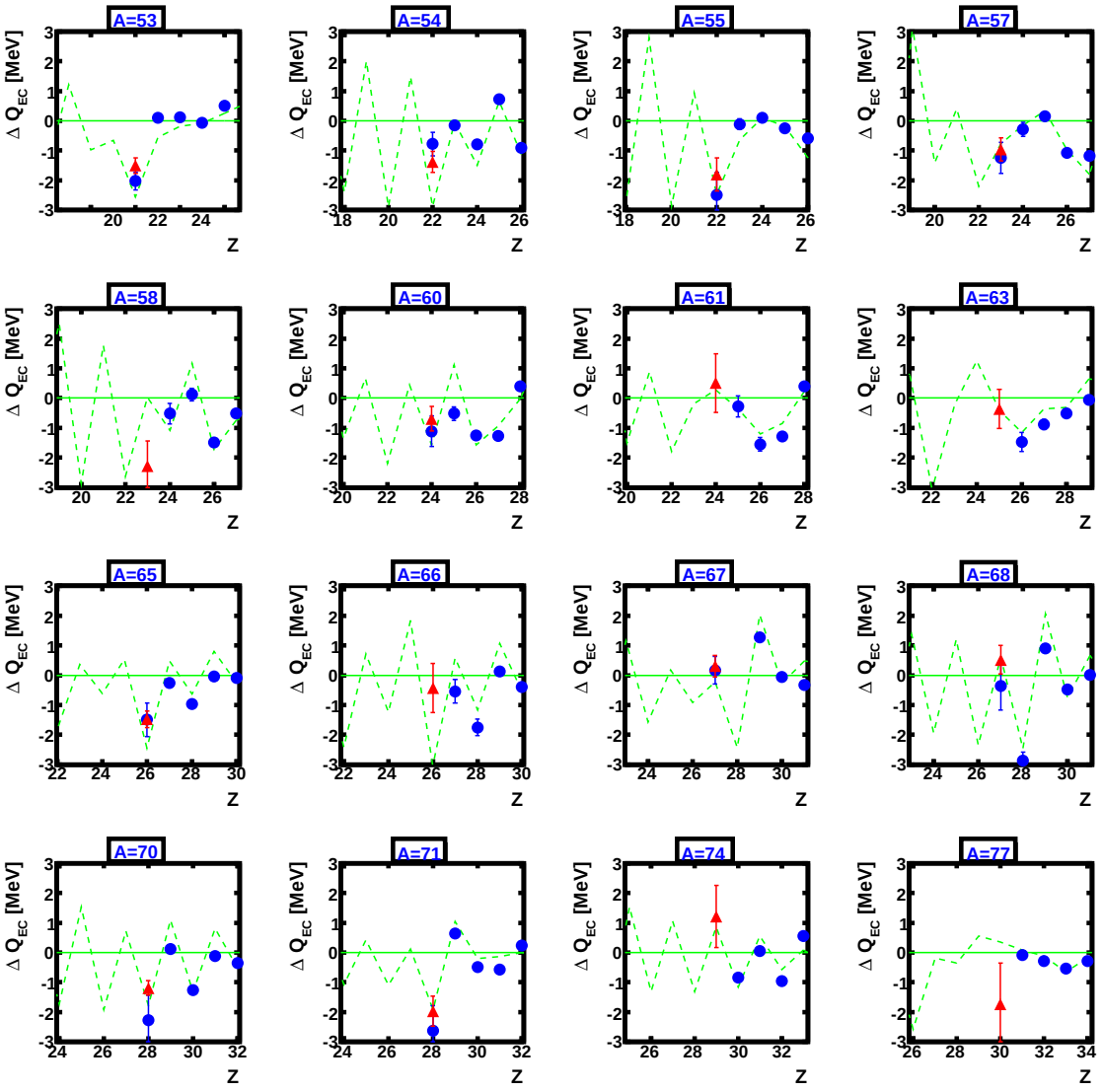

Figure 5.3: Electron capture Q-values determined with the masses measured in this experiment. The Q-values are shown with respect to those calculated with the HFB-14 mass model ($\Delta Q_{\mathrm{EC}} = Q_{\mathrm{EC}}(\mathrm{i}) - Q_{\mathrm{EC}}(\mathrm{HFB}-14)$). The blue circles correspond to values calculated with the literature masses, the red triangles are calculated with the results of the present experiment. In addition, the dashed green line shows the results for the FRDM model.

experimental masses is in between the predictions of the HFB-14 and the FRDM models. The magnitude of the electron capture Q-values (negative for neutron-rich nuclei) predicted by the FRDM model is larger than the HFB-14 results for the even-even nuclei (more negative), and smaller for the odd-odd nuclei. Therefore, the FRDM model predicts a larger odd-even staggering for the even mass chains in this region, which would result in a larger neutron star crust heating (Chapter 6). Figure 5.3 also shows that this difference in the predicted odd-even staggering between the two models seems to increase towards more unstable nuclei (for example, for A=70, A=58, and A=54), stressing the need of mass measurements to constrain this behavior for astrophysical simulations. In the case of the new Q-values determined in the present experiment there is no conclusive evidence to favor one model over the other. The Q-values for ^{61}V, ^{63}Cr, and ^{74}Ni agree better with the FRDM odd-even staggering, but ^{66}Mn agrees better with HFB-14, while for ^{58}Ti and ^{77}Ni neither model agrees with the experimental data.

5.2 Mass resolution of the experimental setup

The resolution and the source of the uncertainty in the final results is presented to characterize the experimental setup used, and to consider possible modifications for future experiments. In particular, a new experiment at the NSCL is planned for the region of ^{60}Ti, taking advantage of the production rates of neutron rich isotopes obtained from a recently developed ^{76}Ge primary beam [65].

The time of flight resolution of the setup was $\sigma_{\mathrm{TOF}} \approx 80$ ps, which gives a relative TOF resolution of $\approx 1.8 \times 10^{-4}$ (Figure 5.4). This TOF resolution corresponds to the TOF_{corr} value that only includes a correction for the Bρ of the beam particles. It was found that additional corrections using the measured angle at the S800 or the timing between the signals from each PMT in the scintillator detectors could improve the resolution (up to 10 %), and remove the discrepancy observed for the lighter isotopes

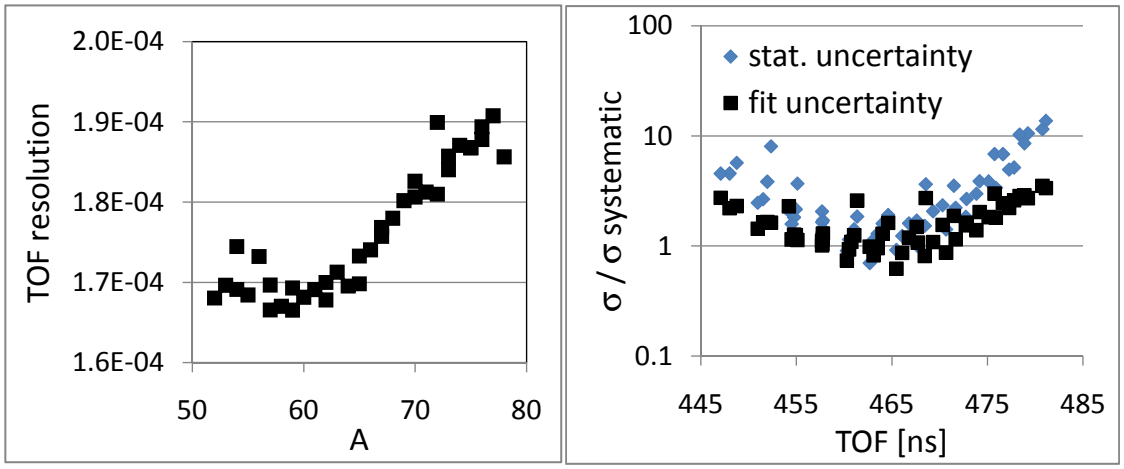

Figure 5.4: Relative time-of-flight resolution of the experimental setup (left), and contributions to the final mass error (right). The statistical uncertainty and the fit error (propagation of the uncertainty of fit parameters) are plotted relative to the systematic error obtained from the fit χ^2 normalization (Section 4.5). The σ_{sys} was 3.4 keV/q, which corresponds to 85 keV for Mn isotopes (Z=25).

and those with A$\gtrsim$65 (these corrections were not used for the final mass fit).

In addition, Figure 5.4 shows the different contributions to the mass uncertainty. As described in Section 4.5, the uncertainty is calculated from the sum of the statistical uncertainty, a fit error due to the uncertainty in the determination of the parameters of the calibration function, and a estimate of the systematic error of the setup:

$$\sigma^2_{\mathrm{mass}} = \sigma^2_{\mathrm{stat}} + \sigma^2_{\mathrm{fit}} + \sigma^2_{\mathrm{sys}} \tag{5.1}$$

From the results shown in this figure it is clear that the statistical uncertainty dominates for the neutron rich masses of interest (the ones with the largest relative TOF).

During the analysis it was found that a correlation of the measured TOF with the timing between the photomultiplier tubes (PMT) signals could be attributed to signal walk in the timing electronics (correlations of the timing with the detector's pulse height). As described in Section 4.3 the resolution could potentially be improved by

about 5 ps if this effect is canceled. With the current setup the walk correction is done by constant fraction discriminator (CFD) modules, even though their dependence was somewhat different over the range of elements in the secondary beam (the detectors signal amplitude is roughly proportional to Z^2). For that reason any TOF correction for the residual timing walk would have to treat differently the various species in the beam, and there is a risk of overcorrecting the TOF in some cases. A possibility for future experiments is to use leading edge discriminator modules for the timing, and explicitly take into account the correlations measuring PMT signal amplitude.

The TOF resolution was also improved by using rejection cuts in the S800 vault temperature spectrum ($\sim$ 2 ps). The correlation of the measured TOF with the temperature of the vault was found to be about 5 ps/°C, and it could introduce systematic shifts in the measured masses. It is not clear whether the origin of this correlation is the response of the electronic modules used to digitize the timing signals, or the change in the magnetic field of the S800 spectrometer dipoles, but probably both are contributing factors. Any measure that could stabilize the temperature of the modules at the level of 1 ° C, or decouple the power supplies of the dipole magnets from the air conditioning unit of the vault (Section 3.3.1), would be an improvement to the experimental setup.

There are different ways in which the setup can be adjusted to increase the number of statistics. About 35 % of the events the events were lost when measuring the TOF with respect to a clock signal because the PMT signals were to close to the clock one (the TAC modules have a blind range of 5 ns; Section 3.3.2). A simple adjustment of the cable delays, so that when the signal from one PMT coincides with the TAC blind range the same things happens for the second signal, would reduce the number of events lost by about one half. As an alternative, a gating scheme can be used so that the TAC skips one clock pulse when their time difference is too small, and that would avoid loosing any events. However, the logic electronic modules can introduce

significant shifts in the timing of the signals, as it was found for the systematic shift of ~ 90 ps observed in 10 % of the measurements using the direct timing TOF_1 (Section 4.3.4). Therefore the effect of any additional modules should be carefully calibrated.

Another option that is being investigated for future experiments is the use of a larger position sensitive detector at the S800 dispersive plane for the Bρ measurement (Section 3.3.3). A detector with a 10 cm active area would provide a two fold increase in the momentum acceptance of the setup (and the statistics), which is now 0.4 %.

In terms of a reduction of the fit uncertainty, it was observed that the number of calibration masses available is more relevant than their uncertainty. Since the weight of each data point in the χ^2 minimization includes the statistical contribution from the mass resolution of the setup, any literature value with an uncertainty better than ~ 100 keV will provide similar constraints to the fit. The calibration function obtained was found to be applicable only to a certain range of Z of the isotopes in the secondary beam, and there were possible calibration isotopes that could not be used (for example Ge, and Ga for high Z, and S for low Z). In that sense it is important for future experiments to minimize the elements of the experimental setup that could introduce Z-dependent systematic shifts in the measured TOF. One of them is the presence of materials in the beamline, where the reduced energy loss of the particles with low Z shifted their momentum distribution with respect to the central Bρ of the beamline, and can result in the asymmetric distributions for the transmitted fragments. A possible improvement is to use a thinner layer of gold coating for the MCP foils.

Chapter 6

Electron capture processes in accreting neutron stars

6.1 Previous work

The crust of a neutron star is a layer that extends for about 1 km between its thin atmosphere and liquid ocean (outer ~ 10 m), and the inner core. Its outermost part is composed of a lattice of nuclei in a free electron gas. The inner crust begins when the density increases above the neutron drip density, $\rho_{\rm nd} \approx 4 \times 10^{-4}\,{\rm baryons/fm^3}$, where neutrons start leaking out of nuclides and forming a free neutron gas. The extreme density conditions in the crust of a neutron star open up a series of reaction channels that can drive the nuclear composition away from the line of β stability. These are electron capture reactions in the outer crust, made possible by the increase of the chemical potential $\mu_{\rm e}$ of the electrons, and pycnonuclear fusion in the inner crust. The latter are nuclear fusion reactions at low temperatures driven by quantum tunneling due to the zero point motion of the nuclei in a very dense lattice [71]. Neutron emission and capture reactions also become important as the nuclear species in the crust become very neutron rich. All these reactions have been proposed as a source of energy for the interior of the star [72]. As discussed in Chapter 1 this energy

generation is especially important in the case of transiently accreting neutron stars, since the heat deposited in the crust during accretion contributes to the star's luminosity during quiescent periods. The heat released in the crust by nuclear reactions could also explain the puzzle of carbon superbursts observed in some systems, where the ignition depth of the burst, inferred from observations, is in disagreement with the calculations of nuclear burning of carbon in the star's ocean [17]. Extra heating in the crust might reduce the ignition depth and bring it into better agreement with the observations [18].

The first calculations of nuclear processes (pycnonuclear reactions and electron captures) in the crust of accreting neutron stars were done by Sato [73], and Haensel and Zdunik [7] (and more recently [74] and [75]) using a single ion composition for the crust. Haensel and Zdunik [7] performed a detailed calculation of the energy generated, and postulated that, because of the odd-even staggering of the nuclear binding energies, the electron captures occur in a two step mode and are the main source of energy in the outer crust. More recently, Gupta et al [18] performed calculations with a full nuclear network and a more detailed treatment of the nuclear physics. For example, they used temperature dependent electron capture rates and considered electron captures to excited states of the daughter. They demonstrated that electron captures into excited states decreases the energy radiated away as neutrinos providing additional heating of the crust. There is ongoing work to provide a more detailed treatment of the physics relevant deep inside the crust, where the density is near or beyond neutron drip. For example, Gupta et al [76] recently included electron capture delayed neutron emissions in their calculations and found a more concentrated energy deposition. Improved pycnonuclear fusion rates have been calculated by Beard et al [71].

The focus of the present calculation is to explore the impact of mass measurements on the heating of the outer crust of the neutron star, where electron captures are the

major contributors to the energy production. The evolution of the nuclear network is followed until the Fermi energy of the degenerate electrons increases to $\mu_e \approx 18$ MeV. This is the range where the nuclear masses are within reach of experimental studies at present and future radioactive beam facilities.

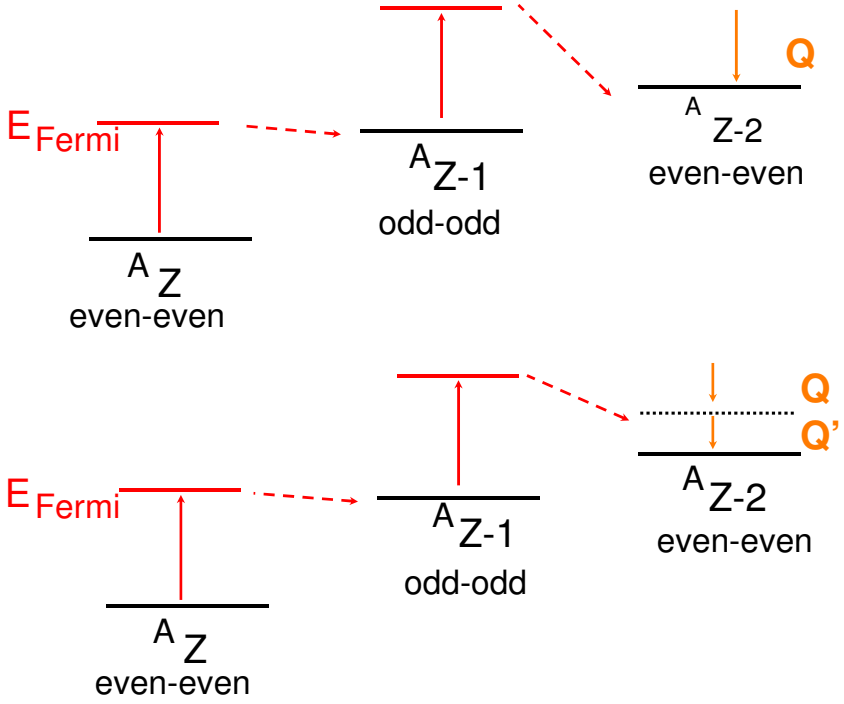

Figure 6.1: Electron captures along a even mass isobaric chain. Because of the odd-even staggering of the nuclear binding energy the second capture happens with an energy excess. If the capture proceeds through an excited state of the daughter nuclei (lower panel) a larger fraction of the excess energy is deposited after the deexcitation to the ground state (Q') because there are no neutrino losses in this last step.

The energy deposited by electron captures in the outer crust is very sensitive to the odd-even staggering of the binding energy. Figure 6.1 shows the typical situation for an even A isobaric chain. Because of the pairing force of the nuclear interaction, the even-even nuclei are more bound than the odd-odd ones, and have more negative electron capture the Q-values. As a result, after an even-even isotope has been pushed to a depth in the crust where the chemical potential of the degenerate electron gas is high enough to make the electron capture energetically possible, it will be directly followed by a second capture into the odd-odd daughter nucleus. About one fourth

of the excess energy ($\mu_e - Q_{EC}$) in the second step is deposited in the crust, and the rest is radiated away as neutrinos. In some cases the electron captures proceed through excited states of the daughter. This significantly reduces the energy fraction lost by neutrinos, because the gamma ray emitted during the deexcitation to the nuclear ground state is absorbed in the crust.

Because the time scale for the motion of the nuclei through the outer crust ($t \sim 1 \times 10^3$ years) is much larger than the capture half-lives, electron captures for each isotope will occur in a very thin layer as soon as the electron Fermi energy reaches the reaction threshold. Therefore, nuclear masses also determine the depth in the crust at which each electron capture takes place.

6.2 Model Description

The calculations are done by integrating a nuclear reactions network along the thermodynamic trajectories for density and temperature ($\rho(t)$ and $T(t)$) calculated by Brown ([72], [77]). The thermodynamic profile of the outer crust is shown in Figure 6.2. This model assumes a neutron star with a radius of 10.8 km and a mass of 1.6 $M_\odot$, accreting at a rate of $\dot{M} = 3.0 \times 10^{17}$ g/s. This is an accretion rate typical for low mass X-ray binaries, which can replace their entire crust during their lifetime. The crust is in hydrostatic equilibrium, and a degenerate and relativistic electron gas supplies the pressure and the thermal transport. For the heat transport calculation it is assumed that the nuclei are arranged in a disordered lattice. The resulting thermal profile of the crust is the same one used by Gupta et al [18]. The evolution of the nuclear reaction network was followed from a density of $\rho = 6.2 \times 10^6 \mathrm{g/cm}^3$ and a temperature of 0.42 GK (10^9 K) until the chemical potential of the degenerate electrons reached $\mu_e \approx 18$ MeV (prior to reaching the neuron drip density that divides the inner and outer crust). Because of energy loss by neutrino emissions from the core, the temperature decreases towards the center of the star in the inner crust.

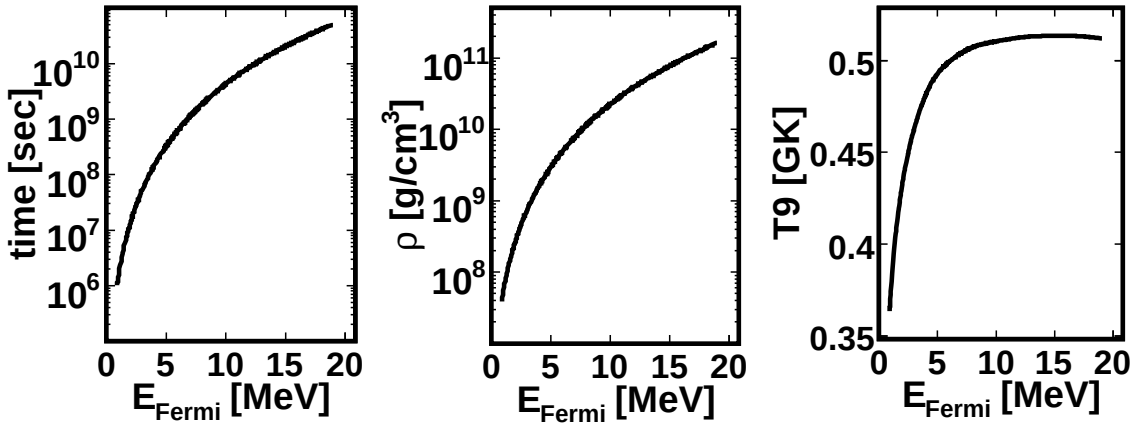

Figure 6.2: Thermodynamic trajectories for the neutron star crust used by the reaction network solver [72].

The energy generated by the nuclear reactions, and the change of thermal conductivity produced by variations in the composition of the crust will affect its thermal properties. Thus, one should iterate the results of the reaction network with the thermodynamic calculations of the neutron star crust. However, this was beyond the scope of the present study.

The nuclear reaction network used is similar to the one of Gupta et al [18]. It contains $\approx$ 1500 isotopes from Z=1 to 52, and extends from the proton rich side of stability (including the rp-process ashes) to the neutron dripline. The electron capture rates are obtained from a table of QRPA calculated Gamow-Teller transition strengths [78], which are integrated over the electrons phase space with a fast analytic approximation valid for the low temperatures of the crust [80]. This provides temperature and density dependent electron capture rates. The beta decay rates are implemented as a tabulation [78], but were not used in the calculations. This is justified since in most situations the β^- decay Q-value is smaller than the electron Fermi energy, so the transitions are blocked. The neutrino loss of each weak transition is also calculated explicitly. The neutron capture rates are calculated with a statistical Hauser-Feshbach code (NON-SMOKER [79]).

The model assumes all nuclear reactions and thermodynamic quantities have

reached a steady state, i.e. have no explicit time dependence at a given depth of the crust. To calculate the steady state crust properties as a function of depth,the nuclear reaction network can be integrated over the thermodynamic trajectories of density and temperature using the Lagrangian time $t(r)$ since a fluid element was deposited on the surface of the star. The time is given by the column depth density $y = P/g$ divided by the mass accretion rate:

$$t(r) = y(r)/\dot{m} \tag{6.1}$$

In each step of the integration the network calculates the change in the abundance of each isotope (Y_i), and the time steps are adjusted accordingly. The energy deposited in the crust is calculated as:

$$\delta Q = \mu_{\rm e} \cdot \delta Y_{\rm e} + \delta E_{\rm nuclear} - \delta t \cdot \dot{E}_{\nu} \tag{6.2}$$

In this equation $Y_{\rm e}$ is the electron abundance, $\delta E_{\rm nuclear} = \sum_i \delta Y_i \cdot M_i$ is the change in the nuclear mass excess of the isotopes in the network, and $\dot{E}_{\nu}$ is the rate of energy loss by neutrino emissions (which is multiplied by the time step δt).

The calculations were performed using two different mass tables; one corresponding to the Finite Range Droplet Model (FRDM [21]), and the other the Hartree-Fock-Bogoliubov model (HFB-14 [22]). They were used to calculate the electron capture Q-values ($Q_{\rm EC}$) and the nuclear energy $\delta E_{\rm nuclear}$. Because of the low temperatures in the outer crust, the energy distribution of the photons is not high enough for photodisintegration reactions to play a role. Therefore the neutron abundance in this region is low and $({\rm n}, \gamma)$ and $(\gamma, {\rm n})$ reactions are not needed for the calculation.

6.3 Results

6.3.1 Calculations with different mass models

Calculations with the FRDM and the HFB-14 mass models were first performed for electron captures in single isobaric chain (i.e. with an initial composition of a single isotope) to illustrate the effect of using different mass models. An interesting case was observed for the A=70 isobars, where the difference in the odd-even staggering predicted by both models differs by about 2 MeV. If, in addition, we consider capture to excited states in the daughter nuclei, there is a clearly distinct behavior for the electron captures calculated with each mass model. Figure 6.3 shows the electron capture Q value for the capture considering the lowest energy transition from QRPA calculations, which typically dominates the electron capture process. These transitions are at excitation energies of about 3 to 4 MeV in the even-even nuclei considered here. Because of the large ground state to ground state odd-even staggering predicted by the FRDM model the captures still proceed in a two step process. On the other hand, for the HFB-14 masses the transition in the second step is blocked, and the electron captures proceed in single steps resembling the odd-mass isobaric chains.

As a result of the different way in which the electron captures proceed for the different mass models there is a difference in the evolution of the composition of the neutron star crust (Figure 6.4). In the case of the HFB-14 mass model the decrease in the nuclear charge of the ions in the crust is more gradual than for the calculations with the FRDM model. Because of different Q values there is also a difference in the depth where the electron captures on the even-even isotopes take place.

When the electron captures go through an excited state of the daughter nuclei all the excitation energy is deposited in the crust regardless of the way the reaction proceeds (at threshold or in a two step process). For the A=70 chain there are three

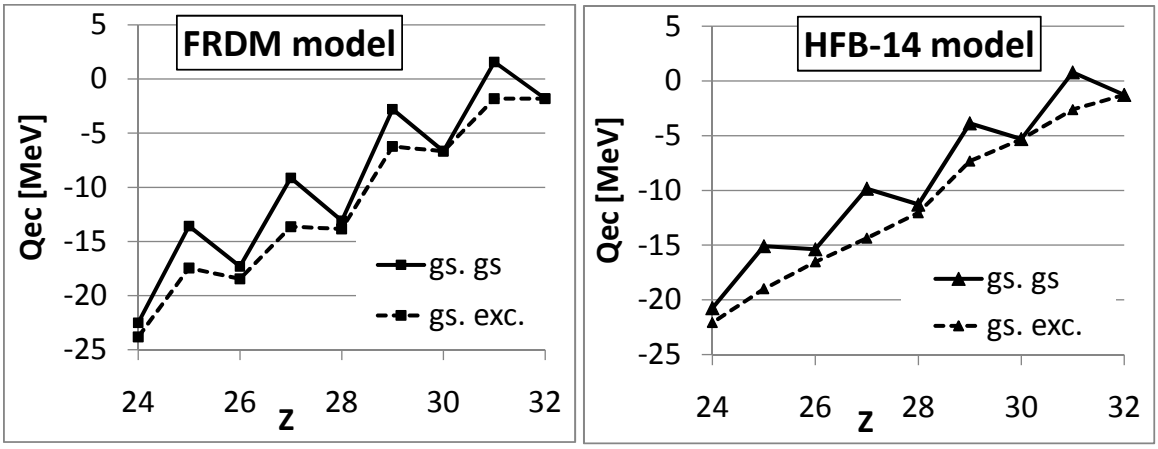

Figure 6.3: Electron capture Q value for A=70 mass chain for the two mass models used in the neutron star crust calculations. The data indicated with a solid line shows the Q value for ground state to ground state electron captures, and the dashed line indicates the Q value for the actual transitions calculated with the QRPA model (the lowest energy one).

cases with excitation energies of a few MeV (^{70}Zn, ^{70}Ni, and ^{70}Fe). Because the deexcitation of these states is the dominant contribution to the energy generation the total energy is similar in both calculations. However, this is not necessarily the case in mass chains where electron captures proceed through transitions near the ground state.

Another difference is that when the electron captures happen as one step transitions at threshold they can actually produce a localized cooling of the crust, as it is the case for $^{70}\text{Zn} \rightarrow {}^{70}\text{Cu}$ at $\mu_e \approx 5.3$ MeV. Because the finite temperature of the crust ($T \approx 0.5 \times 10^9$ K) there is a finite distribution of electrons with energies above the Fermi energy[1]. Therefore, each transition actually happens a bit before the chemical potential reaches the threshold set by the Q values. Since the more energetic electrons are the ones captured in these sub-threshold reactions there is cooling of the crust as less energetic electrons have to be promoted to fill the gaps left in the Fermi distribution. If there are many captures that happen at threshold, as it is the case

[1]The spreading of the Fermi distribution around the electron's chemical potential can be estimated as $k_B T \approx 45$ keV for the temperature of the outer crust (k_B is the Boltzmann constant.)

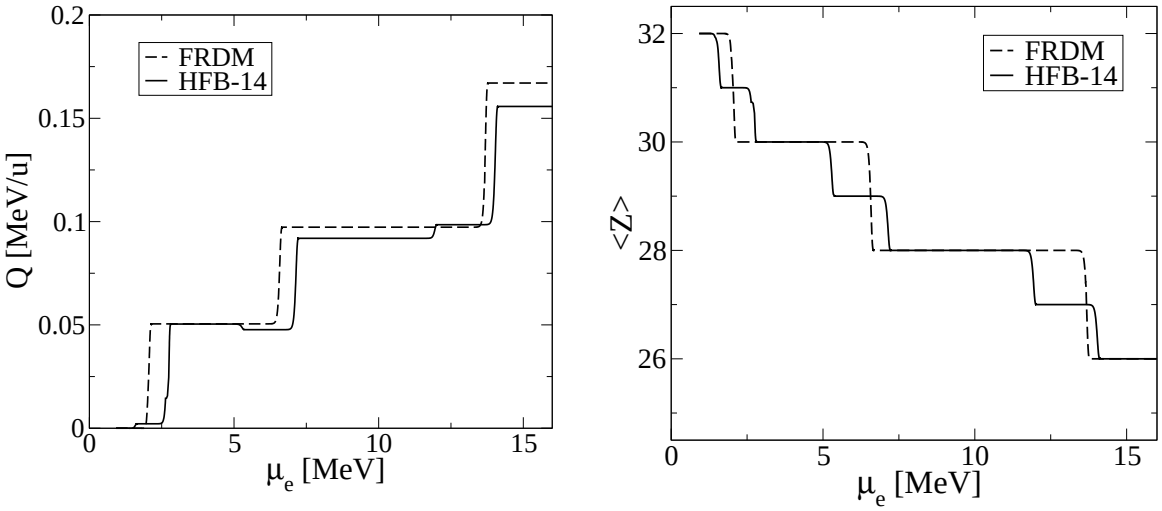

Figure 6.4: Energy released in the neutron star crust (left) and composition (right) for calculations with a single ion initial composition (^{70}Ge). Subsequent electron captures as the electron Fermi energy μ_e shift the composition towards more neutron-rich isotopes along the A=70 isobaric chain. Because of the smaller odd-even staggering predicted by the HFB-14 model the electron captures occur as one step mode processes for this case.

in the calculation with the HFB-14 model, these small energy losses will accumulate and result in smaller energy deposition.

The calculations were performed using as the initial composition for the neutron star crust the results of rp-process calculations of Schatz et al. [16]. These X-ray burst ashes are shown in Figure 6.5; they span most mass chains up to A=110. Gupta et al. [18] found that a few electron captures provide the largest contribution to the energy generated in the outer crust: $^{104}\mathrm{Ru} \rightarrow {}^{104}\mathrm{Mo}$ at $\mu_e \approx 5.2$ MeV, and $^{68}\mathrm{Fe} \rightarrow {}^{68}\mathrm{Cr}$ at $\mu_e \approx 11.8$ MeV. These captures proceed through excited states of the daughter, so the calculations with both mass models provide a similar energy deposition in each step. The main difference is in the depth at which the transitions happen, in particular the capture on ^{104}Ru that happens 330 keV earlier in the calculations with the FRDM model due to the lower electron capture Q value. The main difference observed in the spectra for the integrated energy deposition (Figure 6.6) is that in

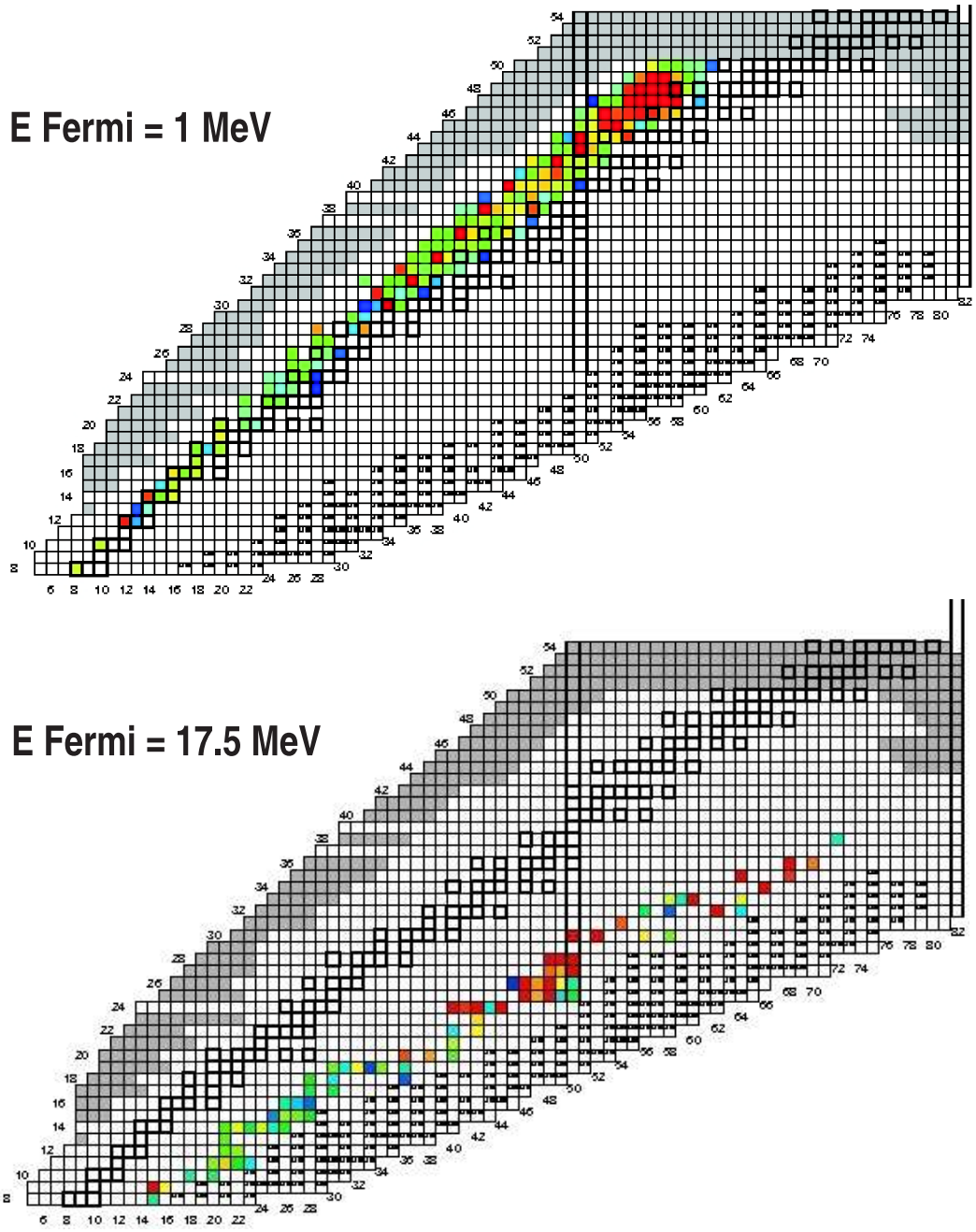

Figure 6.5: The top panel shows the composition of the X-ray burst ashes calculated by Schatz et al. [16] that are used as the initial condition for the crust calculation. The lower panel shows the neutron star composition at the end of the calculations ($\mu_e = 16.5$ MeV) using the HFB-14 mass model. The color scale goes from red (more abundant isotope) to blue (less abundant).

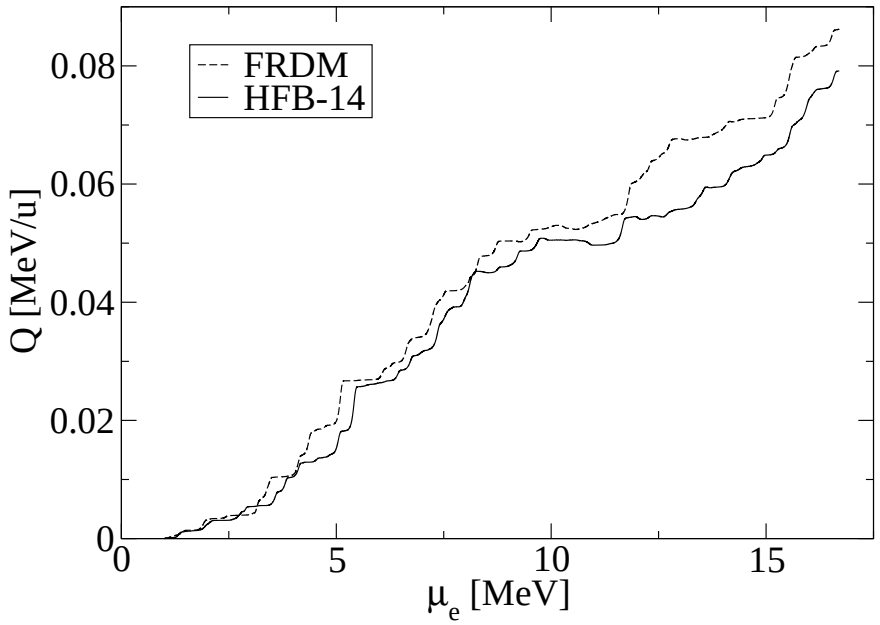

Figure 6.6: Energy released in the neutron star crust (Q) for calculations with an initial composition made up of the ashes of X-ray bursts [16]. The dashed line are the results for the FRDM mass model, and the solid line for the HFB one.

some regions the profile obtained with the HFB-14 model is much flatter than the one for the FRDM model. An example is the region from $\mu_{\rm e} \approx 10$ - 13 MeV, where there is even some cooling in some segments of the crust. This happens because most transitions predicted by the HFB-14 mass model in this region happen at threshold, and not as a two step capture. As a result, the total integrated energy deposited in the crust in the calculations with this model is 8 % smaller than the energy deposited in the calculations using the FRDM mass model (at a depth of $\mu_{\rm e} = 16.5$ MeV).

The calculations were repeated using as the initial composition the ashes of carbon superbursts [19]. These are shown in Figure 6.7. As the superbursts happen in the outer layers of the neutron star crust, at about $\mu_{\rm e} \approx 4$ MeV, the composition of their ashes is slightly neutron-rich and the electron capture reactions will not start until this depth is reached. For a complete study of the crust heating the capture reactions at shallower depths should be calculated using the ashes of stable H and He burning,

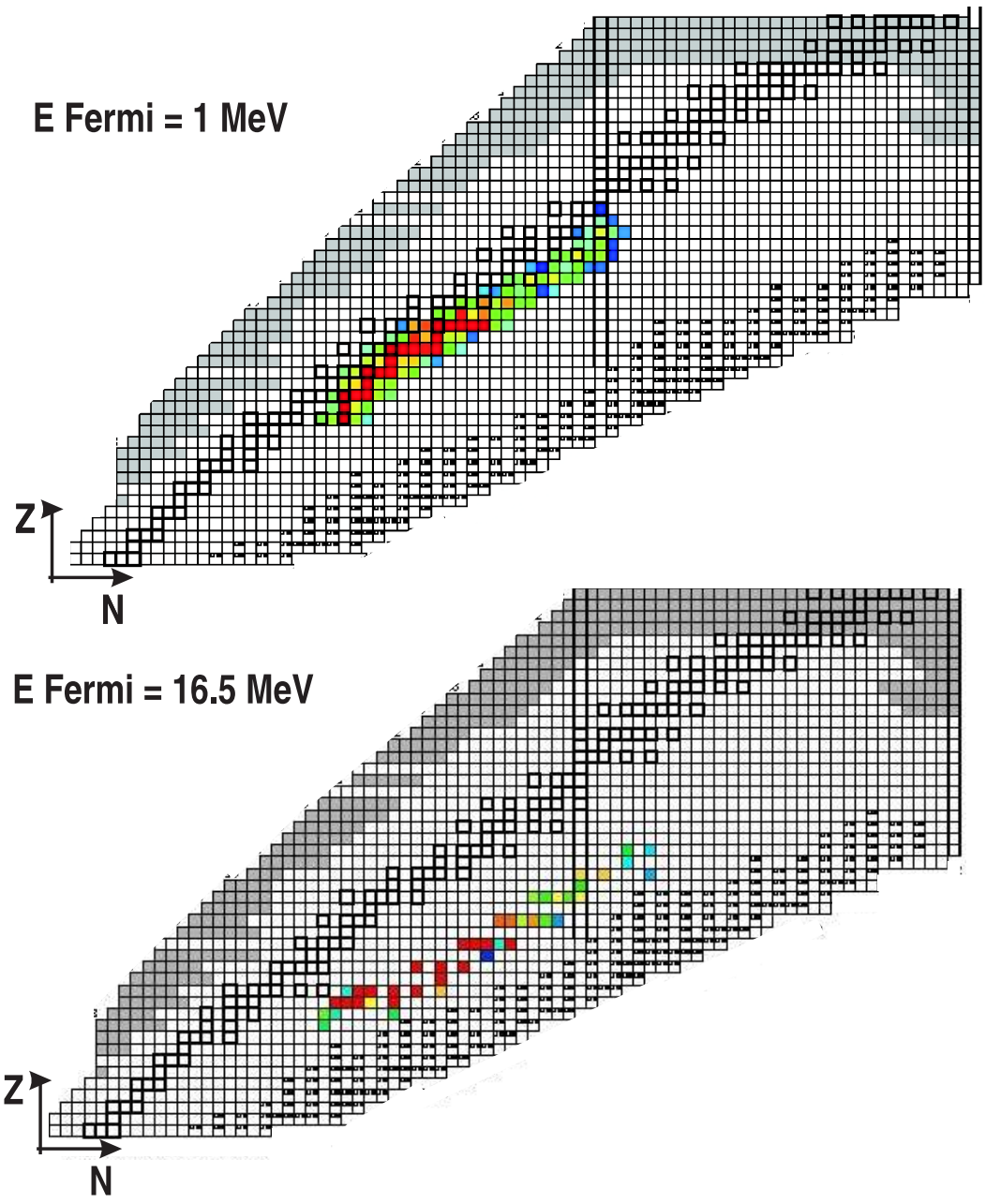

Figure 6.7: The top panel shows the composition of the C superburst ashes calculated by Schatz et al. [19] that are used as the initial condition for the crust calculation. The lower panel shows the neutron star composition at the end of the calculations ($\mu_e = 16.5$ MeV) using the FRDM mass model. The color scale goes from red (more abundant isotope) to blue (less abundant).

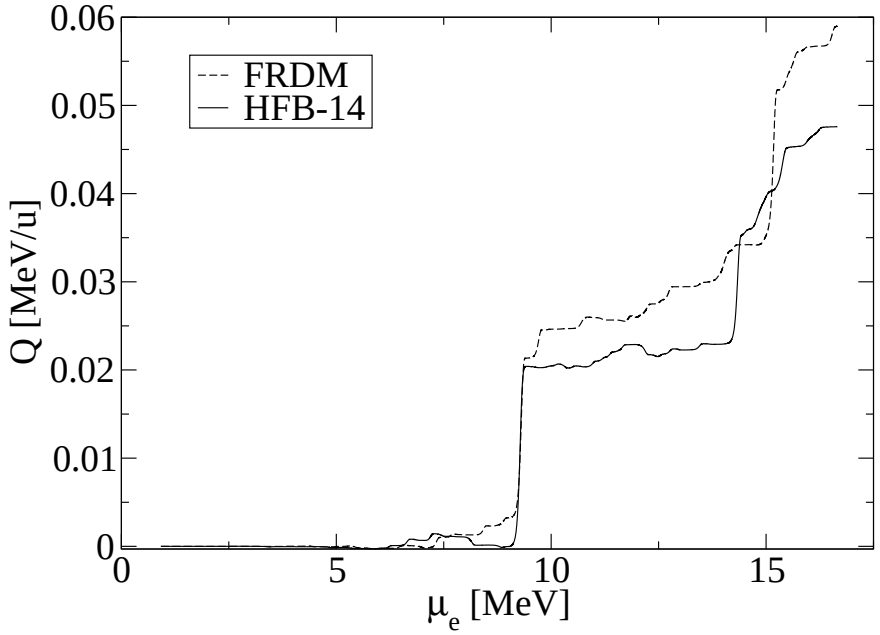

Figure 6.8: Energy released in the neutron star crust (Q) for calculations with an initial composition made up of the ashes of C superburst [19]. The dashed line are the results for the FRDM mass model, and the solid line for the HFB one.

which is believed to be the precursor material for superbursts.

Because the composition of the superburst ashes includes fewer isobaric chains ($40 \leq \mathrm{A} \leq 68$) single transitions have a larger weight in the results and the differences between calculations with the two mass models is more pronounced. The results are shown in Figure 6.8. Again there are two transitions that contribute the most to the energy deposited: $^{66}\mathrm{Ni} \rightarrow {}^{66}\mathrm{Fe}$ at $\mu_\mathrm{e} \approx 9.3$ MeV, and $^{66}\mathrm{Fe} \rightarrow {}^{66}\mathrm{Cr}$ at $\mu_\mathrm{e} \approx 15$ MeV. The first capture appears to happen at the same chemical potential for both calculations when looking at the energy deposition profile, but in fact their nature is different. In the calculations with the FRDM mass model the transition happens as a two step capture on an even-even nucleus. On the other hand, the when the HFB-14 Q-values are used the capture on ^{66}Ni happens at $\mu_\mathrm{e} \approx 8.18$ MeV but it does not proceed immediately to a capture into ^{66}Co because of the smaller odd-even staggering of the model. The subsequent capture on ^{66}Co, through a 3.6 MeV excited state of ^{66}Fe, happens then at $E_\mathrm{exc} - Q_\mathrm{EC} = 9.58$ MeV, which by chance coincides

with the capture threshold calculated with the FRDM model. The same situation happens in the electron capture on ^{66}Fe calculated with the HFB-14 model: the threshold for the capture on the even-even isotope ^{66}Fe (12.24 MeV) is smaller than the sum of the Q-value of the odd-odd ^{66}Mn and the excited state of the daughter ($E_{\rm exc} - Q_{\rm EC} = 14.66$), so the two captures happen at different depths.

It is also observed that the calculations with the HFB-14 mass model have a flatter energy deposition profile, and the integral of its energy deposition down to $\mu_{\rm e} = 16.5$ MeV is 20 % smaller than for the calculations with the FRDM mass model.

6.3.2 Impact of experimental masses

The isobaric chains relevant for the calculations of electron captures on carbon superburst ashes ($40 \leq$ A ≤ 68) coincide with the masses measured in the present experiment. Figure 6.9 shows the depth up to which experimental nuclear masses are available. The new measurements provide information on transitions happening around $\mu_{\rm e} \approx 10$ MeV. In addition, the new measurement of the ^{66}Mn mass provides a experimental value for the electron capture Q value on ^{66}Fe, which is one of the two large transitions for the calculations with superburst ashes.

Figure 6.10 compares the results of calculations where the electron capture Q-values and mass excesses are calculated with the FRDM mass models, or using experimental data complemented with the FRDM table when these are not available. One of the calculations with experimental data is performed using only the data in the literature prior to our experiment (the 2003 Atomic Mass Evaluation). As mass models are much more reliable in predicting mass differences, we follow the usual procedure and do not mix experimental and theoretical masses to calculate a Q-value. Therefore, the calculation with experimental AME 2003 masses does not include an experimental $Q_{\rm EC}$ value for ^{66}Fe. In that case the capture on ^{66}Fe happens as pre-

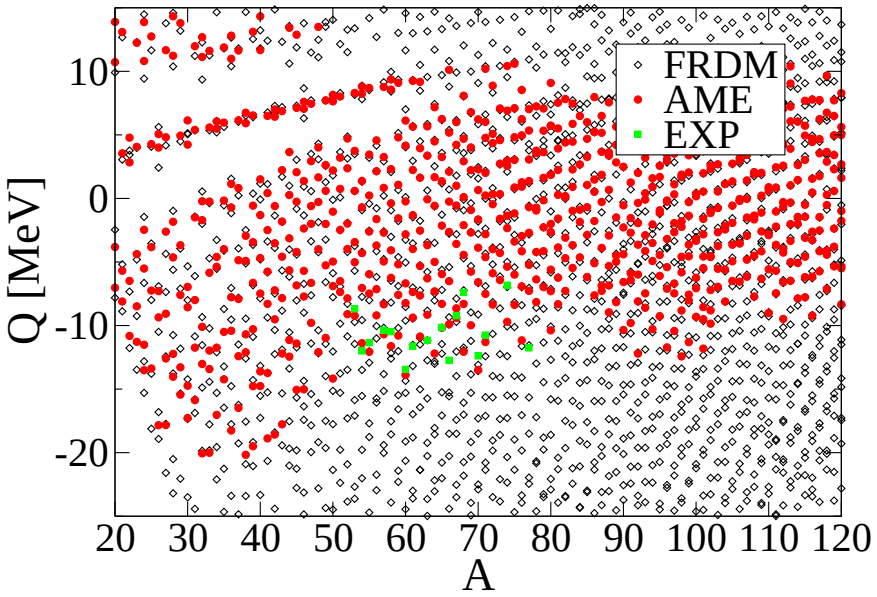

Figure 6.9: Availability of experimental data for electron capture calculations. The electron capture Q value, which directly determines the depth at the crust where each electron capture is energetically favorable, for the isotopes included in the reaction network is shown as a function of A. Only the region relevant for the calculations with X-ray burst ashes (up to A $\sim$ 105) and the carbon superbursts ($40 \leq A \leq 68$) is shown. In the latter case experimental data is available up to $\mu_e \approx 12 - 15$ MeV.

dicted by the FRDM model and there are not significant differences in the energy deposited in the crust. The mass of ^{66}Mn measured in the present experiment leads to a threshold for the electron capture on ^{66}Fe that is 2.5 MeV smaller than for the FRDM mass model. Therefore, the transition occurs at a significantly shallower depth providing a more efficient heating of the region of superburst ashes.

The electron capture on other large transition, that for ^{66}Ni, is shifted in the calculation using experimental masses compared to the results for the FRDM model. The mass of the isotopes involved in this transition are all taken from the 2003 Atomic Mass Evaluation, so the results for both calculations with experimental data are the same. The masses predicted by the FRDM model for these isotopes are increasingly more bound away from stability. They are 260 keV, 810 keV, and 1920 keV smaller than the experimental values for ^{66}Ni, ^{66}Co, and ^{66}Fe, respectively. This results in

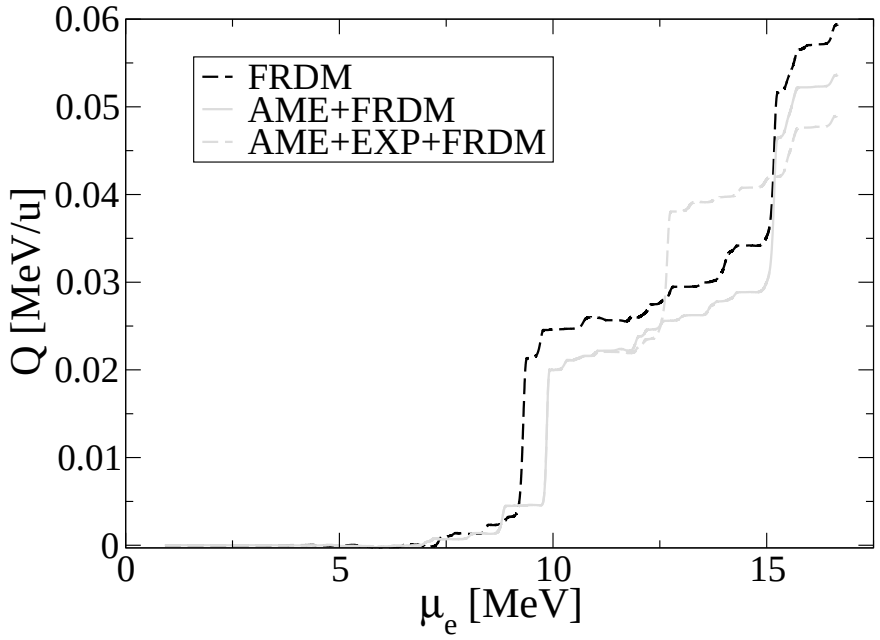

Figure 6.10: Energy released in the neutron star crust (Q) for calculations with an initial composition made up of the ashes of C superburst [19]. The dashed black line are the results for the FRDM mass model, and the grey lines are calculations using experimentally known masses complemented by the FRDM mass table. The solid grey line is the result using masses in the 2003 Atomic Mass Evaluation, and dashed grey line shows the calculation where the results from the present experiment are also included.

a threshold for the electron capture on ^{66}Ni that is about 550 keV smaller for the FRDM model. In addition, because the FRDM predicts a larger odd-even staggering for the masses of these isotopes the total energy deposited is larger than in the calculation with experimental masses (it corresponds to the energy released in the non-equilibrium electron capture on ^{66}Co).

6.3.3 Summary

In the calculations of Gupta et al. [18] it was found that electron capture transitions through a few excited states in the daughter isotopes were the major contributors to the energy deposited by nuclear reactions in the outer crust of an accreting neutron star, for both X-ray burst ashes and carbon superburst ashes. Since the energy of these excited states is independent of the nuclear mass data used in the calculations,

the largest difference observed in calculations with different sets of nuclear masses was on the depth at which electron capture reactions happened. On calculations with our new experimental mass of ^{66}Mn the electron capture on ^{66}Fe is predicted to be 2.5 MeV more shallow (smaller Q value), which would be conductive to a lower ignition depth for carbon superburst (a quantitative analysis of the effect is beyond the scope of this work but is planned for the future).

The most remarkable difference between the calculations using masses predicted with the FRDM or the HFB-14 mass models was that, because of the different magnitude of the predicted odd-even staggering of the nuclear masses, there is a significant difference in the way the electron captures on the even-even isotopes proceed. The HFB-14 model in general predicts a lower difference in the Q-value for the electron capture on an even-even isotope, and that of the subsequent capture in the odd-odd nuclei of the isobaric chain. In the case that the second capture proceeds through an excited state this is in many cases above the threshold of the capture in the even-even isotope, so the process proceeds as two captures at different depths. For the FRDM model most of the captures on an even-even isotope are immediately followed by a non-equilibrium capture in the odd-odd daughter. Such differences affect the thermal profile of the crust because, when the captures proceed as a one step process (i. e. at threshold), there is in general less energy deposited. In addition, there can even be a negative energy deposition (a slight cooling) when the electrons in the tail of the Fermi distribution are captured in reactions that happen at subthreshold. Integrated over many electron captures, these small differences resulted in an energy deposition profile that is smaller for the calculations with HFB-14 masses.

The calculations presented here clearly indicate that the choice of the mass model can have a significant impact on the results of the energy generated by electron capture reactions in the outer crust of an accreting neutron star. The most relevant property is the pairing strength predicted by each model. The experimental data

(both for previous measurements and those presented in this experiment) has a better agreement with the odd-even staggering of the nuclear mass predicted by the FRDM model in the region relevant for the carbon superburst ashes (see Figure 5.3 in the previous chapter). However, there are cases with large disagreements and where the HFB-14 model performs better. One example is the Q-value for the electron capture on ^{66}Fe, which is one of the critical reactions for the superburst ashes). Therefore, the new measurements obtained in this experiment are not sufficient to make a choice between both models. Since the odd-even staggering of the nuclear masses predicted by the HFB-14 and the FRDM models diverges away from stability, new mass measurements (specially for the even A chains) are important to settle this question.

For a completely self-consistent result, the present calculations should be iterated with the calculations of the thermal profile of the neutron star crust because the energy released will have a feedback in the variables involved in the heating mechanism. For instance, the temperature of the crust will change the electron distribution around the Fermi surface, which in turn could affect the electron captures that happen slightly before threshold.

Appendix A

TOF spectra for individual isotopes

A.1 TOF vs Bρ distributions

The TOF distribution as a function of the momentum (x_{mcp}) of the beam fragments is shown for for individual isotopes in the secondary beam. A linear and a quadratic correction functions, obtained from a global parameterization of the fit results for individual spectra (Section 4.2), is also shown.

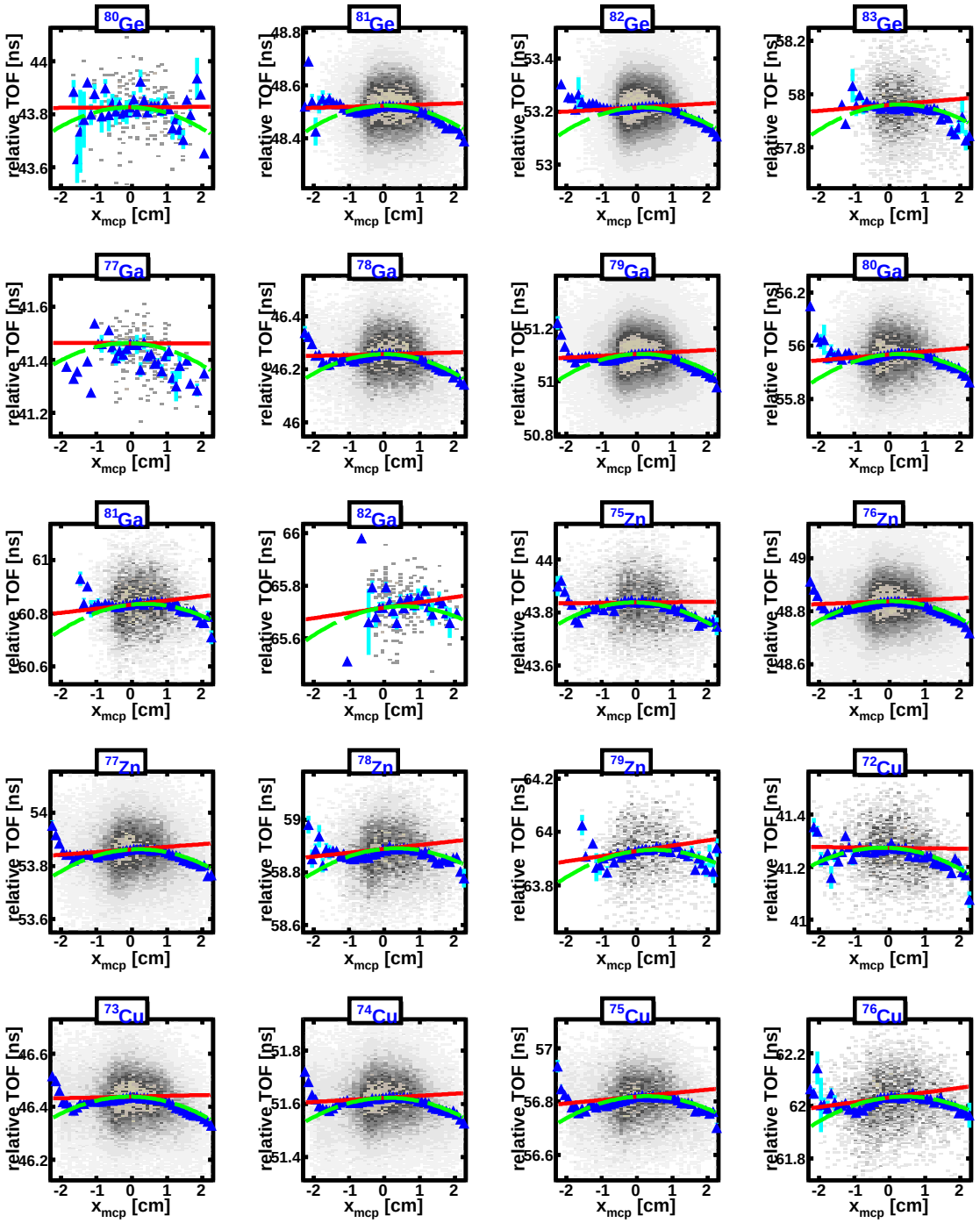

(a) First Part

Figure A.1: TOF vs x_{mcp} position at the S800 dispersive plane. The lines show results of the fits with the global momentum correction function for a linear (solid red) and a quadratic (dashed yellow) case, as described in section 4.2. A constant slope of $300\,ps/cm$ is subtracted from the data, which is also shown as a profile histogram (blue triangles).

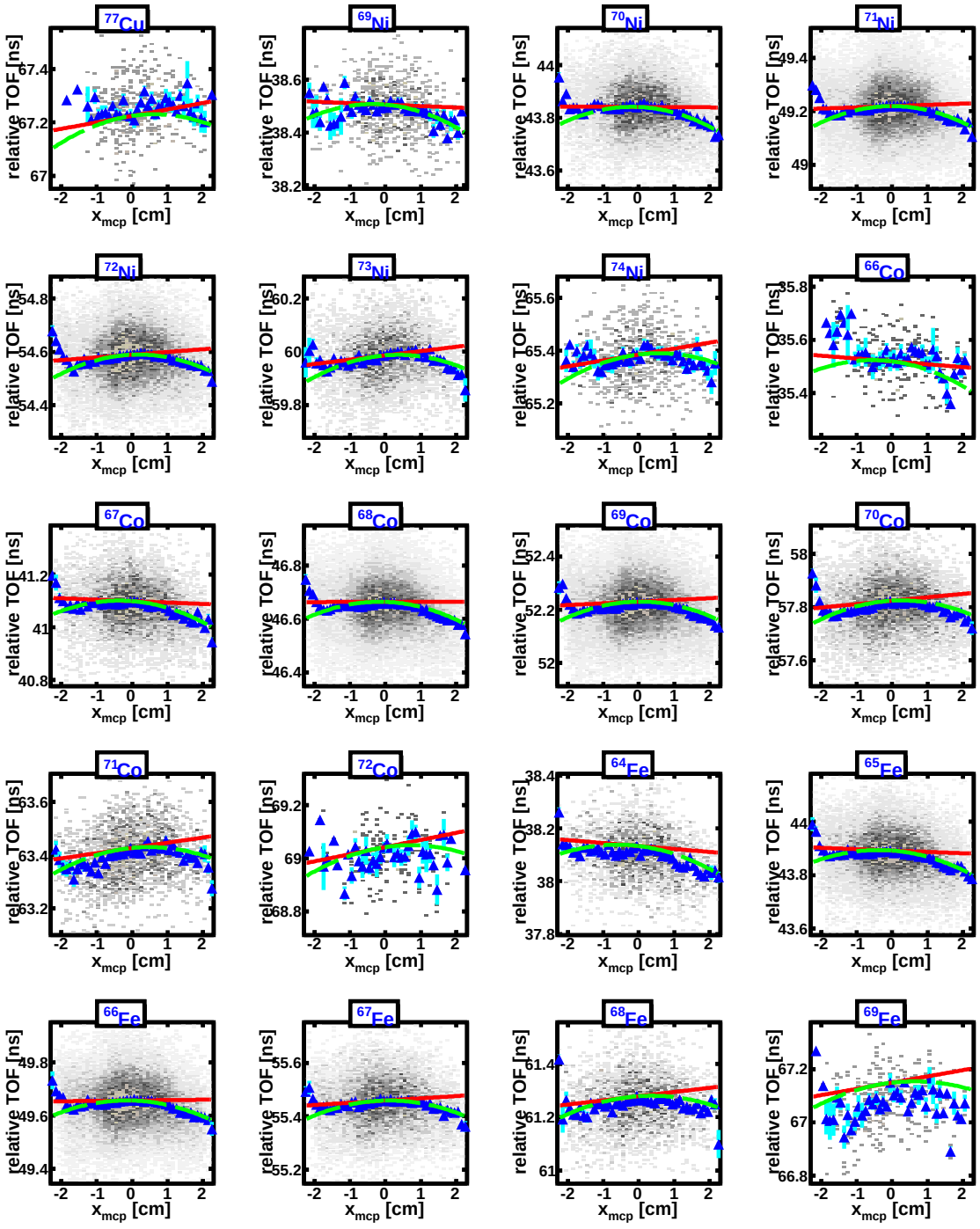

(b) Second Part

Figure A.1: Continued from previous page.

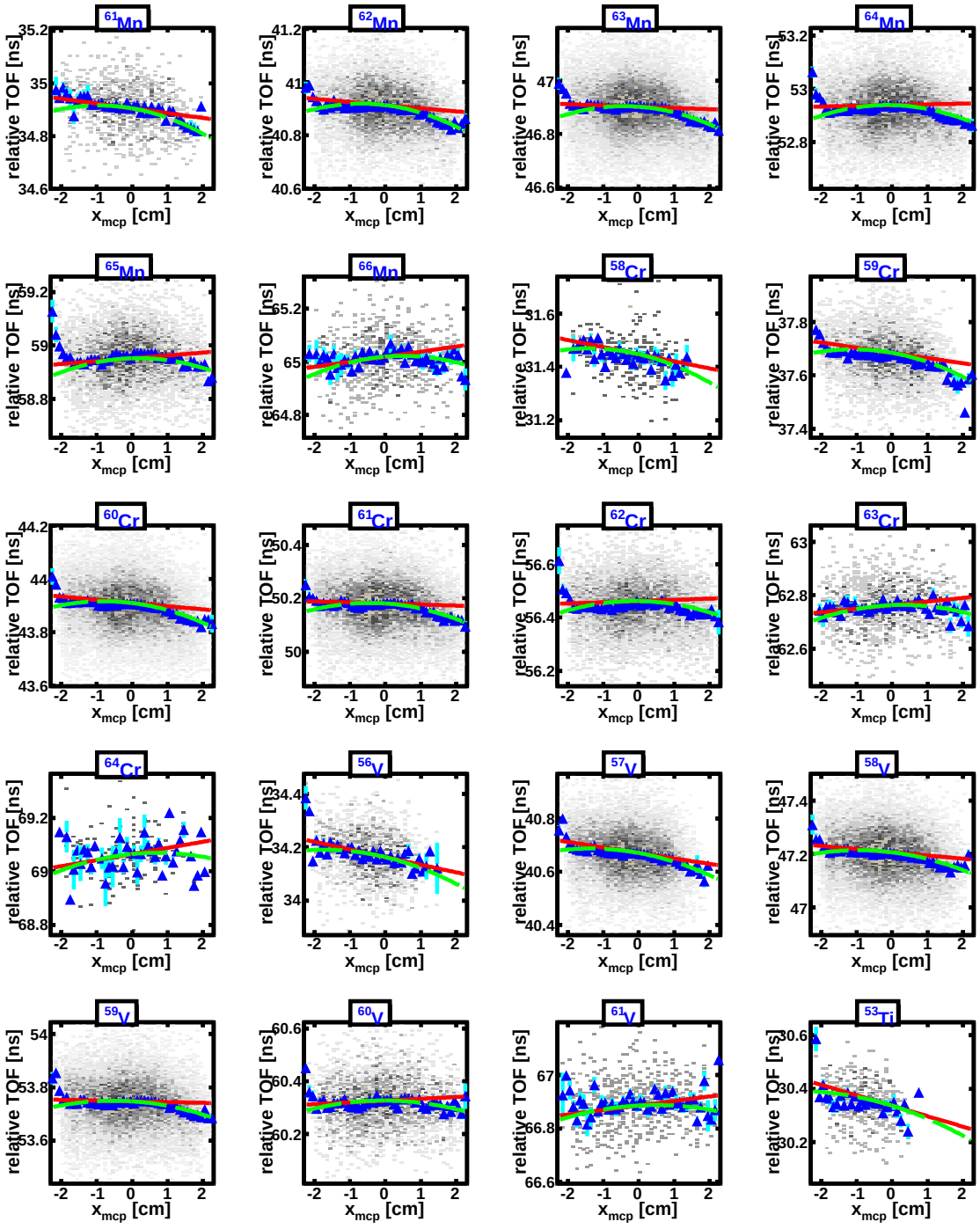

(b) Third Part

Figure A.1: Continued from previous page.

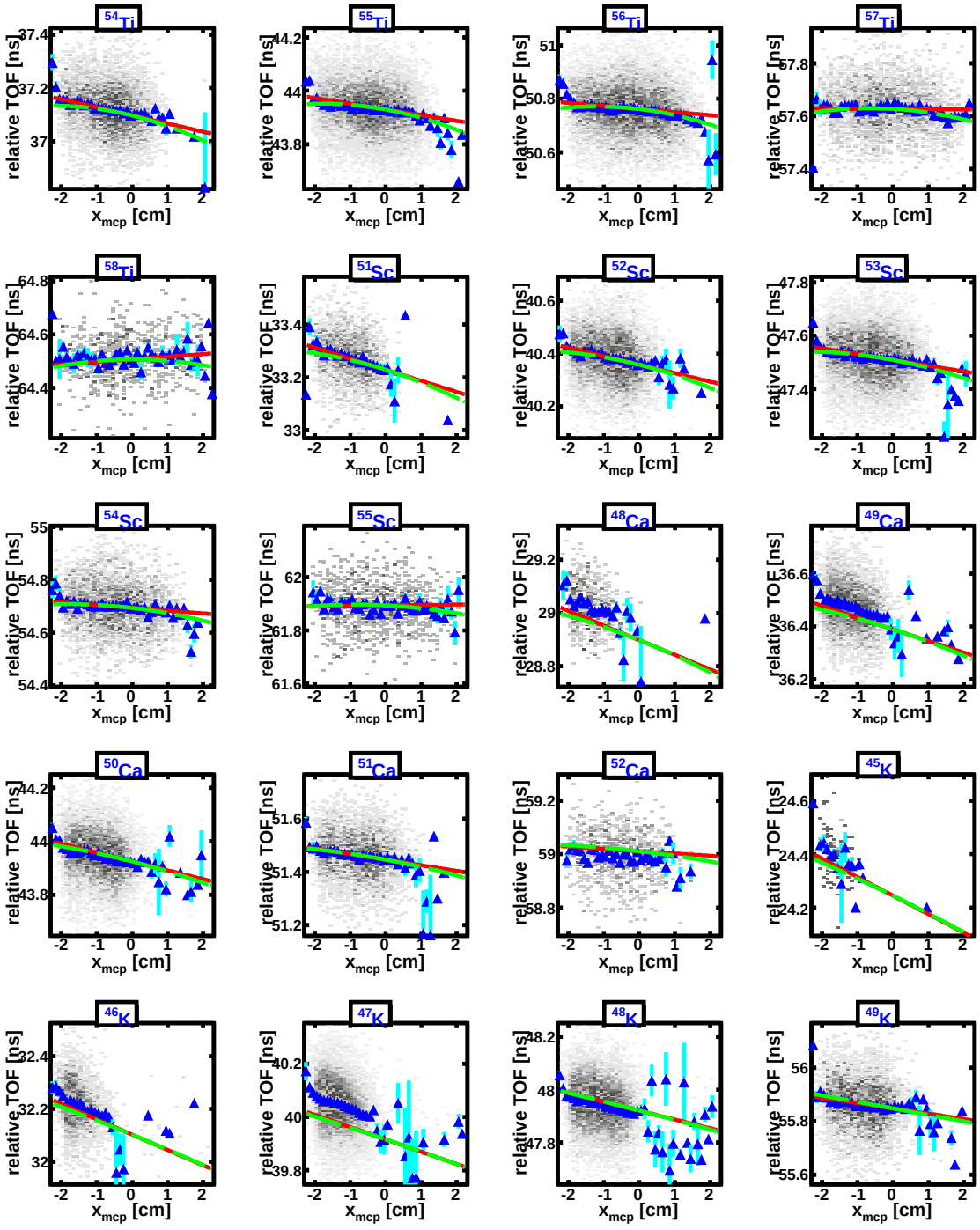

(b) Fourth Part

Figure A.1: Continued from previous page.

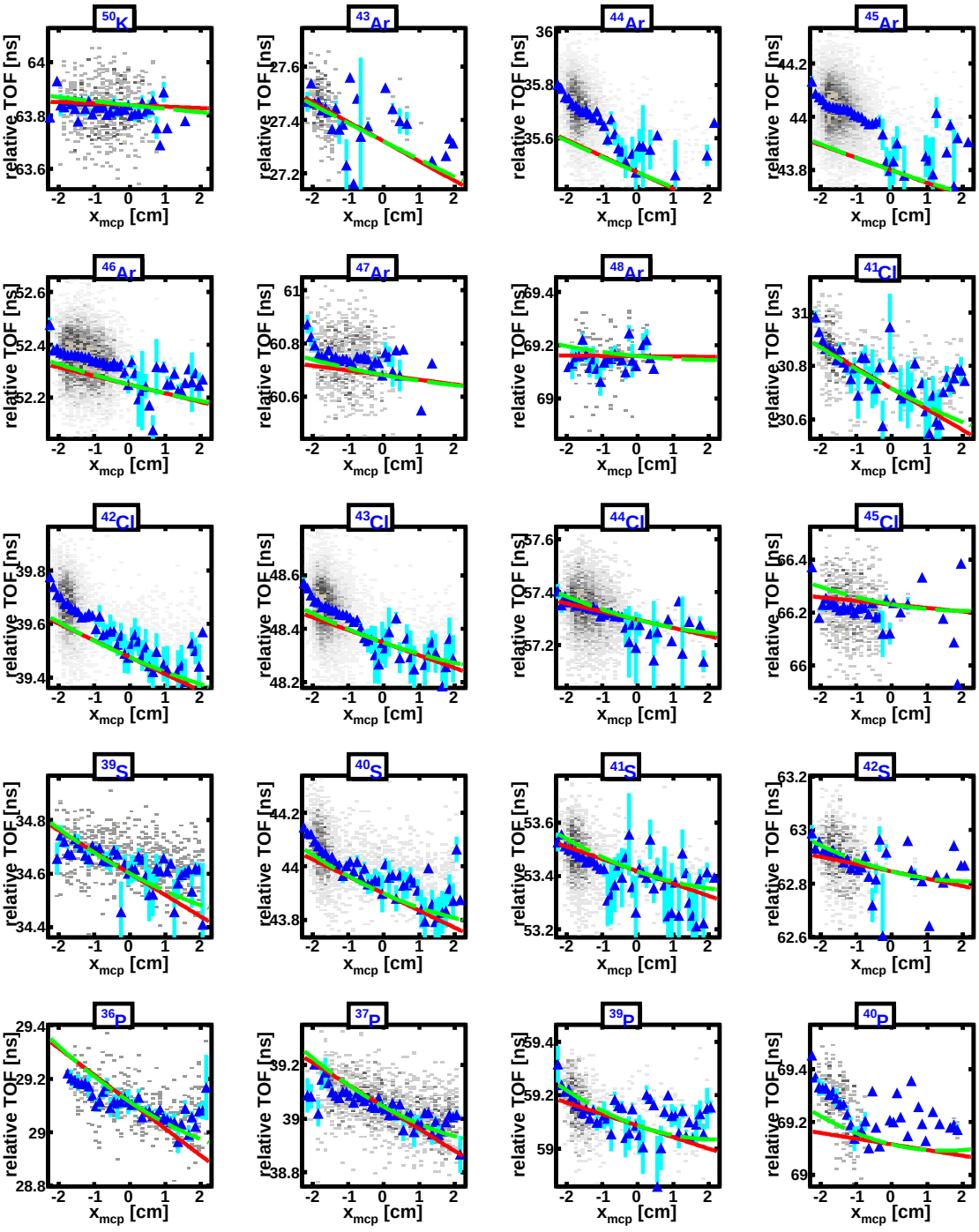

(b) Fifth Part

Figure A.1: Continued from previous page.

A.2 Determination of the TOF centroid

Distribution of the momentum corrected TOF (using the TOF_{clk} value) for selected isotopes in the secondary beam. The histograms for the isotopes used as calibration points in the mass fit are shown in grey. The isotopes for which a new mass was measured in the present experiment are shown in black. The fit of a Gaussian function used to determine the centroid of the distribution (Section 4.4) is supperimposed to the histograms.

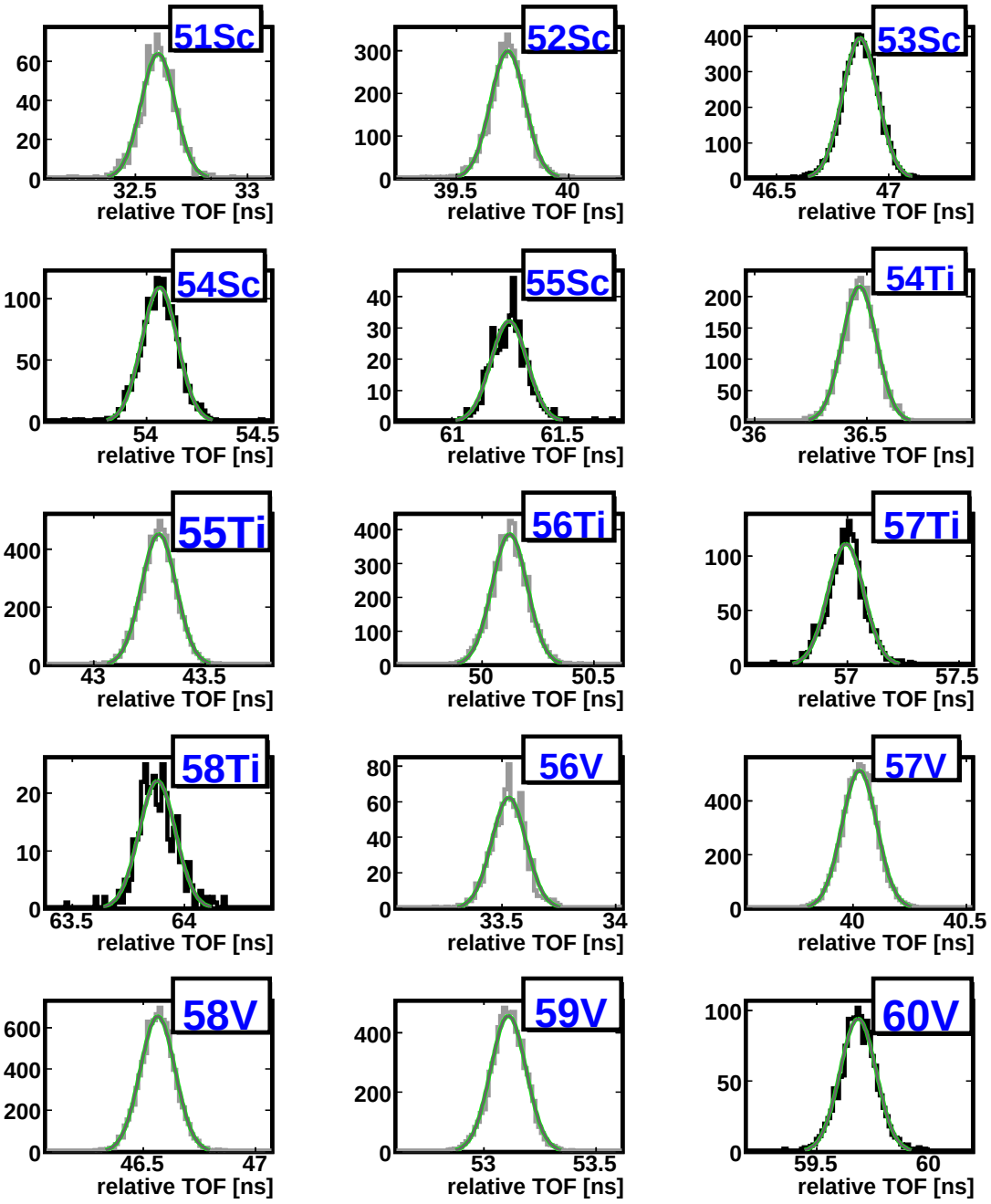

(a) First Part

Figure A.2: Momentum corrected TOF distribution for reference isotopes (grey), and for the isotopes where a mass was measured in this experiment (black). The Gaussian function was fit to the distribution to determine its centroid is supperimposed. For the isotopes with less than 1500 events the width of the distribution was not a free parameter, and a value from trends in the width of isotopes with higher statistics was used (Sectioon 4.4).

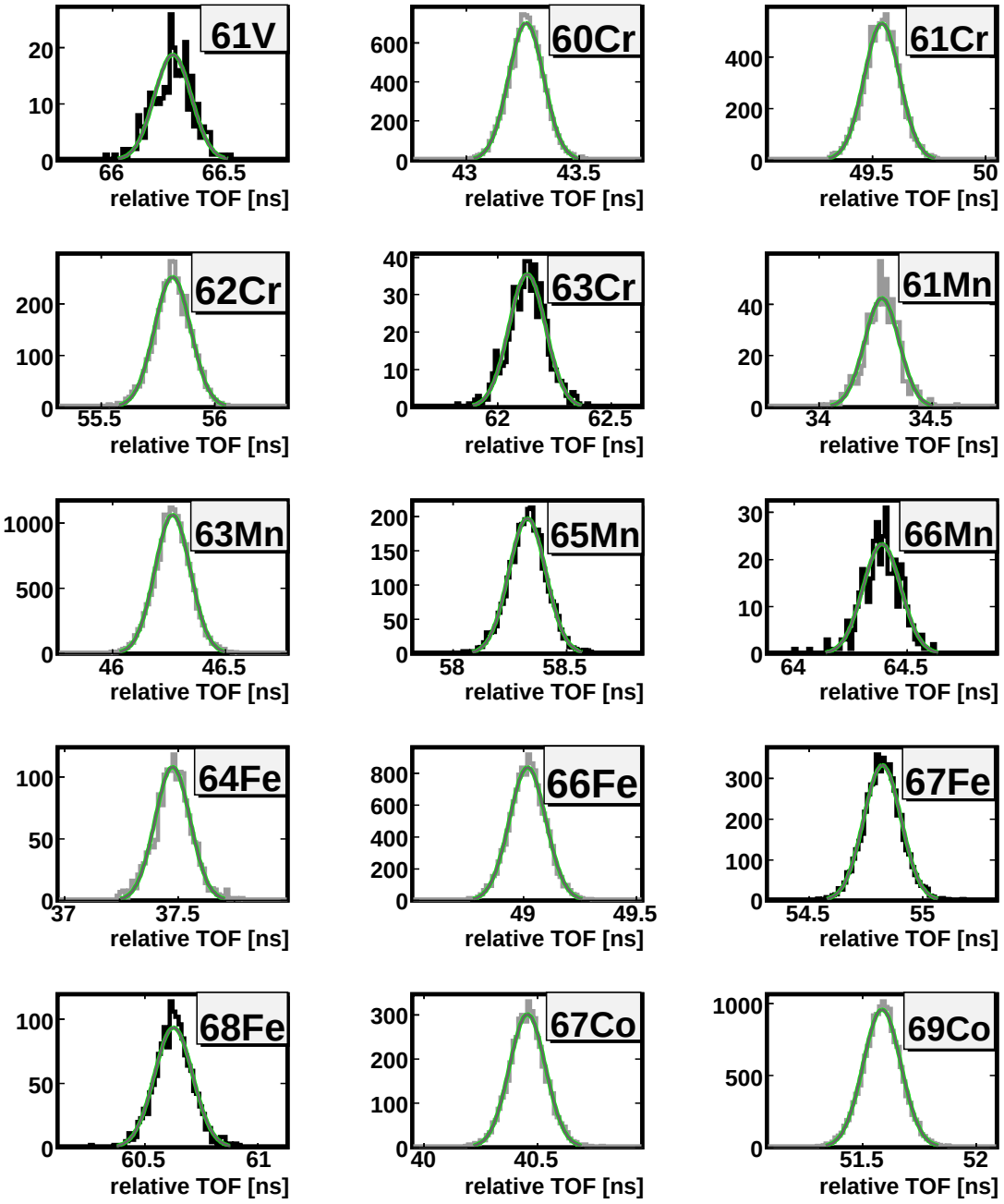

(b) Second Part

Figure A.2: Continued from previous page.

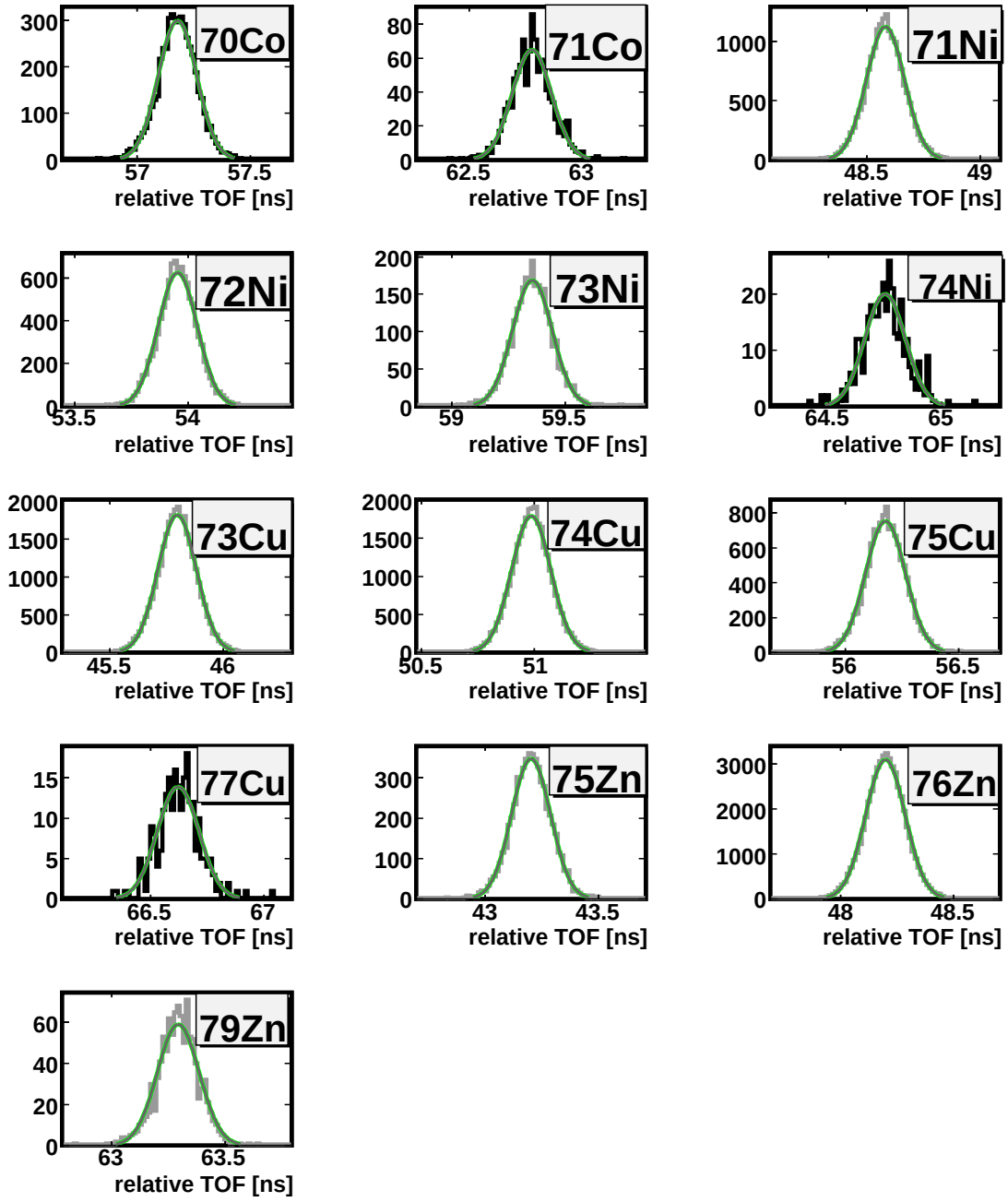

(b) Third Part

Figure A.2: Continued from previous page.

A.3 S800 vault temperature distributions

Distribution of the temperature measured at the S800 vault for during events that correspond to selected isotopes in the secondary beam. The histograms for the isotopes used as calibration points in the mass fit are shown in grey. The isotopes for which a new mass was measured in the present experiment are shown in black. Events with a temperature outside the range of $26.^{\circ}C \leq T \leq 27.65^{\circ}C$ were not included in the mass fit (Section 4.6.5).

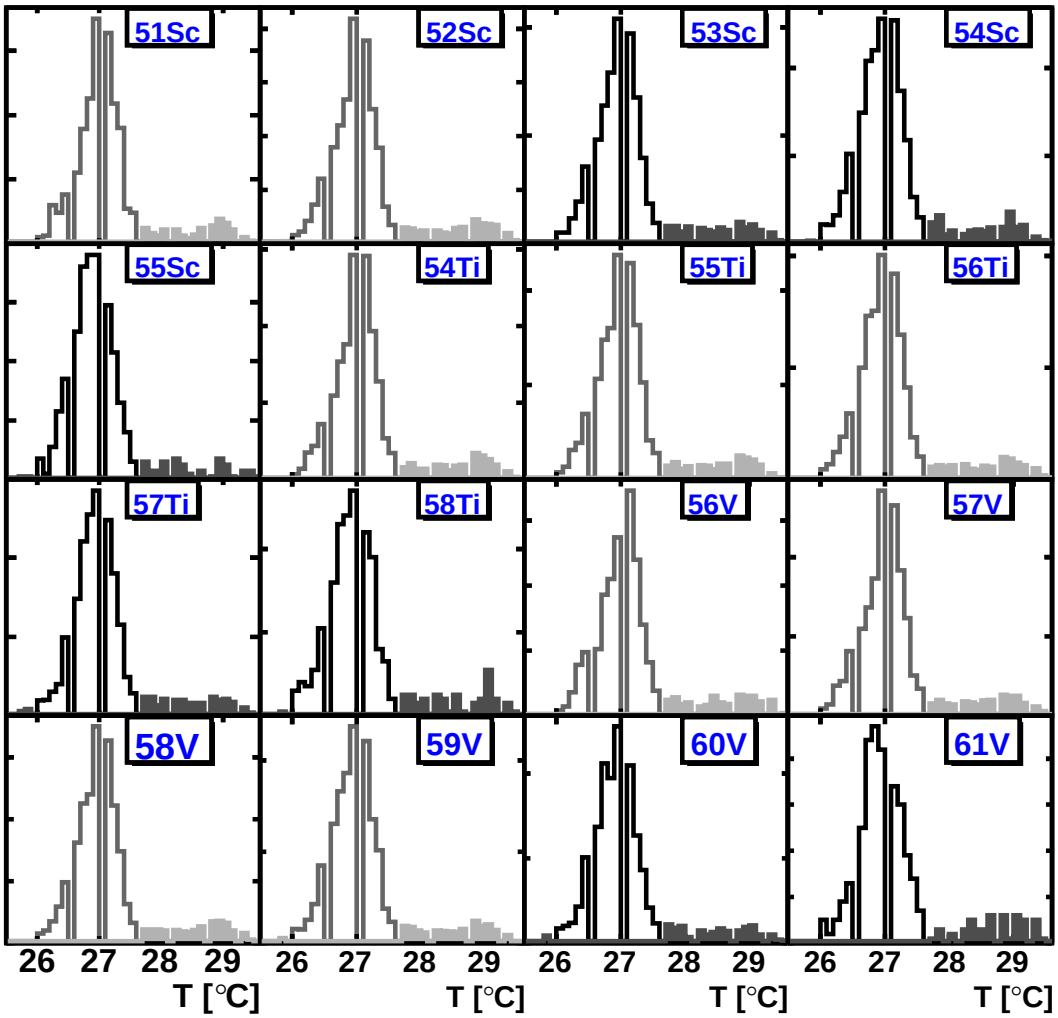

(a) First Part

Figure A.3: S800 vault temperature distribution for events corresponding to selected isotopes in the secondary beam. The histograms for the isotopes used as calibration points are shown in grey, and those for isotopes isotopes with unknown masses in black. The shaded area corresponds to events not used in the final mass fit ($T < 26.°C$ and $T > 27.65°C$).

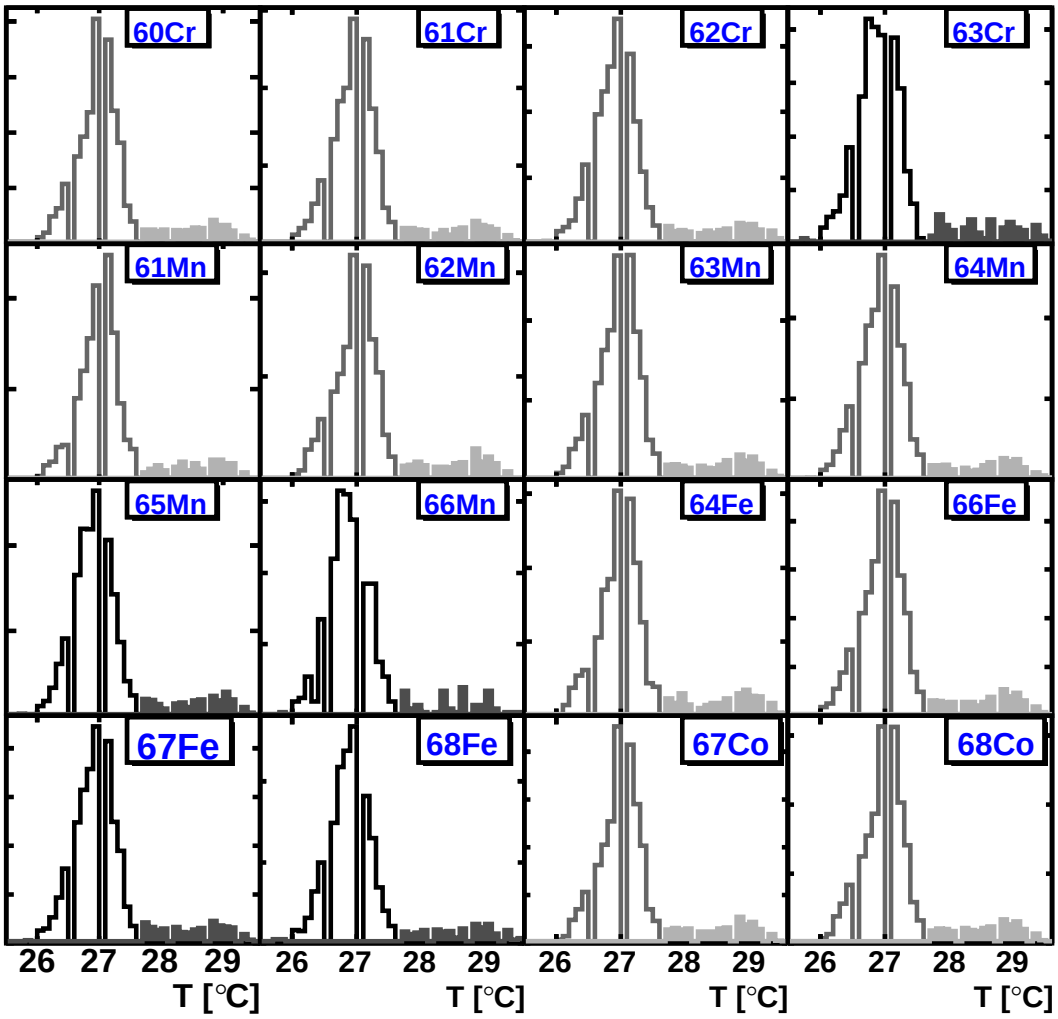

(b) Second Part

Figure A.3: Continued from previous page.

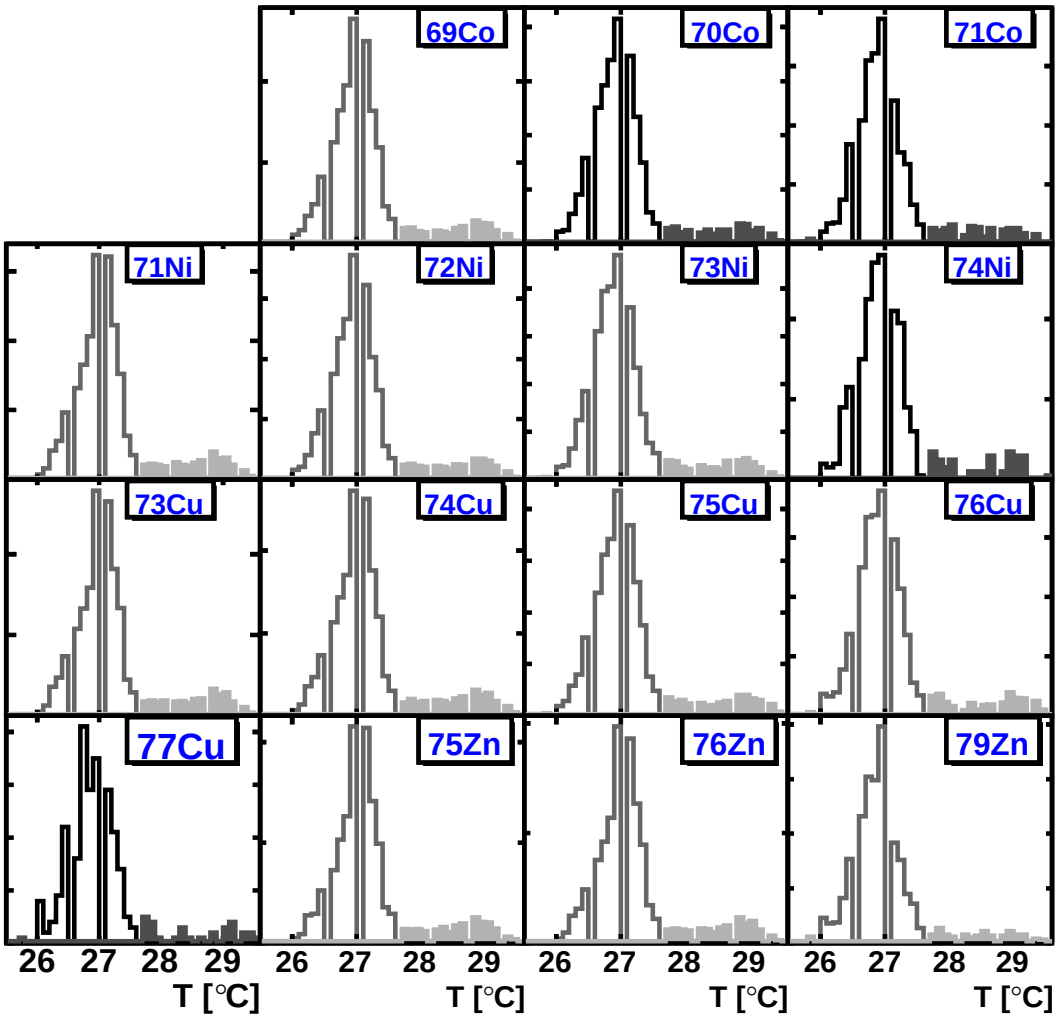

(b) Third Part

Figure A.3: Continued from previous page.

BIBLIOGRAPHY

[1] F.W. Ashton, *Nature*, (105), 617 (1920).

[2] A. S. Eddington, *The Internal Constitution of the Stars*, Cambridge University Press. (1926).

[3] E. M. Burbidge, G. R. Burbidge, W. A. Fowler, and F. Hoyle, *Rev. Mod. Phy.* **29**, 547 (1957).

[4] G. Audi, A. H. Wapstra, and C. Thibault, *Nucl. Phys.* **A729**, 337 (2003).

[5] D. Lunney, J.M. Pearson, and C. Thibault, *Rev. Mod. Phys.* **75**, 1021 (2003).

[6] J. J. Cowan, F.-K. Thielemann, and J. W. Truran, *Phys. Rep.* **208**, 267 (1991).

[7] P. Haensel and J. L. Zdunik, *A & A* **227**, 431 (1990).

[8] H. Schatz, *Int. Jour. Mass Spect.* **251**, 293 (2006).

[9] T. M. Tauris, and E. van den Heuvel, arXiv:astro-ph/0303456v1.

[10] W. Chen, C.R. Shrader, and M. Livio, *ApJ* **491**, 312 (1997).

[11] E. Brown, and A. Cummings *ApJ* **698**, 1020 (2009).

[12] C. J. Horowitz, and D. K. Berry, *Phys. Rev.* **C79**, 065803 (2009).

[13] C. Monrozeau, J. Margueron, and N. Sandulescu1, *Phys. Rev.* **C75**, 065807 (2007).

[14] D. G. Yakovlev, K. P. Levenfish, and P. Haensel, *A & A* **407**, 265 (2003).

[15] E. Brown, L. Bildsten, and R. Rutledge, *ApJ* **504**, L95 (1998).

[16] H. Schatz, et al., *Phys. Rev. Lett.* **86**, 3471 (2001).

[17] A. Cumming and L. Bildsten, *ApJ* **559**, L127 (2001).

[18] S. Gupta, et al., *ApJ* **662**, 1188 (2007).

[19] H. Schatz, et al., *Nucl. Phys.* **A718**, 247 (2003).

[20] H. Geissel, G. Münzenberg, and K. Rüsager, *Annu. Rev. Nucl. Part. Sci.* **45**, 163 (1995).

[21] P. Möller, et al., *At. Data Nucl. Data Tables* **59**, 185 (1995).

[22] S. Goriely, M. Samyn, and J.M. Pearson, *Phys. Rev.* **C75**, 064312 (2007).

[23] C. F. von Weizsacker, *Z. Phys.* **96**, 431 (1935).

[24] G. Martinez-Pinedo, et al., *Prog. Part. Nucl. Phys.* **59**, 199 (2007).

[25] H. A. Bethe, and R. F. Bacher, *Rev. Mod. Phys.* **8**, 82 (1936).

[26] M. Samyn, et al., *Nucl. Phys.* **A700**, 142 (2002).

[27] J. Duflo, and A.P. Zuker, *Phys. Rev.* **C52**, R23 (1995).

[28] R. Broda, et al., *Phys. Rev. Lett.* **74**, 868 (1995).

[29] P. Mantica, et al., *Phys. Rev.* **C77**, 014313 (2008).

[30] C. Guenaut et al., *Jour. Phys. G* **31**, S1765 (2005).

[31] O. Sorlin, et al., *Phys. Rev. Lett.* **88**, 092501 (2002).

[32] W. F. Mueller, et al., *Phys. Rev.* **C61**, 054308 (2000).

[33] C. Guenaut, et al., *Phys. Rev.* **C75**, 044303 (2007).

[34] S. Rahaman, et al., *Eur. Phys. J.* **A34**, 5 (2007).

[35] H. Savajols, et al., *Eur. Phys. J.* **A25**, 23 (2005).

[36] B. Jurado, et al., *Phys. Let.* **B649**, 43 (2007).

[37] H. L. Seifert, et al., *Z. Phys.* **A349**, 25 (1994).

[38] Y. Bai, et al., *AIP Conf. Proc.* **455**, 90 (1998).

[39] B. Ekstrom, et al., *Phys. Scripta* **34**, 614 (1986).

[40] J. R. Erskine, et al., *Phys. Rev.* **142**, 633 (1966).

[41] W. Mayer, et al., *Phys. Rev.* **C22**, 2449 (1980).

[42] M. Brauner, et al., *Phys. Let.* **B150**, 75 (1985).

[43] M. Block, et al., *Phys. Rev. Lett.* **100**, 132501 (2008).

[44] H. Savajols, *Hyper. Int.* **132** 245 (2001).

[45] J. M. Wouters, et al., *Nucl. Instr. and Meth.* **B26**, 286 (1987).

[46] Y. Litvinov, et al., *Nucl. Phys.* **A787**, 315 (2007).

[47] G. F. Knoll, *Radiation Detection and Measurement*, John Wiley & Sons, Inc. (2000).

[48] S. Nishimura et al., *Nucl. Instr. and Meth.* **A510**, 377 (2003).

[49] D. Swan, J. Yurkon, D.J. Morrissey, *Nucl. Instr. and Meth.* **A348**, 314 (1994).

[50] P. Miller et al., *Proceedings of the 2001 Particle Accelerators Conference*, Chicago, IL, IEEE 01CH37268, 2557 (2001).

[51] D.J. Morrissey et al., *Nucl. Instr. and Meth.* **B204**, 90 (2003).

[52] D. Bazin et al., *Nucl. Instr. and Meth.* **B204**, 629 (2003).

[53] A. Stolz et al., *Nucl. Instr. and Meth.* **B241**, 858 (2005).

[54] M. S. Ouellette, *Ph.D. Thesis*, Michigan State University, (2005).

[55] D. Bazin et al., *Nucl. Instr. and Meth.* **A482**, 307 (2002).

[56] PSI Graphic Transport Framework by U. Rohrer based on K. L. Brown et al., CERN 73-16 (1973) and CERN 80-04 (1980).

[57] D. Bazin, private communication.

[58] A. Dolinskii et al., *Nucl. Instr. and Meth.* **A574**, 207 (2007).

[59] D. Shapira et al., *Nucl. Instr. and Meth.* **A449**, 396 (2000).

[60] D. Shapira, T. A. Lewis, L. D. Hulett, *Nucl. Instr. and Meth.* **A454**, 409 (2000).

[61] M. S. Wallace, *Ph.D. Thesis*, Michigan State University, (2005).

[62] National Nuclear Data center, `http://www.nndc.bnl.gov` .

[63] P. R. Bevington and D. K. Robinson, *Data Reduction and Error Analysis*, McGraaw-Hill (2003).

[64] ROOT, `http://root.cern.ch` .

[65] O. Tarasov, et al., *Phys. Rev.* **C80**, 034609 (2009).

[66] M. Hannawald, et al., *Phys. Rev. Lett.* **82**, 1391 (1999).

[67] O. Sorlin, et al., *Eur. Phys. J.* **A16**, 55 (2003).

[68] H. L. Crawford, et al., *Phys. Rev.* **C79**, 054320 (2009).

[69] J. J. Valiente-Dobon, et al., *Phys. Rev.* **C78**, 024302 (2008).

[70] W. A. Ritcher, et al., *Nucl. Phys.* **A586**, 445 (1995).

[71] M. Beard, et al., *Nuclei in the Cosmos X Conference Proceedings*, PoS(NIC-X) 182 (2008).

[72] E. Brown, *ApJ* **531**, 998 (2000).

[73] K. Sato, *Prog. Th. Phys.* **62**, 957 (1979).

[74] P. Haensel and J. L. Zdunik, *A & A* **404**, L33 (2003).

[75] P. Haensel and J. L. Zdunik, *A & A* **480**, 459 (2008).

[76] S. Gupta, T. Kawano, and P. Möller, *Phys. Rev. Lett.* **101**, 231101 (2008).

[77] E. Brown, *ApJ* **614**, L57 (2004).

[78] P. Möller, and J. Randrup, *Nucl. Phys.* **A514**, 1 (1990).

[79] T. Rauscher, and F. Thielemann, *At. Data Nucl. Data Tables* **75**, 1 (2000).

[80] A. Becerril, et al., *Nuclei in the Cosmos IX Conference Proceedings*, PoS(NIC-IX) 075 (2006).